ISSN 0288-4534
CODEN: KONAE7

粉体

KONA

POWDER SCIENCE AND TECHNOLOGY IN JAPAN

No. 7 (1989)

Published by The Party of Powder Technology (JAPAN)

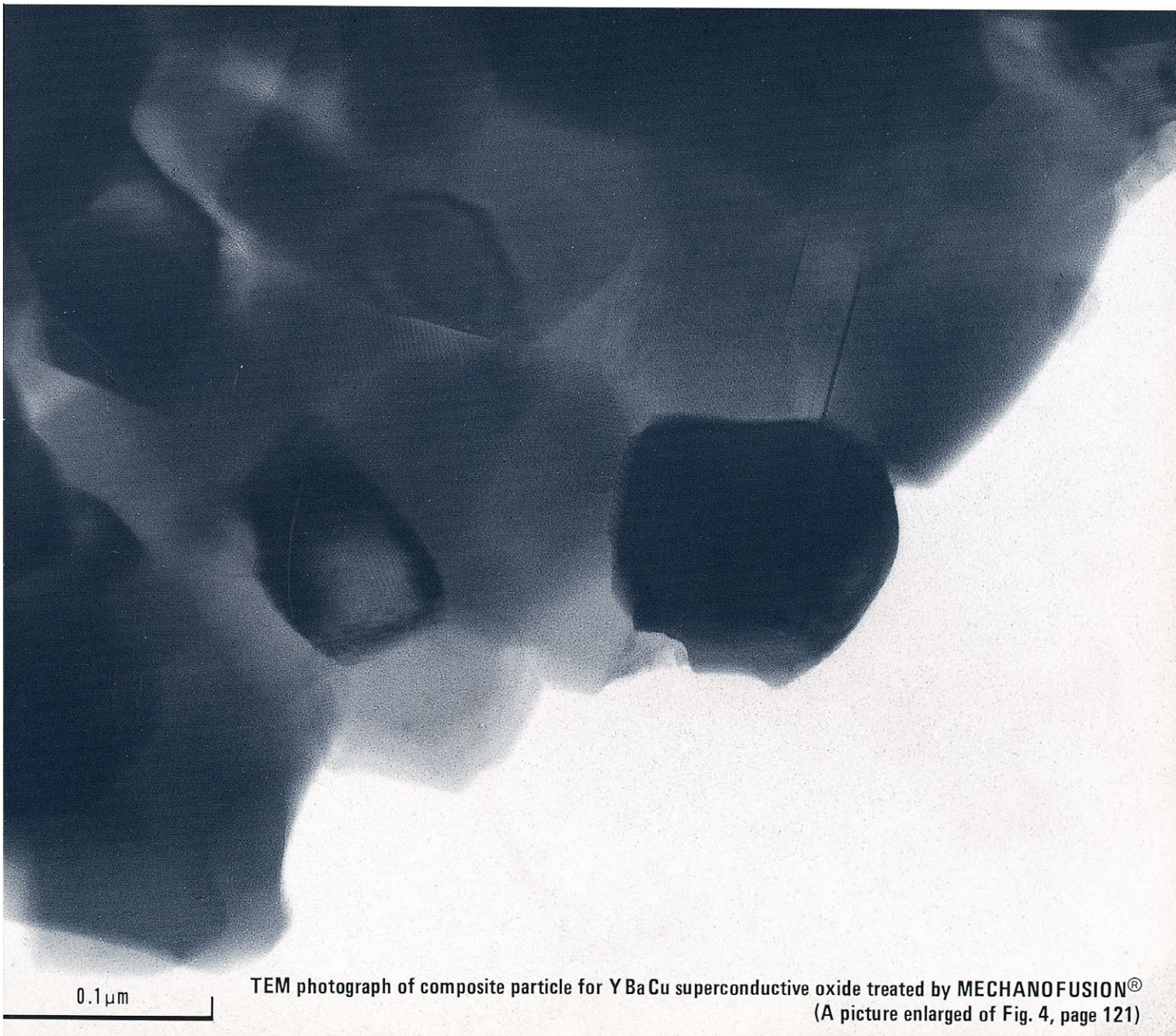

TEM photograph of composite particle for Y Ba Cu superconductive oxide treated by MECHANOFUSION®
(A picture enlarged of Fig. 4, page 121)

KONA is aimed, as its subtitle indicates, to introduce annually the recent works on powder science and technology in Japan to the interested parties in the world. It consists of the English version of reports and reviews carefully selected out of the latest papers which were originally written in Japanese.
KONA is distributed without charge to senior researchers, institutions and libraries in this field throughout the world under the sponsorship of Hosokawa Micron Corporation. Within these limits the editors are always glad to consider the addition of names to the mailing list.

Explanation of the Cover
" 粉 "; This Chinese character is pronounced as "KONA" in Japanese and means "Powder"
" 粉 " on the front page was written by the late Mr. Eiichi Hosokawa, founder of Hosokawa Micron Corporation.

Hosokawa Micron Corporation and its R&D Center

Publication Office and Owner of Copyright
The Party of Powder Technology (Japan)
in **Hosokawa Micron Corporation**
No.9, 1-chome, Shoudai Tajika, Hirakata-shi, Osaka 573 Japa

(Complimentary Copy)

Printed in Japan

KONA Powder Science and Technology in Japan *No. 7 (1989)*

Contents

See page 119 for description of the cover photograph.

Letter from the editor

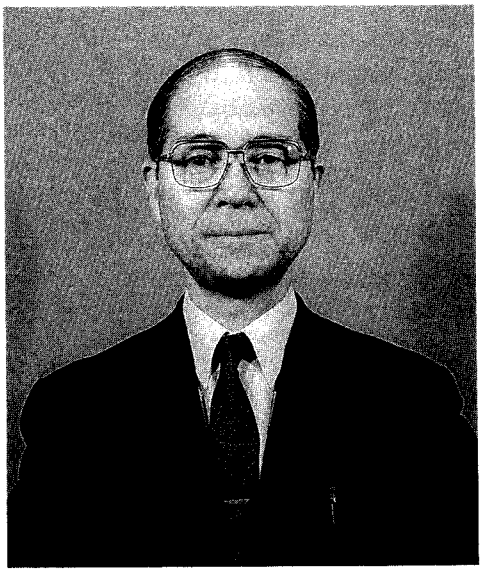

Editor in chief
G. Jimbo

Letter from the editor

It is six years since the first issue of KONA appeared, and the word of KONA is now, I believe, becoming an international symbolic word related to powder technology.

Translation of a word into another language is always very difficult, sometimes almost impossible. It is especially so when we try it between Japanese and western languages because of their different cultural backgrounds.

KONA, the title of this journal, would be one of the best examples. The simple translation of KONA is "powder". But the image which Japanese people imagine from KONA is certainly different from those which English speaking people imagine from "powder".

Nobody will deny that powder technology as a science is and must always be the same all over the world. However, powder technology in each country has its own characters, just like the word, powder or KONA, has those of its own. There is no Japanese powder technology, but powder technology in Japan might have some specific characters, which this journal, KONA, has been trying to convey to the powder scientists and technologists of the world. I believe that attempt has been successfully achieved under the leadership of Professor N. Yoshioka, the former chairman of the editorial committee of this journal.

Since I succeeded Professor Yoshioka's position one year ago, there has indeed been no change of philosophy in editing this journal. But as powder technology is changing very rapidly in this innovation era, the journal about it should also change. KONA can not be an exception. The change will be on the line of internationalization, on which Japanese powder technology is now proceeding, as the organization of the Second World Congress Particle Technology in Kyoto shows. Very rapid internationalization of Hosokawa Micron Corporation, the sponsor of this journal, might be another very important factor in the trend.

Still however, KONA will keep its unique character in a more international perspective, and, I believe, will continuously be adding some new phase to powder technology.

The Effects of Particle Properties on the Parameters of Impact Sound between Two Particles†

Jusuke Hidaka, Atsuko Shimosaka and Shigeo Miwa
Department of Chemical Engineering
*Doshisha University**

Abstract

The parameters of impact sound between two particles are discussed to measure the particle size and velocity of colliding particles by the analysis of that impact sound. The radiation mechanism of the impact sound is considered theoretically, and the pressure waveform of the sound is estimated on the basis of the radiation mechanism. The calculation of pressure waveform takes account of the reflection of the impact sound from the surface of the colliding spherical particle. The estimated waveform agrees well with the measured one.

The parameters of impact sound related closely to the particle size and impact velocity between particles.

The results show that it is possible to measure the particle size and velocity of flowing particles by the analysis of flow noise.

1. Introduction

Many particles having comparatively large masses move vigorously in powder industrial process. The particles, therefore, cause a large collision and friction among particles and between particles and the container walls. This discharges energy with high sound out of the process line. That is, such radiated sound stems from the movement of particles inside the process system. The parameters of this radiated sound is determined by the properties and movement of these particles. This leads us to suppose that elucidating the relationship between the particle properties and parameters of radiated sound will make it possible to make particle size measurements using radiated noise waveforms.

One of the most widely-known pulverization measurement methods using radiated sound is the long-history measurement of the intra-mill residual quantity during cement pulverization. Another measurement, consisting of measuring rates of powder flow from hoppers, has been conducted experimentally[1]. However, all these measurement methods use the empirical correlation between the target quantity of state and radiated sound parameters. No report has been released on the acoustic pulverization measurements.

Most of the radiated sound stemming from the flow or mixture of particles in a hopper or the vigorous movement of particles in an air transportation pipeline results from the noise released by particles colliding with one another. The first step in a basic study of such radiated sound should consist of elucidating the relationship between the parameters of two colliding particles, particle properties, and particle movement status. Several experiments on the impact sound released from two steel balls have been reported to basically examine ways to inhibit machine noise. Nishimura and Takahashi[2] indicated that impact sound pressure is proportional to the gravity center acceleration and sectional area of steel balls as deformed by collision. Koss and Alfredson[3] determined the impulsive velocity potentital of a steel ball and synthesized a sound pressure waveform on the

* Karasumaru, Imadegawa, Kamigyo-ku, Kyoto-shi, 602
TEL. 0750-251-3847

† This report was originally printed in *J. Soc. Powder Technology, Japan,* **24**, 655-663 (1987) in Japanese, before being translated into English with the permission of the editorial committee of the Soc. Powder Technology, Japan.

assumption that two steel balls form a dipole. Tomita *et al.*[4] estimated a sound pressure waveform by synthesizing sound released from each of the ultrasmall portions of the sphere surface, at the observation point.

Sound pressure waveforms estimated using the above methods agree comparatively well with observed waveforms in the direction of impact axis, where sound pressure peaks, but does not agree well in other directions. This, we believe, is because the above methods do not allow for effects of the reflection and diffraction conducted by colliding balls.

Our study consists of three parts:

(1) estimating sound pressure waveforms of impact sound released from colliding particles, with due consideration given to the reflection effect of colliding particles; and
(2) conducting collision tests on two steel balls and indicating that observed waveforms of impact sound agree well with calculated waveforms at all observation points;
(3) examining the relationship between impact speed and resulting sound pressure, and between the diameters of colliding steel balls and resulting waveforms.

2. Impact sound generation mechanism and estimation of sound pressure waveforms

2. 1 Acceleration during collision

Impact sound from spherical particles stems from the particle surfaces quickly accelerated by the colliding particles[2]. An acceleration waveform acting on two particles colliding elastically can be obtained using Hertz's elastic contact theory[5] described below. When spherical particles (1) and (2) having diameters of a_1 and a_2 respectively as shown in **Fig. 1** collide with each other at relative speed v_0, the following equation holds for the elastic deformation $\xi(t)$ and deformation acceleration $\ddot{\xi}(t)$:

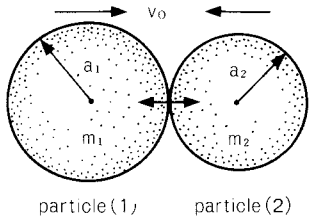

Fig. 1 Collision between two elastic particles

$$\ddot{\xi}(t) = -q_1 q_2 \xi(t)^{\frac{3}{2}} \tag{1}$$

where

$$q_1 = \frac{m_1 + m_2}{m_1 m_2}, \quad q_2 = \frac{4}{3\pi}\left(\frac{1}{\delta_1 + \delta_2}\right)\sqrt{\frac{a_1 a_2}{a_1 + a_2}},$$

$$\delta_{1,2} = \frac{1 - \nu_{1,2}^2}{\pi E_{1,2}} \tag{2}$$

and m_1 and m_2 are the masses of particles (1) and (2), ν_1 and ν_2 are their Poisson's ratios, and E_1 and E_2 are Young's moduli. Elastic deformation $\xi(t)$ can be expressed approximately as:

$$\xi(t) = \xi_m \sin \frac{1.068 v_0 t}{\xi_m} \tag{3}$$

where ξ_m is the maximum deformation of the colliding particles and can be expressed as:

$$\xi_m = \left[\frac{15\pi v_0^2 (\delta_1 + \delta_2) m_1 m_2}{16(m_1 + m_2)}\right]^{\frac{2}{5}} \times \left[\frac{a_1 + a_2}{a_1 a_2}\right]^{\frac{1}{5}} \tag{4}$$

The following two equation holds for contact time T and maximum deformation acceleration $\ddot{\xi}_m$ and impact velocity:

$$T = 4.53\left[\frac{(\delta_1 + \delta_2) m_1 m_2}{m_1 + m_2}\right]^{\frac{2}{5}} \times \left[\frac{a_1 + a_2}{a_1 a_2}\right]^{\frac{1}{5}} v_0^{-\frac{1}{5}} \tag{5}$$

and

$$\ddot{\xi}_m = 2\alpha_m = -q_1 q_2 \left[\frac{15\pi(\delta_1 + \delta_2) m_1 m_2}{16(m_1 + m_2)}\right]^{\frac{3}{5}} \times \left[\frac{a_1 + a_2}{a_1 a_2}\right]^{\frac{3}{10}} v_0^{\frac{6}{5}} \tag{6}$$

Assuming that the particle deformation acceleration equals gravity center acceleration, the acceleration waveform $[\alpha(t) = \frac{1}{2}\ddot{\xi}(t)]$ of the particle surfaces due to collision can be obtained from Eqs. (1) and (2).

2. 2 Estimation of sound pressure waveforms of impact sound

The first step is to determine the sound pressure waveform (impulse response) radiated by a particle when unit impulse acceleration acts on it. The velocity potential $\phi'(r, \theta, t)$ of sound

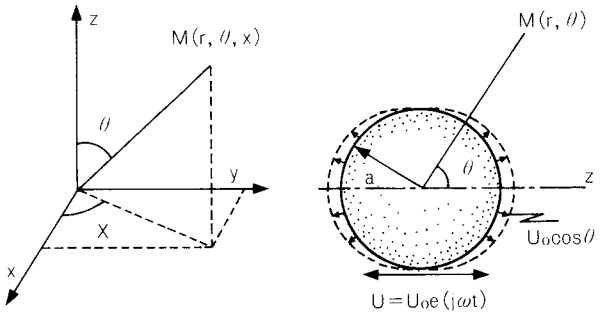

Fig. 2 Oscillating particle

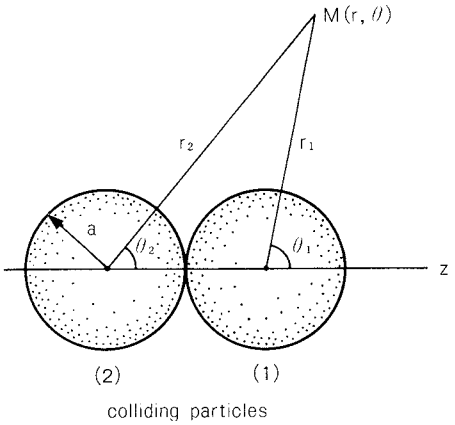

Fig. 3 Impact sound radiated from two colliding particles

occurring when a spherical particle oscillates reciprocatingly along the Z-axis at a speed of $U_0 \exp(jwt)$ satisfies the following wave equation:

$$\frac{\partial^2\phi'}{\partial r^2}+\frac{2\partial\phi'}{r\partial r}+\frac{1}{r^2\sin\theta}\frac{\partial}{\partial\theta}(\sin\theta\frac{\partial\phi'}{\partial\theta})+k^2\phi'=0 \tag{7}$$

where k is the wave number. When one has solved Eq. (7) using the boundary condition which indicates that the speed of the particle surface equals that of the medium, the following velocity potential is obtained:

$$\phi'=\frac{a^3U_0}{r^2}\frac{(1+jkr)\cos\theta\, e^{j[wt-k(r-a)]}}{[2(1+jka)-k^2a^2]} \tag{8}$$

Based on Eq. (8), we can obtain sound pressure radiated by the particle subjected to unit impulse acceleration as follows using the method employed by Koss *et al.*[3]:

$$P_{imp}=\frac{\rho_0 Ca\cos\theta}{r}[\cos(\frac{C}{a}t')-(1-\frac{a}{r})\sin(\frac{C}{a}t')]e^{-(\frac{C}{a}t')} \tag{9}$$

where $t'=t-(r-a)/C$, ρ_0 is medium density, while C is sound speed.

The sound pressure waveform of sound radiated by a particle when subjected to a given acceleration $\alpha(t)$ can generally be expressed as follows[6]:

$$P(r,\theta,t)=\int_0^t P_{imp}(t-\tau)*\alpha(\tau)d\tau \tag{10}$$

If we approximate the acceleration resulting from Eqs. (1) and (2) by $\alpha(t)=\frac{1}{2}\xi_m\sin bt$ for easier calculation, we obtain the following equation[3] from Eqs. (9) and (10) where $b=\frac{\pi}{T}$:

When $0<t'<T$,

$$\begin{aligned}P(r_i,\theta_i,t_i)=&\frac{\rho_0\alpha_m a_i^3\cos\theta_i}{8(b^4+4l_i^4)}\frac{1}{r_i^2}\\&\times\Big[(\frac{2r_i}{a_i}-1)\{(8l_i^3b-4l_ib^3)\cos bt_i'\\&+8l_i^2b^2\sin bt_i'\}-4b^4\sin bt_i'\\&-(8l_i^3b+4l_ib^3)\cos bt_i'\\&+(\frac{2r_i}{a_i}-1)[(4b^3l_i-8bl_i^3)\cos l_it_i'\\&-(8bl_i^3+4b^3l_i)\sin l_it_i']\exp(-l_it_i')\\&+[(4b^3l_i-8bl_i^3)\cos l_i(t_i'-\frac{\pi}{2l_i})\\&-(8bl_i^3+4b^3l_i)\sin l_i(t_i'-\frac{\pi}{2l_i})]\exp(-l_it_i')\Big]\\&+\frac{\rho_0\alpha_m a_i^3\cos\theta_i}{2r_i^2}\sin bt_i'\end{aligned} \tag{11}$$

When $T<t'$

$$\begin{aligned}P(r_i,\theta_i,t_i)=&\frac{\rho_0\alpha_m a_i^3\cos\theta_i}{8(b^4+4l_i^4)}\frac{1}{r_i^2}\\&\times\Big[(\frac{2r_i}{a_i}-1)\{[(4b^3l_i-8bl_i^3)\cos l_i(t_i'-T)\\&-(8bl_i^3+4b^3l_i)\sin l_i(t_i'-T)]\exp[-l_i(t_i'-T)]\\&+[(4b^3l_i-8bl_i^3)\cos l_it_i'\\&-(4b^3l_i+8bl_i^3)\sin l_it_i']\exp(-l_it_i')\}\\&-[(8bl_i^3-4b^3l_i)\cos l_i(t_i'-T-\frac{\pi}{2l_i})\\&+(8bl_i^3+4b^3l_i)\sin l_i(t_i'-T-\frac{\pi}{2l})]\end{aligned}$$

$$\times \exp[-l_i(t_i'-T)]$$

$$-[(8bl_i^3-4b^3l_i)\cos l_i(t_i'-\frac{\pi}{2l_i})$$

$$+(8bl_i^3+4b^3l_i)\sin l_i(t_i'-\frac{\pi}{2l_i})]\exp(-l_it_i')\Big] \quad (12)$$

where the subscript i is an index of spherical particle, $l_i = \frac{C}{a_i}$. Sound pressure $P(r, \theta, t)$ from two colliding particles at the observation point $M(r, \theta)$ shown in **Fig. 3** must allow for the sum of sound pressures radiated from particles (1) and (2) and waves reflected between the particles.

2. 3 Sound pressure waveforms of reflected waves

Calculations related to the scattering of one particle's sound waves due to the other are very complex. This paper, therefore, considers reflected waves alone.

Let's now consider the case in which impact sound radiated from particle (1) is reflected particle (2). The velocity potential $\phi(r, \theta, t)$ of sound rediated by one particle subjected to Hertz's acceleration can be obtained in the same matter as in Eqs. (10) and (11) and expressed as follows[3]:

When $0 < t' < T$,

$$\phi_i(r_i, \theta_i, t_i) = -\frac{\alpha_m a_i^3\cos\theta}{4(b^4+4l_i^4)2r_i^2}\Big[(\frac{2r_i}{a_i}-1)$$

$$\times(4l_ib^2\sin bt_i' - 8l_i^3\sin bt_i' + 8bl_i^2\cos bt_i')$$

$$-(4b^3\cos bt_i' - 4l_ib^2\sin bt_i' - 8l_i^3\sin bt_i')$$

$$-\{(\frac{2r_i}{a_i}-1)(8bl_i^2\cos l_it_i' + 4b^3\sin l_it_i')$$

$$\times\exp(-l_it_i') + [8bl_i^2\cos l_i(t_i'-\frac{\pi}{2l_i})$$

$$+4b^3\sin l_i(t_i'-\frac{\pi}{2l_i})]\exp(-l_it_i')\}\Big]$$

$$+\frac{\alpha_m a_i^3\cos\theta}{2r_i^2b}(1-\cos bt_i') \quad (13)$$

When $T < t'$

$$\phi_i(r_i, \theta_i, t_i) = -\frac{\alpha_m a_i^3\cos\theta}{4(b^4+4l_i^4)2r_i^2}\Big[(1-\frac{2r_i}{a_i})$$

$$\times[8bl_i^2\cos l_i(t_i'-T) + 4b^3\sin l_i(t_i'-T)]$$

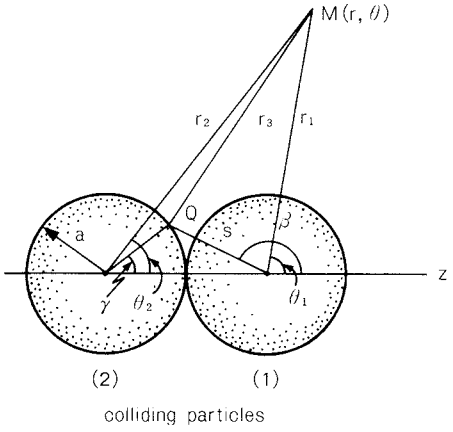

Fig. 4 Reflection of the impact sound from colliding particles

$$\times\exp[-l_i(t_i'-T)] - [8bl_i^2\cos l_i$$

$$\times(t_i'-T-\frac{\pi}{2l_i}) + 4b^3\sin l_i(t_i'-T-\frac{\pi}{2l_i})]$$

$$\times\exp[-l_i(t_i'-T)] - \{(\frac{2r_i}{a_i}-1)$$

$$\times(8bl_i^2\cos l_it_i' + 4b^3\sin l_it_i')\exp(-l_it_i')$$

$$+[8bl_i^2\cos l_i(t_i'-\frac{\pi}{2l_i}) + 4b^3\sin l_i(t_i'-\frac{\pi}{2l_i})]$$

$$\times\exp(-l_it_i')\}\Big] + \frac{\alpha_m a_i^3\cos\theta}{r_i^2b} \quad (14)$$

The velocity component u_n, in the direction of its surface normal, of the sound wave from particle (1) at a given point Q of the surface of particle (2) can be expressed as per **Fig. 4** as:

$$u_n = -\frac{\partial\phi_1(s, \beta, t)}{\partial s}\frac{a_1-(a_1+a_2)\cos\gamma}{s} \quad (15)$$

By expanding the above u_n using the Legendre function, we obtain:

$$u_n = \sum_{n=0}^{\infty} G_nP_n(\cos\gamma) \quad (16)$$

where

$$G_n = (n+\frac{1}{2})\int_{-1}^{1} -\frac{\partial\phi_1(s, \beta, t)}{\partial s}$$

$$\times\frac{a_1-(a_1+a_2)h}{s}P_n(h)\mathrm{d}h \quad (17)$$

$P_n(h)$ refers to the Legendre function.

Assuming that velocity potential ϕ_r of a wave reflected by particle (2) is an ordinary is a

spherical wave, the following equation holds[7]:

$$\phi_r(r, \theta, t_r) = \sum_{n=0}^{\infty} C_n [J_n(kr) - jY_n(kr)] \times P_n(\cos\theta) e^{jwtr} \quad (18)$$

where $t_r = (r_2 - a_2)/C$, $J_n(kr)$ is the spherical Bessel function, $Y_n(kr)$ is the spherical Neumann function, and C_n is an undetermined coefficient. Velocity component u_r of a scattered wave in the direction of its normal on the spherical surface can be expressed in the same manner as in Eq. (15) as:

$$u_r = -\frac{\partial \phi_r}{\partial r_{r=a}} = -\sum_{n=0}^{\infty} C_n [J_n'(kr) - jY_n'(kr)] \times kP_n(\cos\theta) \quad (19)$$

At point Q on the particle surface, $u_n + u_r = 0$ holds. This determines coefficient C_n as:

$$C_n = \frac{aG_n}{[nh_n^{(2)}(ka) - kah_{n+1}^{(2)}(ka)]} \quad (20)$$

where $h_n^{(2)}$ is the Bessel function of the second kind of the Hankel type. As a result, velocity potential $\phi(r, \theta_2, t)$ of a wave scattered by particle (2) at observation point M can be expressed as:

$$\phi_r = \sum_{n=0}^{\infty} \frac{aG_n h_n^{(2)}(kr) P_n(\cos\theta_2) e^{jwtr_2}}{[nh_n^{(2)}(ka) - kah_{n+1}^{(2)}(ka)]} \quad (21)$$

The wave P_{r21} from particle (2) reflected by particle (1) can be calculated in exactly the same way.

The sound pressure waveform $P(r, \theta, t)$ of sound from two colliding particles can be expressed as:

$$P = p_1 + p_2 + p_{r12} + p_{r21} \quad (22)$$

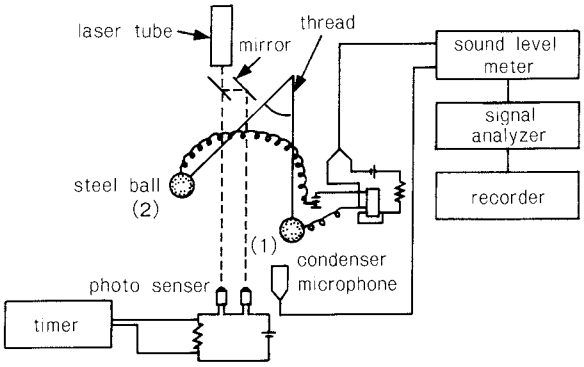

Fig. 5 Experimental apparatus

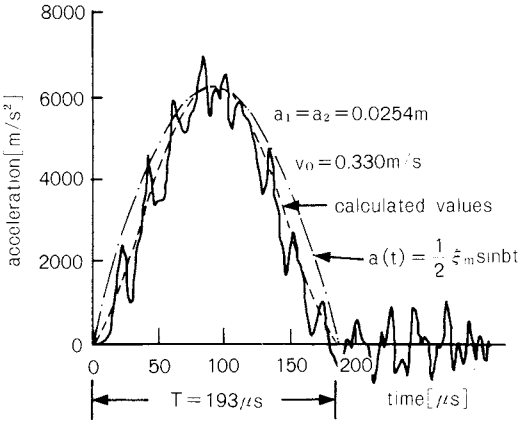

Fig. 6 Waveforms of acceleration for collision of two steel balls

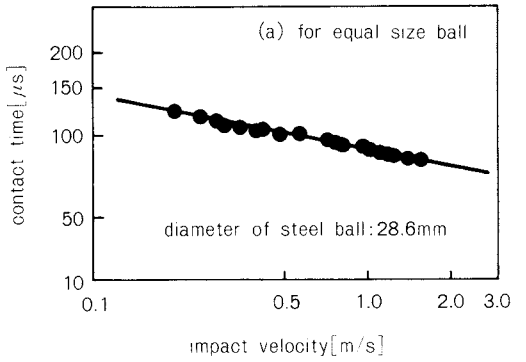

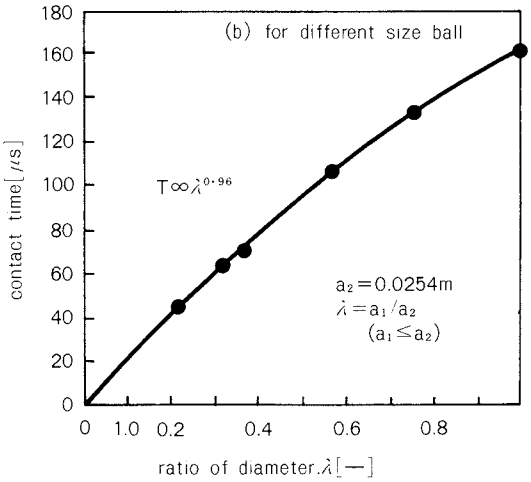

Fig. 7 Effects of impact velocity and the ratio of particle diameter on the contact time between two steel balls

3. Experiment Method

Figure 5 outlines the experimental apparatus that we employed to measure impact sound from two colliding steel balls. We hung two balls, lifted one of them to a relative height h

with regard to the other, and then made them collide. We calculated impact velocity v_0 using equation $v_0 = \sqrt{2gh}$ and confirmed the result using a laser-type measuring instrument illustrated in the figure. Time T of the contact (or collision duration time) between two particles was observed using an electric circuit illustrated in the figure. The waveform of acceleration acting on the steel balls was observed using an acceleration pickup (manufactured by Lion; Type PV-90A; weight: 1 g) installed on the opposite side of the collision point. Impact sound was detected using a condenser microphone (manufactured by Bruel & Kjaer, Type 4135), passed through an amplifier (manufactured by B & K, Type 2607), stored in a waveform analyzer (manufactured by Iwatsu Electric, SM-2100), and then subjected to peak sound pressure measurements and frequency analyses.

The steel balls used measured 0.0508, 0.0381, 0.0284, 0.0183, 0.0161, and 0.0111 m. They had a density ρ_p of 7.8 kg/m^3, a Young's modulus E of 2.09×10^{11} N/m^2, and a Poisson's ratio ν of 0.287.

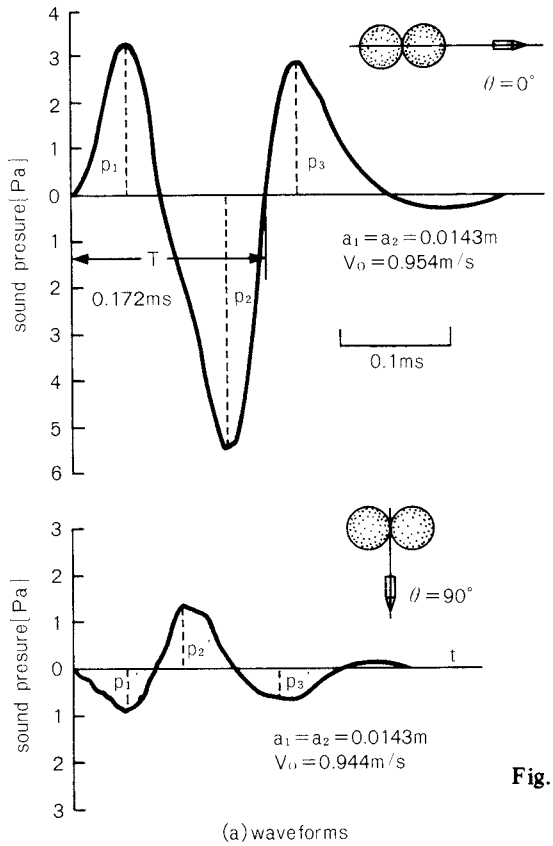

(a) waveforms

4. Results and discussion

4. 1 Acceleration waveform and contact time

Figure 6 shows a typical acceleration waveform observed. The broken lines in the figure have been calculated using Eqs. (1) and (2). High-frequency oscillation included in the observed waveform corresponds to the characteristic frequency of the particles. T indicated in the figure is contact time. **Figure 7** indicates the relationship between contact time T and impact velocity v_0 measured using the above electric circuit. The values calculated using Eq. (5) agree very well with the observed values. These results prove that, as reported by Nishimura *et al.*[2], Hertz's elastic contact theory is sufficiently applicable to this collision. These results also confirm that the following equation, obtained by deforming Eq. (5), holds:

When the two steel balls have the same diameter,

$$T \propto D_p \tag{23}$$

When the diameter ratio is λ,

$$T \propto \lambda \left\{ \frac{(1+\lambda)}{(1+\lambda^3)^2} \right\}^{0.2} \propto \lambda^{0.96} \tag{24}$$

where $\lambda = a_1/a_2$, $a_1 \leqq a_2$.

4. 2 Sound pressure waveforms of impact sound

Figure 8 and **9** gives typical examples of the sound pressure waveforms of impact sound and

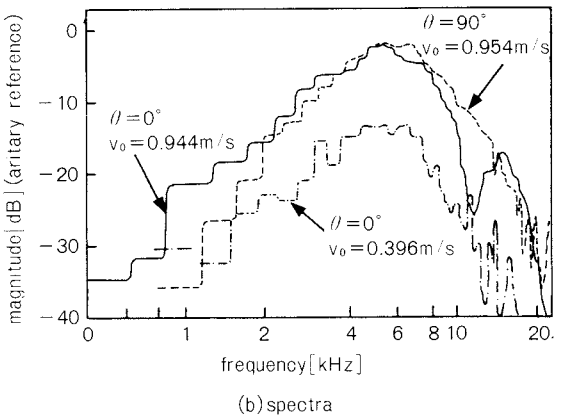

(b) spectra

Fig. 8 Pressure waveforms and frequency spectra of the sound radiated from the collision of two steel balls

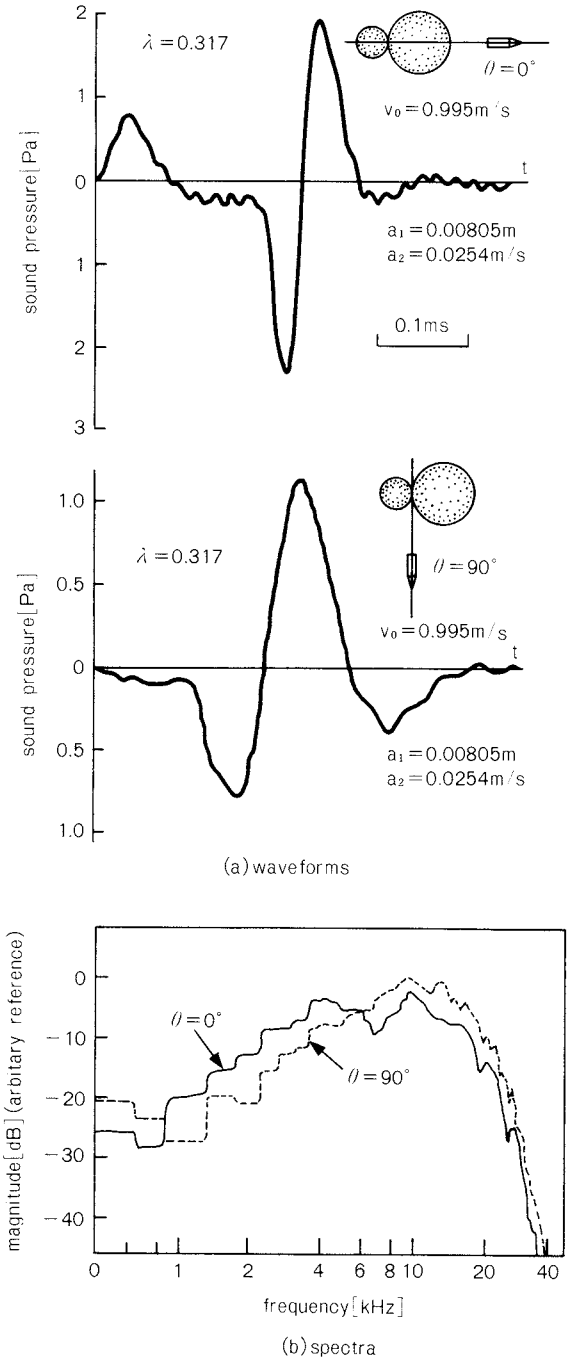

Fig. 9 Pressure waveforms and frequency spectra of the sound radiated from the collision of two steel balls having different diameters

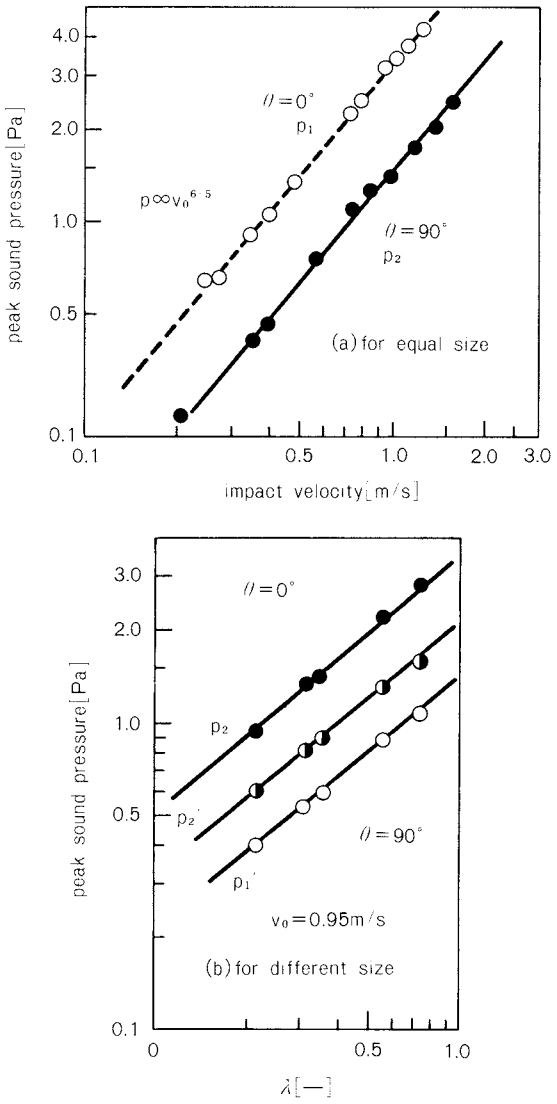

Fig. 10 Relationship among peak pressure of impact sound, impact velocity and the ratio of particle diameters

their frequency spectra. As the figure indicates, the particle impact sound consists of the pulsatory sound during the initial stage of collision (transitory sound) and the subsequent characteristic oscillation of the balls. This paper focuses on the transitory sound. The relationship between the peak sound pressures $P_1 \sim P_3$, along with $P'_1 \sim P'_3$, and the impact velocity v_0 satisfies the following relational expression derived from Eqs. (5) and (9), in all cases as shown in **Fig. 10.**

$$P_m \propto v_0^{\frac{6}{5}} \tag{25}$$

Between particle diameter λ and peak sound pressure P_m, the following relational expression holds:

$$P_m \propto \lambda^{0.85} \tag{26}$$

Figures 8 and **9** indicate the sound pressure waveform of impact sound in the direction along the collision axis ($\theta = 0°$) and in the di-

rection perpendicular ($\theta = 90°$) to it. The waveform varies depending on the observation point. As is evident from the given typical frequency spectra, however, the peak frequency remains almost constant on a specific spectrum regardless of changes in sound pressure waveform or impact velocity according to the observation point. Although with slight changes depending on the impact velocity and observation point as will be mentioned later, the following relational expressions hold between the diameter of the colliding balls and their frequency f as shown in **Fig. 11**.

When the two balls have the same diameter,

$$f \propto D_p{}^{-1} \tag{27}$$

When the diameter ratio is λ,

$$f \propto \lambda \left\{ \frac{(1+\lambda)}{(1+\lambda^3)^2} \right\}^{-0.2} \propto \lambda^{-0.96} \tag{28}$$

The above indicates that measuring particle impact sound makes it possible to measure its sound pressure, particle motion speed, frequency, and particle diameter D_p.

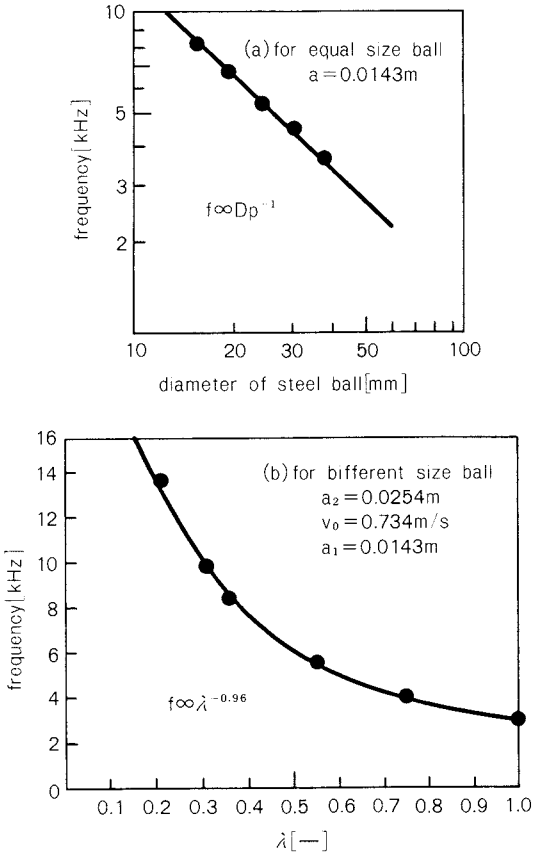

Fig. 11 Relationship among the frequency of impact sound, particle size and the ratio of particle diameters

4. 3 Sound pressure waveform calculations

Figure 12 indicates a typical example of sound pressure waveform calculations under the conditions shown in **Fig. 8**. The dotted line in the figure represents the waveform calculated using the aforementioned method allowing for scattering. The continuous line gives the same observed waveform as that in **Fig. 8**. The alternate long and short dash line is the waveform calculated using Koss's method. Since the waveforms correspond in the direction in which the maximum acceleration acts, the waveform at the observation point ($\theta = 0°$) indicating the maximum sound pressure agrees comparatively well in every case of calculation. Koss's waveforms, however, slip on the time axis. With the value θ being large, or being equal to 90° in particular, calculated values differ greatly from observed values. Our calculated values allowing for reflection approach the observed values much more than they do Koss's values. Okamoto[7] took photos of the

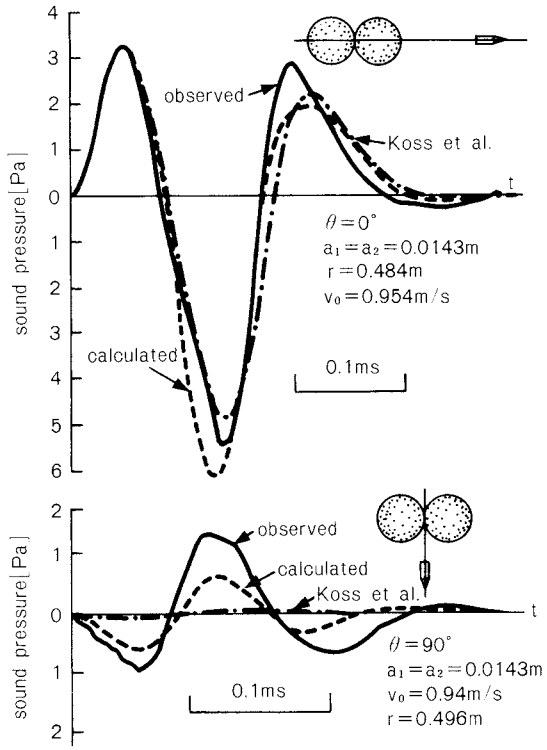

Fig. 12 Comparison of the calculated pressure waveforms of impact sound

compression status of the air around balls at the moment they collided, using the Schlieren method. His photos show how complexly the air density changes between two balls. This, we believe, is partly due to the disturbance of the air near the colliding balls and partly due to considerably strong reflection between the balls. The effect of this reflection increases as θ rises (**Fig. 13**). Calculated values, therefore, become smaller than observed values. This leads us to suppose that more strict calculations, allowing for frequent reflection between the balls, will achieve results nearer to the observed waveforms. Taking into account calculated values applicable to impact sound from a number of colliding particles, this paper considers one-time reflection alone.

4. 4 Relationship between impact sound frequency and particle diameters

Figure 14 indicates the structure of the impact sound pressure waveforms shown in **Fig. 12**. These sound pressure waveforms are composed by overlapping

- radiated sound wave p_1 from steel ball (1);
- sound wave p_2 resulting from steel balls (2) – which has its center away from ball (1) by the distance equal to the latter's diameter – accelerated in the opposite direction of steel ball (1); and

sound wave p_{r12} reflected by ball (2). The above calculations excludes sound wave p_{r12} reflected by steel ball (1), because the ball's reflection face is geometrically hidden from the viewpoint of the observation point. When θ = 90°, the above calculations include both p_{r12} and p_{r21}.

For frequency f_m, which peaks in the frequency spectrum of impact sound, $f_m \propto D_p^{-1}$ holds as mentioned before when the colliding particles have the same diameter. Furthermore, experiments show that the frequency f_m equals the inverse number of time τ (**Fig. 8**) from the rise of the sound pressure waveform to its second intersection with the time axis[8]. The time τ in **Figs. 8** and **14** is proportional to D_p. This is because the sound pressure waveforms from particles (1) and (2), as mentioned before, result from the convolution of the impulse sound pressure P_{imp} and the acceleration wave-

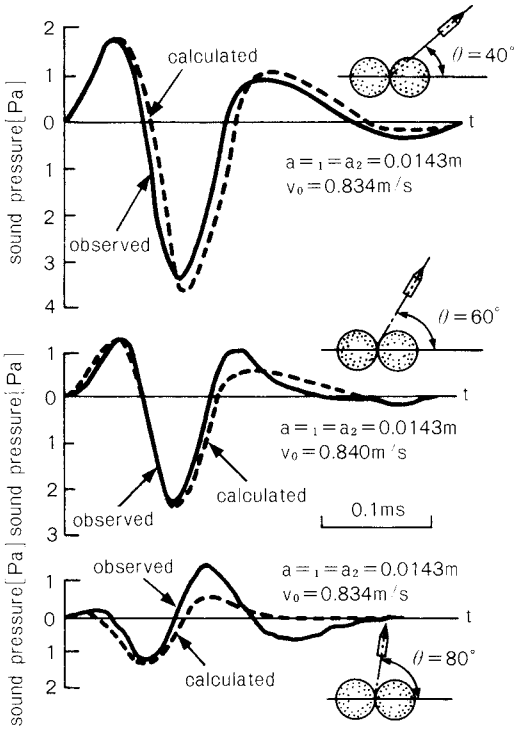

Fig. 13 Influence of the observation point on the calculated pressure waveforms of impact sound

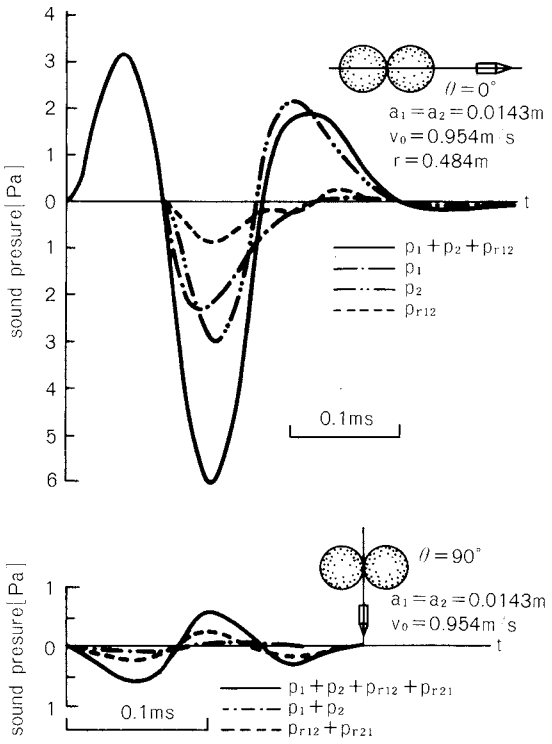

Fig. 14 Calculated pressure waveforms of impact sound

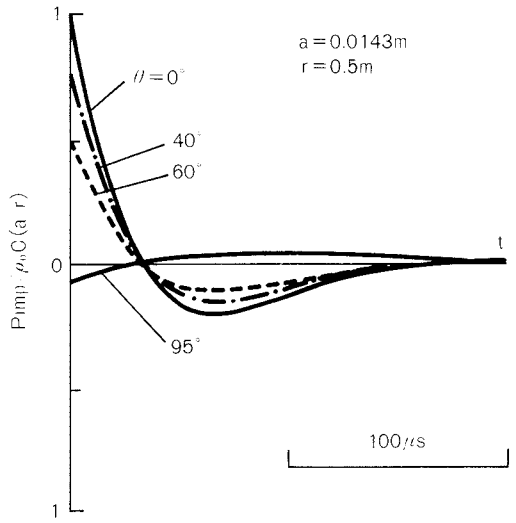

Fig. 15 Impulse sound pressure P_{imp}

form $\alpha(t)$ indicated in **Fig. 15**. The basic waveform of P_{imp} is determined by the particle diameter as shown in **Fig. 15**, while the degree of its sound pressure is determined by the location of the observation point. The time during which acceleration acts equals the contact time, which is proportional to D_p when the particles have the same diameter. The duration of sound radiated by one particle in the form of sound pressure waveform on the time axis is therefore proportional to D_p. The distance between the particles is very small. With the sound attenuation due to distance neglected, the result is that two waveforms with different phases are given. We find that the frequency of resulting synthetic waveform is proportional to D_p. When the diameter ratio is λ, the comparable frequency is determined by the relationship between contact time and λ, so that it relates to the diameter ratio λ as indicated in Eq. (24).

Contact time relates to impact velocity as follows:

$$T \propto v^{-0.2}$$

Furthermore, sound wave arrival time varies slightly depending on the observation point. Impact sound frequency is therefore expected to vary when impact velocity varies greatly or impact sound is observed from a nearby point.

5. Conclusion

As a basic study of pulverization measurements using particle impact sound, we examined the relationship between the parameters of impact sound stemming from two colliding particles, particle properties and particle motion velocity.

Particle impact sound (transitory sound) results from the quick acceleration of the particle surfaces due to collision. To check the radiation mechanism, we calculated impact sound pressure waveforms, allowing for reflection between the particles. Waveforms thus calculated agreed well with observed values.

A quantitative relationship holds between particle impact sound pressure and particle impact velocity, and between frequency and particle diameter. We can therefore measure the motion velocity and diameters of colliding particles by analyzing impact sound.

Nomenclature

a	:	radius of spherical particle	[m]
b	:	$=\pi/T$	[rad/s]
C	:	sound speed	[m/s]
D_p	:	particle diameter	[m]
E	:	modulus of elasticity	[N/m^2]
f	:	frequency of impact sound	[Hz]
$h_n(kr)$	:	spherical Bessel function of the third kind	[–]
i	:	index of spherical particle	[–]
j	:	imaginary unit	[–]
$J_n(kr)$	:	spherical Bessel function of the first kind	[–]
k	:	wave number ($=\omega/C$)	
m	:	mass of spherical particle	[kg]
P_{imp}	:	impulse sound pressure	[Pa]
$P_n(h)$	:	Legendre function	
r	:	distance between particle and observation point	[m]
t	:	time	[s]
T	:	contact time between two spherical particles	[s]
u	:	particle velocity of fluid	[m/s]
U_0	:	amplitude of velocity of oscillating particle	[m/s]
v_0	:	impact velocity	[m/s]
$\alpha(t)$	:	acceleration of colliding particles	[m/s^2]
β	:	angle	[degree]
γ	:	angle	[degree]
θ	:	angle	[degree]
λ	:	ratio of particle radius ($=a_1/a_2$)	[–]
ν	:	Poisson's ratio	[–]
$\xi(t)$	:	elastic deformation of colliding particles	[m]
ξ_m	:	maximum deformation of colliding particle	[m]

ρ_0	:	density of fluid	[kg/m^3]
ρ_p	:	particle density	[kg/m^3]
τ	:	characteristic time in **Fig. 8**	[s]
ϕ	:	velocity potential of impact sound	[m^2/s]
ω	:	angular frequency	[rad/s]

References

1) Horiuchi, T.: *Nihon Kikaigakkaishi,* **77**, [668], 769 (1974).
2) Nishimura, G. and K. Takahashi: *Seimitsu Kikai,* **28**, 220 (1962).
3) Koss, L.L. and R.J. Alfredson: *J. of Sound and Vibration,* **27**, [1], 59 (1973).
4) Tomita, Y. and T. Horiuchi: *Nihon Onkyogakkaishi,* **34**, [5], 318 (1978).
5) Goldsmith, W.: "Impact", p. 89, Edward Arnold (1960).
6) Akay, A. and T.H. Hodgson: *J. Acoustic Soc. Am.*, **63** [2], 313 (1978).
7) Ito, T.: "Onkyo-kougaku Genron", p. 254, Korona-sha (1970).
8) Okamoto, H.: *J. of the Faculty of Eng., The Univ. of Tokyo,* **36**, [1], 37 (1981).
9) Hidaka, J. and S. Miwa: Proc. of International Symp. on Powder Technol. '81, Soc. of Powder Technol. Japan, p. 323 (1981).

Charge Transfer between a Single Polymer Particle and Metal Plate by Impact†

Tatsushi Matsuyama and Hideo Yamamoto
Institute of Industrial Science
*University of Tokyo**

Abstract

This paper describes an experimental investigation of the charge acquired by a single particle when striking a metal plate. The particle was projected from a pneumatic gun onto the metal plate. The initial charge carried on the particle before impact and impact charge were measured under various conditions of impact velocity, v_0 (7 ~ 18 m/s) and angle, θ (0° ~ 60°).

The charge transfer is dependent not only on the impact conditions but also on the initial charge of the particle. The impact charge almost proportionally decreases with an increase in the initial charge. There is a particular value of this charge which results in no net transfer and which is independent on the impact conditions. This special point can be utilized to estimate the effective work function of insulating particles.

While a larger impact velocity leads to a larger charge transfer because in the increase of the contact area, the data cannot be arranged with the maximum contact area derived from the normal component of the impact velocity, $v_0 \cos\theta$. A much larger enhancement of the charge transfer is caused by the tangential component of velocity, $v_0 \sin\theta$. This fact is extremely different from the previous works (Refs. 2 and 4) which describe that the tangential component had no effect on the charge transfer by collision.

1. Introduction

In the powder processes such as size reduction, classification and transportation, generation of static electricity is an unavoidable phenomenon, particularly in a dry and high-insulating powder process. Static electricity causes coagulation, adhesion of powders onto apparatus walls and discharge of accumulated charge; therefore it is one of the obstructive factors of the powder process.

On the other hand, static electricity is one of the effective methods to control particle motion. It is therefore utilized aggressively in the various branches of technology, including electrostatic precipitation, electrostatic photography and electrostatic painting.

Considering both its advantages and disadvantages, elucidation of the powder electrification mechanism is regarded as a very important issue.

Basic knowledge of static electricity has not been currently acquired enough. As for the contact electrification of solids, for example, well-compiled quantitative discussions are available only on the concept of "contact potential difference" in the metal-to-metal contact. The rest of the subjects remain to be discussed qualitatively. This is solely due to the delayed investigation with regard to electric properties and solid states of insulating materials. Nonetheless in the actual powder processes, indeed, the polymers and other insulators are handled.

In an attempt to obtain basic knowledge of the impact electrification of insulating particles, we have been measuring the amount of

* 7-22-1, Roppongi, Minato-ku, Tokyo, 106
TEL. 03-402-6231

† This report was originally printed in *J. Soc. Powder Technology, Japan*, **24**, 765-770 (1987) in Japanese, before being translated into English with the permission of the editorial committee of the Soc. Powder Technology, Japan.

charge transfer generated on the metal-to-polymer contact point when a polymer collides with a metal plate. Experiments on a single particle, rather than on a group of particles, will probably show the electrification phenomenon in a more simplified form, and then makes it easier to study the results quantitatively; however most of the existing reports on the electrification of colliding particles describe the collision of a group of particles with a wall[1,2], and very few of them deal with the electrification of a single particle in a one-time collision[3,4]. By making a single particle collide with a metal plate, Masui *et al.*[3] reported that charge transfer declined with rise of the initial charge of the particle and that charge transfer caused by collision became zero when initial charge increased to a certain amount. Observation of the same phenomenon was reported in our previous paper[5], which also indicated that it was possible to calculate work function of the polymer and metal plate on the bases of initial charge measurements when charge transfer is reduced to zero. This paper deals with two subjects: the first one is to observe the same result with a polymer-metal combination different from one used in our previous report, and the second is to examine dependency of charge on collision angle. Masui *et al.*[4] reported that charge transfer caused by collision did not depend on collision angle, but on the maximum contact area determined by the vertical speed component of the particle to the wall, i.e., the speed components in the tangential direction (the direction along the wall surface) scarcely contributing to electrification. The same result was reported by Masuda *et al.*[2]; however our experiments indicated that the tangential speed components contributed to collision electrification to too great an extent to be neglected. Here is our report:

2. Experimental apparatus and experiment method

Figure 1 gives a schematic view of our experimental apparatus. The apparatus is composed of an air gun, Faraday-cage and a target.

The air gun has a mechanism in which compressed air drives the particle-packed cartridge. When the driven cartridge reaches the top of the air gun, it collides with the damper, stops and launches the particle alone.

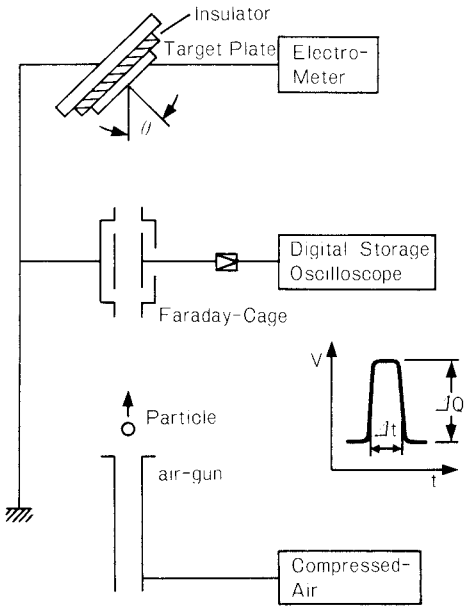

Fig. 1 Schematic view of the apparatus

The air-gun-launched spherical particle first pass through double-cylindrical approximation Faraday-cage (ϕ20 mm × 50 mm). The Faraday-cage is connected to the digital storage oscilloscope (Hitachi Electronics' VC-6050) via the pre-Amplifier. In response to the charge held by the passing particle, the cage provides a voltage peak equal to $V = Q/C$. At this time, it is difficult to measure or calculate the electrostatic capacity C of the entire measurement system, including connection cables. We, therefore, measured particles with a known charge in advance and determined the electrostatic capacity C of the entire measurement system. Measurements indicated that the above electrostatic capacity was 100 pF.

Based on the above electrostatic capacity, we determined the charge ("initial charge") of a particle before collision took place. The width of output waveforms corresponds to the time required for the particle to pass through the Faraday-cage. We used the above time duration to determine particle collision speed*1.

After passing through the Faraday-cage, the particle collides with the target metal plate at an angle of θ. The metal plate is insulated from

*1 The center of the Faraday-cage is separated from the target plate by only 80 mm. Particle deceleration between these can therefore be neglected.

its support and the surrounding environment and connects directly to the electrometer (Takeda Riken's TR-8401). Using of the "charge measurement range" of this electrometer, the charge generated by impact and left on the metal plate can be determined.

This paper reports the results of our experiments consisting of making Nylon66 and Teflon spherical particles (ϕ 3 mm) collide with a mirror-finished high-purity aluminum plate (50 × 50 mm, 5 mm thick) at an angle of 0 ~ 60° and a velocity of 7 ~ 18 m/s.

We conducted these experiments under a normal-pressure air atmosphere with its temperature and humidity maintained at 24 ± 5°C and 25 ± 3% respectively.

3. Results and discussion

One set of experiments was conducted with each different amount of initial charge of the particles with regard to a experimental condition of collision speed and angle*2.

For an example, **Fig. 2** shows the results of a collision experiment using aluminum plate and Teflon particles at a velocity v_0 of 11 m/s and an angle θ of 60°. The X-axis is the initial charge of the particles, while the Y-axis is the amount of charge that moved to the particle at the time of collision. (The Y-axis is not the entire charge of the particle after collision, but the charge that moved at the contact point.) In a series of frictional electrification, Teflon ranks nearest the negative end of all polymers and is negatively charged by impact with aluminum. The graph indicates that impact charge depends on initial charge in a linear manner. The intercept on the Y-axis indicates the impact charge (−72 pC in this example) when the initial charge of the particle is zero, i.e., initial charge exercises no influence. The intercept on the X-axis, on the other hand, is −1,100 pC. The intersection of the X-axis with the graph indicates the point at which no charge transference at the time of collision occurs due to initial charge. The initial charge at this point is called the equilibrium charge Q_e.

*2 Initial charge was controlled by shaking a metal or plastic vessel containing the particles to different degrees of intensity.

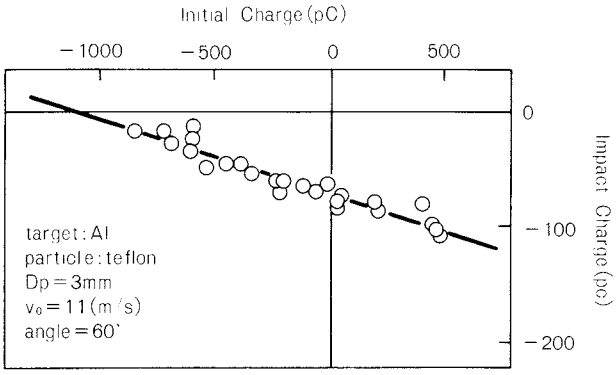

Fig. 2 Impact charge vs initial charge (Aluminum plate vs Teflon)

i) Equilibrium charge

Davies's[6] concept of the "effective work function" made it possible to use the concept of contact potential difference in a metal-to-metal contact as a driving force for charge transfer (ΔQ) in a polymer-to-metal contact. With the simplest condenser model, the impact charge ΔQ can be expressed as:

$$\Delta Q/S = c(V_c - V_i)\{1 - \exp(-\Delta t/\tau)\} \qquad (1)$$

where S is the contact area between a particle and a metal plate, and c is capacitance per unit area of model condenser. Δt is contact time, and τ is time constant of model condenser. V_c is contact potential difference between polymer and metal. V_i is potential induced by initial charge of a particle.

The intercept on the X-axis, or the point at which charge is not transferred due to initial charge, is the point at which $\Delta Q = 0$ (i.e., $V_c - V_i = 0$) in Eq. (1). This means that the electrostatic potential V_i between the contact surfaces induced by the equilibrium charge Q_e of the particle equals the contact potential difference V_c, and that Q_e is determined solely by contact potential difference V_c, i.e., a combination of the metal plate and the particle, without help of the particle collision conditions (such as impact velocity and impact angle).

Figures 3~5 show how the eqilibrium charge Q_e remains constant under different collision conditions.

Figure 3 gives the results of a collision experiment with an aluminum-Nylon66 combination. It compares the results of experiments with an impact angle θ of 60° and three differ-

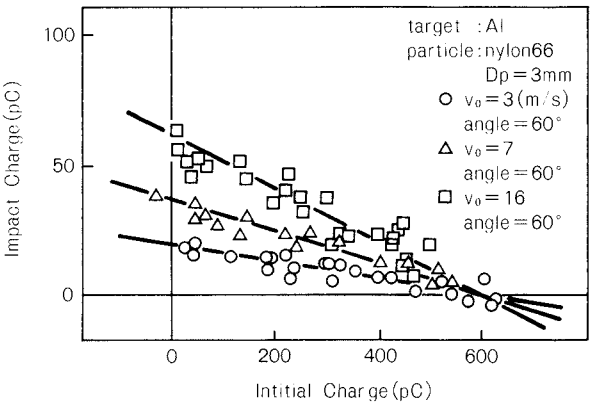

Fig. 3 Impact charge vs initial charge (Aluminum plate vs Nylon 66)

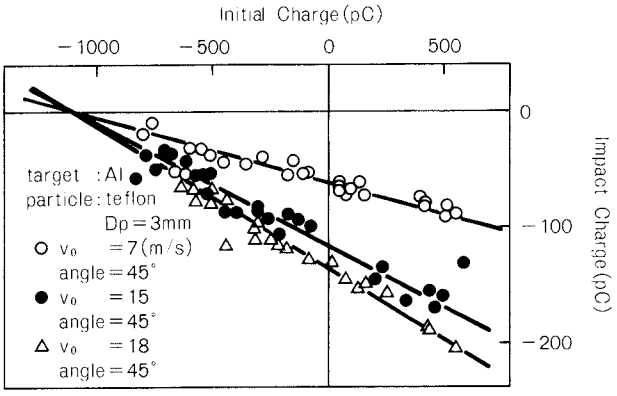

Fig. 4 Impact charge vs initial charge (Aluminum plate vs Teflon)

ent impact velocities v_0 of 3, 7, 16 m/s. The intercept on the Y-axis increases as impact velocity rises, while the X-axis intercept (equilibrium charge) remains constant at 600 pC.

Similarly, **Figs. 4** and **5** indicate the results of a collision experiment with an aluminum-Teflon combination. **Figure 4** gives the results with an impact angle θ of 45° and impact velocities v_0 of 7, 15, 18 m/s. The X-axis intercept remains constant at −1,100 pC despite an increase in the Y-axis intercept accompanying a rise in impact velocity. **Figure 5** gives the results with impact velocity v_0 of 7 m/s and impact angles θ of 15° and 45°. In this case, too, the X-axis intercept remains constant at −1,100 pC.

As mentioned above, the X-axis intercept gives

$$V_c - V_i = 0 \tag{2}$$

in Eq. (1). Let's express V_i at this time as V_{ie}. V_{ie} is an electrostatic potential induced by equilibrium charge Q_e, so that it can be expressed as:

$$cV_{ie} = (Q_e/A) \tag{3}$$

where A refers to the surface area of the particle, and c is the capacitance per unit area of model condenser, used in Eq. (1).

V_c is the contact potential difference between the polymer and metal based on the difference in work function, and this can be expressed as:

$$V_c = (W_M - W_P)/e \tag{4}$$

where W_P is the work function of the polymer and W_M is that of the metal.

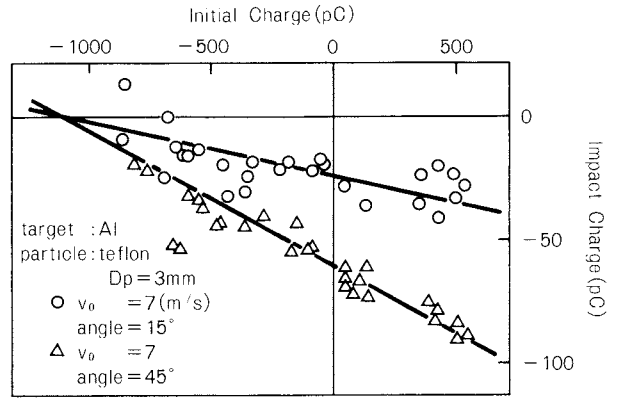

Fig. 5 Impact charge vs initial charge (Aluminum plate vs Teflon)

From Eqs. (2) ~ (4), we obtain the following equation regarding eqilibrium charge Q_e:

$$(W_M - W_P)/e = Q_e/(cA) \tag{5}$$

Assuming that value c remains constant throughout collision experiments, we can evaluate the work function of the particle or metal plate by determining Q_e through collision experiments using two different matter combinations (e.g., by using two kinds of particle with one kind of metal plate)[5].

Here, we used an aluminum plate and ϕ 3 mm Nylon66 and Teflon particles. So let's express their respective work functions as W_{Al}, W_N and W_T, and equilibrium charges for the respective combinations as Q_{eN} and Q_{eT}. Then, for the respective collision conditions, Eq. (5) can be expressed as:

$$\begin{cases} (W_{Al} - W_N)/e = Q_{eN}/(cA) \\ (W_{Al} - W_r)/e = Q_{eT}/(cA) \end{cases}$$

Both particles measure 3 mm in diameter, so that they share the same surface area A. On the basis of the above, cA can be eliminated from the above equations. These equations can then be solved as:

$$W_{Al} = \frac{Q_{eN} W_T - Q_{eT} W_N}{Q_{eN} - Q_{eT}} \tag{6}$$

Let's evaluate the work function of aluminum using

- Q_{eN} = 600 pC derived from **Fig. 3**
- Q_{eT} = −1,100 pC derived from **Figs. 2** and **4**
- W_N = 4.08 and W_T = 4.26 eV, which are the work functions of Nylon66 and Teflon introduced by Davies[6].

The result is W_{Al} = 4.14 eV, and agrees well with the value reported[7] (W_{Al} = 4.25 eV).

ii) Impact angle

The Y-axis intercept indicates the point at which initial charge exercises no influence. On this point, the term of the potential difference between surfaces in Eq. (1) is $V_i = 0$. Equation (1) can therefore be changed to:

$$\Delta Q_0 = Sc V_c \{1 - \exp(-\Delta t/\tau)\} \tag{7}$$

where ΔQ_0 indicates the Y-axis intercept.

If the contact time is sufficiently short with regard to the time constant of the condenser formed on the contact surface, Eq. (7) can be changed to:

$$\Delta Q_0 = Sc(\Delta t/\tau) V_c \tag{8}$$

Assuming that c and τ remain constant under different collision-deformation conditions, we can say that the only value that varies according to the collision condition is $S \cdot \Delta t$, on which alone ΔQ_0 changes dependently. Let's assume again that S is the contact area between the particle and metal plate and Δt is the time during the contact, and together with the conclusion derived from the elasticity theory[8], we can express S and Δt within the elasticity limit*3 as:

$$S = \pi \left\{ \left(\frac{5}{4}\right) \left(\frac{1}{E}\right) R^2 m \right\}^{\frac{2}{5}} \cdot v_\perp^{\frac{4}{5}}$$

$$\frac{1}{E} = \frac{3}{4}\left(\frac{1-\sigma_1^2}{E_1} + \frac{1-\sigma_2^2}{E_2}\right) \tag{9}$$

$$\Delta t = 2B\left(\frac{2}{5}, \frac{1}{2}\right) \left\{ \left(\frac{5}{4}\right) \frac{1}{E\sqrt{R}} m \right\}^{\frac{2}{5}} \cdot \left(\frac{1}{v_\perp}\right)^{\frac{1}{5}} \tag{10}$$

where R is the radius of the particle and m is the mass of the particle. $v_\perp$ is the normal impact velocity component. E_i and σ_i (i = 1, 2) are the Young's modulus and Poisson's ratio of the colliding object respectively. $B(r, s)$ is a beta-function.

On the basis of Eqs. (9) and (10), $S \cdot \Delta t$ can be expressed as:

$$S \cdot \Delta t = 2\pi B\left(\frac{2}{5}, \frac{1}{2}\right) \left\{ \frac{5}{4} \left(\frac{1}{E}\right) m \right\}^{\frac{4}{5}} R \cdot v_\perp^{\frac{3}{5}} = K \cdot v_\perp^{\frac{3}{5}} \tag{11}$$

where K is a constant determined by the properties of the colliding objects, without depending on the collision conduction. Equation (8) can therefore be changed to:

$$\Delta Q_0 = K(v_\perp)^{\frac{3}{5}} \cdot (c/\tau) \cdot V_c = k v_\perp^{\frac{3}{5}} \tag{12}$$

Equation (12) indicates that, when a certain particle-metal combination is selected (i.e., when the properties related to contact potential difference and collision deformation are determined), ΔQ_0 can be uniquely determined by the normal impact velocity component.

Figure 6 shows the Y-axis intercept ΔQ_0 with regard to the normal impact velocity component ($v_\perp = v_0 \cos\theta$), based on a series of experiments conducted with an aluminum-Teflon combination. As the impact angle increases, absolute value $|\Delta Q_0|$ of the impact charge rises greatly. This finding refutes our conclusion derived from Eq. (12) that ΔQ_0 is determined uniquely by the normal impact velocity component $v_\perp$, and opposes the results reported so far[2),4)]. Masuda *et al.*[2] conducted collision

*3 The contact area of objects in the plastic deformation region, surpassing the elastic limit, is expressed, for example, by Bitter[9] as:

$$S = K(v_\perp - v_e) \tag{13}$$

where K is the constant and v_e is the impact velocity giving the elastic limit. The maximum contact area, in any case, is determined by the normal impact velocity.

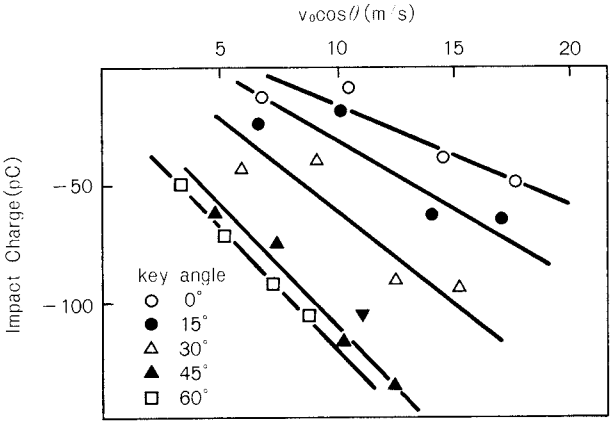

Fig. 6 Impact charge vs normal velocity (Aluminum plate vs Teflon)

experiments with aspherical-particle morandum (a group of particles with eight different average diameters: 55, 71, 93, 120, 180, 290, 450, 660 μm) made to collide with a copper plate, rather than measurements of charge of single particles. Their results, therefore, cannot be compared strictly with our results; however, Masui *et al.*[4] made collision experiments using 3.18 mm Nylon66 and 2.19 PMMA spherical particles, together with chrome and brass plates. They used almost the same impact velocities (3.7 ~ 20.3 m/s) and impact angles (0 ~ 80°) as we did but produced different results. The reason is still unknown. The Nylon66-brass plate collision experiment reported in our previous paper[5] also indicated a considerable degree of dependency on the angle. It is, therefore, clear that, in our experiment, charge also depends greatly on the tangential velocity component.

This implies that we cannot elucidate the particle impact charge phenomenon merely by analyzing the simplest condenser model mentioned above, i.e., a model assuming a condenser consisting of the maximum contact surface determined by the normal impact velocity component. It is, therefore, necessary to study the influence of the possibility that the slip or rotation of the particle due to collision may bring about a real rise in the number of contact points and contact area.

4. Conclusion

We made a polymer particle collide with a metal plate and measured the charge transfer (impact charge) occurring at the contact point.

The collision experiment with different initial charges (the charge which the particle had before collision) indicated that impact charge depended in a linear manner on changes in initial charge and that there was a point at which no impact charge took place. The equilibrium charge (the initial charge of the particle corresponding to the above point at which no impact charge takes place) is determined by the type of metal plate-particle combination alone, without depending on impact velocity or impact angle. The experiment indicated that the effective work function of the metal or polymer surface could be evaluated on the basis of the above equilibrium charge.

Impact charge rose as the normal velocity component climbed. Even with the same normal velocity component, equilibrium charge rose greatly as impact angle increased. Impact charge therefore cannot be elucidated merely by analyzing the normal velocity component. Our future mission is to study how the tangential velocity component contributes to impact charge, including how the slip and rotation of the particle exercise their influence.

Nomenclature

A	:	surface area of a particle	[m^2]
c	:	capacitance per unit area of model condenser	[F/m^2]
E_i	:	Young's modulus (i = 1, 2)	[pa]
e	:	elementary electric charge	[C]
K	:	constant in Eq. (11) or (13)	
k	:	constant in Eq. (12)	
m	:	mass of impacting particle	[kg]
ΔQ	:	impact charge	[C]
ΔQ_0	:	impact charge at $Q_i = 0$	[C]
Q_i	:	initial charge of a particle	[C]
Q_e	:	equilibrium charge	[C]
R	:	radius of a particle	[m]
S	:	contact area between a particle and metal plate	[m^2]
Δt	:	contact time	[s]
V_c	:	contact potential difference between polymer and metal	[V]
V_i	:	potential induced by initial charge of a particle	[V]
V_{ie}	:	potential induced at $Q_i = Q_e$	[V]
v_e	:	velocity when elastic limit is reached	[m/s]
v_0	:	impact velocity of a particle	[m/s]
$v_\perp$	:	normal component of impact velocity	[m/s]
W	:	work function	[eV]
θ	:	impact angle	[deg]
σ_i	:	Poisson's ratio (i = 1, 2)	[−]

τ : time constant of model condenser [s]

< Subscript >

P : particle
M : metal plate
N : Nylon 66
T : Teflon
Al : aluminum

References

1) Masuda, H., T. Komatsu and K. Iinoya: *A. I. Ch. E. Journal*, **22**, 558 (1976).
2) Masuda, H. and K. Iinoya: *A. I. Ch. E. Journal*, **24**, 950 (1978).
3) Masui, N. and Y. Murata: *Jpn. J. Appl. Phys.*, **23**, 550 (1984).
4) Masui, N. and Y. Murata: *Jpn. J. Appl. Phys.*, **22**, 1057 (1983).
5) Yamamoto, H. and B. Scarlett: *Part. Charact.*, **3**, 117 (1986).
6) Davies, D. K.: *J. Phys. D*, **2**, 1533 (1969).
7) "Seidenki Handbook", Ohmu-sha (Tokyo) (1981).
8) Takeuchi, H.: "Daigaku-Enshu Danseiron", Shoukabu (Tokyo) (1969).
9) Bitter, J. G. A.: *Wear*, **6**, 5 (1963).

Relationship between Average Coordination Number and Void Fraction in Randomly Packed Systems of Uniform-sized Spheres Developed by Four Kinds of Computer Simulation†

Michitaka Suzuki and Toshio Oshima
Department of Chemical Engineering
*Himeji Institute of Technology**

Abstract

The relationship between the average coordination number and void fraction in a randomly packed system of uniform-sized spheres was investigated by four different kinds of computer simulated results to judge whether or not the coordination number could be uniquely estimated from the voidage. The relationship between the coordination number and voidage depends on the type of the computer simulation program used and our research results showed clearly that the coordination number cannot be uniquely estimated from the void fraction. These computer simulated results were compared with the calculated results using some empirical or model equations which have already been reported in the literature. The model equations by Gotoh and Suzuki et al. and the empirical equations by Sunada et al. and Nagao were found to be in fairly good agreement with some of our simulated results.

1. Introduction

The coordination number of a particle system or the number of contacts per particle, is not only a means of expression for particle arrangement structures but also a very important value related to the dynamic, heat-conduction and electric characteristics of powder. Empirical formulae or model formulae expressing the relationship between the average coordination number and void fraction in randomly packed systems of uniform-sized spheres have been proposed and put into practical use by Rumpf[1], Meissner *et al.*[2], Ridgeway and Tarbuck[3], Haughey and Beveridge[4], Nakagaki and Sunada[5], Smith *et al.*[6], Gotoh[7], Nagao[8], the authors[9], Ouchiyama and Tanaka[10] and others. However, the average coordination number obtained from the void fraction using the above formulae varies according to the formula. This variation, in the case of empirical formulae, appears depending on whether the base experimental values stemming from regular packing, liquid bridging or computer simulation. In the case of model formulae, variation occurs according to the type of model used to obtain the formulae, such as whether it is a regular-packing combination model or random-packing model.

This paper reports on two surveys:

(1) A survey, using results of four different computer simulation algorithms, regarding whether the average coordination number of randomly packed systems of uniform-sized spheres can be determined uniquely by the void fraction.

(2) A survey as to the extent to which the above empirical and model formulae[1~10] are applicable to the computer simulated results.

2. Computer simulation

The form randomly-packed systems of uniform-sized spheres, we used four computer simulation programs expressing different packing methods. These programs *a* to *d* are out-

* 2167, Shosha, Himeji-shi, Hyogo, 671-22
TEL. 0792-66-1661

† This report was originally printed in *J. Soc. Powder Technology, Japan,* **25**, 204-208 (1988) in Japanese, before being translated into English with the permission of the editorial committee of the Soc. Powder Technology, Japan.

lined below:

2. 1 Program *a*

Spheres, whose X-Y coordinates have been respectively determined by uniform random numbers, were dropped and packed into a rectangular-parallelepiped container whose base plane is a square, each side of which is 15 times longer than the particle diameter. This, if one had done nothing more, would have resulted in void fraction ϵ being constant at 0.423[11]. To obtain layers with different void fractions, therefore, we introduced the concept of the interparticle friction angle. That is, we modified the program[9] in such a way as to allow particles to remain in the same place when the zenithal angle ϕ is smaller than interparticle friction angle ϕ_c, and to roll down along the particles when the angle is larger. (Here, the zenithal angle ϕ is the angle of the contact point at which a falling particle comes in contact with an already-dropped particle.) This revised program enables the obtaining of particle-packed layers with different void fractions by packing particles for various interparticle friction angles ϕ_c. **Figure 1** illustrates a typical Y-Z cross section of a particle-packed layer simulated by this revised program (where void fraction ϵ = 0.7 and ϕ_c = 0.73 rad*.) The base plane is provided with irregular ups and downs to prevent the effect of base plane on the packing structure. We, therefore, calculated the void fraction and coordination number of particle-packed layers in such a range that is not affected by the base plane and the packed layer surface.

To prevent the sidewalls of the container from affecting the particle layers, we used the periodic boundary conditions with complete continuity at the boundaries, so that, for example, a part of the particles which were protruding out of the right side of the container could emerge on the left side of the container. The maximum void fraction that could result from this program, when ϕ_c is maximized (= $\pi/2$), is 0.841.

On the cross section, we drew a straight line connecting the centers (i.e., the centers of circles representing the cross sections of particles) of the particles contacting one another to allow the particle packing structure to be easily understood. We can see how the particles are arranged in a dendroid structure in the Z direction in **Fig. 1**.

2. 2 Program *b*

As in program *a*, we determined the X-Y coordinates of spheres in random numbers and applied particles one by one. Like in the simulation program developed by Nakagaki and Sunada[5,12], a uniform random number was set up when a falling particle comes in contact with an already-packed particle. When this uniform random number is smaller than predetermined particle adhesion probability P_c, a specific particle stays adhered there. And when larger, the particle rolls over the surface of such a packed particle. Particle layers with different void fractions can be obtained by varying interparticle adhesion probability P_c. **Figure 2** shows typical Y-Z cross section of a particle layer

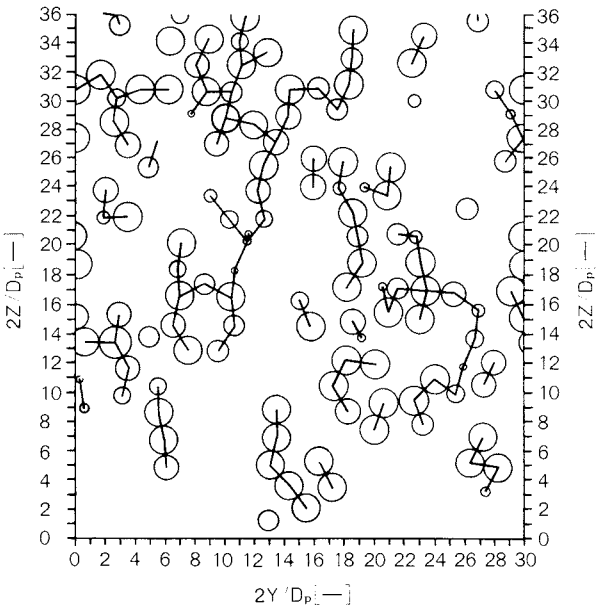

Fig. 1 Cross section of particle system by computer simulation program *a*

* For programs *a* and *b*, we calculated interparticle friction angle ϕ_c and particle adhesion probability P_c which make void fraction ϵ=0.7, as follows:
(1) changing ϕ_c and P_c, several creating particle layer patterns, and calculating value ϵ of each pattern;
(2) applying the least squares method to the result of step (1) above and calculating an approximate expression indicating the relationships of $\phi_c - \epsilon$ and $P_c - \epsilon$; and
(3) using an approximate expression to set up ϕ_c and P_c to make ϵ=0.7.

simulated by this program, where void fraction ϵ = 0.7 and P_c = 0.4867*. Like in program *a*, we set up void fraction and coordination number for a particle layer in such a range that is not affected by the unevenness of the base plane or surface of the layer, and used the periodic boundary conditions to prevent the sidewalls of the container from affecting the layer. The maximum void fraction that can stem from this program, where P_c is maximized (=1), is 0.837.

Like in program *a* again, the particles were arranged in a dendroid manner. However, the use of adhesion probability results in less orientation in the *Z* direction than in the case of program *a*, which used interparticle friction angle.

2.3 Program *c*

The first step we took on this program was to apply spheres without using interparticle adhesion or friction angle, i.e., under the same condition as in program *a*, where ϕ_c = 0 or, as in program *b*, where P_c=0. This, if one had done nothing more, would have resulted in a void fraction of 0.423[11]. We, therefore, created particle layers with different void fractions by using a uniform random number to selectively remove a specified number of particles from the particles in the particle layer (which are numerized in order of arrival). The particle layer created on this program contains cavities randomly. This layer is thus equal to a version made by applying the model of Shinohara *et al.*[13),14)], which combines regularly-packed portions and cavities, to a randomly-packed layer.

Figure 3 gives a typical *Y-Z* cross section of a particle layer simulated on this program, where void fraction ϵ = 0.7. Here, the once-formed particle layer is deprived randomly of the particles, so that particles are scarcely structured in a dendroid manner or in a certain orientation.

2. 4 Program *d*

Unlike programs *a*, *b* and *c*, this program creates a particle system by determining all the *X*, *Y*, and *Z* coordinates of spheres by a uniform random number, instead of dropping spheres with the help of gravity in the *Z* direction. When particle B whose *X*, *Y*, and *Z* coordinates had been set up by random numbers happened to overlap existing particle A, we moved particle B along the straight line connecting particles A and B center-to-center to a position where it did not overlap. We, thus, obtained a contact point between particles A and B. The particle layer simulated on this pro-

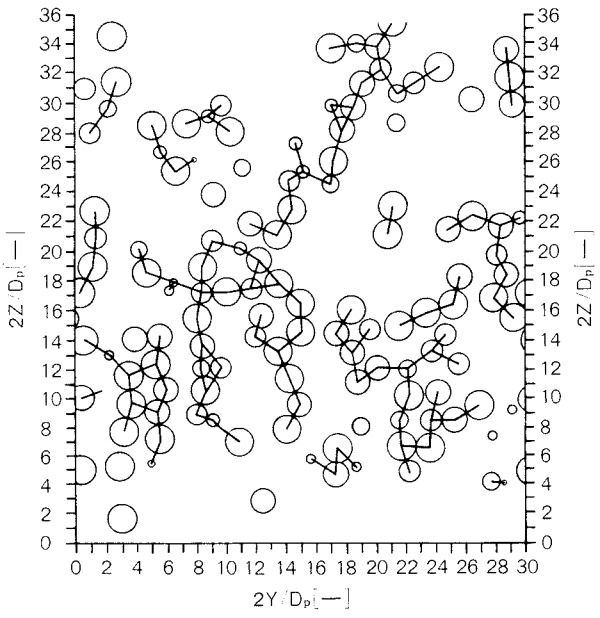

Fig. 2 Cross section of particle system by computer simulation program *b*

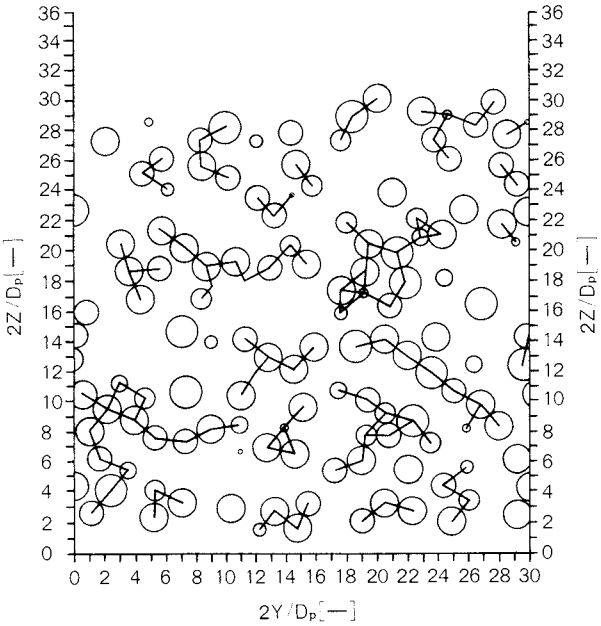

Fig. 3 Cross section of particle system by computer simulation program *c*

gram, we believe, shows a particle arrangement pattern similar to partially-coagulated aerosol.

Figure 4 indicates a typical cross section of a particle system created using this method, where void fraction $\epsilon = 0.7$. This pattern gave particles randomly in space so that contacts formed only when a particle happened to overlap an existing particle. This pattern, therefore, shows a smaller number of contacts and less orientation than those given in **Figs. 1 ~ 3.**

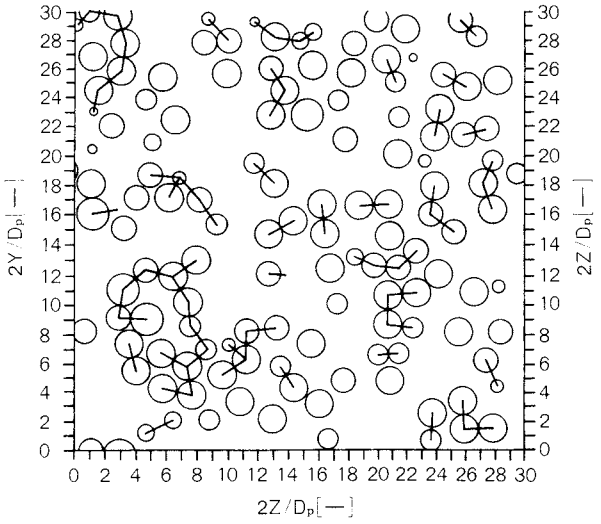

Fig. 4 Cross section of particle system by computer simulation program *d*

3. A comparison of computer simulation with estimation equations

3. 1 Results of calculations using conventional equations for average coordination number

Table 1 lists the conventional equations showing the relationship between void fraction ϵ and average coordination number $\bar{N}_c$. Of the listed equations, Eqs. (1) ~ (5) proposed by Rumpf[1], Meissner *et al.*[2], Ridgeway and Tarbuck[3], Haughey and Beveridge[4] and Nagao[8] are based on experimental results. Equation (6) by Nakagaki and Sunada[5] is an empirical formula based on their computer simulated results. Equations (7) and (8) by Smith *et al.*[6] and Gotoh[7] are model formulae stemming from a regular packing pattern. And Eqs. (9) and (10) by the authors[9] and Ouchiyama and Tanaka[10] are model formulae based on a randomly-packed pattern.

Figure 5 compares the results of calculations using the above equations with the results of the aforementioned four kinds of computer simulation. Of the curves representing the calculation results, the broken lines show the results of empirical formulae, while the solid

Table 1 Equations for relation between average coordination number and void fraction in uniform-sized particle system

Equations	References
$\bar{N}_c = 3.1/\epsilon$	(1) Rumpf[1]
$\bar{N}_c = 2e^{2.4(1-\epsilon)}$	(2) Meissner, *et al.*[2]
$\epsilon = 1.072 - 0.1193\bar{N}_c + 0.00431\bar{N}_c^2$	(3) Ridgeway, *et al.*[3]
$\bar{N}_c = 22.47 - 39.39\epsilon \quad (\epsilon \leq 0.5)$	(4) Haughey, *et al.*[4]
$\bar{N}_c = \{8\pi/(0.727^3 \times 3)\}(1-\epsilon)^2$	(5) Nagao[8]
$\bar{N}_c = 1.61\epsilon^{-1.48} \quad (\epsilon \leq 0.82)$ $\bar{N}_c = 4.28 \times 10^{-3} - \epsilon^{17.3} + 2 \quad (0.82 \leq \epsilon)$	(6) Nakagaki, *et al.*[5]
$\bar{N}_c = 26.49 - 10.73/(1-\epsilon) \quad (\epsilon \leq 0.595)$	(7) Smith, *et al.*[6]
$\bar{N}_c = 20.7(1-\epsilon) - 4.35 \quad (0.3 < \epsilon \leq 0.53)$ $\bar{N}_c = 36(1-\epsilon)/\pi \quad (0.53 \leq \epsilon)$	(8) Gotoh[7]
$\bar{N}_c = \dfrac{2.812(1-\epsilon)^{-1/3}}{(b/D_p)^2(1+(b/D_p)^2}$ (b/D_p) is obtained by following equation $(1-\epsilon)^{-1/3} = \dfrac{1+(b/D_p)^2}{1+(b/D_p)e^{(D_p/b)^2}\,\mathrm{Erfc}(D_p/b)}$ Erfc means Error function	(9) Suzuki, *et al.*[9]
$\bar{N}_c = (32/13)(7-8\epsilon)$	(10) Ouchiyama, *et al.*[10]

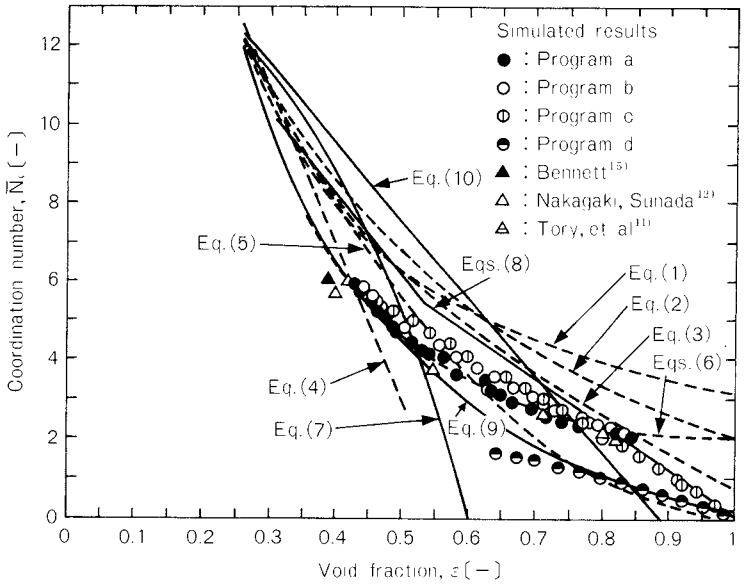

Fig. 5 Comparison of computer simulated results with calculated curves by estimation equations in Table 1

lines are the results of model formulae. As is evident from this figure, conventional estimation equations representing the relationship between void fraction ϵ and average coordination number $\bar{N}_c$ in randomly-packed layer or system of uniform-sized spheres produce different calculation results depending on the type of equation. For example, an estimated average coordination number based on particle-layer void fraction actually measured varies according to the type of equation used. This variation, in the case of empirical formulae, stems from the diversity of methods of creating particle layers and of measuring coordination numbers used in setting up the formulae. In the case of model formulae, this variation is due to the difference in particle layer models depending on the researcher who envisions each model.

3. 2 Results of computer-simulated packing

Figure 5 illustrates the relationship between the void fraction ϵ and average coordination number $\bar{N}_c$ of particle layers simulated by four different computer programs, which can clearly prescribe particle packing conditions. Here, when void fraction ϵ ranged from 0.423 to 0.8, computer simulation on programs *a*, *b* and *c* produced almost the same results, despite some dispersion. However, when ϵ was equal to or more than 0.8, programs *a* and *b* produced average coordination number $\bar{N}_c$ gradually approaching 2, and program *c* produced $\bar{N}_c$ approaching 0, as ϵ approximated 1. This, we believe, was because of the following:

- On programs *a* and *b*, particles were arranged in a dendroid pattern despite an increase in interparticle friction angle ϕ_c and particle adhesion probability P_c, so that each particle contacted two neighboring particles, one above and the other below:
- On program *c*, particles contacting no neighboring particles increased in number when a once-packed particle layer had been deprived of many particles. Compared with the above programs, program *d* produces a small average coordination number $\bar{N}_c$ at the same void fraction and $\bar{N}_c$ gradually approached 0 as ϵ neared 1. This $\bar{N}_c$ decline with the same ϵ, we presume, is because of the appearance of contacts only when particles whose X, Y and Z coordinates had been determined by random numbers happen to overlap existing particles. In addition to the results of simulation using these four programs, **Fig. 5** indicates the results of other major computer simulated results[11),12),15)] reported so far.

3. 3 A comparison of computer simulation results with estimation equations

We compared the results of four kinds of

computer simulation with the results of calculations using equations for average coordination number to find which equation applies best to which packing condition. This reveals that, in the void fraction ϵ range between 0.42 and 0.8, the results of calculations using Nakagaki and Sunada's[5] empirical Eq. (6) corresponds well to the results of simulation using programs *a*, *b*, and *c*. This, we believe, is because this empirical formula is based on the above researchers' computer simulation using the concept of interparticle adhesion probability. Even when ϵ is equal to or more than 0.8, this formula corresponds well to the results of program *a* and *b*. To the results of program *c* with ϵ equal to or more than 0.8, Gotoh's[7] model Eq. (8) corresponds well. To the results of program *d*, on the other hand, Nagao's[8] empirical Eq. (5) and the authors'[9] model Eq. (9) based on random packing corresponds comparatively well. Equation (9) also corresponded well to the results of simulation using programs *a*, *b* and *c* with ϵ in the 0.42 ~ 0.55 range. This, we believe, is because this model formula is based on the homogeneous isotropy of particle arrangement so that it corresponds well to the case when interparticle friction angle and adhesion probability are small and the particles in the particle layer are arranged less directionally and more homogeneously.

Many of the other empirical and model formulae did not correspond well to our simulation results or main conventional simulation results. In fact, the coordination numbers calculated based on these formulae exceeded the comparable simulation results. This, we presume, is because of the following:

- Empirical Eqs. (1) ~ (3): They stem from coordination numbers measured using liquid bridging. As point out by Bernal and Mason[16], when coordination numbers are measured by liquid bridging, and it occurs also between particles not in contact, but placed near each other resulting in coordination numbers determined at values exceeding their real values.
- Equations (7): It is based on a model combining two regularly-packed systems so that it fails to correspond to comparable simulation results. Despite being a model formula based on random packing, Eq. (10) fails to correspond to comparable computer simulation results.

4. Conclusion

Using four different computer programs, we simulated randomly-packed systems of uniform-sized spheres to determine their average coordination number and void fraction. This revealed that the relationship between average coordination number and void fraction varied according to the type of program used so that no average coordination number could be determined uniquely by voidage. This led us to conclude that there existed no equation applicable to all circumstances. We then compared simulation results with various empirical and model formulae proposed so far. This comparison showed that Sunada *et al.*'s empirical formula corresponded well to three, out of the above four, simulation results over a wide void fraction range. Some of the above simulation results corresponded well to the authors' and Gotoh's model formula and Nagao's empirical formula in a certain void fraction range.

Nomenclature

b	:	constant in Eq. (9)	
D_p	:	particle diameter	[m]
$\bar{N}_c$	:	average coordination number	[–]
P_c	:	adhesive probability in program *b*	[–]
X, Y, Z	:	coordinates	[–]
ϵ	:	void fraction	[–]
ϕ	:	zenithal angle at the first contact in program *a*	[rad]
ϕ_c	:	angle of friction in program *a*	[rad]

References

1) Rumpf, H.: *Chemie Ing. Techn.*, **30**, 144 (1958).
2) Meissner, H.P., A.S. Michaels and R. Kaiser: *Ind. Eng. Chem., Process Design and Dev.*, **3**, 202 (1964).
3) Ridgeway, K. and K.J. Tarbuck: *Brit. Chem. Eng.*, **12**, 384 (1967).
4) Haughey, D.P. and G.S.G. Beveridge: *Can. J. Chem. Eng.*, **47**, 130 (1969).
5) Nakagaki, M. and H. Sunada: *Yakugaku Zasshi*, **88**, 651 (1929).
6) Smith, W.O., P.D. Foote and P.F. Busang: *Phys. Rev.*, **34**, 1271 (1929).
7) Gotoh, K.: *J. Soc. Powder. Technol., Japan*, **15**, 220 (1978).
8) Nagao, T.: *Trans. J.S.M.E.*, **44**, 1912 (1978).
9) Suzuki, M., K. Makino, M. Yamada and K. Iinoya: *Kagaku Kogaku Ronbunshu*, **6**, 59 (1980).

10) Ouchiyama, N. and T. Tanaka: *Ind. Eng. Chem. Fundam.*, **19**, 340 (1980).
11) Tory, E.M., B.H. Church, M.K. Tam and M. Ratner: *Can. J. Chem. Eng.*, **51**, 484 (1973).
12) Nakagaki, M. and H. Sunada: *Yakugaku Zasshi*, **83**, 73 (1963).
13) Shinohara, K., H. Kobayashi, K. Gotoh and T. Tanaka: *J. Soc. Powder Technol., Japan*, **2**, 352 (1965).
14) Shinohara, K. and T. Tanaka: *Kagaku Kogaku*, **32**, 88 (1968).
15) Bennett, H.: *J. Appl. Phys.*, **43**, 2727 (1972).
16) Bernal, J.D. and J. Mason: *Nature*, **188**, 910 (1960).

The Mechanism and Grinding Limit of Planetary Ball Milling†

Qian-Qiu Zhao, Shigeki Yamada and Genji Jimbo
Department of Chemical Engineering
*Nagoya University**

Abstract

To clarify the mechanism and characteristics of planetary ball milling, batch grinding experiments were carried out under various conditions. The motion of the balls in the mill was observed and analyzed by using multistroboscope photography connected to an image analyzer, and the contact force on the mill wall by the balls was measured using a pressure sensor.

The surging phenomenon of the balls in the mill was confirmed by the photographic analysis. Based on this result, it is predicted that the grinding mechanism in the planetary ball mill consists of compressive, abrasive and shear stress of the balls, which is believed to be effective in producing very fine particles.

About thirty percent of ball filling of the mill was found to be the optimum. This was explained by an analysis of the motion of the balls and the measurement of the contact force.

It was found that the grinding limit is greatly dependent on ball size. An experimental equation expressing the relationship between the finest average size of the ground product and the ball size is also given in this article.

1. Introduction

Techniques for producing submicron particles are urgently required by many advanced industries due to the rapid development of new materials. This trend leads to an active study of submicron grinding. Most of submicron grinding, however, is wet grinding in traditional ball mills.

In this paper, the grinding of dry silica sand in a batch type planetary ball mill is reported. The effects of various technical parameters, such as ball size and density of ball material, frequency of revolution of the equipment, volume of balls in the mill etc., on both the grinding rate and grinding limit are systematically investigated. In addition, the motion of the balls in the mill is observed and analyzed, and the contact force of balls on the mill wall is measured so that the mechanism of fine grinding in the planetary ball mill can be predicted.

2. The experiment

2. 1 Planetary ball mill

A schematic diagram of the planetary ball mill used in this study is shown in **Fig. 1**. Two

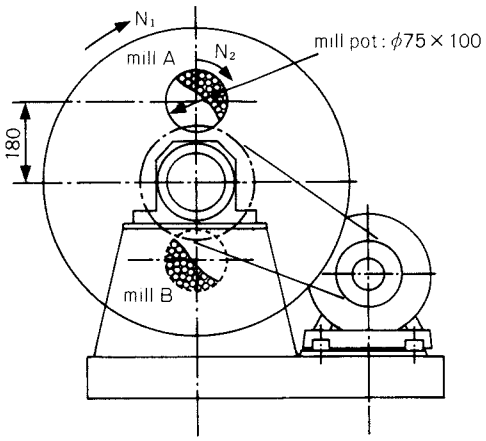

Fig. 1 Schematic diagram of the planetary ball mill

* Furo-cho, Chikusa-ku, Nagoya, 464
TEL. 052-781-5111

† This report was originally printed in *J. Soc. Powder Technology, Japan,* **25**, 297-302 (1988) in Japanese, before being translated into English with the permission of the editorial committee of the Soc. Powder Technology, Japan.

Table 1 The Grinding Media Used

Diameter of grinding media (mm)	
Steel ($\rho_B = 7.8 \times 10^3$ kg/m^3)	8 4 2 1*
Alumina (3.5×10^3)	10 5 1.4
Glass (2.5×10^3)	4 1.5

*Steel shot selected by an inclined plate

balanced mill bodies are mounted on a casing cover and are carried by the cover revolving around the central axis. At the same time, rotation gears mounted at the mill bodies bite the stationary gear fixed at the central axis and carry the mill bodies to rotate around their own axes in the same direction as the revolution. By this equipment, as high as about 100 g centrifugal acceleration can be obtained as the frequency of revolution is 11.76 Hz (700 rpm). In this study, the revolution to rotation gear ratio is fixed at 0.5, the rotation speed ratio is 69% of the critical value of the equipment which can be calculated by the equation given by Bradley[1] or by the authors[5].

2. 2 Grinding media and samples

The grinding media used in this experiment are shown in **Table 1**. Silica sand composed of 88.62% SiO_2 is used as the sample.

2. 3 Measurement of particle size distribution

The particle size distributions of the ground products are measured from 1 to 192 μm using a laser diffractometry sizer, granulometre CILAS 715 with a 150~200 W ultrasonic dispersing bath, and 0.15 to 20 μm by a Microtrac SPA. The specific surface area of the products is measured by using the air permeability method.

2. 4 Observation of the motion of balls in the mill[4]

Photographs of the motion of balls in the mill are taken by using multistroboscope photography and are analyzed by an image analyzer.

2. 5 Measurement of contact force

A direct measurement method of the maximum value of the contact force due to the balls on the mill wall by using a pressure sensor has been developed[5]. The sensor consists of two films which trace the contact force by the change of color on a film and a rubble plate with sensor points. The measuring principle is that the contact force applied to the sensor attached to the mill wall leads to a certain change of sensor points on the rubber plate, and the change in the sensor points is recorded by the change in the color on the film.

3. Eexperimental results

3. 1 Size distribution of the ground product

An example of size distributions of the product ground by 2 mm steel balls in the mill is given in **Fig. 2**. It is seen that the distribution

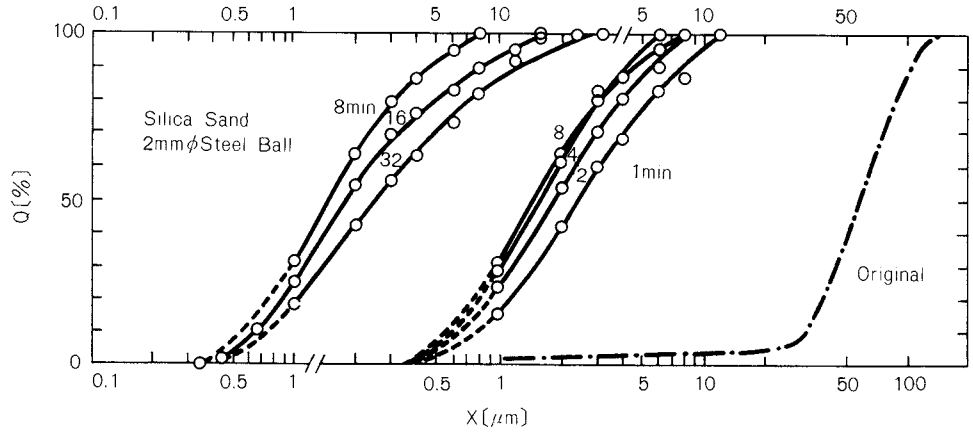

Fig. 2 Particle size distribution of the ground product by 2 mm steel ball ($J = 0.3$, $U = 0.3$, $N_1 = 11.67$ Hz)

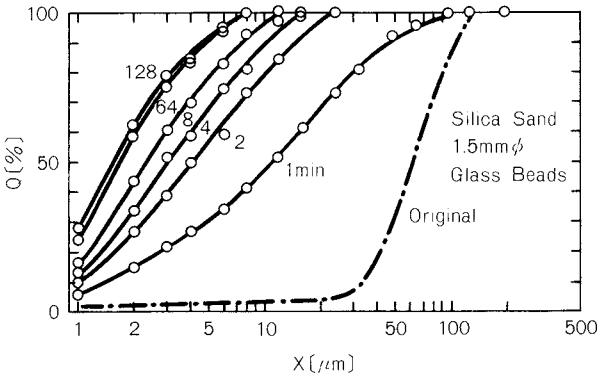

Fig. 3 Particle size distribution of the ground product by 1.5 mm glass beads ($J=0.3$, $U=0.3$, $N_1=11.67$ Hz)

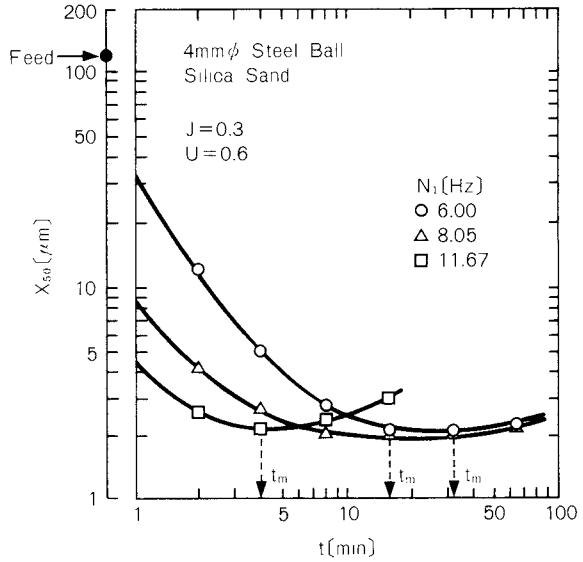

Fig. 4 Effect of revolution speed on the grinding process

is shifted quickly to the finest and then moved negatively to the coarse with the increase in grinding time. It should be noted that the rate of grinding in the mill is so fast that the average size of the feed silica sand is reduced from 53 μm to 2.5 μm in only one minute, down to 1.5 μm after 4 min with 30% of the product under 1 μm which seems to be the limit of grinding under this condition. From this result, the rate of grinding in the planetary ball mill is known to be about 100 times greater than that in a tumbling ball mill and about 50 times greater than that in a stirred ball mill[2].

Another result is given in **Fig. 3**, from which it is seen that even small glass beads with a low density can be used to grind hard materials such as silica sand in the planetary ball mill because of the great centrifugal acceleration.

Based on this observation, the significant effect of centrifugal acceleration by the planetary motion of the mill on the rate of grinding is confirmed. Further investigation of the technical possibilities of the mill is definitely required.

On the other hand, note that the rate of grinding is so fast and the product so fine that it is very difficult to describe the complicated process adequately by a phenomenological approach that studies the kinetics of grinding in the mill in terms of the comprehensive batch grinding equation.

In the following a necessary first approach, 50% average size of the product will be used as a basis to evaluate the effect of technical parameters. This is because the size distribution curves of the ground product are similar, as shown above.

3. 2 Characteristics of planetary ball milling

3. 2. 1 The effect of the revolution speed

Since the speed of revolution of the mill has a very great effect on the rate of grinding, the first factor to be studied should be the speed of the mill. A set of experimental results relating to the grinding of silica sand using of 4 mm steel balls at three speeds, namely, 6 Hz, 8.05 Hz and 11.67 Hz, are given in **Fig. 4**.

It is at once seen that the higher the speed of revolution, the greater the rate of grinding and the shorter the time to produce the finest product. The grinding limit under this condition is 2 μm in average size, independent of the speeds. The effect of the speed of revolution on the rate of grinding can therefore be obtained by plotting the grinding time needed to produce the finest product against the speed. Such results are given in **Fig. 5**.

It is easy to find from this figure that the rate of grinding in the planetary mill is directly proportional to the cube of the speed of revolution of the mill. A similar result of wet grinding in a planetary mill has also been reported by Bradley[1].

Since centrifugal acceleration is proportional to the square of the speed, the rate of grinding should be proportional to 1.5 power of the

centrifugal acceleration. It is perhaps of interest to point out that this result is also supported by vibration milling[3]. This suggests that the vibration ball mill can be considered to be one type of the planetary mill in which the radii ratio is smaller than unit, and the mill body is not rotated around its own axis.

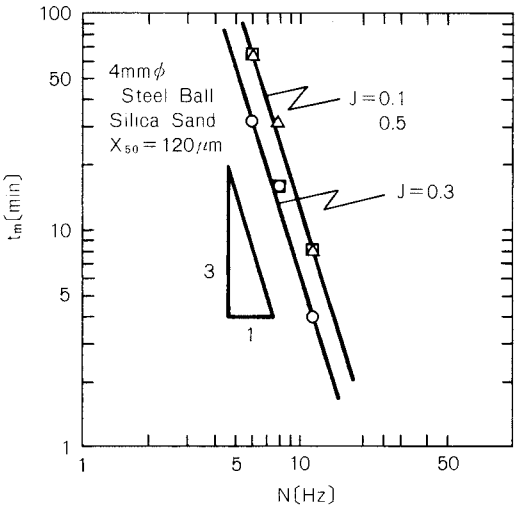

Fig. 5 Plot of t_m vs. N_1

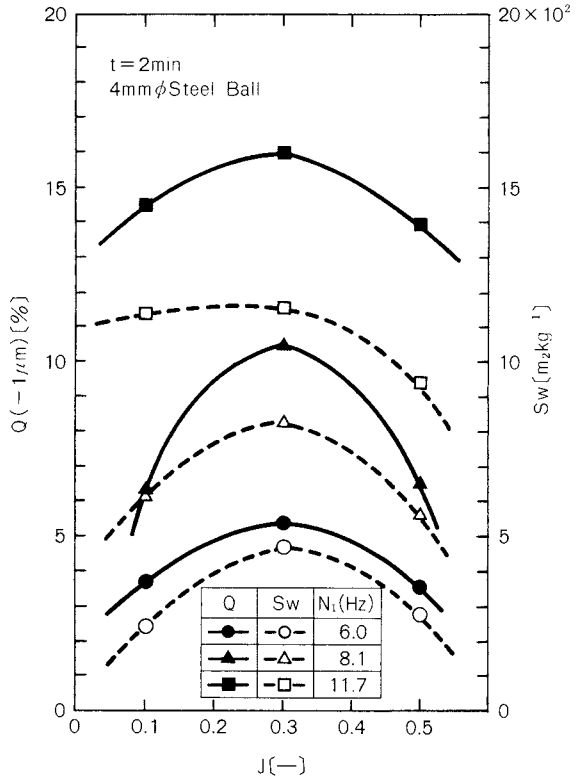

Fig. 6 Effect of fractional ball filling

3. 2. 2 The effect of fractional ball filling of mill

Examination of **Fig. 5** reveals another interesting subject for evaluating mill filling. It suggests that 30% of mill filling requires the shortest time to produce the finest product.

This result is supported by another result shown in **Fig. 6**. In it, both the fine fraction under 1 μm measured by a granulometre, and the specific surface of the product measured by a permeability method, ground for 2 minutes for three different degrees of mill filling are given when the quantity of powder is 30% of the space between the grinding balls.

3. 2. 3 The effect of fractional powder filling

In **Fig. 7** a set of curves are given showing the effect of the powder fraction for 4 mm steel balls and 1.5 mm glass balls. It is seen that the rate of grinding increases as the quantity of powder in the mill decrease, something well known to practical mill operators. The finest product which can be attained in the mill, however, is not greatly affected by this quantity.

3. 2. 4 The effect of ball diameter and the density of ball material

In **Fig. 8** test results are given for the use of various kinds of balls. It is seen that all the curves show a similar tendency, that is the mean size of the product is reduced to a minimum and then increases with increased grinding time. It is interesting, however, to note that

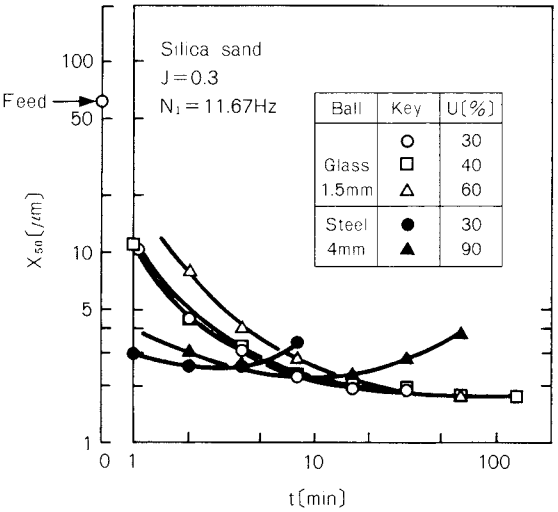

Fig. 7 Effect of fractional powder filling

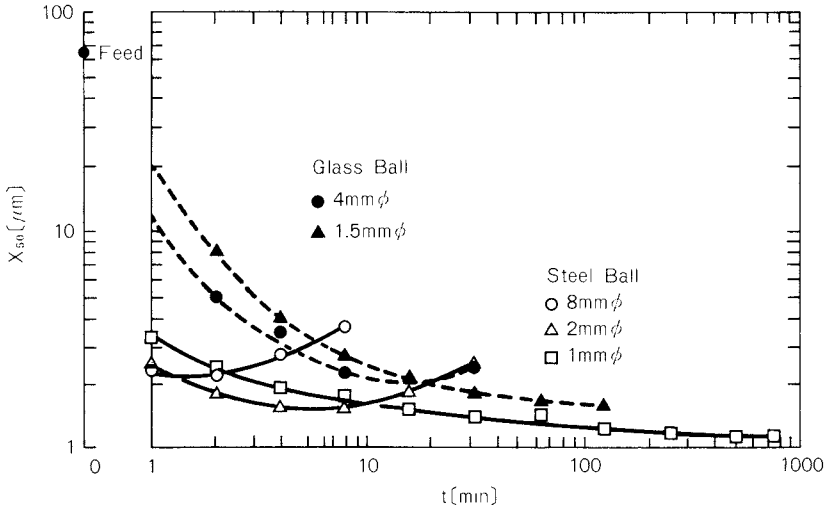

Fig. 8 Effect of ball size and density of ball material ($J=0.3$, $U=0.3$, $N_1=11.67$ Hz)

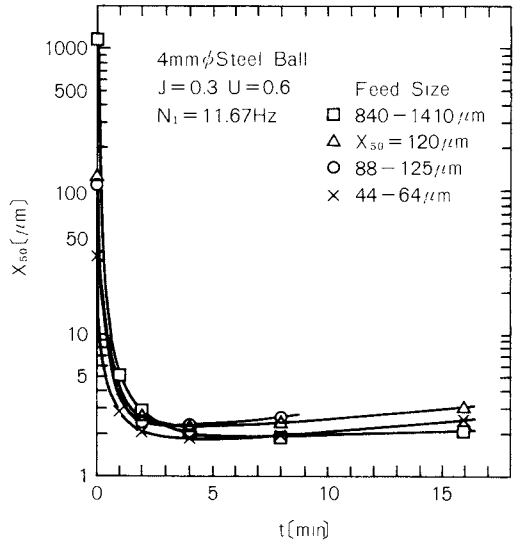

Fig. 9 Effect of feed size of the material

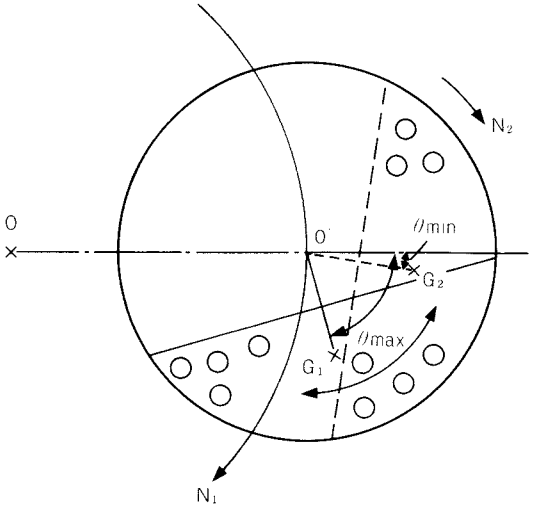

Fig. 10 Schematic representation of the motion of balls in the mill (G_1 and G_2 are gravity centers of ball masses)

the rate of grinding by larger balls with greater density is faster and reaches an equilibrium of grinding corresponding to a coarser limited fineness of product in a shorter time, then turning to negative grinding; while smaller balls give a finer product for longer term grinding.

3. 2. 5 Effect of feed size of material

In **Fig. 9** a set of curves are given showing the grinding of feeds of various sizes by 4 mm steel balls. It is seen that no significant difference in the grinding could be found over the broad size range of from about 50 μm to 1000 μm. It should be pointed out, however, that there must be an optimal ball diameter which gives the best breakage of a given feed. It is therefore convenient to consider ball size and feed size together[6].

4. Discussions

4. 1 The motion of balls and the grinding mechanism

A schematic picture is given in **Fig. 10** showing the motion state of balls in the mill based on photographic analysis.

It is shown that the cascading of balls does not occur in the mill. It is also known from the analysis result that the entire charge of the

mill, as a coherent mass, is surging on the mill wall. Thus, for one part of the cyclical motion, the charge is moving around the axis of the mill in the same direction as the mill shell, while during the second part of the motion, it moves in the opposite direction. It could be expected that most of the comminution, under this condition, occurs between the mill wall and the balls by the compressive, friction, abrasive and shear stresses of the ball mass applied on the particle layer that adhered to the mill wall and it is partly occurred within the ball mass by the shear stress due to the speed gradient of moving balls.

On the basis of this consideration, the moving distance, frequency and the contact force of the surging appear to be important quantities affecting the rate of grinding. It is predicted that these quantities will be determined by the fractional ball filling of the mill.

A set of results expressing the relationships of both the surging range and frequency between mill filling are given in **Fig. 11**, in which the parameter ($\theta_{max} \sim \theta_{min}$) expresses the largest difference between the angles shown in **Fig. 10** and f_s the statistic frequency of appearance of the largest displacement of the balls. Clearly, each of the curves has a maximum at 30% mill filling.

Furthermore, a curve expressing the maximum contact force for various degrees of mill filling is given in **Fig. 12**. It is seen that the contact force increases almost directly with ball charge for small mill filling, reaching a maximum at 30%. It then decreases slightly to a constant value for greater fractional ball filling.

The most important point given by all the results is that a maximum rate of grinding can be attained at about 30% mill filling for a planetary mill operating under such condition. This can be explained by the grinding mechanism occurring in the mill.

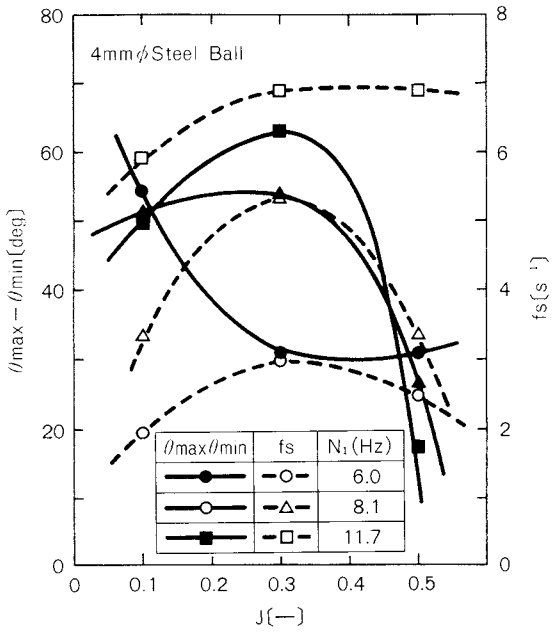

Fig. 11 Effect of fractional ball filling on the motion of balls

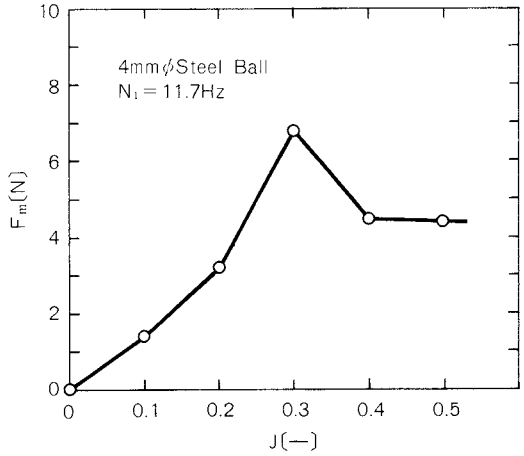

Fig. 12 Effect of fractional ball filling on the contact force

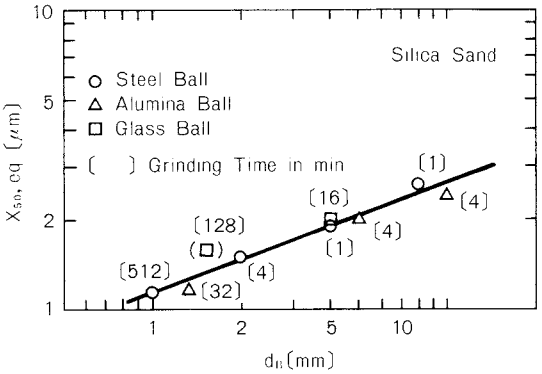

Fig. 13 Effect of ball size on the average equilibrium size of the ground product

4. 2 The effect of ball size on grind limit

In **Fig. 13** plots of the finest size are given from the minimum of the curves expressed in **Fig. 5** corresponding to the equilibrium of grinding against ball diameter.

A straight line can be approximated over the range of ball diameters used in these tests, and

over the range of particle size down to 1 micron on the log-log paper for all the data by various steel, alumina and glass balls. This result suggests that a finer product can be attained by the use of smaller balls, independent of the density of the ball material, provided the grinding time is not important. This relation can be expressed as,

$$x_{50,eq} = 1.15 \times 10^{-3} d_B{}^{0.36} \qquad (3.1)$$

Furthermore, in **Fig. 14** the size distributions of the finest products for various balls are given. It is seen that the distributions become sharper with reduced ball size.

Examination of this phenomenon has revealed one of the most important advantages of the planetary mill over conventional mills. The combination of a great number of small grinding beads with a greatly impressed centrifugal acceleration in a planetary mill can produce fine particles which cannot be attained in conventional mills.

The grind limit in a mill is probably determined by an equilibrium between the rate of grinding and the rate of negative grinding. The impact of large balls leads to a great contact force and could grind coarse particles quickly. The grinding rate, however, will decrease rapidly with the decreased size of particles since the number of particles is greatly increased, and the possibility of a particular particle to be stressed is greatly decreased. On the other hand, the coating of particles on the mill wall and on the grinding balls will be increased with the decrease of particle size because of the increased cohesive force. The rate of negative grinding can be increased by the excess impacting force, which will lead to a strong agglomeration of already ground particles. This is why the grind of dry materials is limited by a few microns in average size, and the negative grinding phenomenon occurs in conventional ball mills. Detail examination of the phenomenon of negative grinding relating to the grinding of limestone in a laboratory tumbling ball mill has been given elsewhere[5].

Based on this consideration, it is believed that the surging motion of balls in the planetary ball mill must give a good mechanism for producing finer particles. This is also another important advantage of the mill over conventional mills.

5. Conclusions

1) The rate of grinding in a planetary ball mill operated under a centrifugal acceleration of about 100 g is about 100 times greater than that in a conventional ball mill. The feed of silica sand in a few millimeters can be ground to about 2 μm in a few minutes. And the grinding rate is directly proportional to the cube of the speed of revolution of the mill.

2) The combination of small beads used as grinding media with a greatly impressed acceleration gives an excellent condition to produce ultrafine particles in the planetary ball mill. As a result, a fine product which cannot be attained in conventional ball mills can be attained in the

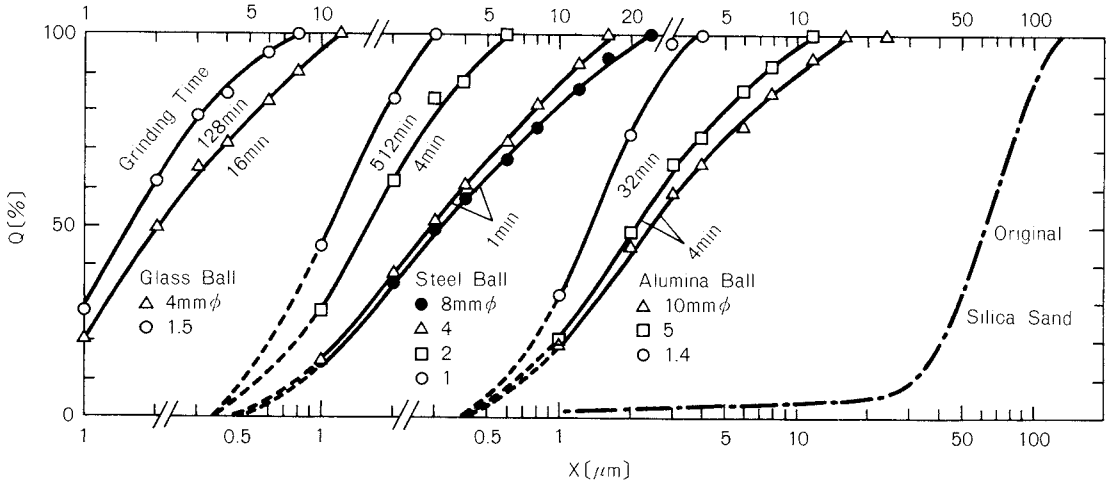

Fig. 14 Limited size distributions of the ground product by various balls (J= 0.3, U= 0.3, N_1 = 11.67 Hz)

planetary ball mill.

3) The surging phenomenon of the motion of balls in the mill is considered good to produce a grinding mechanism by compressive, friction, abrasive and shear stress without impact.

4) Fractional ball filling shows an optimum at about 30% of the volume of mill, which gives the best grinding, under the surging condition. This is explained by the analysis of the motion of balls and the contact force.

5) The grinding limit is dependent on the diameter of balls, but it is independent of the density of the ball material. The relationship between ball size and the limited average size of the ground product can be expressed by Eq. (1). It is also confirmed that a reduced size of balls can sharpen the size distribution of the ground product.

Acknowledgments

We gratefully acknowledge the financial assistance of the Science Foundation of the Ministry of Education of Japan (Grant No. B-60470114) and the equipments assistance of KURIMOTO, LTD. and Dr. Y. Kuwahara and Mr. K. Suzuki, Government Industrial Research Institute, Nagoya.

Nomenclature

d_B	:	ball diameter	[m]
F_m	:	maximum contact force applied by balls on the mill wall	[N]
f_s	:	frequency of the largest displacement of balls	[1/s]
g	:	gravitational acceleration	[m/s^2]
J	:	fractional ball filling of the mill	[−]
N_1	:	revolution speed of the mill	[1/s]
N_2	:	rotation speed of the mill	[1/s]
Q	:	under-size percent	[%]
S_w	:	specific surface area	[m^2/kg]
t	:	grinding time	[min]
U	:	fraction of powder filling the void volume within the ball charge	[−]
x	:	particle size	[m]
x_{50}	:	50% average particle size	[m]
$x_{50,eg}$	:	50% average particle size at grinding equilibrium	[m]
θ	:	angle expressed in **Fig. 10**	[deg]
ρ_B	:	density of the ball material	[kg/m^3]

References

1) Bradley, A.A.: Dechema-Monographien, 35 Vortrage, Zerkleinern, Symposion in Cannes, Bd. 69, Nr. 1292-1326, Teil 2, 781 (1971).
2) Jimbo, G., T. Shibata, S. Yamada, S. Masuda and Y. Sakurai: 1st World congr. Particle Technol., Nurnberg, (1986).
3) Rose, H.E. and R.M.E. Sullivan: Vibration Mills and Vibration Milling, Constable & Co., London (1961).
4) Yamada, S : Master Thesis, Dept. of Chem. Eng., Nagoya University (1985).
5) Zhao, Q.Q.: Doctoral Dissertation, Nagoya University (1989).
6) Zhao, Q.Q. and G. Jimbo: *J. Soc. Powder Technology, Japan,* **25**, 603-608 (1988).

The Compressive Crushing of Powder Bed†

Yoshiteru Kanda, Shunsuke Takahashi
Yuji Hata, and Torajiro Honma
Department of Chemical Engineering
*Yamagata University**

Abstract

Roller mills have come to be actively used for the fine grinding of solids. In this paper, the compressive crushing of powder beds was carried out to study a roller mill. The effect of the applied load, the mass of feed and the particle size on the probability of crushing and on the crushing resistance were studied. The sample used was quartz. The following results were obtained:

1) When the applied load was constant, the deformation of the powder bed increased with the increase in the mass of feed and particle size.
2) The probability of crushing increased with the increase in the applied load, but the rate of increase of the probability gradually decreased.
3) The mass of the feed with a low crushing resistance was observed, and it had a certain range. This range narrowed with the decrease in the particle size.
4) The crushing resistance increased with the decrease in the particle size.

1. Introduction

In Japan today, much powder is being processed and most of it is going through an energy-consuming crushing process. Research and development, currently being conducted to find energy-saving crushing processes, include modification of crushers.

The fine grinding process in the cement and coal industries used to employ ball mills alone and currently use roller mills frequently. A roller mill is believed to save crushing energy 20 ~ 30% in comparison to ball mills. Its other advantages include its capability to perform grinding, drying and classification by one unit alone, along with its reduced floor area requirement and reduced noise. The roller mill crushes solids while conducting compressive shearing of its walls or solids on the disc with the help of the roller's centrifugal force or vertical load. The roller mill's crushing mechanism is thus based mainly on compressive load[1].

Studies on the compressive crushing of powder beds reported so far include:

- Matsui *et al.*'s[2] study of a method for estimating net crushing workload and specific surface area increment based on load conditions and solid properties; and
- Hanish *et al.*'s[3] experiments on the effect of the plunger's stress geometry on the load-deformation curve, a comparison of compressive strength with single-particle crushing, and the particle size distribution of crushed product.

These studies, however, do not give enough information.

As such, we conducted a basic experiment on roller mills, consisting of conducting compressive crushing of powder beds with different feed mass, particle sizes and applied loads. We then studied compressive crushing in terms of crushing probability and energy efficiency. Here are the results:

2. Specimen and experimental method

2. 1 Experimental apparatus

Figure 1 illustrates the experimental apparatus used. (1) represents a load cell, (2) differen-

* 4-3-16, Zyounan, Yonezawa-shi, 992
TEL. 0238-22-5181

† This report was originally printed in *J. Soc. Powder Technology, Japan,* **25**, 292-296 (1988) in Japanese, before being translated into English with the permission of the editorial committee of the Soc. Powder Technology, Japan.

Table 1 Properties of quartz

ρ [kg/m^3]	Y [Pa]	ν [–]	W_i [kWh/t]	$H.G.I.$ [–]	H_v [Kg/mm^2]	H_m [–]	S_s [–]
2.62×10^3	8.71×10^{10}	0.16	13.3	37	245	6.5	1.1×10^7

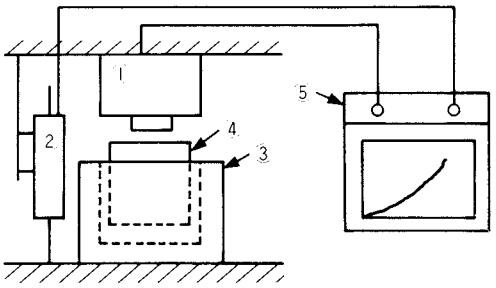

1 Load Cell
2 Differential Transformer
3 Grinding Vessel
4 Plunger
5 x-y Recorder

Fig. 1 Experimental apparatus

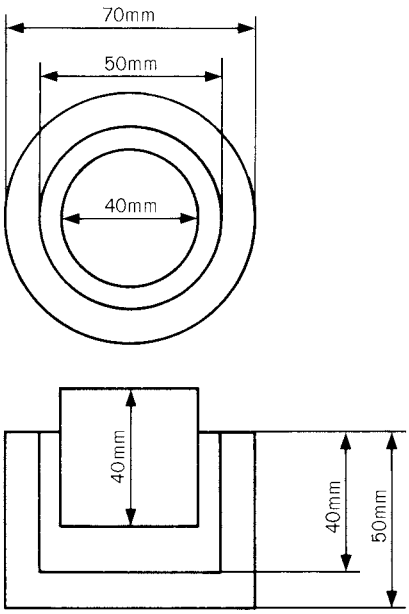

Fig. 2 Crushing apparatus

tial transformer, (3) and (4) the two major parts of a crushing apparatus. (3) is a grinding vessel, while (4) is a plunger. Both of them are made of silicon nitride. (5) is an X-Y recorder.

Figure 2 gives a detail diagram of the crushing apparatus.

2. 2 Specimen

We used quartz as a specimen, whose properties are summarized in **Table 1**[4~6]. Quartz was roughly crushed and pulverized by a jaw crusher and then by hand. The resulting quartz powder was classified by $2^{1/4}$ sieves and a rotating and tapping shaker into six grain-sized categories: 3.5 ~ 4 (5.660) ~ 4.760 mm), 7 ~ 8 (2.830 ~ 2.380 mm), 12 ~ 14 (1.410 ~ 1.190 mm), 24 ~ 28 (0.710 ~ 0.590 mm), 48 ~ 60 (0.297 ~ 0.250 mm), and 80 ~ 100-mesh (0.177 ~ 0.149 mm). To obtain the above classification, powder was first classified roughly into approximate categories. Some 100 grams of powder was put into each sieve. It was then sieved by the rotating and tapping shaker for about ten min.

2. 3 Experimental method

We conducted a crushing test by applying compressive load to a quartz specimen filled flatly in the grinding vessel via the plunger using Showa Sokki's pellet tester. In the interest of the experimental apparatus, the crosshead speed was made constant at 0.5 mm/min as specified by the apparatus supplier in all experiment sessions. The minimum compressive load applied was 10^3 N and maximum 10^4 N. In the interest of the particle size and feed mass, two series of load conditions were used: 10 conditions in increments of 10^3 N and 5 conditions in increments of 2×10^3 N. The feed masses were integral multiples of 9 g, i.e., 8 feed ranging 9 ~ 72 g. We set up the standard feed mass of 9 g as follows: We filled the grinding vessel with particles in the 3.5 ~ 4-mesh range, which was the maximum particle size range used in this experiment, in one layer as visually seen, and we weighed it (weight: about 9 g). This 9-g weight was equal to the specimen mass calculated on the assumption that some 50% of the grinding vessel's base area was occupied by the projected area of one layer of assumed particles with a diameter equal to the calculated average diameter of the

sieve mesh used to classify the specimen into categories. The feed mass was then decided on with the 9-g weight as the standard.

For four particle size categories in the 3.5 ~ 28-mesh range, we also conducted a crushing experiment on the one-layer feed mass calculated as described above.

We defined crushed product as a mass of particles that have passed through a small-meshed sieve used to classify the specimen into categories. After the crushing experiment, the specimen was manually sieved, classified and weighed. We defined crushing energy E[J] as the energy determined by graphical integration of the load-deformation curve recorded on the X-Y recorder[7]. Crushing probability P_f[−] was defined as:

$$P_f = \frac{m}{M \times 0.64} \quad (1)$$

where M[kg] represents the feed mass, m[kg] representing the mass of crushed product and the constant 0.64 representing the quotient of the base area of the plunger divided by that of the grinding vessel.

Here, we defined E/m[J/kg] as the crushing resistance and used it to evaluate crushability.

3. Result and discussion

3. 1 Load-deformation curve

Figures 3 and **4** indicate typical examples of curve-deformation curve based on actual measurements. **Figure 3** gives a load-deformation curve in the particle size range between 12 and 14-mesh with feed mass varied. The figure also gives a load-deformation curve calculated based on the elasticity theory when particles with a diameter of 1.3 mm, equal to the calculated average diameter of 12 ~ 14-mesh meshes, are crushed by a parallel plane plate[8,9]. **Figure 3** shows that,when constant load was applied to the specimen, deformation rose and energy consumption increased as the feed mass climbed. **Figure 4** indicates a load-deformation curve obtained when the feed mass remained constant at 18 g and the average particle diameter $\bar{x}$ (the calculated average diameter of two meshes used for classification) varied. Deformation rose and energy consumption climbed upon the constant load as the particle size of the feed increased. As the particle size increased, partial destruction became more effective, resulting in a more complex-shaped load-deformation curve.

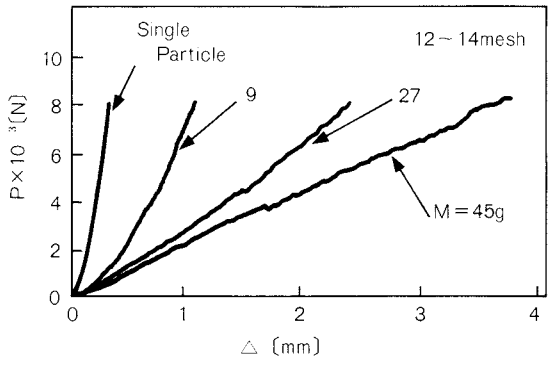

Fig. 3 Load-deformation curve

3. 2 Effect of feed mass on crushing probability and crushing resistance

Figure 5 indicates the relationship between crushing energy E and crushing probability P_f, where feed particle size remained constant at 12 ~ 14-mesh and feed mass M[g] was used as a parameter. At any feed mass, needless to say,

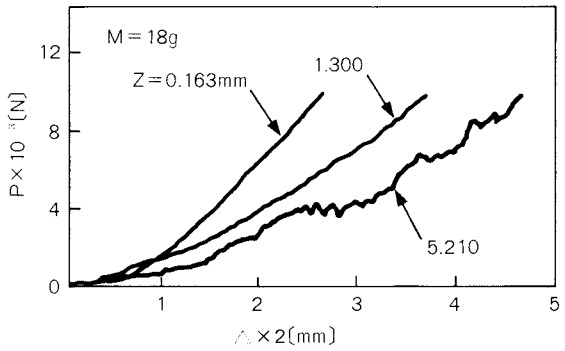

Fig. 4 Load-deformation curve

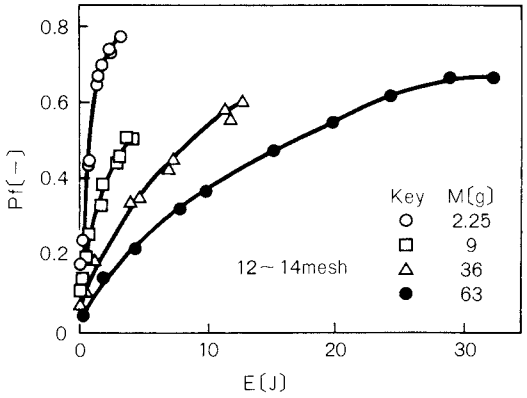

Fig. 5 Variation of probability of crushing with input energy

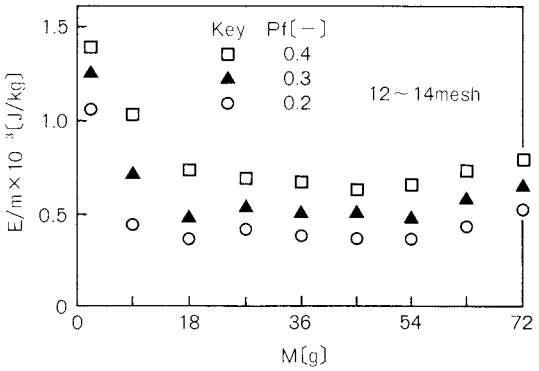

Fig. 6 Effect of mass of feed on crushing resistance

crushing probability increased as applied energy rose. However, with an energy rise, the increment of crushing probability declined and energy efficiency dropped as applied energy climbed[10]. As is evident from **Fig. 5**, the energy needed to obtain the same crushing probability climbed as feed mass rose. But the crushed product, obtained at that time, also increased. This finding shows that we should allow for energy consumption per unit mass of crushed product. To allow the readers to view how feed mass affected crushing efficiency, **Fig. 6** shows the relationship between the crushing resistance E/m (i.e., the energy needed to produce a unit mass of crushed product) and the feed mass M, with crushing probability used as a parameter. The crushing energy to produce a given crushing probability was calculated based on **Fig. 5**. **Figure 6** shows that there is such a mass range that makes crushing resistance comparatively low at any crushing probability, and that there is an optimum range of feed mass. The figure leads us to confirm that an increase in crushing probability expands crushing resistance and declines energy efficiency. That is, it is necessary to classify feed at the early stage of crushing, when crushing probability is low, and to repeat the crushing-and-classification procedure.

3. 3 Effect of particle size on crushing resistance

In the preceding parts on this paper, we have discussed 12 ~ 14-mesh feed. This clause describes our study of feed with different particle sizes.

Figure 7 (a) through **(c)** relate to feed with particle sizes 24 ~ 28, 48 ~ 60, and 80～100-mesh, respectively. As for particle sizes other than that 3.5 ~ 4-mesh range, not covered in **Fig. 7**, we found that there was an optimum range of feed mass, like in the case of the 12 ~ 14-mesh range shown in **Fig. 6**. Why didn't we find an optimum range of feed mass for particle sizes ranging 3.5 ~ 4-mesh? This, we believe, was because:

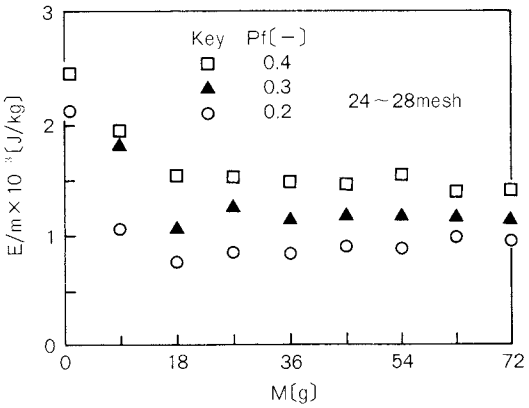

Fig. 7 (a) Effect of mass of feed on crushing resistance

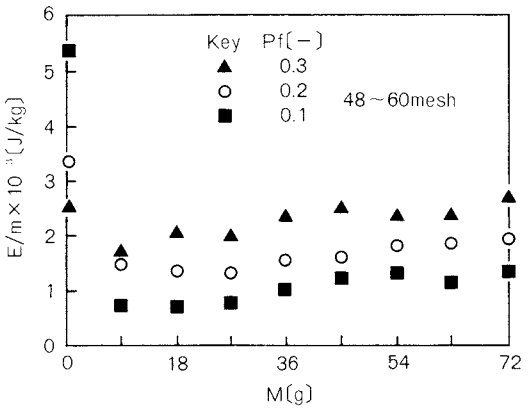

Fig. 7 (b) Effect of mass of feed on crushing resistance

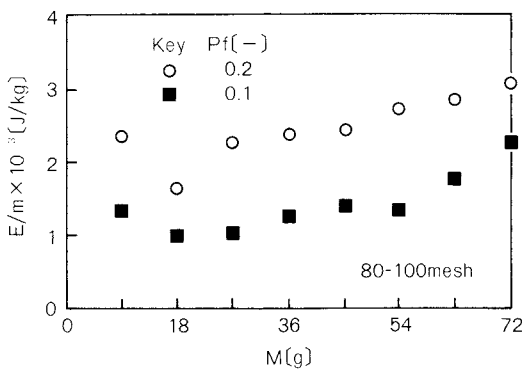

Fig. 7 (c) Effect of mass of feed on crushing resistance

- feed particle sizes were excessively large compared to the dimensions of the crushing apparatus; and
- the number of plunger-loaded particles, when the feed mass was 9 g, was as small as about 31, which was not enough to be treated as a powder bed.

The above circumstances prompted us to exclude the 3.5 ~ 4-mesh particle range. The following, we believe, is the reason why there is an optimum feed mass. Destruction in general proceeds selectively in fragile parts of solids[11]. When we consider a particle group forming a powder bed, in the case of a thin powder bed, applied load makes it harder for particles in the powder bed to move (especially in the case of a single layer) and for fragile parts of solids to be selected, resulting in a decline in crushing efficiency. When, on the other hand, the powder bed is excessively thick, particle movement (or deformation of the powder bed) consumes most of the energy, resulting in the applied energy not being effectively used for particle destruction. This is how crushing efficiency declines. This assumption leads us to conclude that, in the case of the optimum feed mass determined in this experiment, particles move appropriately while being loaded and, in the meantime, fragile parts of particles become destroyed selectively, resulting in improved energy efficiency.

Let's now look at changes in the optimum feed mass range in response to different particle sizes. **Figure 8** indicates the relationship between crushing resistance and feed mass, with a crushing probability of 0.2 (common for all particle sizes), and with particle size as a parameter. As is evident from **Fig. 8**, when the particle size was large, the optimum feed mass range widened and feed mass affected crushing resistance less. However, when the particle size was small, the optimum range narrowed and the slightest change in feed mass affected crushing resistance sensitively.

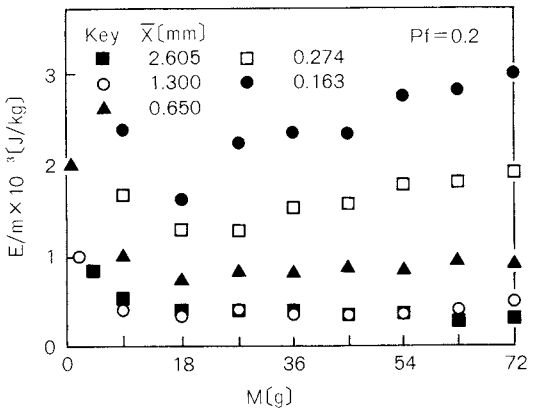

Fig. 8 Effect of mass of feed on crushing resistance

Figure 8 led us to set the feed mass decreasing resistance at 18 g for all experiment sessions. On this basis, **Fig. 9** shows the relationship between crushing resistance and the volume of particles having a diameter equal to the average particle diameter of specimen feed, with a crushing probability of 0.2. We found that crushing resistance climbed as the particle volume plunged.

4. Conclusion

We conducted a basic study of roller mills, consisting of crushing a quartz specimen with changes in its mass, particle size and compressive load applied to the powder bed. This experiment revealed the following:

(1) As for the load-deformation curve, when the load applied to the powder bed remained constant, deformation rose as feed mass climbed or particle size increased.
(2) Crushing probability rises as crushing energy climbs, but its increment declines as applied energy rose.
(3) There is a feed mass range that reduces crushing resistance to some extent.
(4) The above feed mass range widened when the particle size was large, and narrowed when the particle size was small.
(5) With feed mass and crushing probability remaining constant, crushing resistance rose as particle volume.

The above shows that, the more finely the

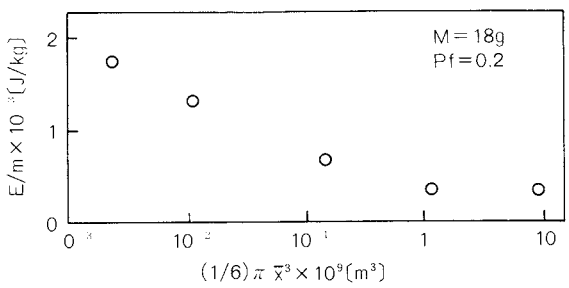

Fig. 9 Relationship between crushing resistance and volume of particle

powder is crushed, the more important factor the control of feed mass becomes.

Nomenclature

E	:	energy	[J]
E/m	:	crushing resistance	[J/kg]
$H.G.I.$	:	Hardgrove grindability index	[–]
H_m	:	Mohs hardness	[–]
H_v	:	Vickers hardness	[Kg/mm^2]
M	:	mass of feed	[g], [kg]
m	:	mass of product	[g], [kg]
P	:	load	[N]
P_f	:	probability of crushing	[–]
S_s	:	compressive strength of sphere which has a diameter of 2 cm	[Pa]
W_i	:	Work index	[kWh/t]
$\bar{x}$	:	mean particle size	[mm]
Y	:	Young's modulus	[mm]
Δ	:	deformation	[–]
ν	:	Poisson's ratio	[–]
ρ	:	density	[kg/m^3]

References

1) Kagaku Kogaku Kyokai: "Funryutai Kogaku", p.36, Maki Shoten (1985).
2) Matsui, K., T. Sekiguchi and H. Ikahata: *Kagaku Kogaku*, **35**, 788 (1971).
3) Hanish, J. and H. Schubert: 15th, Int. Conf of Mineral Processing, Cannes, Tone 1, 201 (1985-6).
4) Yashima, S., S. Morohashi, O. Awano and Y. Kanda: *Kagaku Kogaku*, **34**, 210 (1970).
5) Kanda, Y. and M. Suzuki: *J. Res. Assoc. Powder Technol., Japan*, **13**, 487 (1976).
6) Honma, T., M. Hasegawa and Y. Asaba: *Kagaku Kogaku Ronbunshu*, **6**, 527 (1980).
7) Kanda, Y., S. Sano, H. Saito and S. Yashima: *Kagaku Kogaku Ronbunshu*, **10**, 108 (1984).
8) Timoshenko, S. and J.N. Goodier: "Theory of Elasticity (2nd Ed.)", p. 372, McGraw-Hill (1951).
9) Kanda, Y., T. Honma and S. Yashima: *J. Soc. Powder Technol., Japan*, **22**, 390 (1985).
10) Tanaka, T.: *Kagaku Kogaku*, **18**, 160 (1954).
11) Griffith, A.A.: Proc. 1st Int. Congr. Appl. Mech. (Delft), 155 (1924).

Characteristics of Wet Grinding of Highly Loaded Coal Water Slurry†

Hayami Itoh, Shuhei Tatsumi, Yoshihiro Kajibata and Shoichi Takao
Technical Institute
*Kawasaki Heavy Industries, Ltd.**

Hironori Ozaki and Tadashi Katahata
Crushing Plant Manufacturing Div.
*Kawasaki Heavy Industries, Ltd.***

Abstract

The wet grinding characteristics of CWM (Coal Water Mixture) at high concentrations was investigated by conducting batch preparation tests using a laboratory-scale ball mill.

Although the grindability became worse with the increase in the slurry concentration, it was found possible to prepare CWM of 65 ~ 75% by use of the proper dispersant. The improvement of grindability was caused by the improved movement of balls owing to the decrease in the apparent viscosity at low shear rates. The graindability greatly changed with the coal type. The difference of grindability among coal types was mainly due to the difference in the flocculation force.

1. Introduction

Since the two oil shocks during the 1970s, the entire world has been making efforts to introduce energy sources other than oil. Under these circumstances, R & D (research and development) has been carried out on coal applications as a means to implement the energy diversification policy. The most spotlighted of all coal versions is CWM, which is believed to be practicable in the near future in comparison to liquefied or gasified coal. CWM, therefore, is attracting a great deal of attention from industry, especially the power generation industry.

CWM typically has a solids loading of 65 ~ 75%. With a 200-mesh pass of 80 ~ 85%, this slurry fuel can be treated as a fluid in all processes ranging from manufacture to combustion and can be burned without being dewatered. Of the several different ways of manufacturing CWM, we have used a high-concentration wet grinding system employing a simple-process wet ball mill; thus, conducting R & D to put CWM into practical use. The ball mill, having a long history, has been frequently researched and reported concerning its grinding theories and scaling up. In manufacturing CWM, however, ball mills provide wet grinding in considerably high slurry concentrations. Few reports have been issued concerning the wet grinding characteristics of CWM at such high concentrations. We, therefore, conducted coal wet grinding tests using a laboratory-scale batch-type ball mill to study the wet grinding characteristics of CWM at high concentrations[2].

2. Experiment

2. 1 Samples

Table 1 lists a total of 12 types of coal used in this experiment. **Table 2** shows a total of three kinds of anion-based dispersants used in the experiment.

2. 2 Batch-type ball mill and CWM preparation

We prepared CWM by wet grinding using a batch-type ball mill illustrated in **Fig. 1**.

* 1-1, Kawasaki-machi, Akashi, 673
TEL.

** 1780, Uetakano, Yachiyo-shi, 276
TEL.

† This report was originally printed in *Kagaku Kogaku, Ronbun-shu*, **14**, 155-160 (1988) in Japanese, before being translated into English with the permission of the editorial committee of the Soc. Chemical Engineers, Japan.

Table 1 Coal properties

Coal type		I	A	U	O	K	Q	C	S	T	P	L	W	M
Heating value	[cal/g]	7650	6540	6330	6830	7130	7070	6740	6740	6190	6750	6880	6820	7140
Proximate analysis														
Moisture	[%]	2.6	3.2	3.5	4.2	3.6	2.1	1.5	2.8	5.7	4.8	3.1	2.6	1.6
Ash	[%]	2.2	15.4	15.7	9.8	9.6	11.8	16.5	14.6	14.2	8.9	12.5	13.2	13.4
Volatile matter	[%]	37.3	30.3	23.3	33.6	33.4	22.4	23.2	27.0	43.0	38.1	29.5	29.4	36.7
Fixed carbon	[%]	57.9	51.1	57.5	52.4	53.4	63.7	58.7	55.6	37.1	48.2	54.9	54.8	48.3
Fuel ratio	[−]	1.55	1.69	2.47	2.60	1.60	2.84	2.53	2.06	0.86	1.27	1.86	1.86	1.32
Hardgrove grindability index	[−]	51	42	48	41	57	78	81	50	34	42	50	47	57
Ultimate analysis														
Ash	[%]	2.3	15.9	16.3	10.2	10.0	12.1	16.8	15.0	15.0	9.4	12.9	13.6	13.6
C	[%]	77.7	67.8	68.7	73.0	74.0	75.6	69.4	70.5	65.2	71.5	71.1	71.8	70.9
H	[%]	5.6	4.5	3.9	4.6	5.2	3.6	3.8	4.0	5.4	5.5	4.2	4.9	5.6
O	[%]	12.09	9.50	9.26	9.93	8.98	7.53	8.77	8.71	13.49	11.7	10.06	7.74	6.46
S	[%]	1.27	0.97	0.32	0.45	0.40	0.35	0.24	0.48	0.05	0.4	0.36	0.54	0.30
N	[%]	1.04	1.33	1.52	1.82	1.42	0.82	0.99	1.31	0.86	1.3	1.38	1.42	1.13

Table 2 Dispersant

Sign	Dispersant
E-1	Sulfoalkyl (meth) acrylate type
F-1	Formalin condensate of sodium naphthalenesulfonate type
A-1	Polystyrene sodium sulfonate type

Using a jaw crusher, we ground coal coarsely to get about 95% of 3 mm or smaller grains. Some 2 kg (dry weight) of this coal was mixed with water and dispersant to obtain the specified slurry concentration and addition ratio. This mixture was then poured into the batch-type ball mill. After wet-grinding, the slurry at 50 rpm for the specified time with the ball mill fully closed, we took out the slurry and tested

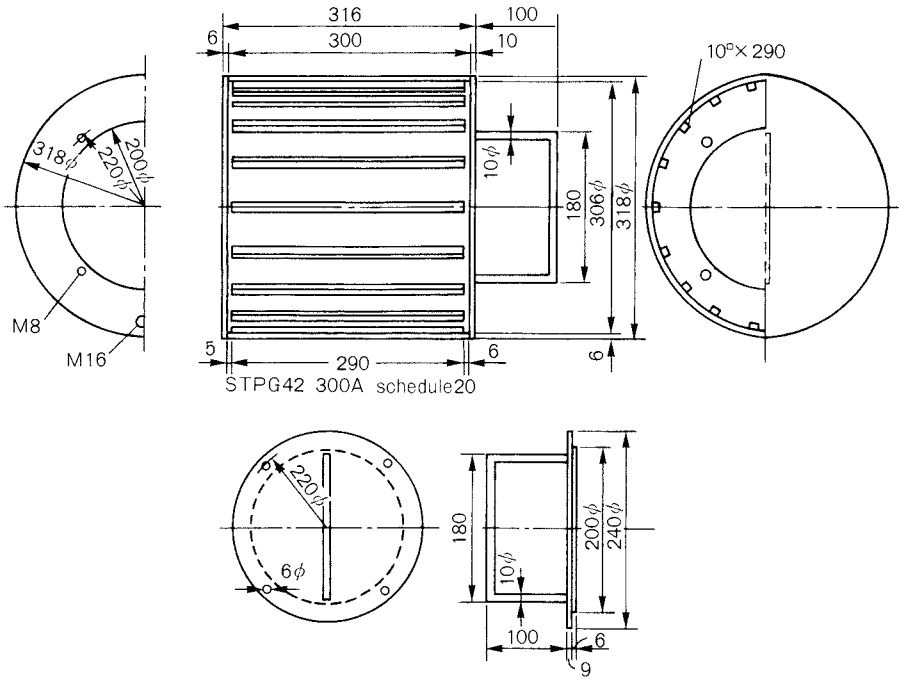

Fig. 1 Batch type ball mill

Table 3 Measurement conditions of viscosity curve

Viscometer	Haake RV-2 Rotational viscometer
Cylinder sensor system	MV-2P
Measuring conditions	T1 = 0.1 min. T2 = 6 min. T3 = 1.0 min.
Temperature	25°C

it for concentration, particle size distribution and viscosity.

2. 3 Analysis

1) Solids loading
Some 20 g of prepared CWM was dried in a drier held at 107±2°C for 3 hrs. The sample was then cooled in a desiccator and weighed. On the basis of weight decrement, we calculated the solids loading. (As per JIS M 8811.)

2) Particle size distribution
Some 50 g of prepared CWM was passed in a wet state through the JIS standard sieves. The sieved CWM samples were dried in a drier held at 107±2°C for three hours. Then, the coal grains remaining in the sieves were weighed finely to obtain particle size distribution. For the particle size distribution for 350 mesh (44 μm) or under, we used a decanter-type particle size distribution measuring machine (Shimadzu SA-CP2).

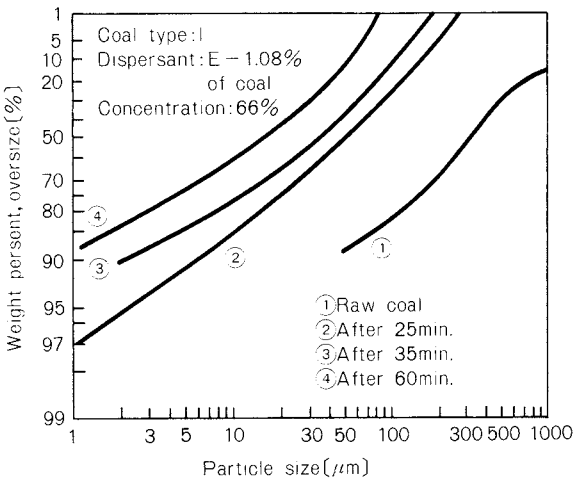

Fig. 2 Change in particle size distribution with grinding time

3) Viscosity
Using a rotational viscometer Haake Rotovisco RV-2, we measured the shear rate-viscosity characteristics of CWM under the conditions indicated in **Table 3**. As representative viscosity of CWM, we used apparent viscosity at a shear rate of 100 sec^{-1} on the downward portion of the viscosity curve obtained by using the above device.

3. Result and discussion

3. 1 Kinetic study of the grinding process

Figure 2 shows how the particle size distribution of I coal changes over grinding time, in the case of batch-type wet grinding. We poured ground coal, water and dispersant with the specified ratio into a batch-type mill and ground the mixture for the specified time. We then took out the resulting slurry and checked it for particle size distribution. The result was that the particle size distribution pattern of the slurry in the 60 ~ 90% range in 200-mesh pass prepared in this experiment moves almost in parallel with the grinding progress on the Rosin-Rammler diagram.

Alyavdin proposes the following formula as a grinding speed formula[1]:

$$R(y, t) = R(y, 0)e^{-kt^m} \quad (1)$$

Using the Alyavdin plot, we examined the results of grinding tests on Q, M and I coal to check whether the above formula is effective. To this end, on the Rosin-Rammler diagram, we replaced the particle size axis with grinding time t and examined the relationship between the grinding time and 200-mesh retention rate. The result is indicated in **Fig. 3**. This figure indicates that, on the Alyavdin plot, a linear relationship is present up to 1% in 200-mesh retention rate and that the above formula applies to the wet grinding of coal at high concentrations. The gradient of the straight line corresponds to value m in the formula. This value approximates 1 in the case of Q coal and exceeds 1 in the case of I and M coal. The value thus varies slightly according to the type of coal.

3. 2 Slurry concentration and grindability

Although value m varies slightly depending on the type of coal, it approximates 1. We,

therefore, based our assumption on value m equaling 1. We then defined coal grindability in accordance with weight standards as:

$$-\{\ln(R_p/R_f)\}/t;$$

that is, the logarithm of the ratio of the particle size of the feed coarse-ground coal to that of product slurry (200-mesh retention rate), which logarithm is divided by grinding time. We thus examined various factors affecting the grindability in the case of high-concentration wet grinding. **Figure 4** indicates how the concentration and presence of a dispersant affect grindability. Q coal declined quickly in grindability after its peak at a coal concentration of 60 wt% when no dispersant was added. When a dispersant was present, on the other hand, Q coal plunged slowly in grindability after its peak at around 60 wt%. Even at 73 wt%, Q coal remained grindable up to the target particle size (15 ~ 20% in 200-mesh retention rate). The grindability, at this time, was almost the same as that when dry-grinding the same weight of coal in a batch-type mill.

Next, we examined the relationship between the representative viscosity (apparent viscosity at 100 sec^{-1} on the downward curve at 25°C) of the slurry and grindability. The result is given in **Fig. 5**. Mill grindability declined as viscosity climbed up to about 1 Pa·s, and remained almost constant 1 ~ 2.5 Pa·s. This, we believe, is due to changes in the movement of the mill balls. The grindability decline in the 0 ~ 1 Pa·s range is believed to have stemmed from a decrease in the impact crushing force with a rise in viscosity. The constant grindability in the 1 ~ 2.5 Pa·s range is attributable to the fact that, with almost no influence of impact crushing, crushing was conducted mainly

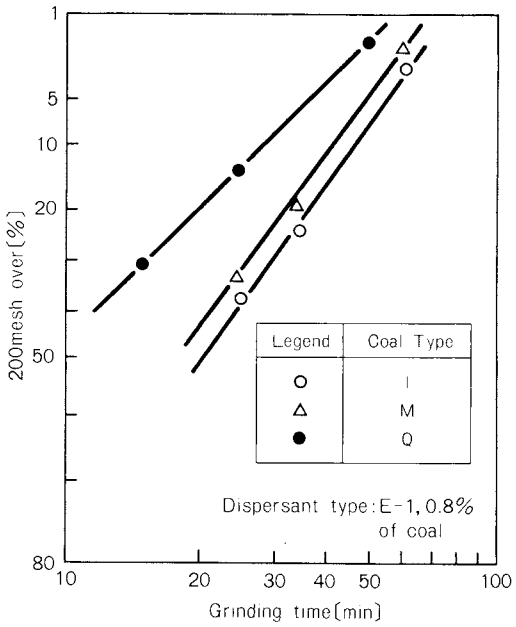

Fig. 3 Alyavdin plot

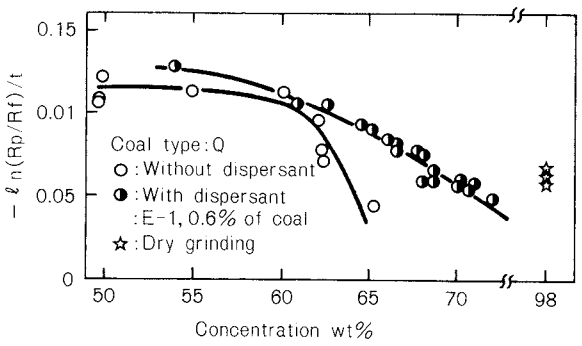

Fig. 4 Change in grindability with concentration

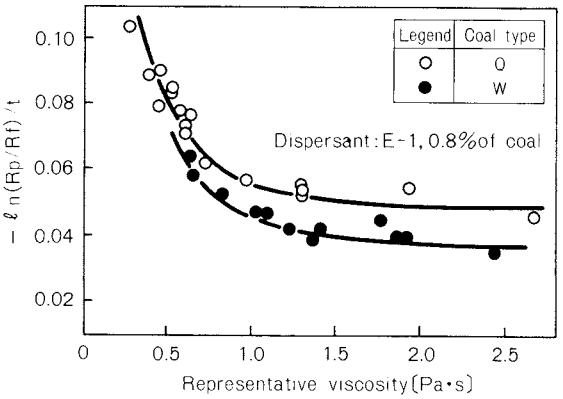

Fig. 5 Change in grindability with viscosity

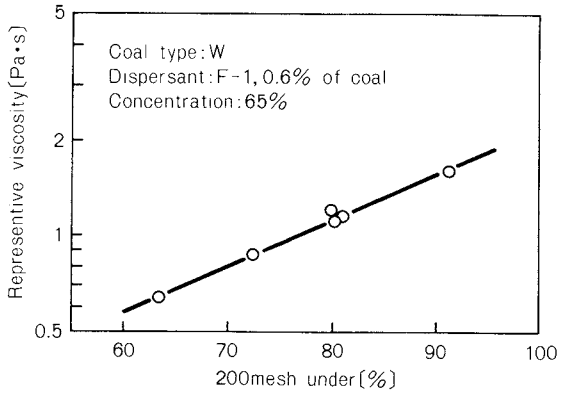

Fig. 6 Relationship between weight percent of 200 mesh under and representative viscosity

buy the inter-ball shear force. **Figure 6** indicates the relationship between the weight percent of 200-mesh under and the representative viscosity of the slurry. Here, we find that the ratio of particle size changes to viscosity changes rise as the particle size decreases. This, we believe, is one of the reason why the rate of change of grindability declined in comparison to viscosity at 1 Pa·s or more.

3. 3 Effect of dispersant

Figure 7 shows typical viscosity curves of slurry without a dispersant. Viscosity climbs as coal concentration rises. Here, we find that, in slurry without a dispersant, coal particles coagulate strongly and viscosity climbs considerably, at low shear rates in particular. **Figure 8** gives typical viscosity curves of slurry without a dispersant and that with a dispersant.

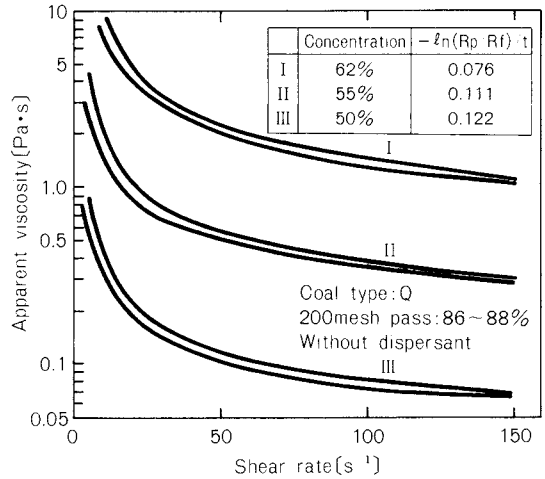

Fig. 7 Viscosity curves of slurry without dispersant

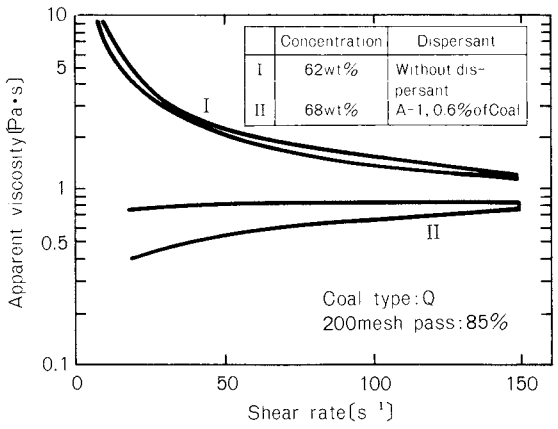

Fig. 8 Change of viscosity curve with dispersant

Use of a dispersant enables low-viscosity slurry to be obtained even at high concentrations. Here, we can clearly see that use of a dispersant reduces the coagulation capability of coal particles and produces a great difference in viscosity, at low shear rates in particular. We, therefore, concluded that use of a dispersant improves the movement status of mill balls and increases grindability greatly.

3. 4 Type of coal and grindability

Using twelve brands of coal, we examined how grindability varies according to the type of coal[3]. The results are given in **Table 4** and **Fig. 9**. Let's now compare the grindability of differ-

Table 4 Change of grindability with coal type

No.	Coal type	Concentration	$-\{\ln(R_p/R_f)\}/t$
1	Q	69	0.045
2	C	68	0.045
3	U	67	0.044
4	S	65	0.042
5	W	66	0.042
6	L	65	0.030
7	P	62	0.029
8	T	59	0.026
9	I	66	0.025
10	K	64	0.024
11	O	64	0.022
12	A	64	0.020

Representative viscosity of slurry is 1 Pa·s

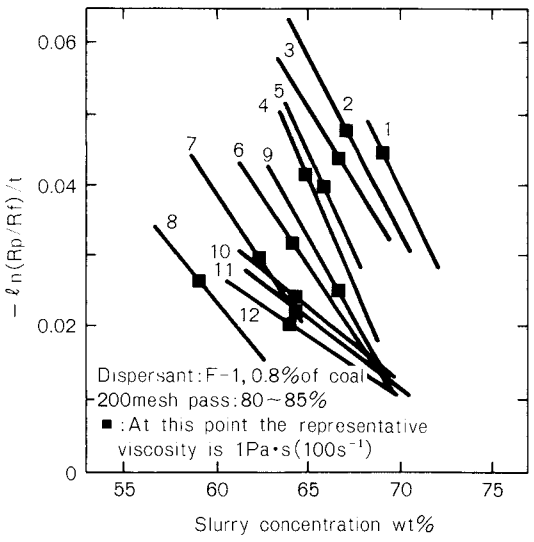

Fig. 9 Change in grindability with coal type

ent types of coal at such a concentration that makes slurry's representative viscosity 1 Pa·s. Among the twelve types of coal, grindability varies between 0.020 and 0.045. We then studied the correlation between the Hardgrove Grindability Index (JIS M 8801), one of the indices for grinding strength of coal, and grindability in the case of high-concentration wet grinding. The result is given in **Fig. 10**. The correlation coefficient was as low as 0.62, showing scarcely any correlation.

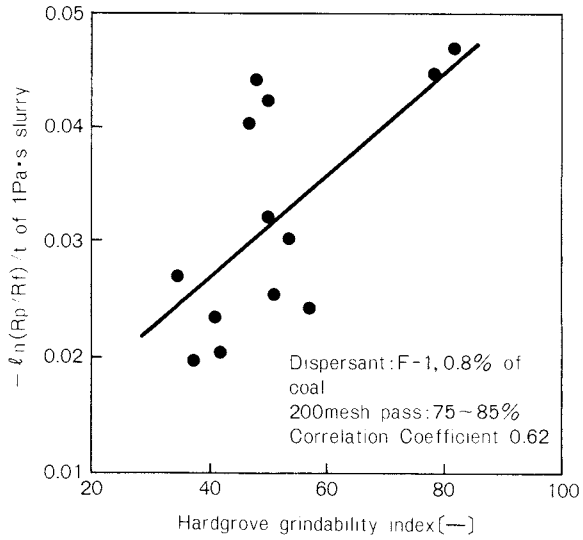

Fig. 10 Relationship between Hardgrove Grindability Index and grindability of slurry of which representative viscosity is 1 Pa·s

We then compared the viscosity curves of slurry showing a representative viscosity of 1 Pa·s and containing different types of coal that showed a great gap in grindability. The results are shown in **Fig. 11**. Let's compare the viscosity curve of slurry samples containing Q coal and U coal that show a grindability of 0.045 with that of A coal slurry showing a grindability of 0.020. We can clearly see that viscosity varies greatly at low shear rates and that K and A coal, which display low grindability, show high viscosity at low shear rates. That is, in the case of types of coal with a low grindability, the coal particles coagulate relatively strongly even in slurry containing a dispersant. This, we believe, reduced grindability.

3. 5 Particle size distribution

Figure 12 indicates the particle size distribution patterns obtained in dry grinding, low-concentration wet grinding, and high-concentration wet grinding. Of all these grinding

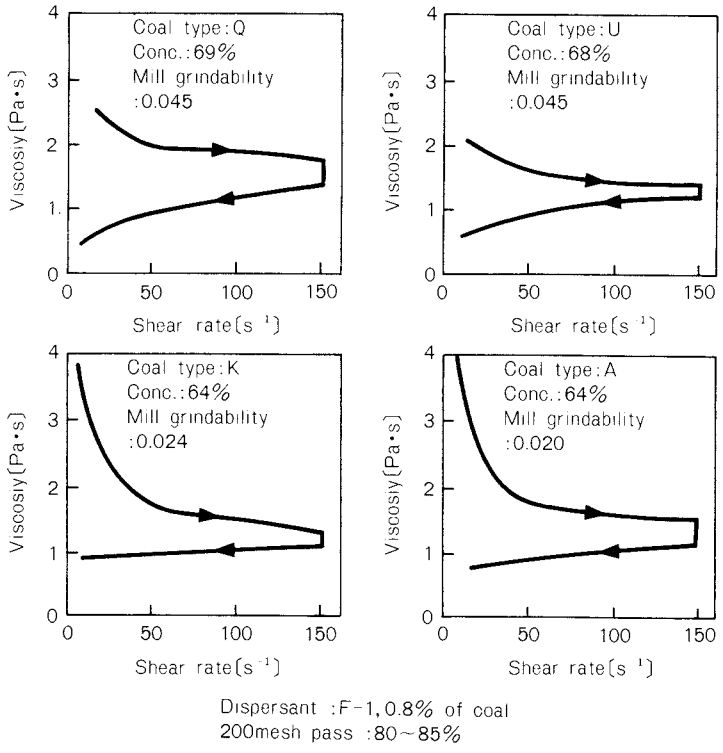

Fig. 11 Change in viscosity curve with coal type

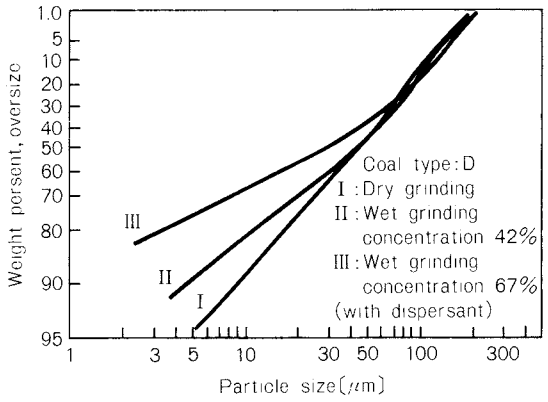

Fig. 12 Comparison in particle size distribution

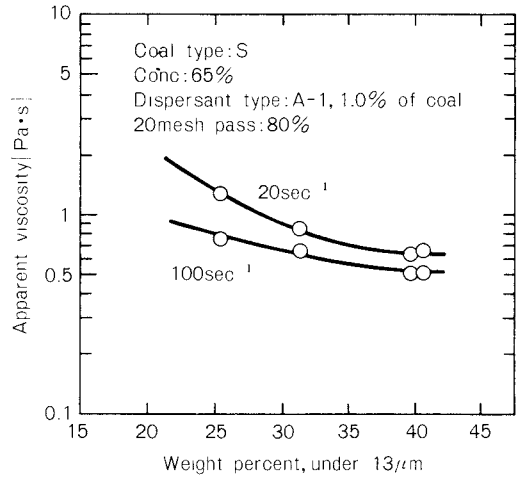

Fig. 13 Effect of fine particles on the apparent viscosity

methods, high-concentration wet grinding produces the largest percentage of fine particles. This, we believe, is because of the following reason: as opposed to dry grinding and low-concentration wet grinding designed mainly for impact crushing, high-concentration wet grinding produces a high apparent viscosity of slurry, resulting in a reduced impact crushing force, so that the major crushing force retained by this method is the inter-ball shear energy. We, therefore, examined how the aforementioned fine particles affect the nature of CWM. **Figure 13** shows a typical relationship between the percentage of fine particles (13 μm or less) and CWM's representative viscosity. CWM's representative viscosity declined as the percentage of fine particles rose, indicating that fine particles helped reduce CWM's representative viscosity. One of the reasons for this, we believe, is that the bulk density of particles rose as the number of particles increased, resulting in a rise in the ratio of free water (water content which is not caught in between the particles and helps CWM flow) which helps CWM flow at the same solids loading.

4. Conclusion

Using a laboratory-scale batch-type ball mill, we conducted wet grinding tests on the wet grinding characteristics of coal at high concentrations. The results were as follows:

1) Use of a dispersant greatly improved coal grindability in high-concentration wet grinding. This, we believed, is due to a decline in apparent viscosity at low shear rates, resulting in the balls' movement improved.
2) Grindability varies greatly according to the type of coal. This is attributable to the difference in the coagulation capability of coal particles.
3) High-concentration wet grinding produces a larger percentage of fine particles than dry grinding and low-concentration wet grinding. Fine particles help reduce CWM's viscosity.

Nomenclature

k, m	:	constant	[–]
R_f	:	weight percent of 200-mesh over of feed	[%]
R_p	:	weight percent of 200-mesh over of product	[%]
$R(y, t)$	:	cumulative weight percent of particles of which size is over y when the grinding time is t	[%]
t	:	grinding time	[min]

References

1) Bela, Beke: "The Process of Fine Grinding", p. 25 (1981).
2) Itoh, H., Y. Kajibata, N. Sato, S. Takao, S. Tatsumi: Preprints of 51th Annual Meeting of The Soc. of Chem. Engrs., Japan, p. 168 (1986).
3) Itoh, H., N. Sato, S. Takao, S. Tatsumi: Preprints of the 49th Annual Meeting of The Soc. of Chem. Engrs., Japan, p. 374 (1984).

The Development of a Ring Ball Mill Simulation Model†

Nobuyasu Meguri and Kazunori Shoji
Kure Research Laboratory,
*Babcock Hitachi K.K.**

Tadashi Hasegawa
*Kure Works, Babcock Hitachi K.K.***

Abstract

The mathematical model previously developed for a ring ball mill based on specific rates of breakage, breakage distributions, and primary and secondary classification actions was further refined. In particular, empirical expressions are presented for both primary and secondary classification actions as a function of the mill and classifier geometry as well as the operating conditions. In addition, the scale-up factor with the make-up feed rate determined in a pilot-scale mill was further developed for larger mills. Model simulations based on parameters measured in the Hardgrove mill with the present classification models and scale-up factors correctly predicted the circuit behavior of industrial-scale mill systems.

Furthermore, some of the factors affecting the mill performance were investigated with the present simulation model. As a result, the feed size distribution and the total crushing load on balls were found to be the dominant factors.

1. Introduction

Roller mills are widely used to prepared pulverized coal for firing in boiler furnaces and are classified into ring roll mills and ring ball mills according to the shape of the roller[1]. The mode of operation of the roller mills depends on that of the boilers, which is different from normal applications of grinding mills where the rate of grinding is usually kept constant. The coal pulverizers are operated mainly on the basis of experience accumulated over many years.

Recent trends in Japanese utility boilers have moved from homogeneous coals to the burning of a variety of imported coals and to the operation of the boiler at various loads with rapid changes. Therefore, advanced coal grinding technology is required to cope with these boiler requirements. To satisfy these new demands, the behavior of roller milling circuits must be quantitatively described.

Over the last two decades, the theory of grinding has been developed based on descriptions of the breakage process, the flow and mixing through the mill, and the classifier behavior all of which are similar to those in chemical reactor theory[2]. In a roller mill system, Murata *et al.*[3] analyzed the pressure exerted in the particle layers between the roller and the grinding table, and they concluded that the roller design is a key factor in the optimization of the roller mill circuit. On the other hand, Austin *et al.*[4~6] constructed a mathematical model for a ring ball mill system based on specific rates of breakage and primary fragment distribution. They obtained breakage parameters in the Hardgrove grindability machine[7] which is a batch ring ball mill. They measured classification parameters in a pilot-scale mill (D= 430 mm) and then determined scale-up factors from the batch mill to the pilot plant mill using a simulation model.

The model gave valuable insights into the mode of operation of the ring ball mill, and it

* 3-36, Takara-machi, Kure-shi, 737
TEL. 0823-21-1161

** 6-9, Takara-machi, Kure-shi, 737
TEL. 0823-21-1161

† This report was originally printed in *J. Soc. Powder Technology, Japan,* **25**, 430-436 (1988) in Japanese, before being translated into English with the permission of the editorial committee of the Soc. Powder Technology, Japan.

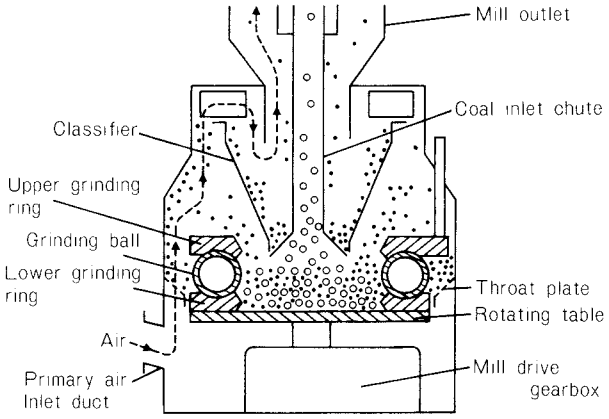

Fig. 1 An industrial ring ball mill

enabled predictions of the effect of operating variables to be made. However, the applicability of the model to mills other than the pilot mill is questionable because they evaluated the classification characteristics within limited tests conducted in a pilot-scale mill and did not refer to the scale-up effect of the classifiers.

In this paper, improvements were made to the model[5] developed by Austin et al., by incorporating scale-up rules for grinding and classification actions which were determined by the analysis of laboratory tests and operating data of industrial-scale mills describing the behavior of this type of mill. The validity of the modified model was verified by operating data from industrial-scale mills. Furthermore, the effect of operating conditions on pulverized-coal fineness was studied by model simulations.

2. Modeling of ring ball mills

2. 1 Air-swept ring ball mills

Figure 1 shows an industrial ring ball mill and the flow patterns of various coals, and the air in the mill is shown in **Fig. 2**. Raw coal enters the center of the rotating table through a central coal inlet chute. The coal on the table is thrown to the area surrounding the table by centrifugal action. The coal is pulverized when going through heavily loaded grinding balls and a lower grinding ring, and then it is transported to the fluidized bed zone above the throat plate.

Air is supplied through an annular throat plate within the mill, and it sweeps up the pulverized coal from the fluidized bed zone. The smaller particles among the materials swept up are conveyed to the inlet of the classifier, and the larger particles are separated from the air streams at the air velocity decreases and returns to the rotating table (primary classification). Air and pulverized coal in the classifier form a swirling stream by classifier vanes, pulverized coals are classified into larger particles and smaller particles by centrifugal action, and larger particles return to the table to be reground (secondary classification).

2. 2 Ring ball mill model

In developing the simulation model of a pilot plant mill, Austin *et al.*[5] constructed a mill circuit model of a ring ball mill which is shown in **Fig. 3** and derived mass-size balance equations.

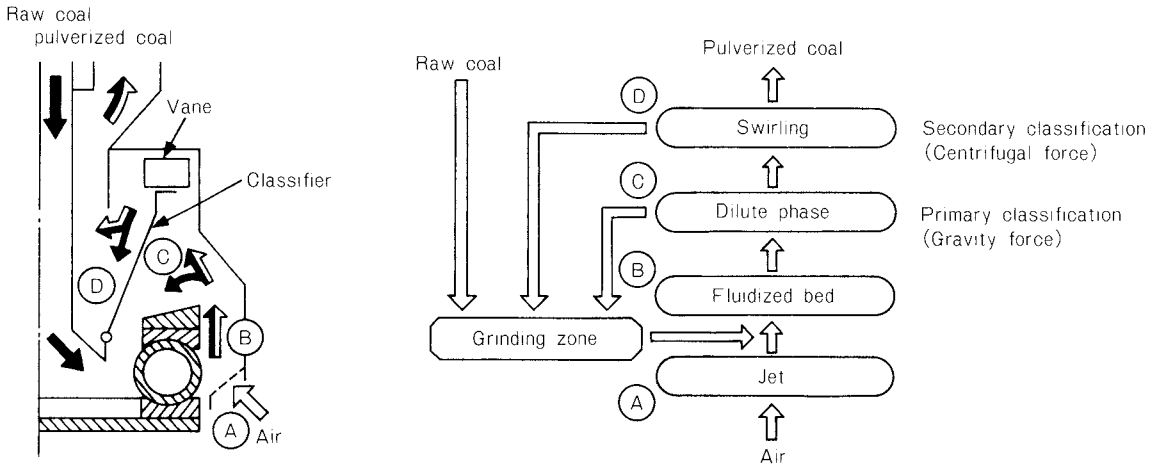

Fig. 2 Flow patterns of coals and air in the mill

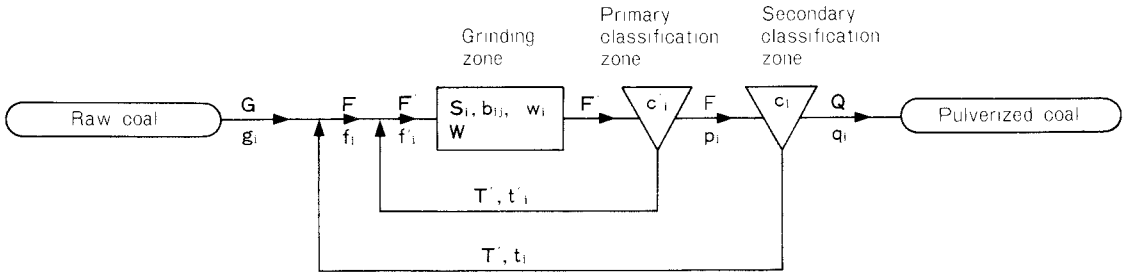

Fig. 3 Nomenclature for the complete circuit with primary and secondary classification

The size range is split into n intervals, and the size intervals which are defined by the $\sqrt{2}$ screen series are called 1, 2, $\cdots$ j, $\cdots$ $i-1$, i, $i+1$, $\cdots$ n from the largest size interval. That is, if the upper size of interval i is x_i, the lower size of interval i; x_{i+1} is equal to $\sqrt{2}\,x_i$. If the grinding zone is fully mixed, the mass balance on material of size i at the grinding zone is expressed by the following equation[5],

$$F'w_i = F'f'_i - S_i w_i W + \sum_{j=1}^{i-1} b_{ij} S_j w_j W \qquad (1)$$

Next, consider the mass balance at the primary classification zone. c'_i is defined as the partial separation efficiency of size i at primary classification. Then Eqs. (2) and (3) are given as;

$$T't'_i = F'w_i c'_i \qquad (2)$$

$$Fp_i = F'w_i(1-c'_i) \qquad (3)$$

The ratio of stream F, which is transported from the primary to the secondary classification zone, to stream T', which is returned to the table, is defined as the circulation ratio of C'. That is, the circulation ratio at the primary classification zone is $C' = T'/F$. Similarly, the rest of the mass balances involved can easily be derived.

When Eq. (1) is rewritten with the wt. fraction of size i in the make-up feed which is fed through the coal inlet chute, the following equation is derived[5],

$$\bar{w}_i = \frac{g_i + (1/F')\sum_{j=1}^{i-1} b_{ij}A_j\bar{w}_j}{(A_i/F') + (1-c'_i)(1-c_i)} \qquad (4)$$

where,

$$A_i = S_i W \qquad (5)$$

$$\bar{w}_i = (1+C')(1+C)w_i \qquad (6)$$

When the both sides of the Eq. (6) are summed from $i = 1$ to $i = n$, then,

$$\sum_{i=1}^{n}\bar{w}_i = (1+C')(1+C)\sum_{i=1}^{n} w_i$$
$$= (1+C')(1+C)$$
$$= (1+\bar{C}) \qquad (7)$$

where $\bar{C}$ is the net circulation ratio.

The relationship between through-put Q and the coal flow rate at the grinding zone *i.e.* F' is (see **Fig. 3**),

$$Q = \frac{F'}{(1+C')(1+C)} \qquad (8)$$

The wt. fraction of size i in mill output *i.e.* q_i is given by,

$$q_i = (1+C')(1+C)(1-c'_i)(1-c_i)w_i \qquad (9)$$

The circulation ratio at the primary classification zone C' and that at the secondary classification zone C are calculated with Eqs. of (10) and (11), respectively.

$$1 + C' = \frac{1}{\sum_{i=1}^{n} w_i(1-c'_i)} \qquad (10)$$

$$1 + C = (1+\bar{C})\sum_{j=1}^{n} w_i(1-c_i) \qquad (11)$$

Equation (4) is the mass-size balance which expresses the grinding characteristics of the ring ball mill. This set of equations is readily computed for the given values of g_i, A_i, b_{ij}, c'_i, c_i, and F', starting with $i = 1$.

The value of $(1+C')(1+C)$ is obtained from Eq. (7), and then value of w_i is gotten from Eq. (6). The value of the wt. fraction of size i in the mill output q_i is obtained from Eq. (9), the value of through-put Q comes from Eq. (8), and the circulation ratios of C' and C are obtained from Eqs. (10) and (11), respectively.

2. 3 Method of analysis

In order to solve Eq. (4), it is necessary that

the factors of A_i, b_{ij}, c_i', c_i, and F' be expressed by functions of coal types, mill sizes, mill conditions, and so on.

A_i which has the physical meaning of the rate of breakage of sizes i, and F' which is the coal flow rate in the grinding zone, are significantly affected by mill sizes and operating conditions. Furthermore, it is difficult to measure those factors in a large-scale mill.

When q_i, b_{ij}, c_i' and c_i are given, an identical value of w_i is obtained for a constant value of A_i/F' in Eq. (4), and therefore an identical value of q_i' follows.

For the following analysis, therefore, we used the values of the breakage parameters reported by Austin *et al.*[4], and the values of the classification parameters of c_i' and c_i based on the analysis of laboratory tests and on operating data of large-scale mills. Furthermore, with scale-up rules based on the mill dimensions and capacity, the mill performance was investigated by a modified simulation model.

3. Ring ball mill simulation model

3. 1 Breakage parameters

The breakage distribution parameter is one of the parameters which describes size reduction as a rate process. If the cumulative type of this breakage parameter, that is, the fraction of material just broken from the size interval j which appears less than the size interval i is represented by B_{ij}, then,

$$B_{ij} = \sum_{k=i}^{n} b_{kj} \qquad (12)$$

It is reported[5] that the B_{ij} values are normalized with respect to the breaking sizes when the breaking sizes are fairly small in comparison with the grinding ball and furthermore are insensitive to mill size. The B_{ij} values are expressed by the following equation,

$$B_{ij} = \phi\,(x_{i-1}/x_j)^{\gamma} + (1-\phi)\,(x_{i-1}/x_j)^{\beta} \qquad (13)$$

where ϕ, γ and β are descriptive parameters for a given coal, and the values measured by Austin *et al.*[5] were used here.

As for specific rates of breakage, Austin *et al.*[5], compared the results of batch tests obtained in the pilot-scale mill with those obtained in the Hardgrove machine. Consequently they reported that S_i passes through the maximum values at a certain size x_{max} and the S_i values for the smaller sizes can be represented by $S_i = ax_i^{\alpha}$. Moreover, the value α is the same for the two mills. The functional form of $S_i = ax^{\alpha}$ is applied in the region of approximately $x_{max} \leqq 0.1d$. Since in a large-scale mill at the material sizes are in this region, it was assumed that the values of S_i obtained in the Hardgrove machine can be represented by $S_i = ax^{\alpha}$ for all the particle size ranges. The values of a and α, which depend on *H.G.I.*, and measured by Austin *et al.*[5] were used for the analysis.

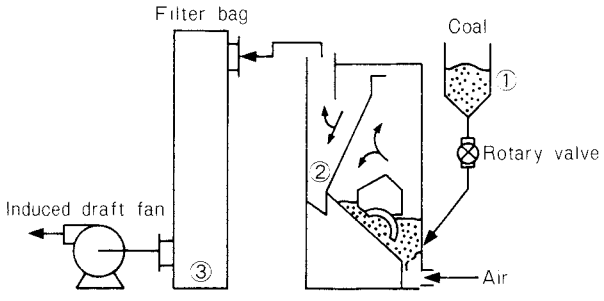

Fig. 4 Experimental apparatus for primary classification

3. 2 Classification parameters

3. 2. 1 Primary classification efficiency

Factors affecting the classification efficiency were investigated using a two-dimensional model apparatus of the primary classification zone in an industrial mill. The experimental apparatus for primary classification is shown in **Fig. 4**. The experiments were conducted under the condition of atmospheric temperature and pressure. The larger particles (particle diameter; 2 ~ 10 mm) which circulate around the primary classification zone, were first charged at the grinding zone. Next, the air flow rate was set at a certain value, and after having the larger particles circulate in the primary classification zone. The smaller particles (weight mean diameter: 0.8 mm) were fed from the coal hopper by means of a rotary valve. Before the particles made one complete circulation around the grinding zone, the air supply and feeding of smaller particles were shut down. The weight and particle size distribution of the feed coal particles and the particles which left the primary classification zone and were recovered at ② and ③ were then measured, and the partial separation efficiency was obtained from these measurements.

Figure 5 shows an example of the primary classification efficiency. It is clear that the primary classification efficiency is strongly affected by the air flow rate A, and the critical cut size x_{50} is proportional to A. Thus the partial separation efficiency of size i at primary classification c_i' is expressed by the following equation,

$$c_i' = 0.98\left[1-\exp\left\{-\left(0.847\,\frac{x}{x_{50}^*}\right)^{2.29}\right\}\right] \quad (14)$$

$$x_{50}^* = k_1 A \quad (15)$$

where k_1 is depends on mill size.

3. 2 2 Secondary classification (classifier performance)

In ring ball mills, cyclone type classifiers have been used. With respect to the classifier performance, the effects of classifier configuration and operating conditions on the grade efficiency of secondary classification were made clear by experiments with a model classifier. Furthermore, scale-up factors were determined by the analysis of the operating data of industrial-scale mills.

The experiments were conducted under the conditions of atmospheric temperature and pressure in the apparatus shown in Fig. 6. After setting the air flow rate, coal particles were fed in for a given time. The larger separated particles in the classifier were collected in a bin which was fitted under the classifier. On the other hand, the smaller particles leaving the model classifier were collected in a filter bag. The weight of both the recovered material and its size distributions were measured, and the partial separation efficiency was then calculated.

An example of the results is shown in Fig. 7, where the performance of the classifier (classifier diameter D_c = 380 mm) is shown with respect to air velocity at the classifier inlet. The air velocity was varied by adjusting the vane angle which is an angle between the vane and the radius at the pivot. Higher velocities due to the larger vane angle θ improves the partial

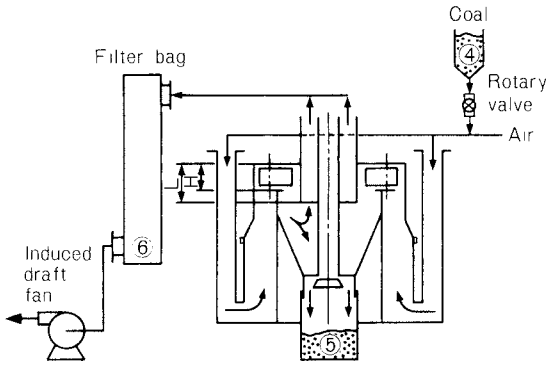

Fig. 6 Experimental apparatus for secondary classification

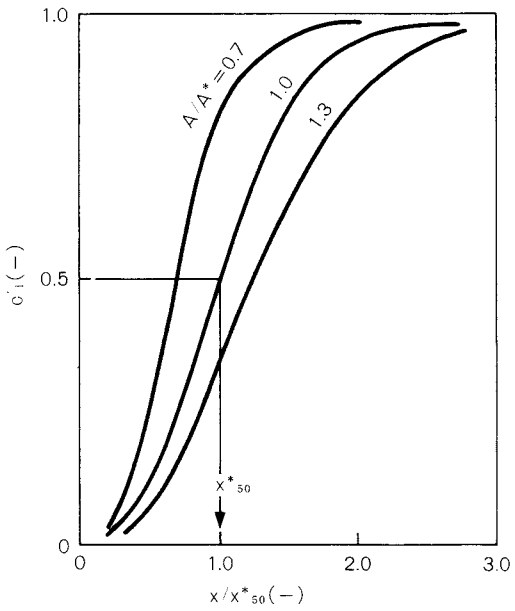

Fig. 5 Grade efficiency curves for primary classification

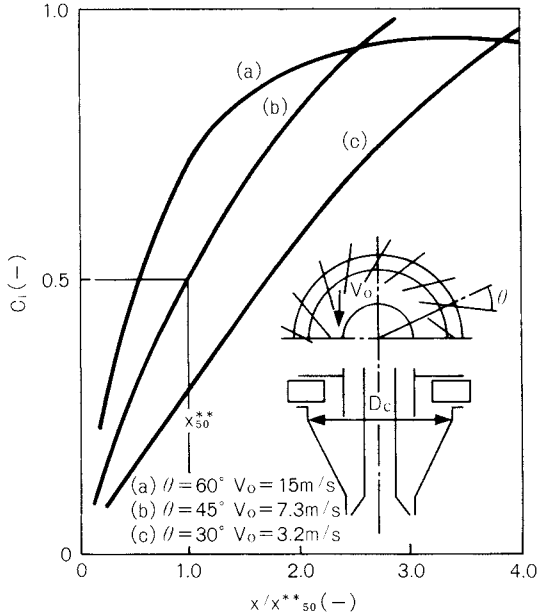

Fig. 7 Effect of the vane angle on the grade efficiency of secondary classification

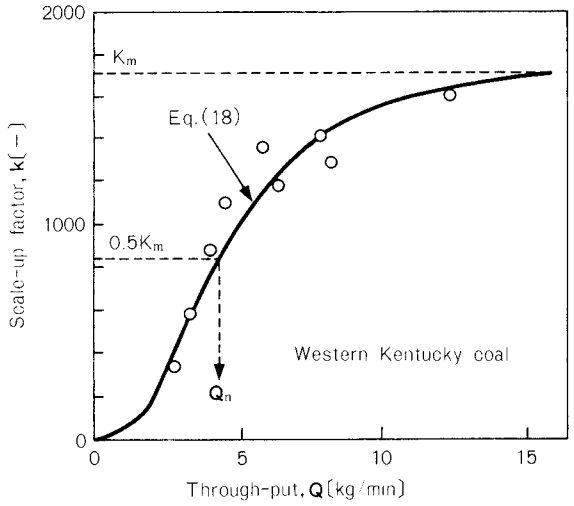

Fig. 8 Scale-up factor as a function of through-put: Pilot mill (after Austin, et al.[5])

separation efficiency c_i. However, beyond a certain velocity, the separation efficiency of larger particles decreases. This reduction in efficiency is considered as the re-entrainment[8] of particles which generally occurs in a cyclone separator.

In addition to this, in terms of factors affecting the classifier performance, there are solid loadings at the classifier inlet (F/A), outlet skirt length L, and so on. For a given geometry of the cyclone type classifier, the partial separation efficiency of size i; c_i can be written as follows,

$$c_i = 0.99\left[1-\exp\left\{-\left(0.715\ \frac{x}{x_{50}^{**}}\right)^{1.12}\right\}\right] \quad (16)$$

$$x_{50}^{**} = k_2\left(\frac{v_0^2}{gD_c}\right)^{-0.56}\left(\frac{F}{A}\right)^{0.15}\left(\frac{L}{H}\right)^{-0.41}\left(\frac{D_c}{D_c^*}\right)^{0.30} \quad (17)$$

where k_2 depends on the classifier configuration. It is noted that the values of the constants on the right hand sides of Eqs. (14) and (16) are 0.98 and 0.99, respectively. This indicates that the separation efficiencies become constant at 0.98 and 0.99, respectively.

3. 3 Scale-up factors

Austin *et al.*[5] computed Eqs. (4) ~ (11) for a range of F' values with the wt. fraction of size i in the make-up feed g_i used in the pilot-scale mill (D = 430 mm) tests, c_i' and c_i measured in the pilot-scale mill, and $A_i(=S_iW)$ measured in the Hardgrove mill until the computed q_i becomes equal to the measured q_i in the pilot plant mill. The mill capacity at the computed q_i value is then treated as the simulated mill capacity Q_{sim} (hypothetical mill capacity in the Hardgrove mill in which separation efficiencies are assumed to be the same as those of a pilot mill). The scale-up factor k is defined as $Q = kQ_{sim}$ with Q_{sim} and the pilot mill capacity Q.

Figure 8 shows the relationship obtained by Austin *et al.* between the scale-up factor k and the mill capacity Q. k increases as Q increases, and then it approaches a certain value. If this maximum value k is denoted as k_m and the value of Q, at $1/2k_m$ is defined as Q_n, the k value for the pilot plant mill is expressed[5] by the following equation,

$$\frac{k}{k_m} = \frac{1}{1+(Q/Q_n)^{-2.7}} \quad (18)$$

$$Q_n \propto k_m S_{16\times20} \quad (19)$$

On the other hand, the absolute rate of breakage of size i, A_i is expressed by the following equation[5,6],

$$A_i \propto M\omega D \quad (20)$$

where M is the total load on the lower grinding ring (hereafter referred to as the crushing load), ω is the rotational speed of the mill, and D is the mean race diameter. Since k_m is proportional to A_i, the value of k_m for industrial-scale mills can be expressed as,

$$k_m = k_0 M\omega D \quad (21)$$

where k_0 is a constant.

4. Studies on the simulation model

4. 1 Verification of the model

The comparison of the simulated and operating capacities and fineness for large-scale mills (D = 1780, D = 2160 and D = 3300 mm) is shown in **Fig. 9**. The feed size distribution used for the model simulation was the Rosin-Rammler distribution with the distribution modulus of n = 0.7 and a top size of 38.1 mm, as shown in **Fig. 10**.

Although the Hardgrove Grindability Index of coal is different for each large-scale mill as shown in the example of **Fig. 9**, the simulated values agree well with the operating data. Thus, it is considered that the validity of the modi-

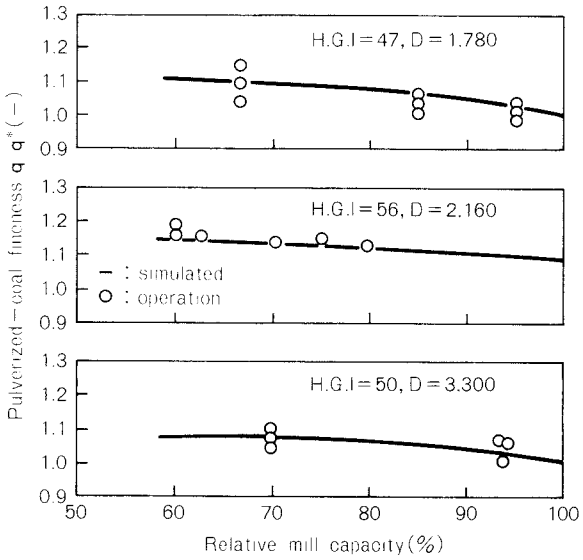

Fig. 9 Comparison of simulated and operating capacities and fineness for large-scale mills

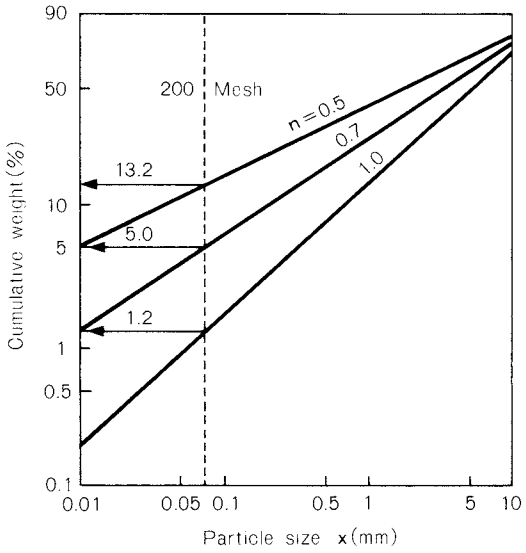

Fig. 10 Particle size distribution of raw coal for simulation

fied simulation model is sufficiently verified.

4. 2 Effect of feed sizes

The effect of feed size distributions on pulverized coal fineness and coal flow rates through the grinding zone were investigated for a coal of 50 *H.G.I.* which is quite common in grindability. Three different feed sizes of the Rosin-Rammler distribution moduli of 0.5, 0.7 and 1.0 with a top size of 38.1 mm shown in **Fig. 10** were used for the simulation test. The weight percentages for less than 200-mesh of feed coal are 13.2%, 5.0% and 1.2%, respectively. The simulated results for a large-scale mill (D = 1780 mm) are shown in **Fig. 11** where computation was performed at a fixed vane angle. The finer feed coal (i.e. the lesser value of n) is the finer product. Furthermore, within a range of 80 ~ 100% mill capacity, decreasing mill capacity results in a finer product. However, the fineness is almost independent of mill capacity below an 80% mill load.

On the other hand, the relative circulating load expressed by F'/G^* where the coal flow rate at the grinding zone was divided by the make up feed rate G at 100% mill capacity, and a finer feed size results in lower coal flow rates in the grinding zone. In particular, within the range of 80 ~ 100% mill capacity, the coal flow rate in the grinding zone varies with the mill capacity. These results are different from those obtained by grinding in dry and wet tube

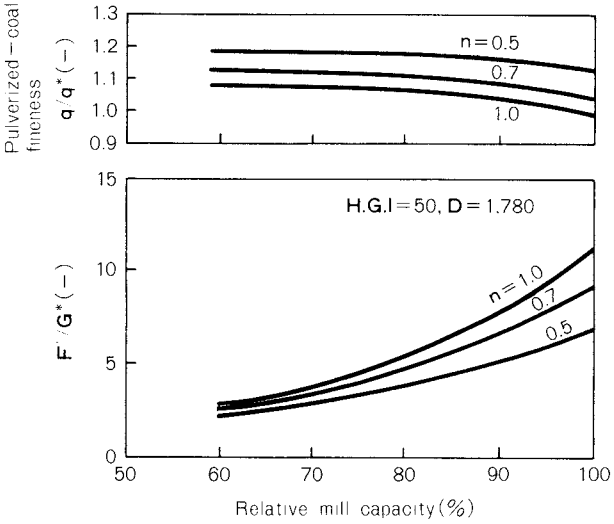

Fig. 11 Effect of feed size on mill performance (simulation)

ball mills. The performance of a tube ball mill is not strongly affected by the feed size distribution because it is a fine grinding mill. In general, a roller mill is considered to be a relatively coarse grinding mill with internal classifiers in which coarser particles are recycled to the grinding zone and finer particles are recovered as the product, minimizing over-grinding. Hence, it appears that the mill performance depends on the coal particle feed size. Moreover, this is one of the reasons why a roller mill requires less mill power than a tube ball mill. A tube mill circuit is usually not operated at such

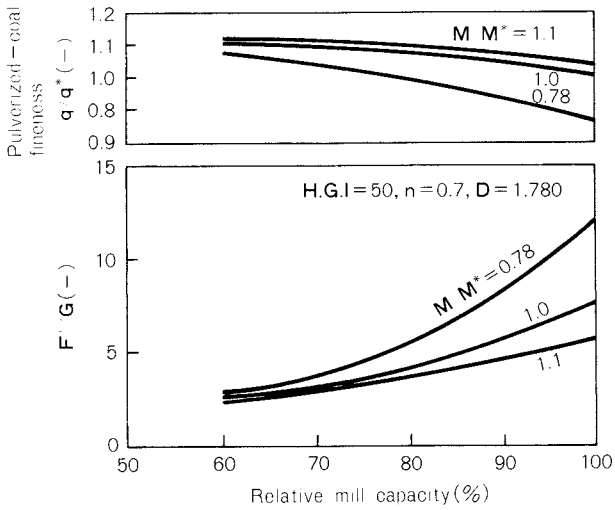

Fig. 12 Effect of the total crushing load on fineness for a large-scale mill (simulation)

a circulating load $(1+\bar{C})$ as 5 ~ 10 in roller mills[9].

4. 3 Effect of crushing loads

Figure 12 shows the effect of the total crushing load M on the pulverized-coal fineness. The effect of M on the pulverized-coal fineness and coal flow rate at the grinding zone is marked over the range of 80% relative mill capacity. Especially at 100% relative mill capacity, a 22% reduction in M results in a substantially coarser product, and the coal flow rate in the grinding zone increases by approximately 1.6 times.

Furthermore, a crushing load 10% higher than the design value results in greater pulverized-coal fineness and approximately a 10% reduction in F'/G^*. On the other hand, at low relative mill capacity, less than 70%, pulverized-coal fineness, and F' are almost independent of M over the range of $M/M^*=0.78$ to $M/M^*=1.1$.

5. Conclusion

The mathematical model previously developed for a ring ball mill was further refined by introducing the scale-up laws on grinding and classification actions. The present steady-state simulation model can describe the operating behavior within the mill for a given mill.

Nomenclature

A	:	air flow rate	[kg/min]
A^*	:	base air flow rate	[kg/min]
A_i	:	absolute rate of breakage of size i	[g/min]
a	:	S_i parameter	[−]
B_{ij}	:	cumulative breakage distribution parameter	[−]
b_{ij}	:	fraction of material just broken from the size interval j which appears in size interval i (smaller size)	[−]
b_1	:	constant	[−]
C	:	circulation ratio at secondary classification zone	[−]
C'	:	circulation ratio at primary classification zone	[−]
$\bar{C}$	:	net circulation ratio	[−]
c_i	:	partial separation efficiency of size i at secondary classification	[−]
c_i'	:	partial separation efficiency of size i at primary classification	[−]
D	:	mean diameter	[mm]
D_c	:	diameter of the cyclone-type classifier	[−]
d	:	diameter of the grinding ball	[mm]
F	:	coal flow rate at the classifier inlet	[kg/min]
F'	:	coal flow rate at the grinding zone	[kg/min]
f_i	:	wt. fraction of size i in the combined feed of raw coal and secondary classifier tailings	[−]
f_i'	:	wt. fraction of size i in feed to the grinding zone	[−]
G	:	coal feed rate	[kg/min]
G^*	:	base coal feed rate	[kg/min]
g	:	acceleration due to gravity	[m^2/s]
g_i	:	wt. fraction of size i in make-up feed	[−]
H	:	vane height	[m]
$H.G.I.$	:	Hardgrove grindability index	[−]
k	:	scale-up factor	[−]
k_m	:	largest value of the scale-up factor	[−]
k_0	:	empirical factor	[−]
k_1, k_2	:	constants	[−]
L	:	outlet skirt length	[m]
M	:	crushing load	[N]
M^*	:	base crushing load	[N]
n	:	distribution constant	[−]
p_i	:	wt. fraction of size i in feed to the secondary classifier	[−]
Q	:	through-put	[kg/min]
Q_H	:	through-put of Hardgrove mill	[kg/min]
Q_n	:	through-put of at k/k_m = 0.5	[kg/min]
Q_{sim}	:	simulated through-put	[kg/min]
q	:	wt. fraction −200-mesh in mill output	[−]
q^*	:	base wt. fraction of −200 mesh in mill output	[−]
q_i	:	wt. fraction of size i in mill output	[−]
S_i	:	specific rate of breakage of size i	[ℓ/min]
$S_{16\times20}$	:	the specific rate of breakage of 16X20-mesh material	[ℓ/min]
T	:	coal flow rate from secondary classification zone to the mill	[kg/min]

T'	:	coal flow rate from primary classification zone to the mill	[kg/min]
t_i	:	wt. fraction of size i in secondary classifier tailings	[–]
t_i'	:	wt. fraction of size i in primary classifier tailings	[–]
v_0	:	air velocity at the classifier inlet	[m/s]
W	:	hold-up in the mill	[kg]
w_i	:	wt. fraction of size i in hold-up	[–]
x	:	particle size	[μm]
x_i	:	particle size of interval i	[μm]
x_{50}	:	critical cut size	[μm]
x_{50}^*	:	base cut size of primary classification	[μm]
x_{50}^{**}	:	base cut size of secondary classification	[μm]
α	:	S_i parameter	[–]
β	:	B_{ij} parameter	[–]
γ	:	B_{ij} parameter	[–]
ϕ	:	B_{ij} parameter	[–]
θ	:	vane angle	[degree]
ω	:	rotational speed of mill	[rpm]

References

1) Funtaikogakukai: "Funtaikogaku-Yogojiten" (Powder Engineering Society Dictionary), p.436, Nikkan Kogyo (1981).
2) Austin, L.G.: *Powder Technol.*, **5**, 1~7 (1971/72).
3) Murata, H., N. Higashihata and M. Nitta: *J. Soc. Powder Technol., Japan,* **22**, 375 (1985).
4) Austin, L.G., *et al.*: *Powder Technol.*, **29**, 263~275 (1981).
5) Austin, L.G., K. Shoji and P.T. Luckie: *Powder Technol.*, **33**, 113~125 (1982).
6) Austin, L.G., K. Shoji and P.T. Luckie: *Powder Technol.*, **33**, 127~134 (1982).
7) ASTM Designation: D409~71 (1980).
8) Svarosky, L.: "Handbook of Powder Technology, Vol. 3: Solid-Gas Separation", p.40, Elsevier (1981).
9) Tanaka, T.: "Funtai Process Nyumon" (Introduction to Powder Processes), p. 143, Kogaku Tosho (1968).

Estimation of Mixing Index and Contact Number by Coordination Number Sampling in an Incompletely Mixed State†

Hisakazu Shindo
Department of Computer Science,
Faculty of Engineering
*Yamanashi University**

Abstract

A statistical model of the distribution of the contact number for a binary mixture in an incompletely mixed state is introduced. The model is derived from the beta-binomial model proposed by Yoshizawa and Shindo[3]. The mixing index based on the contact number is defined and described by only one parameter in this model.

The precision of the estimation of the mixing index, based on the contact number by coordination number sampling in an incompletely mixed state, has been derived and simulated on a computer.

1. Introduction

Many of conventional solid mixes indicates their mixing indexes based on the variance of target components among spot samples. However, the variance is macroscopic and cannot provide any definite physical meaning, though it is very important statistically. Thus, it is difficult to get a definite meaning of variance when a mixing index is applied to the microscopic analysis of a reaction rate in a solid reaction.

From the above viewpoint, Akao, Fan and others have proposed the representation of a mixing index with a contact number. The purpose of this is to estimate the number of contacts in a mixed substance to represent the mixing index by a sampling method, called coordination number sampling, which measures the number of target component particles in contact with specific component particles extracted randomly. The mixing index based on the contact number, which is both microscopic and geometric, can provide a definite physical meaning.

Yoshizawa and Shindo[3] have proposed a model based on the β-binomial model to describe any mixed state of a binary mixture and investigated the precision of the estimation of the Lacey's mixing index[4] in an incompletely mixed state as well as the relationship of the model with the Polya urn scheme[5].

We found the distribution of the contact number in an incompletely mixed state, up-until-now still unknown, with the same model configuration as that of Yoshizawa and Shindo, discussed about an estimation method for the population contact number and investigated the validity of the theory through computer simulation. The following is a description of our findings.

2. Distribution of contact number and its mixing index

2. 1 Completely segregated state and completely random state

Now, we consider a mixture of a two-dimensional regular array consisting of two kinds of equal diameter particles, A_0 and A_1. Their population concentration is assumed to be X_0 and X_1 $(=1 - X_0)$, respectively. A particle extracted randomly from the mixture is called a sample particle and the total number of particles in contact with the sample particle is called the total coordination number n^*. Total coordination number n^*, which is determined by

* 4-3-11, Takeda, Kofu-shi, 400
TEL. 0552-52-1111

† This report was originally printed in *J. Soc. Powder Technology, Japan*, **24**, 521-526 (1987) in Japanese, before being translated into English with the permission of the editorial committee of the Soc. Powder Technology, Japan.

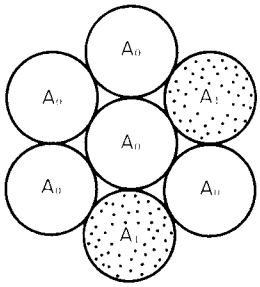

Fig. 1 Illustration of a coordination number sampling of size $n^*=6$

the array structure of the mixture, is 4 for the square array and 6 for the hexagonal array. When the sample particles are restricted to A_0 particles, and A_0 particle is called the specified particle. The number of A_1 particles in contact with specified particle A_0 is defined as the contact number (see **Fig. 1**). The sampling, on the basis of the definition, is called the coordination number sampling of size n^*.

The random variable indicating the contact number and the realized value are denoted by $C_{1(0)}$ and $c_{1(0)}$, respectively. In the completely segregated state of the particles of two kinds, it is clear that the contact number $C_{1(0)}$ can be expressed by the one-point distribution shown below, with the boundary ignored:

$$P_r[C_{1(0)} = c_{1(0)}] = \begin{cases} 1 & \text{if } C_{1(0)} = 0 \\ 0 & \text{otherwise} \end{cases} \quad (1)$$

Both expected value μ_s and variance σ_s^2 of the contact number $C_{1(0)}$ are zero as follows:

$$\mu_s = E(C_{1(0)}) = 0 \quad (2)$$

$$\sigma_s^2 = V(C_{1(0)}) = 0 \quad (3)$$

In the completely random state, the contact number $C_{1(0)}$ follows the binomial distribution as

$$P_r[C_{1(0)}=c_{1(0)}] = \binom{n^*}{c_{1(0)}} \bar{X}_1^{c_{1(0)}} (1-\bar{X}_1)^{n^*-c_{1(0)}} \quad (4)$$

thus, as is well known, the expected value, μ_r and the variance, σ_r^2, are expressed as follows:

$$\mu_r = E(C_{1(0)}) = n^*\bar{X}_1 \quad (5)$$

$$\sigma_r^2 = V(C_{1(0)}) = n^*\bar{X}_1 (1-\bar{X}_1) \quad (6)$$

Now focusing on the changes in the expected values in Eqs. (2) and (5), we define mixing index M of the two kinds of particles with the contact number as shown in the equation below:

$$M = (\mu - \mu_s)/(\mu_r - \mu_s) = \mu/(n^*\bar{X}_1) \quad (7)$$

where μ is the expected value of the contact number in any mixed state. Therefore, contact number mixing index M is 0 in the completely segregated state and 1 in the completely random state. In addition, the mixing index can take an exclusive value between 0 and 1 because $0 \leq \mu \leq n^*\bar{X}_1$.

While conventional mixing indexes such as Lacey's mixing index[4] is based on the variance

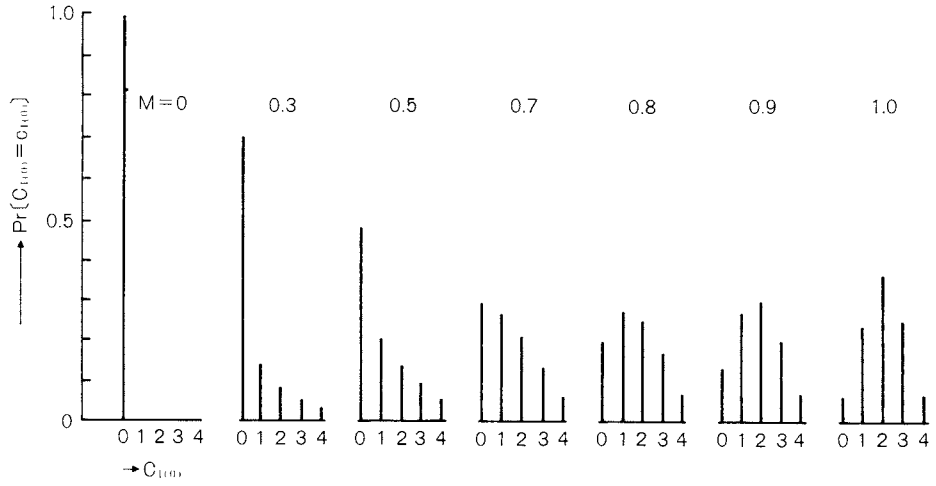

Fig. 2 Distribution of the contact number and the mixing index M with the total coordination number $n^*=4$ and the population concentration $\bar{X}_1 = 0.5$

or secondary moment, contact number mixing index M is based on the expected value or primary moment, as known from Eq. (7).

2. 3 Incompletely mixed state

In an incompletely mixed state, the local concentration of the target particles is largely non-uniform and the concentration of the entire mixture is not capable of being uniform. Thus, it should be considered that the local concentration itself is a random variable following a certain distribution. Therefore, we assume the random variable z of the local concentration and the probability density function $f(z)$, which has the β density with parameters τ and $\bar{X}_1$ as expressed by :

$$f(z) = \frac{z^{\tau\bar{X}_1 - 1}(1-z)^{\tau(1-\bar{X}_1)-1}}{B(\tau\bar{X}_1, \tau(1-\bar{X}_1))} \tag{8}$$

where τ is the positive parameter and $B(\cdot\,,\cdot)$ is the β function.

Now, under the condition that local concentration Z is known, the probability that the sample particle is A_0 and the y particles in the n^* particles around the sample particle are A_1 particles is expressed by the equation,

$$P_r[Y = y, A_0 \mid z] = \binom{n^*}{y} z^y (1-z)^{n^*-y+1} \tag{9}$$

where Y is the random variable against y. Therefore, $P_r[Y = y, A_0]$ can be expressed by the equation below as the marginal probability of the simultaneous probabilities in Eqs. (8) and (9):

$$\begin{aligned} P_r[Y = y, A_0] &= \int_0^1 P_r[Y = y, A_0 \mid z] f(z)\,dz \\ &= \int_0^1 \binom{n^*}{y} z^y (1-z)^{n^*-y+1} \\ &\quad \times \frac{z^{\tau\bar{X}_1 - 1}(1-z)^{\tau(1-\bar{X}_1)-1}}{B(\tau\bar{X}_1, \tau(1-\bar{X}_1))}\,dz \\ &\quad y = 0, 1, 2, \cdots\cdots, n^* \end{aligned} \tag{10}$$

This gives us the probability that the y A_1 particles are in contact with the sample particle which is assumed to be an A_0 particle to be expressed by the following equation:

$$P_r[Y = y \mid A_0] = P_r[Y = y, A_0]/P_r[A_0]$$

$$\begin{aligned} &= \frac{1}{1-\bar{X}_1}\int_0^1 \binom{n^*}{y} z^y (1-z)^{n^*-y+1} \\ &\quad \times \frac{z^{\tau\bar{X}_1 - 1}(1-z)^{\tau(1-\bar{X}_1)-1}}{B(\tau\bar{X}_1, \tau(1-\bar{X}_1))}\,dz \\ &= \frac{1}{1-\bar{X}_1}\binom{n^*}{y} B(y + \tau\bar{X}_1, n^* - y \\ &\quad + \tau(1-\bar{X}_1) + 1)/B(\tau\bar{X}_1, \tau(1-\bar{X}_1)) \end{aligned} \tag{11}$$

As a result of $P_r[Y = y \mid A_0] = P_r[C_{1(0)} = y]$, the distribution presented by Eq. (11) indicates the contact number distribution in an incompletely mixed state.

In contact number distribution Eq. (11), i-th factorial moment $\mu_{(i)}$ of $C_{1(0)}$ can be,

$$\begin{aligned} \mu_{(i)} &= n^{*(i)}\tau[(\tau\bar{X}_1 + i - 1)\cdots(\tau\bar{X}_1)] \\ &\quad /[(\tau + i)\cdots(\tau)] \end{aligned} \tag{12}$$

where $n^{*(i)} = n^*(n^*-1)\cdots(n^*-i+1)$. This enables expected value μ and variance σ^2 of the contact number $C_{1(0)}$ in an incompletely mixed state to be determined by the following equations, respectively:

$$\mu = \mu_{(1)} = n^*\bar{X}_1\tau/(\tau + 1) \tag{13}$$

$$\begin{aligned} \sigma^2 &= \mu_{(2)} + \mu_{(1)} - \mu_{(1)}^2 \\ &= \frac{\tau}{\tau+1} n^*\bar{X}_1\left(1 - \frac{\tau}{\tau+1}\bar{X}_1\right)\frac{\tau + 1 + n^*}{\tau + 2} \end{aligned} \tag{14}$$

The limits of the expected value and variance when parameter τ is made close to zero or infinity are,

$$\lim_{\tau\to 0}\mu = 0 = \mu_s \qquad \lim_{\tau\to 0}\sigma^2 = 0 = \sigma_s^2 \tag{15}$$

$$\lim_{\tau\to\infty}\mu = n^*\bar{X}_1 = \mu_r \quad \lim_{\tau\to\infty}\sigma^2 = n^*\bar{X}_1(1-\bar{X}_1) = \sigma_r^2 \tag{16}$$

The changes when parameter τ is altered from zero to infinity corresponds to the status that the distribution of contact number $C_{1(0)}$ moves gradually from the one-point distribution of the completely segregated state in Eq. (1) to the binomial distribution of the completely random state in Eq. (4), as shown in **Fig. 2.**

Substituting the expected value (13) of contact number $C_{1(0)}$ in an incompletely mixed state for the mixture defining Eq. (7), we come up with the following equation associating mixture M with parameter:

$$M = \tau/(\tau + 1) \tag{17}$$

This relationship coincides with the relationship between Lacey's mixing index and the parameter τ in the β-binomial model proposed by Yoshizawa and Shindo.

3. Estimation of mixing index and its accuracy

We now consider the problem that the mixture is estimated with k coordination number samples of size n^* from the mixture including target particles of population concentration $\bar{X}_1$. In the mixing problem, $\bar{X}_1$ is assumed to be already known because it is often given when the mixture is supplied. This causes the denominator of the mixture defining Eq. (7) to be constant. At last, we may estimate the contact number through the equation,

$$\hat{c} = \sum_{i=1}^{k} c_i/k \tag{18}$$

then substitute it for Eq. (7).

From Eqs. (13) and (14), expected value $E(\hat{c})$ and variance $V(\hat{c})$ of the estimate of the contact number $\hat{c}$ can be expressed as follows:

$$E(\hat{c}) = n^*\bar{X}_1\,\tau/(\tau + 1) \tag{19}$$

$$V(\hat{c}) = \frac{1}{k} \cdot \frac{\tau}{\tau + 1} \cdot n^*\bar{X}_1 \left(1 - \frac{\tau}{\tau + 1}\bar{X}_1\right) \times \frac{\tau + 1 + n^*}{\tau + 2} \tag{20}$$

Equation (19) indicates that $\hat{c}$ is an unbiased estimator. Depending on the above equations, standard error $D(\hat{c})$ and relative standard error $RSE(\hat{c})$ of the estimate $\hat{c}$ can be expressed by the following equations, respectively:

$$D(\hat{c}) = \sqrt{V(\hat{c})} = \left[\frac{1}{k} \cdot \frac{\tau}{\tau + 1} \cdot n^*\bar{X}_1 \times \left(1 - \frac{\tau}{\tau + 1}\bar{X}_1\right) \frac{\tau + 1 + n^*}{\tau + 2}\right]^{1/2} \tag{21}$$

$$RSE(\hat{c}) = D(\hat{c})/E(\hat{c}) = \left[\frac{(\tau + 1 - \tau\bar{X}_1)(\tau + 1 + n^*)}{kn^*\bar{X}_1\,\tau(\tau + 2)}\right]^{1/2} \tag{22}$$

To find the number of samples k satisfying the specified relative standard error $RSE(\hat{c})$ in the sampling design, we may use the following equation, which results from solving Eq. (22) regarding k:

$$k = \frac{(\tau + 1 - \tau\bar{X}_1)(\tau + 1 + n^*)}{n^*\bar{X}_1\,\tau(\tau + 2)\{RSE(\hat{c})\}^2} \tag{23}$$

Equations (21), (22), and (23) are equations to find the standard error, relative standard error and the number of samples k of estimate $\hat{c}$ in the completely random state. They are presented as the limits when parameter τ is made close to infinite, as shown below:

$$D(\hat{c}) = [n^*\bar{X}_1(1 - \bar{X}_1)]^{1/2} \tag{24}$$

$$RSE(\hat{c}) = [(1 - \bar{X}_1)/kn^*\bar{X}_1]^{1/2} \tag{25}$$

$$k = (1 - \bar{X}_1)/n^*\bar{X}_1\ RSE(\hat{c})^2 \tag{26}$$

These equations can be obtained by estimate Eq. (5) and variance Eq. (6) of the binomial distribution Eq. (4), which is the distribution of the contact number in the completely random state.

4. Results and discussions of computer simulation

To determine the validity of estimate accuracy Eqs. (22) and (25), we carried out computer simulation. As shown in **Fig. 2**, the distribution of the contact number is a discrete distribution. Using the following recurrent equation which satisfied between adjacent probabilities,

$$P_r[C_{1(0)} = c_{1(0)} + 1] = P_r[C_{1(0)} = c_{1(0)}] \cdot \frac{n^* - c_{1(0)}}{c_{1(0)} + 1} \cdot \frac{c_{1(0)} + \tau\bar{X}_1}{n^* - c_{1(0)} + \tau(1 - \bar{X}_1)} \tag{27}$$

we found the accumulated probability and generated random numbers obeying Eq. (11) with the reverse conversion method[6].

We made a simulation using the following procedure:

(i) First mixture M, population concentration $\bar{X}_1$ and sample size n^* were specified.

(ii) Next, the number of samples k to a certain value were set.

(iii) Then, assuming the j-th sample in the i-th count to be c_{ij}, mean contact number $\hat{c}_i$ $(i = 1, \cdots, N)$ with the following equation was estimated:

$$\hat{c}_i = \sum_{j=1}^{k} c_{ij}/k \tag{28}$$

(iv) Next, average $\bar{\hat{c}}$ and standard error $D(\hat{c})$ of

the mean contact number of N particles using the following respective equations were calculated:

$$\bar{\hat{c}} = \sum_{i=1}^{N} \hat{c}_i / N \tag{29}$$

$$D(\hat{c}) = \left\{ \sum_{i=1}^{N} (\hat{c}_i - \bar{\hat{c}})^2 / (N-1) \right\}^{1/2} \tag{30}$$

(v) Then, relative standard error $RSE(c_{1(0)})$ by $D(\hat{c})/\bar{\hat{c}}$ could be estimated.

Figure 3 (a) plots the relationship of relative standard error $RSE(C_{1(0)})$ with the number of samples k on log-log graphs in the completely random state with total coordination number $n^* = 4$ and population concentration $\bar{X}_1 = 0.1$ or 0.5. The solid lines indicate the theoretical values calculated from Eq. (25), which are just suited to the simulation results. Since the lines with population concentration $\bar{X}_1 = 0.5$ are always drawn below those with $\bar{X}_1 = 0.1$, the relative standard error is smaller to have higher estimate precision as the population concentration $\bar{X}_1$ is closer to 0.5.

As a sample result in an incompletely mixed state, **Fig. 3 (b)** shows the same relationship as in **Fig. 3 (a)** with mixture $M = 0.5$. The solid lines in the figure are the theoretical values found from Eq. (22). The relative standard error is larger to be less estimate precision in comparison with **Fig. 3 (a)**.

Actually, it is better to estimate the contact number by the coordination number sampling for an appropriate number of samples prior to mixing. **Figure 4** shows the relationship of the relative standard error with mixture for population concentration $\bar{X}_1 = 0.1$ and 0.5 with the number of samples k fixed to 20 and total coordination number $n^* = 4$. This indicates that the relative standard error is decreased gradually to make the estimate precision higher prior to mixing.

In designing sampling operation, it is easy to use **Figs. 3 (a)** and **3 (b)**, while it can be designed by using Eqs. (23) and (26). **Table 1** shows the results of calculating the number of samples using Eqs. (23) and (26) to estimate the contact number with the relative standard error of 10% in two cases of the population concentration $\bar{X}_1$ of 0.1 and 0.5 with the total coordination number $n^* = 4$. This also indicates that the estimate precision is higher and the number of samples may be less as population concentration $\bar{X}_1$ becomes closer to 0.5 and the mixture becomes closer to the completely random state.

5. Conclusion

Akao and others have already proposed a method to indicate mixture using the contact number. However, with this method, we could not discuss the estimate precision because it did not clarify the distribution of the contact number in an incompletely mixed state.

This report introduced the theoretical distri-

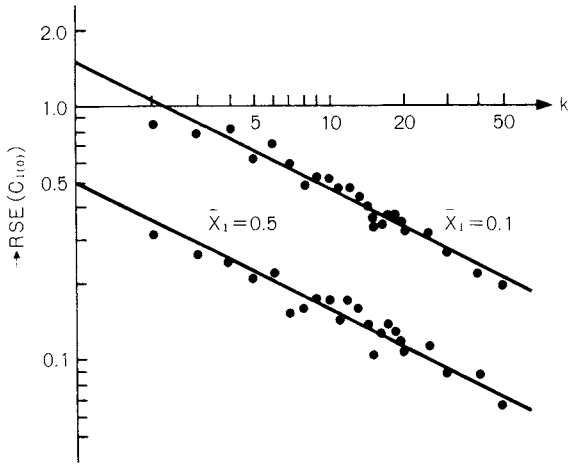

Fig. 3(a) Comparison of theoretical relative standard errors with those of numerical experiments in log-log scale in the completely random state : $M = 1.0$, $n^* = 4$ and $N = 100$

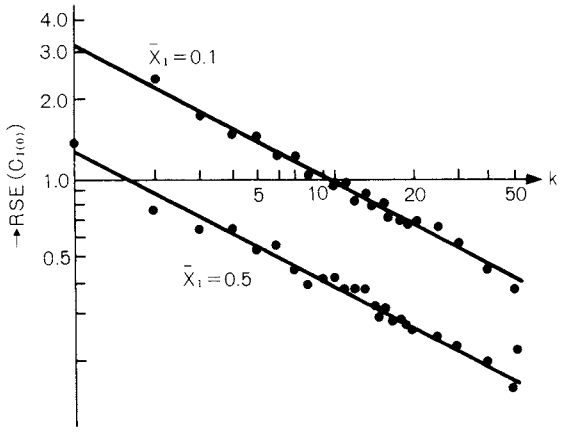

Fig. 3(b) Comparison of theoretical relative standard errors with those of numerical experiments in log-log scale in an incompletely mixed state : $M = 0.5$, $n^* = 4$ and $N = 100$

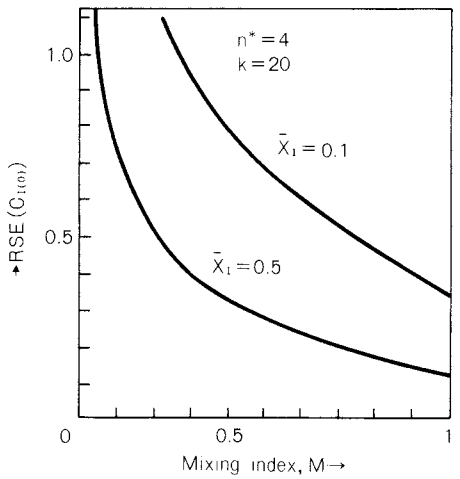

Fig. 4 Relative standard errors vs the mixing index in the case of a constant number of samples

bution of the contact number in an incompletely mixed state through the similar prerequisite as the β-binomial model proposed by Yoshizawa and Shindo, investigated the estimate precision of the contact number based on the model and indicated examples of the sampling designs.

In estimation of the contact number, spot sampling can be used instead of coordination number sampling. The spot sampling method has already been reported.

Acknowledgments

The information in this report was created during the research work for the "Study on Solids Mixing", a Japan-U.S. joint scientific cooperation project of the Japan Society for the Promotion of Science carried out for two years from 1978. The author would like to thank Prof. Y. Akao of Yamanashi University (who is now Professor of Tamagawa University) and Prof. T. Yoshizawa of Yamanashi University (who is now Professor of the University of Tsukuba), Japanese representatives of the project for their guidance. The author also would like to thank Prof. L.T. Fan of the Kansas State University, Asst. Prof. F.S. Lai, and Mr. J.R. Too for their useful discussions and help in creating this report.

Nomenclature

A_0, A_1	:	kinds of particles	[–]
B	:	beta function	[–]
$C_{1(0)}, \hat{c}_{1(0)}$	:	random variable denoting the contact number and its value	[–]
c_{ij}	:	the j-th sample used in the i-th estimation	[–]
$\hat{c}$	:	estimate of the contact number	[–]
$\hat{c}_i$	:	the i-th estimate of the contact number	[–]
$\bar{\hat{c}}$	:	mean of the N estimates	[–]
D	:	standard error	[–]
$D(\hat{c})$	:	standard error of the N estimates	[–]
E	:	expectation operator	[–]
$f(z)$	:	probability density function of Z	[–]
k	:	number of samples	[–]
M	:	mixing index	[–]
N	:	number of iterations of the simulation	[–]
n^*	:	total coordination number or sample size	[–]
$n^{*(i)}$	:	factorial function	[–]
RSE	:	relative standard error	[–]
V	:	variance operator	[–]
$\bar{X}_0, \bar{X}_1$	:	population concentration of each kind of particles	[–]
Y, y	:	random variable denoting the number of particles within a coordination number sample and its value	[–]
Z, z	:	random variable denoting the local concentration and its value	[–]
μ, σ^2	:	expectation and variance of the contact number in an arbitrarily mixed state	[–]
μ_r, σ_r^2	:	ditto in the completely random state	[–]
μ_s, σ_s^2	:	ditto in the completely segregated state	[–]
$\mu_{(i)}$	:	the i-th factorial moment	[–]
τ	:	parameter	[–]

Table 1 Examples of the sampling designs: the number of samples required to assure the relative standard error is less than 10%

	$M = 0.5$	$M = 1.0$
$\bar{X}_1 = 0.1$	950	225
$\bar{X}_1 = 0.5$	150	25

References

1) Fan, L.T., S.J. Chen and C.A. Watson: *Ind. Eng. Chem.*, **62**, [7], 53 (1970).
2) Akao, Y., H. Kunisawa, L.T. Fan, F.S. Lai and R.H. Wang: *Powder Technol.*, **15**, 267 (1976).
3) Yoshizawa, T. and H. Shindo: *Journal of the Japan Society for Quality Control*, **7**, 3 (1977).

4) Lacey, P.M.C.: *J. App. Chem.*, **4**, 257 (1954).
5) Johnson, N.L. and S. Kotz: "Distributions in Statistics: Discrete Distributions", Houghton Mifflin Boston (1969).
6) Naylor, T.H., J.L. Balintfy, D.S. Burdick, and K. Chu: "Computer Simulation Techniques (2nd Ed.)", John Wiley & Son (1967).
7) Shindo, H., et al.: *Powder Technol.*, **21**, 105 (1978).

The Influence of Relative Humidity on the Strength of Spray-Dried Products†

Noriyuki Yamada, Hideharu Hirosue and Eiichi Abe

*Government Industrial Research Institute, Kyushu**

Abstract

A slurry feed composed of water, PVA and fine particles are sprayed in droplet from into a spray dryer, with porous and spherical spray-dried products being recovered. However, the PVA binder is so hygroscopic that the strength of the products changes as the relative humidity changes.

For the purpose of clarifying this phenomenon quantitatively, the specific surface area, hygroscopic moisture content and strength of the spray-dried products are examined experimentally and theoretically.

The conclusions obtained are summarized as follows:

1. *The hygroscopic moisture content of the products is estimated by the total of the moisture adsorbed on the surface of constituent fine particles covered somewhat with PVA and the moisture adsorbed by PVA itself.*
2. *The strength of the products is measured under various conditions of relative humidity. The measured values are compared with the results calculated from the previously derived equation. As a result, it was found that the strength of the products could be estimated very well by taking account the effect of the variation in humidity on binder strength in the derived equation.*

1. Introduction

During the manufacture of 10- to 44-$\mu m\phi$ carriers for DL dust, which is a kind of agricultural solid formulation, less-than-10-$\mu m\phi$ clayey particles of roseki, talc and similar matter are discarded. To make it possible to recycle these particles, we have been studying the spray-drying method as a means to enlarge their size and formulate them. Our study includes:

- examination of the spraying characteristics of a suspension of clayey particles due to a two-fluid nozzle and rotating disc[1,2]; and
- measurement and theoretical review of the crushing strength of spray-dried particles in a dry environment[3]. The above study, however, has not sufficiently revealed the moisture adsorption characteristics, strength and related characteristics of dried particles in a wet environment. This paper, therefore, aims at investigating the strength of spray-dried products ("products") containing highly-hygroscopic polyvinyl alcohol (PVA) as a binder.

2. Specimen

We obtained the products from the same apparatus as that described in our previous paper[3]. As for particles constituting a product ("constituent particles"), roseki was used in most experiments and silicon carbide and kaolin in the rest of the experiments. **Figure 1** shows the particle size distribution of these constituent particles, while **Table 1 (a)** indicates their characteristics. The binder used was PVA; Nippon Synthetic Chemical Industry's Gohsenol GL05, GH20 and NH20. Here, *G* means the partially saponified type, while *N* refers to the perfectly saponified type. The

* Shuku-machi, Tosu, 841
TEL: 0942-82-5161

† This report was originally printed in *J. Soc. Powder Technology, Japan*, **24**, 582-587 (1987) in Japanese, before being translated into English with the permission of the editorial committee of the Soc. Powder Technology, Japan.

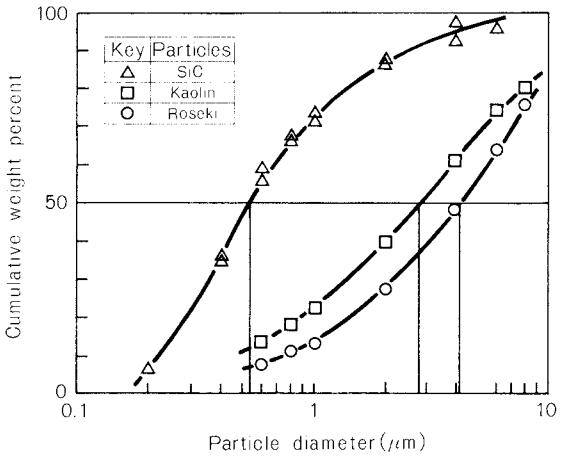

Fig. 1 Size distribution of constituent particles

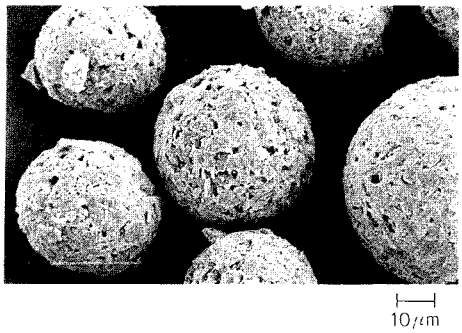

Fig. 2 SEM of spray-dried products

figures correspond to the respective degrees of polymerization: 05 and 20 represent 500 and 2,000 in degree of polymerization respectively.

The products used are shaped like shown in **Fig. 2**. They are spherical and porous. The pore sizes of products made of roseki, kaolin and silicon carbide account for about 20% of the diameters of their own constituent particles [**Table 1 (b)**]. The porosity was about 0.5 for all products.

3. Experiment method

We assumed that changes in product strength due to moisture adsorption would be brought about by the binder's moisture adsorption. We, therefore, measured the amount of adsorbed water vapor and specific surface area of the products. We also measured the relationship between the amount of PVA adsorption and relative humidity using two kinds of products: commercially-available powder-like products and their variation made by dissolving them and shaping them like a sheet. The amount of

Table 1 Physical properties of constituent particles and spray-dried products

(a) Constituent particles

	Mass median diameter (μm)	Specific surface diameter d (μm)	Specific surface area S_V (m^2/m^3)	Density ρ_p (kg/m^3)
Roseki	4.1	1.6	3.75×10^6	2720
Kaolin	2.8	1.3	4.62×10^6	2620
SiC	0.53	0.5	12.0×10^6	3200

(b) Spray-dried products

Constituent particle	Pore size*			Porosity* ϵ (−)
	Range (μm)	a_{50} (μm)	a_{50}/d (−)	
Roseki	0.08 ~ 0.8	0.35	0.22	0.5
Kaolin	0.03 ~ 0.6	0.20	0.15	0.5
SiC	0.04 ~ 0.4	0.10	0.20	0.5

* Based on mercury porosimetry

adsorbed water vapor was measured using the weight method employing a quartz spring (Shibata Scientific Technology LTD. model P-850), while the specific surface area was determined using the nitrogen adsorption method (BET method) and the constant-pressure ventilation-type surface area measuring method (air permeation method). The measuring temperature was 303K.

The strength of water-adsorbed products was measured using the two methods indicated in **Fig. 3**. One is a direct method[3] consisting of crushing a product particle on a balance. The other is an indirect method consisting of evaluating strengths based on the compression characteristics of the powder bed. Our previous report[3] indicated that there was a good correlation (its relational expression will be mentioned later) between the above two methods.

As indicated in **Fig. 4**, the products reached adsorption equilibrium within an hour. For direct-method strength measurements, we used specimens left in a laboratory subject to little temperature changes. The temperature remained about 293K throughout the experiment period.

4. Results and discussion

4. 1 The specific surface area of products

Specific surface area S_W of a roseki-made

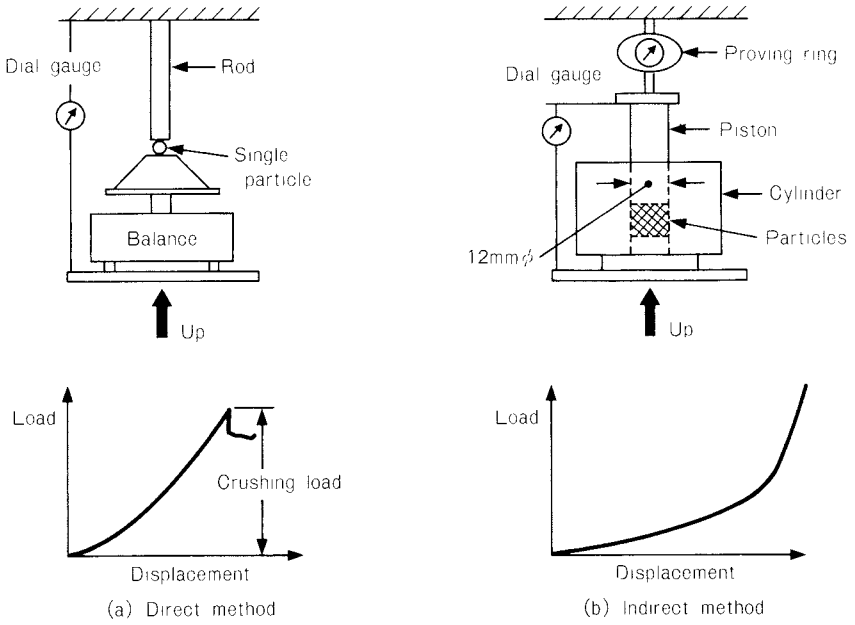

Fig. 3 Experimental apparatus for measurement of strength of products

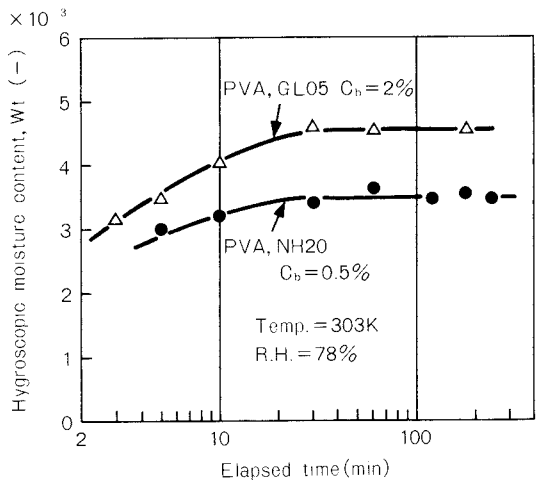

Fig. 4 Change of hygroscopic moisture content of products with time

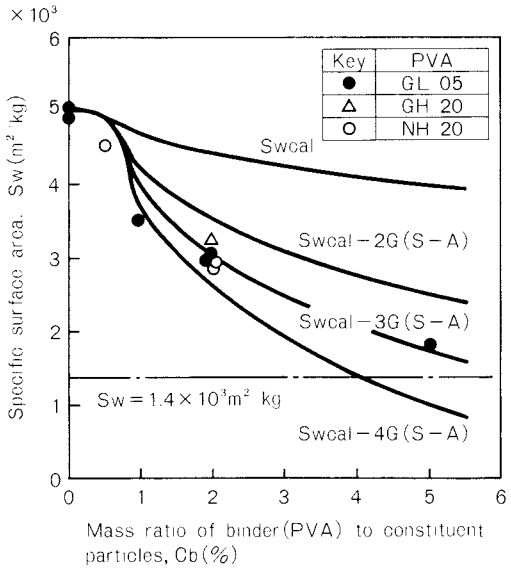

Fig. 5 Change of specific surface area of products with additive amount of binder

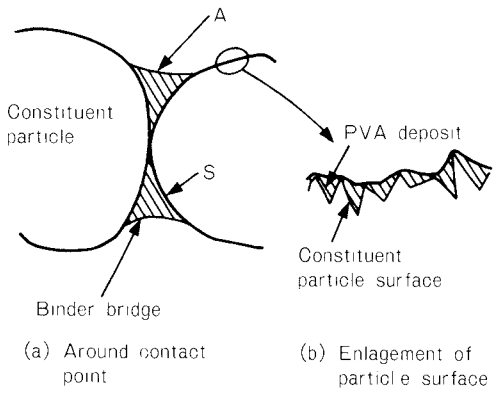

Fig. 6 Model showing PVA deposit around contact point and on constituent particle surface

product measured using the BET method declined as the amount of PVA added climbed, as shown in **Fig. 5**. This, we believe, is because PVA, which formed a bridge between constituent particles as illustrated in **Fig. 6 (a)**, reduced the surface area of the product.

To simplify our study, let's now consider constituent particles with a diameter of d. Assuming that the number of constituent particles per unit mass is N $(=6/(\pi\rho_p d^3))$, the total surface area is $\pi d^2 N$. This total surface area is

subject to surface area increment A due to PVA bridging, along with decrement S due to the hiding of constituent particles by this bridge. If PVA contributes to the contact points alone in increasing and decreasing the surface area of the product, the specific surface area of the product can be expressed as:

$$S_W = \pi d^2 N \frac{1}{1 + C_b} - G(S - A) \quad (1)$$

where C_b is the amount of binder added per unit mass of constituent particles and G is the number of contact points per unit mass of product. Then, the following holds:

$$G = \frac{\pi}{2\epsilon} N \frac{1}{1 + C_b} \quad (2)$$

where π/ϵ is the coordination number. On the basis of the geometrical relationship of the binder solidified around a contact point, A/S can be expressed approximately as:

$$A/S = 1.5\ (4v/\pi d^3)^{0.22} \quad (3)$$

where v is the volume of binder solidified around a contact point. When a C_b amount of binder with a density of ρ_b is added, the equation below holds. This is based on the amount of PVA accumulated in the product when it is dry. This is basically the same as that used in the theoretical study of strength[3].

$$v = \frac{\alpha(C_b - C_{ad})}{G\rho_b(1 + C_b)} \quad (4)$$

where $\alpha = C_W w_C/(1 - C_W)$. w_C is the critical moisture content, C_W is the amount of a binder adsorbed on the constituent particles. At this time, the amount $(1 - \alpha)(C_b - C_W)$ of binder gathers on the product surface. We believe that this gathering brings about negligible changes in surface area. This, together with $S \fallingdotseq 10v^{2/3}$ [4], leads us to convert Eq. (3) into:

$$S - A = 10v^{2/3}\ \{1 - 1.5(4v/\pi d^3)^{0.22}\} \quad (5)$$

Figure 5 shows the results of calculations of Eq. (1) using Eqs. (2), (4) and (5). These calculated results do not agree with measured values, which indicates that it is hard to represent a decline in surface area in the above model.

The experiments indicate that:

- The specific surface area derived from the BET method using roseki (5×10^3 m^2/kg) differs greatly from that obtained from the air permeation method (1.4×10^3 m^2/kg); and
- A rise in PVA causes the specific surface area obtained from the BET method to approximate the surface area derived from the gas permeation method. This leads us to conclude that the discord of the calculated specific surface area with the measured one of the product is partly due to the fact that PVA reduces the specific surface area of the product by hiding not only the contact point but, as illustrated in **Fig. 6 (b)**, the microscopic ups and downs (too small to detect hydrodynamically) of the particle surface. We examined how many times $G(S\text{-}A)$ the decrement in the specific surface area of the product would be on the basis that this decrement was due to the hiding of the above ups and downs and that C_b does not exceed 5%. The result was that measured values almost agreed with calculated values when the decrement in the specific surface area of the product was about three times $G(S\text{-}A)$, as is evident from **Fig. 5**.

4. 2 Water vapor absorption characteristics of products

Figure 7 indicates the amounts of water vapor adsorbed on the products obtained by spray-drying roseki slurry adjusted by different binder densities. The broken line in the figure given the values measured by Arai *et al.*[5], in which case water was adsorbed on the surface without being subject to capillary condensation. In the case of roseki powder containing no PVA, the equivalent average thickness of water adsorbed on the surface shows a linear relationship with adsorption potential up to about 500 J/mol (R.H. $\fallingdotseq$ 80%) in a logarithmic graph. This almost agreed with Arai *et al.*'s result. As for PVA-added products, water was adsorbed into the inside, as well as on the surface of PVA, resulting in a larger adsorbed amount than this broken line. We, therefore, assumed that amount W_t of water vapor adsorbed on a PVA-added product equaled the sum of the amount of water adsorbed on the PVA-curved surface of constituent particles and the amount of water adsorbed inside the PVA. This assumption is formulated as:

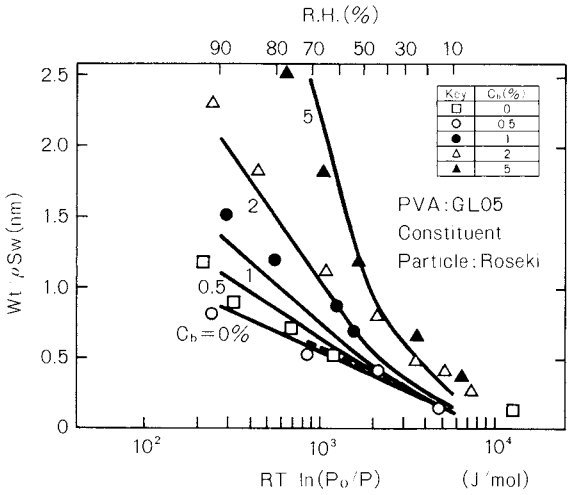

Fig. 7 Relationship between adsorption potential of water vapor and thickness of the adsorption layer

$$W_t = \frac{W_s}{1+C_b} + \frac{C_b W_b}{1+C_b} \tag{6}$$

where W_s and W_b refer to the amounts of adsorbed water vapor per unit mass of constituent particle and PVA, respectively. Measurements indicated that W_t, W_b and W_s could be expressed approximately as:

$$W_s = 2.43\times 10^{-8}\,[-\ln\{RT\ln(P_o/P)\}+9.2]\,\rho S_W \qquad 0.1 < P/P_o < 0.8 \tag{7}$$

$$W_b = 1.40\times 10^{-2}\,[-\ln\{RT\ln(P_o/P)\}+9.2] \qquad 0.1 < P/P_o \leq 0.4$$

$$W_b = 8.40\times 10^{-2}\,[-\ln\{RT\ln(P_o/P)\}+7.9] \qquad 0.4 < P/P_o < 0.8 \tag{8}$$

where ρ is water density.

Assuming that the amount of water vapor adsorbed on the product can be expressed as Eq. (6), we substituted Eqs. (7) and (8) for Eq. (6). The result is indicated by the solid line in **Fig. 7**. Measured values almost agreed with calculated values, showing that the relationship formulated by Eq. (6) holds approximately. This leads us to conclude that the entire binder contained in the product adsorbed water vapor equally.

4. 3 Strength of wet products

In our previous report[3], we proposed the following equation as a formula of the compressive strength of products:

$$\sigma_t = 0.86\,\frac{1-\epsilon}{\sigma^{1/2}}\left\{\alpha\,\frac{\rho_p}{\rho_b}\,(C_b - C_{ad})\right\}^{1/2}\sigma_z \tag{9}$$

where σ_z is the binder strength. Equation (9) indicates that binder strength alone relates to the strength of wet products. The subsequent part of our study describes the relationship between the strength of the binder and that of products.

The strength of wet products was evaluated using the indirect method mentioned in 3. Experiment method, i.e., employing the characteristics of a crushed powder bed. The advantages of this method include:

- products is highly resistant to atmospheric changes;
- even very fragile particles can be detected; and
- the average value of many particles can be obtained.

We adopted this method because the constant $1/b$ in the compression equation Eq. (10) proposed by Kawakita *et al.*[6] showed a good correlation with the strength of single particles constituting a powder bed[6].

$$P_K\,\frac{V - V_\infty}{V_{ao} - V_\infty} = \frac{1}{b}\,\frac{V_{ao} - V}{V_{ao} - V_\infty} \tag{10}$$

where P_K is compressive pressure, V_∞ is the net volume of the powder, V_{ao} is the initial apparent volume of the powder bed, and V is the apparent volume of powder bed under applied load. The above equation is besed on the assumption that the real density of the product is $\rho_p(1-\epsilon)$.

Our previous report[3] (**Fig. 10**) indicated the measurement results of σ_t and $1/b$ regarding dry products. This figure revealed that σ_t had a good correlation with $1/b$, just like in Kawakita *et al.*'s report[6] and that the following equation holds for dry products:

$$\sigma_t \approx \frac{2}{3}\,\frac{1}{b} \tag{11}$$

Figure 8 gives an example of Kawakita's plot for the case in which humidity is 52 and 80%. Kawakita *et al.* reported that $(V_{ao} - V)/(V_{ao} - V_\infty)$ shows a linear relationship up to about 0.7. Such particles composed of microparticles as the products dealt with in this report, however, show the quite different particle properties

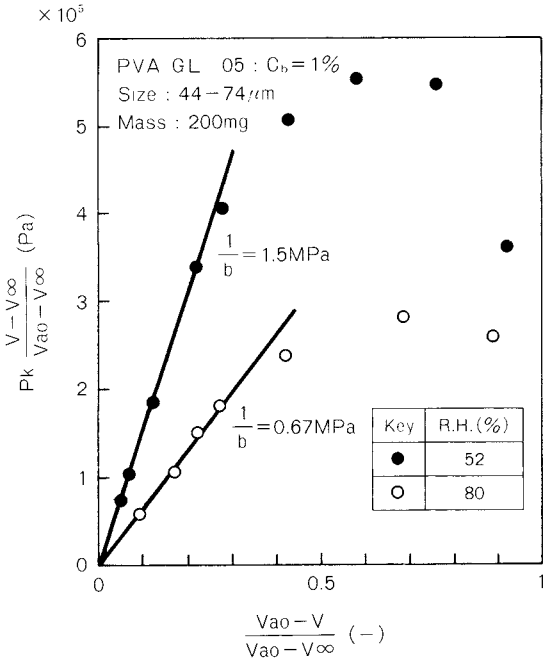

Fig. 8 Compaction behavior (Kawakita's plot) of products under different relative humidity conditions

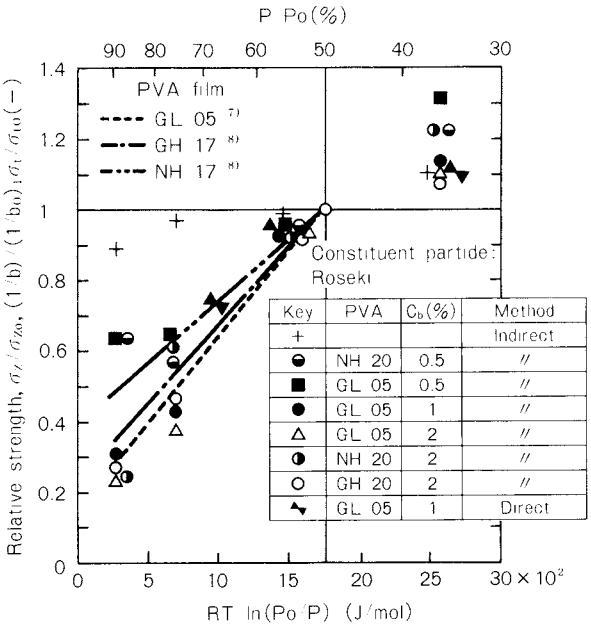

Fig. 9 Influence of relative humidity on strength of products

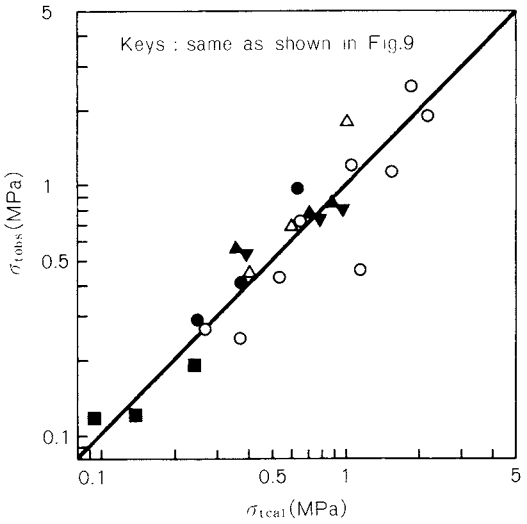

Fig. 10 Comparison of $\sigma_{t\,cal}$ and $\sigma_{t\,obs}$

from their initial ones after destruction. Observations of the linear relationship were, therefore, limited to the initial stage of compression. We therefore set the gradient of the linear portion at $1/b$. In this experiment, we set the product particle size range at 44 ~ 74 μm and the mass at 200 mg. **Figure 8** shows that $1/b$ at high humidity is smaller than that at low humidity and that product strength lowers as humidity increases.

As mentioned before, the following relationship holds for dry products:

$$\frac{1}{b} \approx \frac{3}{2}\,\sigma_t \propto \sigma_z \tag{12}$$

If Eq. (12) holds also for wet products, the following relational expression holds:

$$\frac{1/b}{1/b_o} \approx \frac{\sigma_t}{\sigma_{to}} = \frac{\sigma_z}{\sigma_{zo}} \tag{13}$$

where $1/b$, σ_t and σ_z at a standard humidity are expressed as $1/b_o$, σ_{to} and σ_{zo}. This leads to the conclusion that the relative value of $1/b$ or σ_t equal the relative value of σ_z. **Figure 9** shows the relationship among the relative strength of the product and PVA film, adsorption potential, and relative humidity. The three lines in the figure indicate the relative values of tensile strength of three kinds of PVA film as opposed to their respective values at a humidity of 50%[7,8]. As for products, we obtained values by interpolating the values at a humidity of 50% and indicated the relative values with regard to the above values. As is evident from this figure, the relative strength of products declines as humidity increases and that this trend almost agrees with that in PVA films. This confirms that Eq. (13) generally holds.

Figure 10 shows the relationship between

σ_{tcal}, calculated on the basis of Eq. (9), and σ_{tobs}. σ_{tobs} consists of (a) the data obtained by converting $1/b$ determined using the indirect method into σ_t using Eq. (11), and (b) the data obtained using the direct method. Calculations based on Eq. (9) require the determination of σ_z accompanying the moisture adsorption of GH20 and NH20. Therefore, this value remained unknown, except when humidity was 50%. We, therefore, determined σ_z in the following sequence:

- GH20 and GH17 or NH20 and NH17 share the same degree of saponification and similar degree of polymerization;
- We therefore assumed that changes in σ_z/σ_{zo} accompanying the moisture adsorption of GH20 and NH20 equal the comparable changes in the case of GH17 and NH17 (**Fig. 9**);
- We then determined σ_z by setting the σ_{zo} of GH20 and NH20 at known 76.6 MPa and 88.3 MPa; and
- As for GL05, we similarly set σ_{zo} at 41.5 MPa and determined σ_z based on the relative strength shown in **Fig. 9**.

To determine α, we used w_C = 0.092, which was employed in our previous report[3]. This figure indicates that $\sigma_{tcal} \approx \sigma_{tobs}$, thus revealing that – as for the crushing strength of a product in a certain humidity – we can simply set σ_z in Eq. (9) at the binder strength at that humidity.

5. Conclusion

We checked spray-dried products for changes in the moisture adsorption characteristics and in the strength due to moisture adsorption and obtained the following results:

(1) The specific surface area of products declined as the amount of added PVA rose;

(2) The amount of water vapor adsorbed on a product equaled the sum of the amount of water vapor adsorbed on the somewhat PVA-covered surface of constituent particles and the amount of water vapor adsorbed by PVA itself; and

(3) The crushing strength of a product in a given humidity can be set at the binder strength derived from strength equation Eq. (9), obtained at that humidity.

Nomenclature

A	:	surface area increased by binder solidified around a contact point	[m^2]
a_{50}	:	median radius obtained from mercury porosimetry	[m]
$1/b$	:	constant in Eq. (10)	[Pa]
C_{ad}, C_b	:	adsorbed and initially added amount of binder to constituent particles, respectively	[–]
C_W	:	solids concentration	[–]
d	:	particle diameter	[m]
G	:	number of contact points per unit mass of spray-dried products	[–]
N	:	number of constituent particles per unit mass	[–]
P, P_o	:	vapor and saturated vapor pessure	[Pa]
P_K	:	compressive pressure	[Pa]
R	:	gas constant	[J/mol K]
S	:	surface area decreased by binder solidified around a contact point	[m^2]
S_V, S_W	:	volume and mass basis specific surface area, respectively	[m^2/m^3] or [m^2/kg]
T	:	temperature	[K]
V	:	apparent volume of powder bed under applied load	[m^3]
V_{ao}	:	initial apparent volume of powder bed	[m^3]
V_∞	:	net volume of powder	[m^3]
v	:	volume of binder solidified around a contact point	[m^3]
W_t, W_s, W_b	:	amount of adsorbed water vapor on the products, constituent particles surface covered to some extent with binder and binder, respectively	[–]
w_C	:	critical moisture content	[–]
α	:	mass ratio of binder remaining in the spray-dried products during drying to unadsorbed binder	[–]
ϵ	:	porosity of a spray-dried products	[–]
ρ, ρ_b, ρ_p	:	density of water, binder and constituent particles, respectively	[kg/m^3]
σ_t	:	crushing strength of single spray-dried products	[Pa]
σ_z	:	tensile strength of binder	[Pa]

References

1) Yamada, N., H. Hirosue, H. Ihara and T. Murayama: *J. Soc. Powder Technol., Japan,* **20**, 211 (1983).

2) Yamada, N., H. Hirosue, E. Abe, N. Ouchiyama and K. Jinnai: *Reports of the Government Industrial Research Institute, Kyushu,* **31**, 2019 (1983).

3) Yamada, N. and H. Hirosue: *J. Soc. Powder Technol., Japan,* **21**, 482 (1984).

4) Tanaka, T.: "Funtai Purosesu Nyumon", p. 62, Kogakutosho (1981).
5) Arai, C., K. Wani, T. Takahashi, H. Segawa and Y. Sano: *J. Soc. Powder Technol., Japan,* **20**, 265 (1983).
6) Kawakita, K., I. Hattori and M. Kishigami: *J. Soc. Powder Technol., Japan,* **11**, 453 (1974).
7) Noro, T.: "Suiyosei Kobunshi", p. 88, Kagaku Kogyosha (1973).
8) Mitarai, T.: Private Communication, Nippon Gosei Kagaku K.K. (1986).

A Coagulation Method for Preparation of Pellet Particles from Polymer Latex†

Hideo Yasui, Wataru Okada, Yasuhiro Miki and Hisashi Morikawa
Engineering Research Laboratory
*Kanegafuchi Chemical Industry Co., Ltd.**

Abstract

A new coagulation method which consists of two stages the generation of seed particles and growth of particles, was developed for the preparation of pellet-like particles from polymer latex.

In this report, first the mechanism of this coagulation was studied through an examination of the coagulating velocity during each stage. Then, the pellet-like particles were characterized by a SEM observation of the inside of a particle and measurement of particle properties.

As a result, experimental equations on the amount of generated seed particles and rate of growth of the particles were obtained. The phenomena in which the latex particles inside the coagulated particle are packed closely by drying and are fused homogeneously by sintering, was confirmed.

1. Introduction

Coagulation is generally conducted, except in some cases of spray drying, when it is necessary to recover solid particles from polymer latex, which is obtained by emulsion polymerization. Polymer latex coagulation, which entails the generation of fine amorphous coagulated bodies, causes many problems; declined productivity in polymer collection, decrease safety, environmental pollution, residual foreign matter and declined workability of molding operations.

To resolve these problems entailed by polymer collection, we developed a method for collecting polymers as high-density pellet particles by generating 1- to 1-mmϕ spherical coagulated particles from polymer latex, which is obtained by emulsion polymerization.

This coagulation method consists of two stages:

(1) A coagulant solution is dispersed within polymer latex to generate speed particles. These seed particles, containing the coagulant in high concentration, are immediately covered with a coagulated layer.

(2) The molecules of coagulant diffuse gradually through the coagulated layer, resulting in lamination of a series of coagulated layers on the surface of each particle. This results in the formation of spherical coagulated particles with latex particles arranged regularly.

The coagulated particles thus generated, when dried, contract and form a more regularly- and densely-packed structure. When held at temperatures exceeding the resin softening temperature (sintering), the resin becomes molten and pressurized and shrinks, finally becoming pellet-type high-density particles with a transparent pearl-like gloss.

This paper studies the mechanism of this new coagulation method through an engineering analysis by dividing the method into two processes: seed particle generation and coagulated particle growth. The paper adopts a two-stage approach:

(1) finding factors promoting the generation of

* 1-8, Miyamae-machi, Takasago-cho, Takasago-shi, 676
TEL. 0794-45-2435

† This report was originally printed in *J. Soc. Powder Technology, Japan*, **24**, 700 ~ 706 (1987) in Japanese, before being translated into English with the permission of the editorial committee of the Soc. Powder Technology, Japan.

seed particles, finding an equation, and describing the concept of this method using a typical example of analysis of the velocity of coagulated particle growth; and

(2) determining the characteristics, such as the internal structure, of dried and sintered particles from coagulated particles.

2. Pelletization mechanism

Polymer latex is stabilized by ion repellency of an interfacial active agent adsorbed to the latex particle surface. The coagulation of such particles is generally dealt with as colloid coagulation. Colloid stability, from the viewpoint of the D.L.V.O. theory, is commonly based on the balance between repulsive potential energy and London-van der Waals' attractive potential energy, both of which appear when an electric double layer[1,2]. Providing the colloid with an electrolyte as a coagulant results in the adsorption of counter-charged ions to the interface, leading to a decline in the Stern Potential, along with a rise in the water-phase ion strength, leading to compression of the electric double layer. When the Stern Potential declines and compression of the electric double layer lowers the interactive potential barrier, colloid particles collide more frequently with one another. This then causes the colloid to cease to be stable and begins to coagulate slowly[3,4]. It then starts coagulating rapidly[5~7] when the Stern Potential drops further and the potential barrier disappears.

The conventional coagulation method consists of homogeneously dispersing a coagulant in polymer latex and increasing coagulant concentration until coagulation occurs, thus coagulating the entire latex. Unlike the conventional method, the new method consists of the following two stages.

The first stage consists of dispersing micro-units (seed particles) or a coagulant in the polymer latex by strong agitation. Seed particles are generated by adding a coagulant to strongly-agitated latex. The coagulation rate is so high that coagulum appears at the same time as the coagulant is added, and then the coagulum is divided and dispersed by strong agitation. Seed particles are therefore not made of the coagulant but congulum containing the coagulant in high concentration. Since these seed particles are coagulum generated by a rapid coagulation process governed by coagulation rate, the seed particles therefore contain latex particles arranged randomly.

In the second stage of the new method, dispersion causes the coagulant contained in these seed particles to seep gradually to the surface. The coagulant becomes larger while coagulating latex particles. That is, the dispersion force transports and resupplies the coagulant to the surface, resulting in the top layer maintaining a certain coagulant concentration equal to or exceeding the concentration required for the startup of coagulation. In order words, coagulated particles grow as a dispersion-velocity-governed system having a coagulant concentration gradient in the direction of the particle radius, while remodeling the particle surface by piling up latex particles on the particle surface. No strong agitation is required in this process. A desirable way is to conduct such gradual agitation that prevents particle precipitation and inhibits particles from colliding and being united. Here, we call randomly-coagulated particles "seed particles" and the subsequent process the "growth of coagulated particles".

3. Material and methods

3. 1 Polymer latex

The latex was made by mixing (A) and (B) described below at a ratio of 2 to 1 and passing the mixture through a 100-mesh sieve. It had a solid content of 33.0%, a specific gravity of 1.01 at 30°C, a surface tension of 58.0 dyne/cm, a viscosity of 9.6 c.p. and a $CaCl_2$ coagulation value of 8.4 m mole-$CaCl_2$/kg. The real specific gravity of the polymer was 1.05.

(A) Polymer latex with a particle diameter of about 0.08 μm made by emulsion-polymerizing monomers of α-methyl styrene 60 PHR, styrene 20 PHR, and acrylonitryl 20 PHR in the presence of emulsifier sodium palmitinate 3 PHR, using paramenthane hydroperoxide 0.6 PHR, by means of redox polymerization startup reaction at 60°C.

(B) Polymer latex with a particle diameter of about 0.18 μm, made by graft-copolymerizing at 60°C
– polybutadiene 70 PHR made by emulsion-polymerizing sodium rosinate 3 PHR and potassium persulfate 0.3 PHR

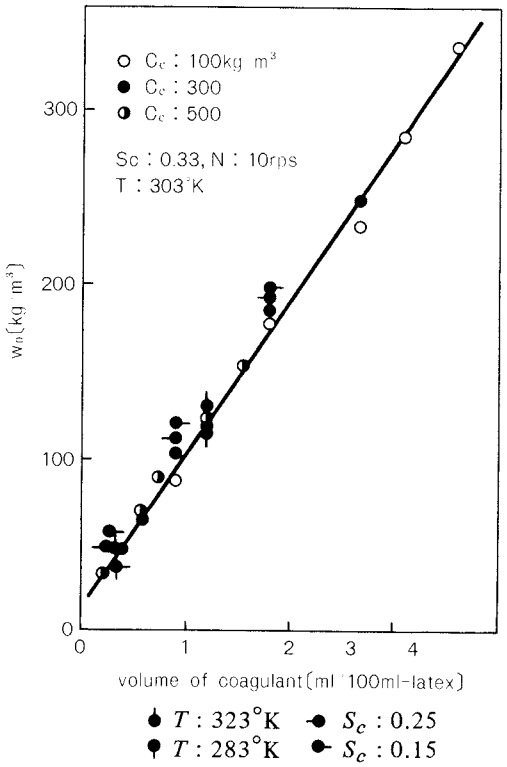

Fig. 1 Effect of volume of coagulant added in latex on the generation of seed particle

at 60°C; with – monomers of styrene 20 PHR and acrylonitryl 10 PHR using paramenthane hydroperoxide 0.5 PHR.

3. 2 Coagulant

A $CaCl_2$ solution made by adjusting a $CaCl_2$ anhydride guaranteed reagent to specified concentration using distilled water.

3. 3 Seed particle generation

As seed particles are generated instantaneously, the quantity of coagulated particles generated 15 sec after adding a coagulant is used as the quantity of seed particles. Since no microparticles appear, the whole quantity of seed particles can easily be separated from latex through a sieve.

We dipped a 500-mℓ beaker containing 300-mℓ latex in a water bath and installed a scraping 3-blade propeller (diameter: 50 mmϕ; d/D= 0.55). While holding the latex at the specified temperature and stirring it with the specified frequency, we added a coagulant using a pipet. Some 15 sec after adding the coagulant, we separated the solid from the liquid using a 100-mesh sieve and weighed the solid content. We used this solid content weight as the quantity of seed particles.

3. 4 Particle growth

To eliminate error due to variable seed particle generation conditions in measuring the speed at which coagulated particles grow, we generated seed particles under constant conditions:

- initial agitation frequency per 15 sec: 600 rpm
- solid content of latex: 33.0%
- latex temperature: 30°C

After seed particles appeared, we lowered the agitation frequency to 200 rpm and held the colloid for a specified time. Then, we immediately divided the colloid into solid and liquid using a 100-mesh sieve and measured the quantity of coagulated particles.

We set the experimental conditions as follows:

- coagulant concentration: 10 ~ 50 w/v%
- coagulant dosage: 0.3 ~ 1.2 mℓ/100 mℓ-Latex
- particle growth time: 2 ~ 10 min

4. Results and discussion

4. 1 Seed particle generation

Figures 1 and 2 show the results of the experiment. **Figure 1** indicates that the quantity of seed particles generated is almost proportional to coagulant dosage regardless of coagu-

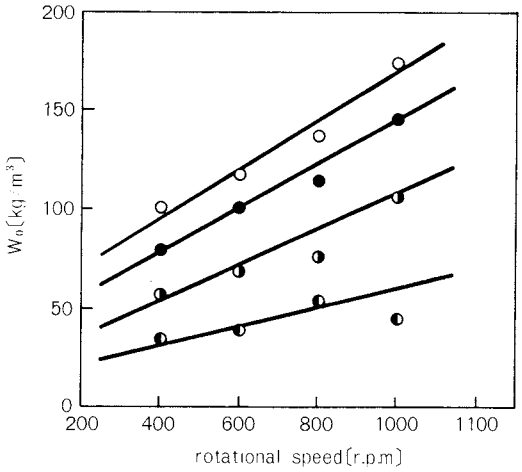

Fig. 2 Effect of rotational speed at the addition of coagulant on the generation of speed particle

lant concentration. **Figure 1** uses the (●) and (◐) symbols to show the results of the experiment with a latex temperature of 10°C and 50°C, respectively. Since latex temperature scarcely affected the results, a straight line could be drawn to approximate the results. Another finding was that the quantity of seed particles increased (◐ and ● marks) as solid content of latex rose. This, we suppose, was because the coagulated seed particles became more fragile as solid content of latex declined, so that coagulated seed particles were divided and increased in number by agitation. **Figure 2**, on the other hand, shows that there was a wider dispersion in data due to latex foaming under high agitation frequency, but the quantity of seed particles generated rose greatly as the agitation frequency increased. This, we suppose, was because agitation dispersed coagulant droplets more finely, resulting in an increase in droplet surface area, leading to a rise in the quantity of random-coagulated particles. **Figures 1** and **2** show that seed particles are generated by instantaneous coagulation, so that such generation is controlled by the condition of dispersion of the coagulant.

Amont W_0 of seed particles in unit volume of latex can be logarithmically expressed with regard to each factor as follows:

$$W_0 = kQ_c^{\alpha} N^{\beta} S_c^{\gamma} \qquad (1)$$

The above enabled us to obtain $\alpha=0.82, \beta=2/3$, $\gamma = -0.45$. The results of all seed particle generation conditions with $Q_c^{0.82} N^{2/3} S_c^{-0.45}$ on the X-axis and quantity of seed particles generated on the Y-axis are plotted in **Fig. 3**. This figure enabled us to determine k = 414.6 and obtain an empirical formula related to seed particle generation.

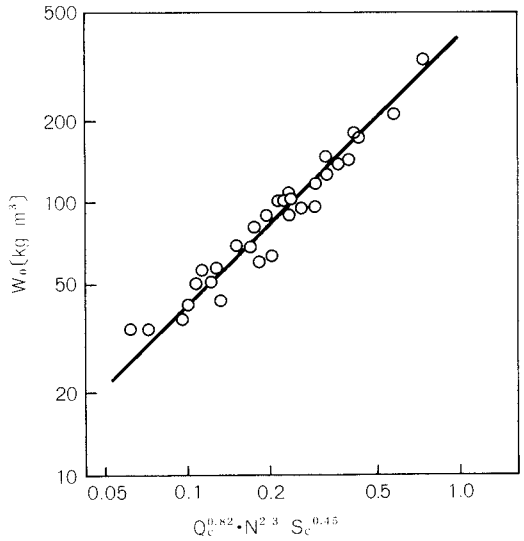

Fig. 3 Correlation for the effect of operational function in Eq. (1) on the generation of seed particle

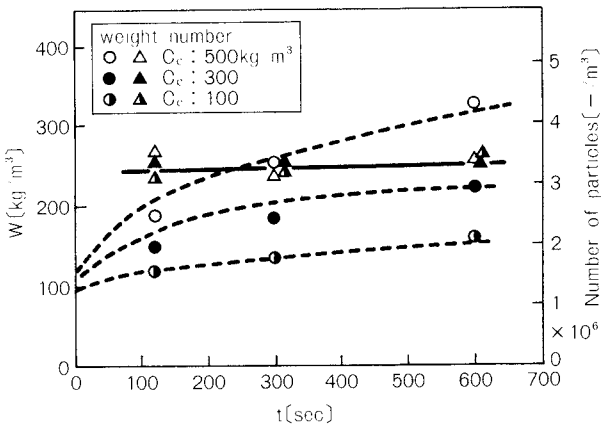

----- is growing line calculated with Eq. (8).
T : 303°K, N : 10 rps, S_c : 0.33, Q_c : 0.012

Fig. 4 Growth of particle and number of particles with time

4. 2 Growth of coagulated particles

Figure 4 plots how the coagulated particles grew with a coagulant dosage of 1.2mℓ/100mℓ-Latex. This figure shows a decline in particle growth rate with time. This, we suppose, was because of a decrease in the coagulant content (which is the driving force behind the mass transfer) of particles as the coagulant was diffused out of the particles. The growth speed of coagulated particles presumably depends on the mass transfer rate of the coagulant in the direction of particle radius, because the coagulation rate is much higher than the dispersion rate.

When particle growth slowed down, particles were separated from one another, which enabled us to count them. **Figure 4** shows that the number of particles remaining constant two or more minutes afterwards and that the particles were almost spherical and uniform in diameter. This led to the assumption that the number of particles remained constant after generation of seed particles. Particle growth rate can therefore be expressed as follows:

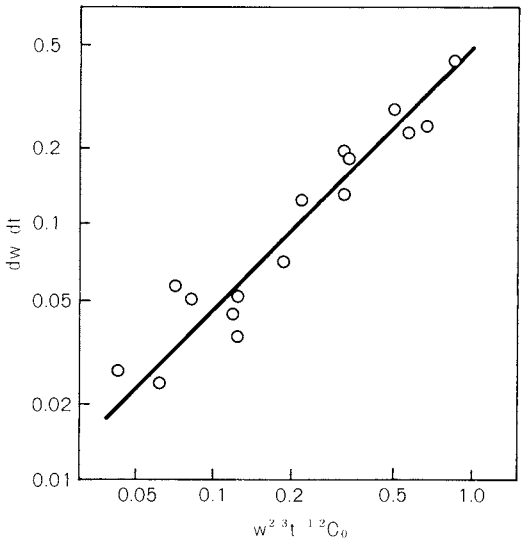

Fig. 5 Correlation for the effect of operational function in Eq. (5) on the growing rate of particle

$$dW/dt = KN_A(t)A \tag{2}$$

We assume that coagulated particles were spherical and a coagulant concentration gradient exists only in the perpendicular direction to the particle surface. By using the one-dimensional diffusion equation in the non-steady state (Higbie's permeation theory[8]) which is driven by the concentration C_0 ($= C_s/W$) of coagulant in particles and the difference ($C_0 - C^*$) in concentration between the inside and the surface of the particle, and by setting particle density and diffusion coefficient as constants, we can determine the mass flux N_A of coagulant inside particles as follows:

$$N_A(t) \propto (C_0 - C^*)/\sqrt{t} \tag{3}$$

Here, C_0 is 80~440 m mole-$CaCl_2$/kg, while C^* is near the coagulation value 8.4 m mole-$CaCl_2$/kg, so that $C_0 \gg C^*$. C_0 can, therefore, represent the term of the driving force due to difference of concentration. On the other hand, the total surface area of particles A is

$$A \propto W^{2/3} \tag{4}$$

so that Eq. (2) can be expressed as:

$$dW/dt = at^{-1/2} C_0 W^{2/3} \tag{5}$$

The value a is the product of the constants and factors from Eqs. (2), (3) and (4), so that it remains constant in the same experiment. We arranged the experiment results in order by using Eq. (5) as a model equation for particle growth rate.

We determined particle growth rate dW/dt by measuring the inclination of the time course of the quantity of the coagulated particles at various experimental conditions.

Figure 5 plots the particle growth rate dW/dt and $t^{-1/2} C_0 W^{2/3}$, which is the right side of Eq. (5). The inclination of the straight line in this figure enabled us to obtain $a = 0.476$ [$mol^{-1} \cdot kg^{4/3} \cdot m^{-1} \cdot s^{-1/2}$].

From $C_0 = C_s/W$ and Eq. (5), we obtain

$$dW/dt = 0.476 t^{-1/2} C_s W^{-1/3} \tag{6}$$

Since C_s is a constant referring to the amount of coagulant added in unit volume of latex, Eq. (5) becomes:

$$\int 1/W^{-1/3}\, dW = K_0 \int t^{-1/2}\, dt + C \tag{7}$$

where $K_0 = 0.476 C_s$ [$kg^{4/3} \cdot m^{-4} \cdot s^{-1/2}$] and C is an integral constant. The resulting equation is:

$$W = (8/3 K_0 t^{1/2} + b)^{3/4} \tag{8}$$

Constant b is determined based on initial particle concentration at the time of $t = 0$ and can be expressed as $b = W_0^{4/3}$.

In **Fig. 4** broken lines show changes in the quantity of coagulated particles with time on the basis of Eq. (8), where a concentration of coagulant added is 10, 30 and 50% and an amount of coagulant added in unit volume of latex is 1.2mℓ/100mℓ-Latex. This figure shows good agreement between experimental and calculated values, which led us to conclude that the growth rate of coagulated particles can be outlined using model equation Eq. (5).

5. Dried and sintered particles

Coagulated particles generated using this coagulation method is sieved and separated from latex, washed with water, and dried at temperatures lower than the resin softening temperature. These particles are then held at temperatures exceeding the resin softening temperature to obtain sintered particles.

At temperatures lower than the resin softening temperature, latex particles are not fused with one another. Drying and resulting water evaporation from coagulated particles, therefore, led to the close packing with latex particles and a shrinkage of coagulated particles.

Sintering melts the latex particles, resulting in a removal of gaps among them and a further shrinkage of the particles.

Figure 6 (a) and **(b)** give optical micrographs of dried and sintered particles. Dried particles have latex particles not fused with one another and having gaps among them. This microscopically porous structure gives these particles an egg-like appearance. Sintered particles, on the other hand, have latex particles fused with one another, resulting in a transparent, pearl-like appearance.

5. 1 Dried particles

Figure 7 (a), **(b)** and **(c)** give scanning electron micrographs (SEMs) of the inside of dried particles. **Figure 7 (a)** shows a general view of a particle, with traces of a seed particle in its center. Random coagulation in the center of the particle occurred when coagulated seed particles were generated in rapid coagulation. **(b)** gives a magnified photo of the border of the random-packed zone. **(c)** and **(d)** show magnified views of the random-packed zone in the center of the particle and closed-packing zone around it, respectively. The random-packed zone has many gaps among latex particles, while the closed-packed zone (generated at the time of particle growth) have latex particles tightly packed. Drying does not cause the random-packed zone to shrink enough, thus they cannot be tightly packed. The tight packing of the inside of a particle requires regular arrangement of latex particles at the time of growth. By observing that particles, when divided, are affected (strong cleavage) in a certain direction and on a certain face and that the regular arrangement of particles results in a formation of distinct layer-like steps, we can confirm that water evaporation leads to more regular arrangement of particles.

Figure 8 indicates the porosity of dried particles measured by an Hg porosimeter. The diameters of pores in a particle are distributed very equally and peak at about 0.05 μm. The cumulative intrusion volume is less than 0.45, rather small despite the particle having a random-packed zone in its core. This corresponds to the fact that a 3-mmϕ dried particle has a concentration of as high as 0.598 g/cm^3 and a bulk density of as high as 0.43. Dried particles are characterized by the fact that the latex particles, of which they are made, are not fused with one another, and as a result, can be readily re-dispersed into latex particles by crushing. This characteristic provides a great advantage in preparing ultra-microparticles and particulate dispersants.

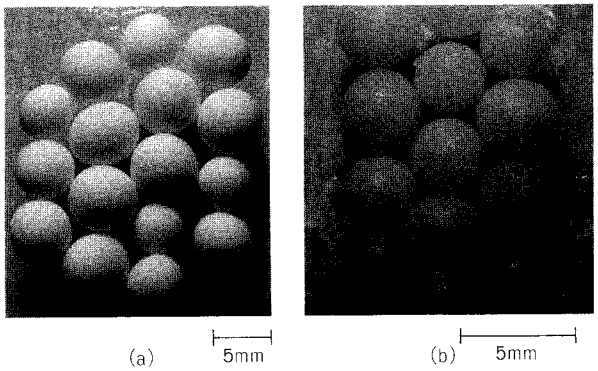

Fig. 6 Photograph of pellet particles by optical microscope
(a) dried particles
(b) sintered particles

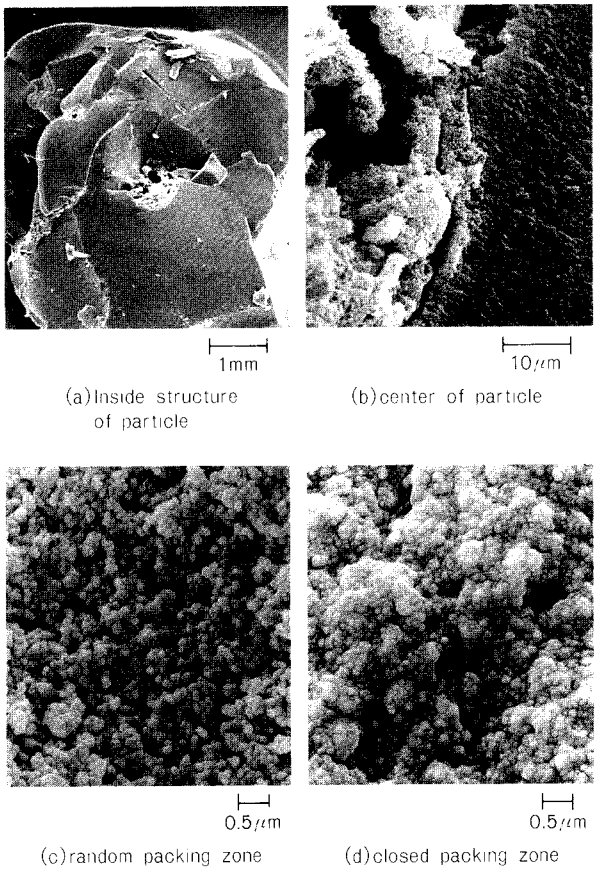

Fig. 7 Photographs of inside dried particle by a scanning electron microscope

5. 2 Sintered particles

Figure 9 (a), (b) and **(c)** given SEMs of the inside of a sintered particle as dipped in liquid nitrogen and divided. Since the softening temperature (HDT: ASTM D-648) of this polymer is 110°C, we sintered this particle by keeping it in an oven at 130°C for 20 min. **Figures (a)** and **(b)** indicate step-like regularly-arranged stripes generated when the particle was divided. This, we suppose, is because the latex particles, regularly arranged already in a cross section of a dried particle, shrunk further and became much more regularly arranged. **Figure (c)** gives a magnified photo of the above section. Although the inside of the particle is macroscopically homogeneous, it microscopically has a network-like structure having voids with similar diameters to those of latex particles. **Figure 10 (a), (b)** and **(c)** show SEMs, with the same magnifying powers as those used for **Fig. 9**, of cross sections of molten pellets made from the above polymer using an extrusion molder (pelletizer with a molding temperature of 242°C). **Figures 9** and **10** resemble each other greatly in internal structure. Microscopically, sintered particles are slightly more tightly packed than molten pellets. The compact structure such as a molten body prepared with a large amount of

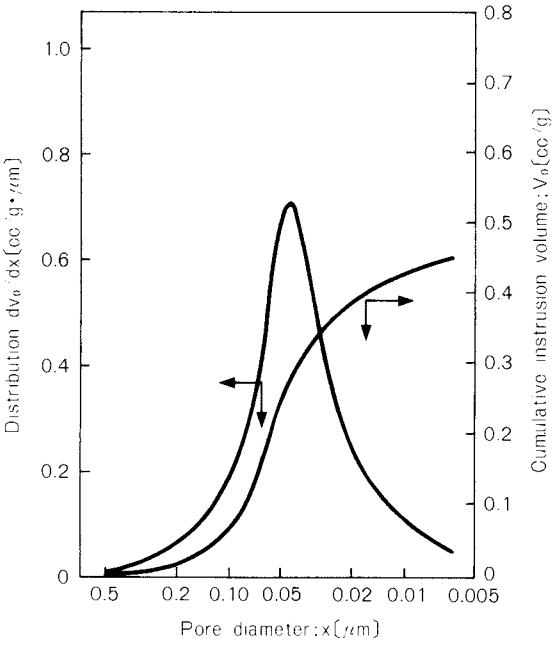

Fig. 8 Porosity measured by Hg porosimeter

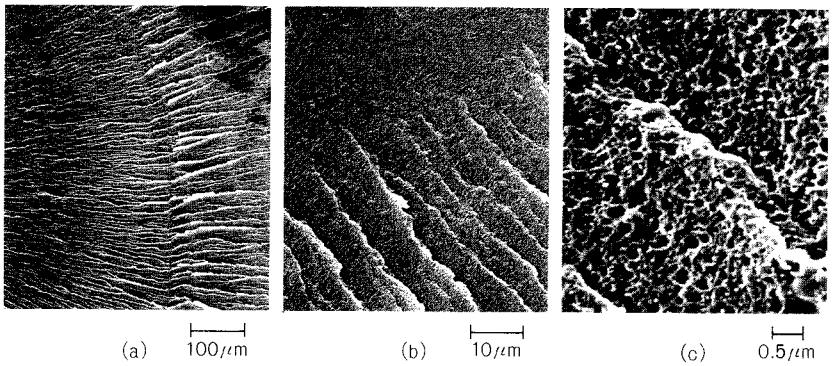

Fig. 9 Photographs of inside sintered particle by a scanning electron microscope

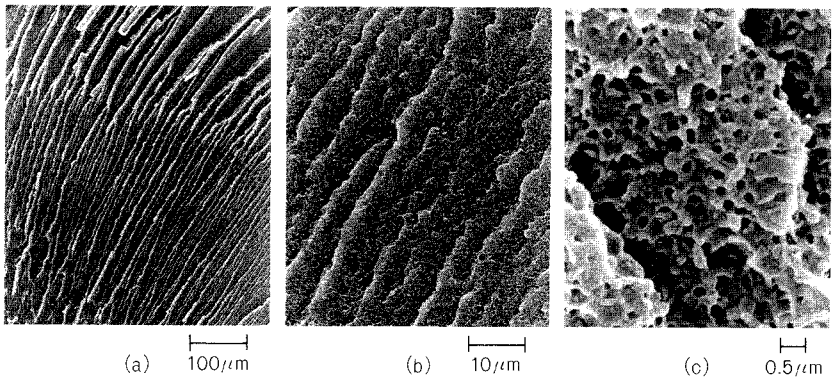

Fig. 10 Photographs of inside pellet, prepared by a pelletizer, with a scanning electron microscope

energy, is obtained with a small amount of low temperature energy in the case of sintering coagulated particles. A cylindrical molten pellet (having the same volume as a 3-mmϕ sphere) and a 3-mmϕ sintered particle have bulk densities of 0.61 and 0.62 and particle concentration of 0.968 and 0.962 g/cm^3, respectively. We can, thus, regard sintered particles as equivalently tightly-packed to molten pellets.

6. Conclusion

Concerning a new coagulation method of collecting pellet-like particles from polymer latex, we estimated the mechanism for the formation of coagulated particles through an engineering analysis and characterized resulting particles in terms of their inner structure.

The particle formation mechanism needs further detailed investigation. To present its concept, however, we divided particle generation rate – as a typical analysis – into seed particle generation and coagulated particle growth, and formulated each of them.

(1) At the time of seed particle generation, we formulated the quantity of particles generated as follows as a function of the amount of coagulant added in unit volume of latex, agitation frequency and latex concentration.

$$W_0 = 414.6 Q_c^{0.82} N^{2/3} S_c^{-0.45}$$

(2) We formulated coagulated particle growth as follows by modeling it based on the one-dimensional diffusion equation in the non-steady state of spherical particles.

$$W = (8/3 K_0 t^{1/2} + W_0^{4/3})^{3/4}$$

where K_0 is a constant resulting from initial amount of coagulant added in unit volume of latex,

$$K_0 = 0.476 C_s$$

Measurements of coagulated particle growth with time corresponded well to the above calculation results.

The second part of this paper describes the inner structure of pellet-like particles obtained using this coagulation method. A desired size of spherical particle can be prepared by selecting a specific condition for coagulation. Furthermore, this coagulated particle can be readily converted into a most-tightly-packed dried particle with its latex particles not fused with one another and having a microscopically porous structure by drying, or into a high-density sintered particle with the same structure as that of molten pellets created by an extrusion molder by sintering.

Even the most recent series of technological developments have not yet succeeded in decreasing fine particles, which makes them hard to handle, of polymers recovered from polymer latex. This defect causes many technical problems in productivity and process efficiency in industrial production and molding operations, and furthermore, a decline in product quality. Our proposed coagulation method can easily obtain dried and sintered particles of desired sizes directly from polymer latex. It is, therefore, expected to give a powerful solution to the most serious technical problems related to the emulsion polymerization.

Acknowledgments

We wish to thank Prof. Yoshio Harano of Osaka City University, and Dr. Yoshio Aoyama of Crystal Engineering Co., Ltd. for their kind and very beneficial advice during the development of our coagulation method.

Nomenclature

A	:	surface area of particle generated in unit volume of latex	[m^{-1}]
a	:	constant in Eq. (5)	[kg$^{4/3}$·mol^{-1}·m^{-1}·s$^{-1/2}$]
b	:	constant in Eq. (8)	[kg$^{4/3}$·m^{-4}]
C_0	:	concentration of coagulant in particle	[mol·kg^{-1}]
C_c	:	concentration of coagulant solution	[kg·m^{-3}]
C_s	:	amount of coagulant added in unit volume of latex	[mol·m^{-3}]
C^*	:	concentration of coagulant at surface of particle	[mol·kg^{-1}]
K	:	coagulatable amount of latex per unit amount of coagulant	[kg·mol^{-1}]
k	:	constant in Eq. (1)	[–]
N	:	rotational speed	[s^{-1}]
N_A	:	mass flux of coagulant inside particle	[mol/m^{-2}·s^{-1}]
Q_c	:	volume of coagulant added in unit volume of latex	[–]
S_c	:	solid concentration of latex	[–]
t	:	time	[s]
W_0	:	amount of seed particle in unit volume of latex	[kg·m^{-3}]
W	:	amount of particles in unit volume of latex	[kg·m^{-3}]
α,β,γ	:	constants in Eq. (1)	[–]

References

1) Verwey, E.J. and J.Th. G. Overbeek: "Theory of Stability of Lyophobic Colloids," Elsevier (1948).
2) Derjaguin, B. and L. Landau: *Acta Physicochem.*, **14**, 633 (1941).
3) Fuchs, N.: *Z. Physik.*, **89**, 736 (1934).
4) Otterwill, R.H.: *Diss. of Farady Soc.*, **42**, 154 (1966).
5) Levich, V.G.: "Physicochemical Hydrodynamics," Prentice Hall (1962).
6) Smoluchowski, M. von: *Z. Physik, Chem.*, **92**, 129 (1917).
7) Watanabe, A.: *Polarography*, **10**, 175 (1962).
8) Higbie, R.: *Transaction of American Institute of Chemical Engineer*, **36**, 365 (1935).

Formation of Silicon Nitride Whiskers from Rice Hulls†

Yasunari Kaneko, Kei Ameyama and Hiromichi Iwasaki
Faculty of Science and Engineering
*Ritsumeikan University**

Abstract

The formation of Si_3N_4 whiskers from rice hulls was studied. Si_3N_4 whiskers were synthesized by nitridation of SiO_2-C system in N_2-gas flows at 1400 and 1450°C. The shape and microstructure of the whiskers were SEM and TEM inspected. The whiskers of a cylindrical shape grew along the $<10\bar{1}1>$ direction without any defects. The phase of the whiskers was of the α-type and their diameter and length were 0.1 ~ 0.5 μm and 300 ~ 1800 μm, respectively. A droplet of Fe-Si system was found at the tip of the whiskers. It is suggested that the VLS mechanism controls the growth of the whiskers.

1. Introduction

Reinforcing fibers for fiber-reinforced metals (FRMs) and fiber-reinforced ceramics (FRCs), which are attracting public attention as next-generation structural materials, include whiskers, stapes (which consist of polycrystal or amorphous materials) and continuous fibers. Commercially available are SiC, Si_3N_4, $K_2O \cdot 6TiO_2$ and other ceramics whiskers. In comparison, many research reports have been released on composite materials using SiC whiskers[1)~6)]. Inoue *et al.* reported the issue and forecast of ceramics reinforcement by ceramics whiskers[7)].

Rice hulls, which are an agricultural waste product, contain 13 ~ 29% ash[8)] depending on the place of origin. The ash contains more than 90% amorphous silica, so that the issue of recycling this ash is attracting a great deal of public attention. Reports have already been released on the formation of SiC powder[9)] and whiskers[10)] from rice hulls. As for the synthesis of Si_3N_4 whiskers, a few typical patents[11)~13)] have been introduced but no report has been released.

Si_3N_4 whiskers can be manufactured by the gas, liquid, or solid phase method, each of which has its advantages and disadvantages. The solid and gas phase methods are used for industrial purposes. The solid phase method consists of making SiO_2 react on N_2 gas on a graphite baffle to form Si_3N_4 whiskers.

Saito *et al.* studied the formation of Si_3N_4 whiskers using the solid phase method employing an SiO_2-C-fluorine-base material to examine reaction temperature and effect of additives[14),15)].

This paper reports on the formation of Si_3N_4 whiskers from rice hulls using the solid phase method and the results of microstructural observations.

2. Experiment

2. 1 Rice hulls

We used rice hulls produced in Ibogawa-cho, Ibo-gun, Hyogo Prefecture, Japan. The ash content remains almost the same for all Japanese-made rice hulls. **Table 1** shows the chemical composition of ash in rice hulls reported by Kai[16)]. We, therefore, did not conduct a chemical analysis of ash.

2. 2 Experiment procedure

A flowchart of the experiment is shown in **Fig. 1**. For acid treatment, we used 20 mℓ of

* 56-1, Tojiinkita-machi, Kita-ku, Kyoto-shi, 603
TEL. 075-465-1111

† This report was originally printed in *J. Soc. Material Science, Japan*, **37**, 65-69 (1988) in Japanese, before being translated into English with the permission of the editorial committee of the Soc. Material Science, Japan.

Table 1 Chemical composition of ash.[16]

	wt%
SiO_2	95.0
P_2O_5	2.0
K_2O	1.0
CaO	1.0
Na_2O Fe_2O_3 MgO	1.0

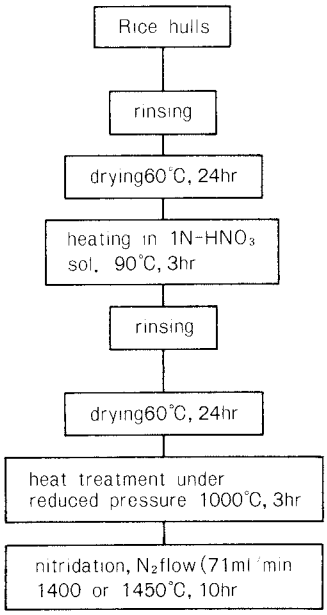

Fig. 1 Flowchart

1N nitric acid for 1 g of rice hulls. This treatment aimed at removing loose organic matter and alkali content. For reduced-pressure firing, we put rice hulls into a screw-equipped tube-shaped carbon container (10 mm outside diameter, 8 mm inner diameter, 100 mm length) and heated it in a 130 Pa electric furnace at the specified temperature for a specified time.

Figure 2 illustrates how the nitriding device is composed. The carbon plate shown in the figure has many 0.5-mm-diameter holes to allow gas to pass easily. The device was fixed in the electric furnace via a carbon pipe (50 mm inner diameter, 65 mm outer diameter). Portions A, B and C are in the furnace. Most of portions A and B are in the equal temperature part of the furnace. In an N_2 flow (71 mℓ/min), we treated the rice hulls at 1,400 and 1,450°C for 10 hours. After this heating, we allowed them to cool. At 300°C, we stopped supplying N_2 gas and, at around room temperature, took the product out.

2. 3 X-ray diffraction

We conducted X-ray diffraction using the powder method to examine the structure of the specimen. The X-ray diffraction device used was a Rotorflex RAD-200B manufactured by Rigaku Denki K.K. We used CuKα as the target and performed measurements at 40 kV and 20 mA.

2. 4 Electron microscopic observation

To observe the microstructure of synthesized whiskers, we used JEOL Ltd.'s scanning electron microscope (SEM) JSM-T20 and JEOL Ltd.'s transmission electron microscope (TEM) JEM-2000FX.

2. 5 Infrared absorption spectrum

We measured the infrared absorption spectrum using KBr tablets and Nippon Bunko's infrared spectrophotometer IR-G. Some 500 mg of KBr was used for 1 mg of the specimen.

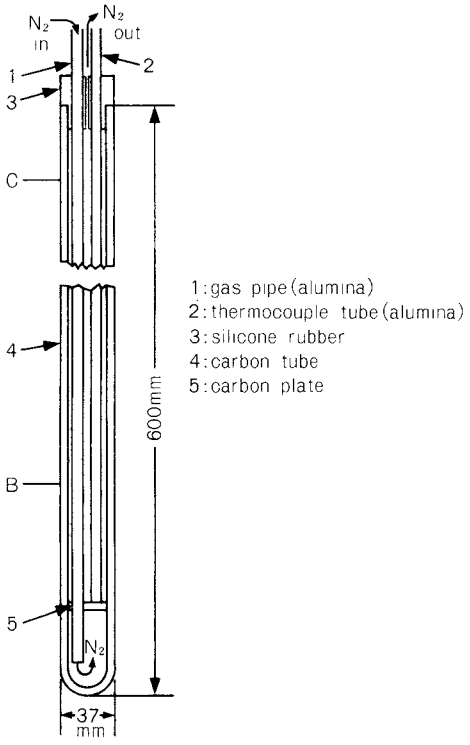

Fig. 2 Schematic diagram of the apparatus

3. Result and discussion

This experiment aims to set up a way to recycle carbon generated by reduced-pressure firing for such reactions as those formulated below in synthesizing Si_3N_4 whiskers. This method is called the silica reduction method.

$$3SiO_2 + 6C + 2N_2 = Si_3N_4 + 6CO \quad (1)$$

$$SiO_2 + C = SiO + CO \quad (2)$$

$$3SiO + 3C + 2N_2 = Si_3N_4 + 3CO \quad (3)$$

After firing acid-treated rice hulls in a 1,300°C atmosphere for 3 hrs, white powder remained. This was identified as α-cristobolite by X-ray diffraction. This firing process reduced the weight of the rice hulls to about 80%. Since firing acid-treated rice hulls at 1,000°C under reduced pressure for 3 hrs reduced the specimen weight to about 68%, we found more than 10% of the carbon residual. Since formula (1) is a full-reaction formula related to the formation of Si_3N_4, the carbon content necessary for reaction is procured by reduced-pressure firing. After the reaction, the unprocessed carbon content can be easily removed by firing it in a 700°C atmosphere for 3 hrs.

Fig. 3 IR spectra of rice hulls which was heated in 1N HNO_3 solution or under reduced pressure

A : Heat treatment in $INHNO_3$ solution.
B : Heat treatment under reduced pressure.

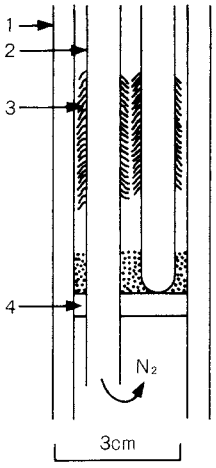

Fig. 4 Schematic diagram of the region where whiskers formed

Figure 3 indicates the infrared absorption spectra of acid-treated rice hulls and reduced-pressure fired rice hulls in the 1,400~400 cm^{-1}. The main absorption peak of acid-treated rice hulls, in general, almost corresponds to the spectrum of quartz glass, although the peak covers a slightly wider region than that of rice hulls fired under reduced pressure. This confirms the fact that silica was already present in the specimen as rice hulls. In a preliminary experiment, on the other hand, we found that reduced-pressure firing was suitable for whisker formation. This firing process, we believe, promotes the reaction of SiO_2 with C.

Figure 4 gives an enlarged view of the region where whiskers formed. Some 1.5 g of rice hulls fired under reduced pressure was placed on a porous carbon plate. After reaction, we found white cotton-like product adhered to the

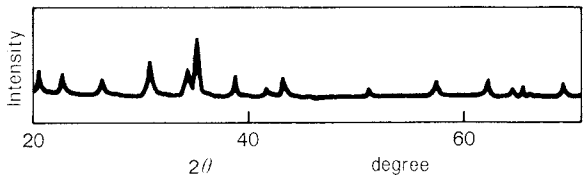

Fig. 5 X-ray diffraction pattern of whiskers

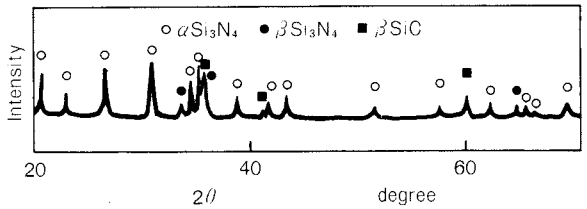

Fig. 6 X-ray diffraction pattern of products on a carbon plate

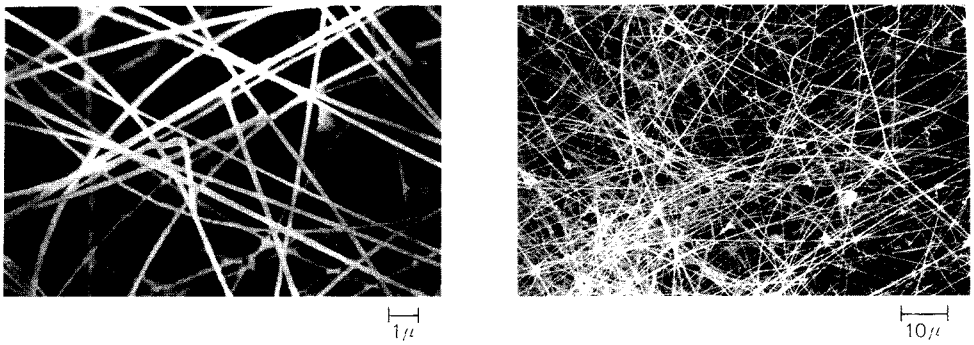

Fig. 7 Scanning electron micrographs (SEMs) of whiskers formed at 1400°C

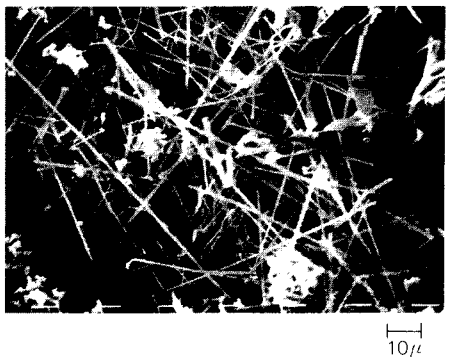

Fig. 8 Scanning electron micrograph (SEM) of the products on a carbon plate

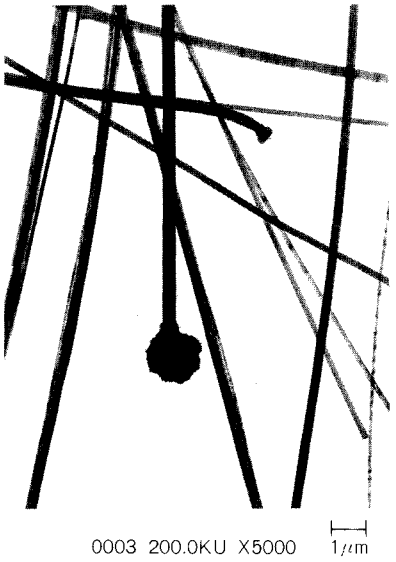

Fig. 9 Transmission electron micrograph (TEM) of whiskers formed at 1400°C

alumina protective tube and gas pipe. The X-ray diffraction pattern of this cotton-like matter is shown in **Fig. 5**. No peak is seen other than that of α-Si_3N_4. **Figure 6** shows the X-ray diffraction pattern of the product left on the carbon plate. This shows the peaks of α-Si_3N_4, β-Si_3N_4, and β-SiC.

β-SiC, we believe, forms as a result of the reaction of SiO generated as in formula (2) with CO, as indicated in the formula below.

$$SiO + CO \longrightarrow SiC + CO_2 \qquad (4)$$

We put β-SiC 1 g into the device and allowed it to react with a 71 mℓ/min flow of nitrogen gas at 1,400°C. The X-ray diffraction of this material after reaction proved the formation of α-Si_3N_4 and β-Si_3N_4. We, therefore, believe that some of the generated SiC changes into Si_3N_4.

A reaction temperature of 1,400°C and a nitrogen gas flow of 40 mℓ/min produce only a small amount of cotton-like matter. A reaction temperature of 1,350°C and a gas flow of 71 mℓ/min produces no cotton-like matter. The X-ray diffraction pattern shows the peaks of α-Si_3N_4 and β-SiC.

The 1,400°C reaction produced about 0.15 g of cotton-like whiskers and about 0.35 g of α-Si_3N_4, β-Si_3N_4 and β-SiC on the carbon plate. If the entire quantity of SiO generated according to formula (2) contributed to the formation of whiskers and β-SiC, we could have obtained about 0.8g of product. However, in fact, we got only about 0.5 g of product indicating that about 40% of SiO had volatilized. **Figure 7** shows SEMs of whiskers formed at 1,400°C. Here, we find the whisker diameters rather equal and scarcely any branching. The whisker lengths were 300 ~ 1,800 μm and their diameters were 0.1 ~ 0.5 μm.

Figure 8 gives a SEM of a product on the carbon plate. The whisker lengths were in the

10 ~ 200 μm range, shorter than in **Fig. 7**, and their diameters were in the 0.2 ~ 2 μm range, larger than in **Fig. 7**. We also found some groups of whiskers about 10 μm long and 0.2 μm in diameter.

Similar observations of whiskers formed at 1,450°C showed no considerable difference with those formed at 1,400°C.

Figure 9 shows a TEM of whiskers formed at 1,400°C. Striped patterns inside the whiskers moved as the specimen was inclined, and showed no twin planes or other defects. The whiskers obtained here, therefore, are believed to have very low defect density. We also found about 1.5-μm-diameter droplets adhered to the tip of the whiskers. These droplets can be seen in a large quantity but can be dropped out very easily.

Figure 10 gives an EDAX analysis of a whisker and droplet. These spectra show the copper content, because a copper mesh was used in measurements. The droplets have an Fe-Si base, which melt at about 1,200°C. These conditions lead us to believe that the droplets were molten at the reaction temperature. The droplets contained small quantities of Ni, Co, and Cr, which stemmed from the soil and whose distribution pattern varies according to the place of origin.

The above findings lead us to conclude that whisker growth is controlled by the VLS mechanism in which, at the time of reaction, the molten Fe-Si body absorbs gases, including SiO, CO, and N_2, and becomes oversaturated. Trace analyses of electron beam diffraction images of whiskers showed that whiskers grow in the $< 10\bar{1}1 >$ direction. This result corresponds to that reported by Sasaki *et al.*[18] and Saito *et al.*[14]. TEMs of whiskers formed at 1,450°C showed no great difference from those formed at 1,400°C.

Improvements to be made in the future include the scaling-up or other modifications of the reaction device to further increase the yield. Another inconvenience lies in the tensile strength of whiskers, when they are used as composite materials. Katsuki *et al.* installed a tensile device in a SEM to perform strength measurements[19]. We are, therefore, planning to make some improvements in the device for strength measurements. Another thing we would like to study is ways to form β-Si_3N_4 whiskers, which are currently being spotlighted.

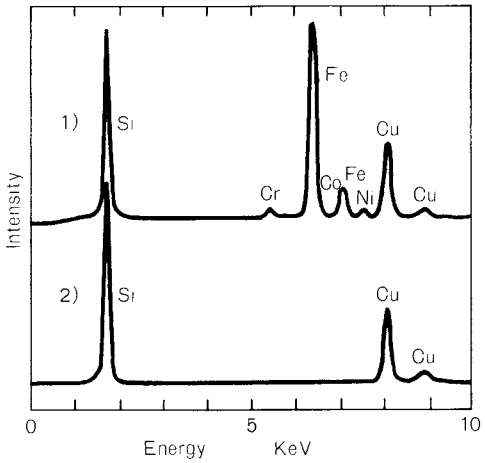

Fig. 10 EDAX analysis of whiskers and droplets

4. Conclusion

We fired rice hulls (treated with 1N nitric acid) under reduced pressure at 1,000°C for 3 hours. The resulting product was nitrided at 1,400 and 1,450°C with a nitrogen flow of 71 mℓ/min for 10 hours. X-ray diffraction, along with SEMs and TEMs revealed the following:

(1) Whisker phase was of the α-type.
(2) Whiskers measured 0.1 ~ 0.5 μm in diameter and 300 ~ 1,800 μm in length.
(3) Whiskers were cylindrical in shape with little branching and showed scarcely any inner defects.
(4) Whiskers were tipped with Fe-Si-based droplets. This led us to conclude that whisker growth is controlled by the VLS mechanism.
(5) Whiskers grew in the $< 10\bar{1}1 >$ direction.

Acknowledgments

We wish to acknowledge the assistance of Mr. Yasuhisa Okashita and Masanori Kimura of the Chemistry Department, the Faculty of Science and Engineering, Ritsumeikan University in carrying out this research. We also wish to express our appreciation to Mr. Teruhiko Inaba of the Metal Division of the Hyogo Prefectural Industrial Laboratory who assisted in electron micrographs.

References

1) Fukunaga, H., K. Gohda and N. Tabata: *J. Soc. Materials, Japan*, **34**, 64 (1985).

2) Becher, P.F., and G.C. Wei: *J. Am. Ceram. Soc.*, **67**, C-267 (1984).
3) Ueno, K., and Y. Okehata: *Yogyo Kyokaishi,* **91**, 491 (1983).
4) Inoue, S., K. Niihara, T. Uchiyama and T. Hirai: Proc. of 2nd Int. Symp. on Ceramic Materials and Components for Engines, p. 609 (1986).
5) Ueno, K. and S. Sodeoka: *Yogyo Kyokaishi,* **94**, 981 (1986).
6) Asanuma, H., K. Hirohashi and E. Kawai: *Nippon Sosei Kakou Gakkaishi,* **27**, 1191 (1986).
7) Inoue, S., T. Uchiyama and K. Niihara: *Ceramics,* **21**, 621 (1986).
8) D.F. Houston: "Rice Hulls", p. 301 (1972), American Association of Cereal Chemist, Inc.
9) Lee, J.G. and I.B. Cultler: *Am. Ceram. Soc. Bull.*, **54**, 195 (1975).
10) Sharma, N.K., W.S. Wiliams and A. Zangvil: *J. Am. Ceram. Soc.,* **67**, 715 (1984).
11) Japan Patent: "Tokukaishow" 57-196711.
12) Japan Patent: ibid., 58-3964.
13) Japan Patent: ibid., 59-102900.
14) Saito, H., T. Hayashi and K. Miura: *Nippon Kagaku Kaishi*, 1371 (1981).
15) Saito, H., T. Hayashi and K. Miura: ibid., 401 (1982).
16) Y. Kai: *Kagaku to Kogyo,* **39**, 972 (1986).
17) Yanagase, T., and Y. Suginohara: *J. Japan Institute Metals,* **33**, 443 (1969).
18) Sasaki, K., K. Kuroda and T. Imura: *Yogyo Kyokaishi,* **94**, 773 (1986).
19) Katsuki, H., M. Egashira, H. Iwanaga and M. Kanda: The preprint of the 25th technical discussion in Ceramics, p.15 (1987).

Simulation of a Maximum Storage Amount of Coal for Preventing Spontaneous Combustion and Degradation in Quality†

Hiroshi Takahashi, Eiji Obata and Takao Takeuchi
Department of Chemical Engineering
*Muroran Institute of Technology**

Tatsuo Tanaka
Department of Chemical Process Engineering
*Hokkaido University***

Abstract

The temperature rise curve due to the natural oxidation of a coal deposit was numerically simulated for a coal bed having a 'spherical' geometry. The maximum temperature occurred at the center of the bed when oxygen was fully supplied within the bed and near the surface when oxygen decreased due to the process of the reaction. The rate of temperature rise was significantly affected by the activation energy and frequency factor of the coal. Furthermore, the measurement of the moisture adsorbed on the oxidized coal samples showed that the loss in mass due to oxidation increased remarkably at temperatures above 120°C. In assuming the limiting temperature in coal storage to be 120°C, a maximum allowable amount of coal storage was estimated for various kinds of coal under the conditions of neither spontaneous combustion nor significant loss in mass.

1. Introduction

The problems faced in long-term coal storage include quality degradation due to natural oxidation and spontaneous combustion due to heat accumulation and temperature rise. The degree of heat accumulation in coal depends on physical factors, including the coal storage method, coal storage quantity, coal particle size and ambient temperature, along with the reactivity of coal. If the heating velocity of the inside of the coal surpasses the speed at which it radiates heat into the atmosphere, oxidation speed rises gradually as the coal layer temperature climbs until it reaches ignition temperature, leading to spontaneous combustion. In coal storage, therefore, there is a maximum allowable coal storage size depending on heat income and outcome. Previous studies concerning the spontaneous combustion of coal dealt with powdered coal inside a coal mine, coal crusher or similar environment with emphasis put on estimating the ignition conditions for the sake of security[1,3,5,7]. However, considering that the basic composition of coal and its content ratio of oxygen and other matter of the functional group change gradually due to oxidation even at lower temperatures than the ignition temperature[10], we believe it important to design such large-capacity coal storage equipment that prevents mass loss and quality degradation as well as spontaneous combustion. This paper aims to evaluate the maximum allowable storage amount (maximum critical size) that satisfies the above requirements. More specifically, this paper aims to evaluate the maximum storage amount by:

- allowing for the effect of coal particle diameter, oxygen density and coal reactivity on heat accumulation and temperature rise; and

* 27-1, Mizumoto-cho, Muroranshi, 050
TEL. 0143-44-4181

** Nishi, 8-chome, Kita-13-jo, Kita-ku, Sapporo-shi, 060
TEL. 011-711-2111

† This report was originally printed in *J. Soc. Powder Technology, Japan*, **25**, 437-442 (1988) in Japanese, before being translated into English with the permission of the editorial committee of the Soc. Powder Technology, Japan.

- empirically studying the relationship between oxidation and mass loss.

2. Theory

2. 1 Basic equations expressing a temperature rise

The shape of coal deposits depends on the coal storage method. Solving the heat balance equations and material balance equations of some shapes of coal deposits are very difficult. This paper excludes factors related to the shape of deposits and assumes the simplest shape: spherical deposits. Sphere diameter, we believe, gives rough guidelines for determining silo diameter and storage height in the case of a silo storage method, and for determining storage height in the case of an outdoor storage method.

On the assumptions listed below, the temperature rise process of a spherical body can be expressed as in Eqs. (1) ~ (3).

Assumption 1) Coal and its ambient gas share the same temperature.

2) Heat and mass transfers due to convection are neglected. Heat is transferred by conduction and radiation, while oxygen is transferred by molecular diffusion.

3) Moisture transfer and resulting heat transfer are neglected.

$$C_v \frac{\partial T}{\partial t} = k_e\left(\frac{\partial^2 T}{\partial r^2} + \frac{2}{r}\frac{\partial T}{\partial r}\right) + \rho_b (-\Delta H)\frac{\partial X_1}{\partial t} \tag{1}$$

$$\frac{\partial C}{\partial t} = \vartheta\left(\frac{\partial^2 C}{\partial r^2} + \frac{2}{r}\frac{\partial C}{\partial r}\right) - \frac{\rho_b}{\epsilon}\frac{\partial X_1}{\partial t} \tag{2}$$

$$\frac{\partial X_1}{\partial t} = A^* \exp\left(-\frac{E_a}{RT}\right) \cdot Po_2^n \; ; Po_2 = RCT \tag{3}$$

where T, C and X_1 mean the temperature, oxygen concentration and the molar amount of oxygen consumed per unit mass of coal, at time t and location r. Oxygen consumption rate $\partial X_1/\partial t$ is commonly expressed at Eq. (3) as a function of Arrhenius' rate constant and oxygen partial pressure[5,11,12]. At the center of the sphere ($r = 0$), the boundary conditions of the above equations are:

$$\frac{\partial T}{\partial r} = 0, \quad \frac{\partial C}{\partial r} = 0 \tag{4}$$

At the sphere surface ($r = D/2$), oxidation occurs so slowly that we assumed:

$$T = T_a, \quad C = C_a \tag{5}$$

where T_a and C_a refer to ambient temperature and concentration.

We performed numerical calculations of Eqs. (1) ~ (3) based on Eqs. (4) and (5). The constants used in these calculations are as follows. We calculated oxygen mass diffusivity based on Fujita's[2] equation and set specific heat at C_v = 963 J/(kg·K)[4,12], and heat of coal oxidation reaction at $\Delta H = -3.7 \times 10^5$ J/mol[11]. Effective thermal conductivity k_e was obtained from the equation[6] for estimating the effective thermal conductivity of packed bed with no fluid flow. For these calculations, we set the void fraction of coal deposit ϵ at 0.4, heat radiation factor (emissivity) at 0.9 and coal thermal conductivity at 1 kJ/(m·h·K)[12], and assumed the gas as air. In the same matter as Iki and Higuchi *et al.*[4], we neglected changes in k_e due to temperature and used effective thermal conductivity at 60°C. Our calculations revealed that k_e rose as coal particle diameter d_p climbed. An example: k_e when d_p = 5 cm is about 2.7 times the k_e when d_p = 0.1 cm. This finding indicates that more heat is radiated into the ambient atmosphere as the particle diameter of coal deposits increases.

2. 2 Estimation of parameters related to coal reactivity

When a coal sample is enclosed in a heat-insulated apparatus containing oxygen, the sample temperature will rise gradually due to oxidation. Assuming that this apparatus has a heater and can be so controlled as to make ambient gas temperature remain the same as the sample temperature, the resulting rise in sample temperature is due merely to oxidation-induced heat generation of the coal itself. Based on Eqs. (1) and (3), the above procedure can be expressed as:

$$C_v \frac{dT}{dt} = A \exp\left(-\frac{E_a}{RT}\right) \tag{6}$$

where

$$A = A^* \rho_b (-\Delta H) \cdot Po_2^n \tag{7}$$

Assuming that the apparent frequency factor when air (oxygen partial pressure $Po_{2,i}$) is used as the gas is A_0, the following holds:

$$A = A_0 (Po_2/Po_{2,i})^n,$$
$$A^* = A_0/\{\rho_b (-\Delta H) Po_{2,i}^n\} \quad (8)$$

Apparent frequency factor A, apparent activation energy E_a and exponent n of oxygen partial pressure are obtained[4,5,12] by determining temperature rise curve (T vs t) with an experimental apparatus, with different oxygen partial pressures, which satisfies Eq. (6) and whose oxygen consumption can be neglected. Onizuka *et al.*[12] conducted experiments on large quantities of coal and revealed:

(1) The temperature rise speed dT/dt has an inflection point at about 120°C, above and below which the reaction mechanism differs;

(2) The apparent frequency factor changes according to the sample particle diameter and can be expressed as $A \propto d_p^{-(0.35\sim0.65)}$; and

(3) The dependency of oxygen partial pressure is $n = 0.44 \sim 0.74$.

For the purpose of this report, we also conducted similar experiments on five representative types of coal with different atomic ratios H/C and O/C. The result was that $n \approx 0.4$ and that changes in apparent frequency factor due to d_p were as shown in **Fig. 1** in the low temperature range covered in our study. Our result almost agrees with Onizuka *et al.*'s results. Based on the above, we conducted simulation using $n = 0.6$ and assuming A vs. d_p as follows:

$$A \propto d_p^{-0.5} \text{ or } A = A_B \left(\frac{d_p}{d_{p,B}}\right)^{-0.5} \quad (9)$$

where $d_{p,B}$ and A_B refer to standard particle diameter and known apparent frequency factor. As is evident from **Fig. 1**, particle diameters used were about 1 mm at the most so that we still do not at all know how applicable and precise Eq. (9) is with regard to grain-type coal with diameters of several centimeters, which is in question in actual coal storage. Since no other appropriate evaluation method is now available, we used Eq. (9) also for grain-type coal. Equation (9) indicates that the apparent frequency factor drops, resulting in a fall in the heat generation speed, as the particle diameter increases. We carried out the calculations in the following order:

(1) converting apparent frequency factor A_B (reports 4, 12) of coal with a particle diameter of d_B derived from air oxidation into comparable A_B value of coal with a desired particle diameter using Eq. (9); and

(2) (with the former A_B value set at A_0), evaluating A and A^* on the basis of Eq. (8).

3. Results and discussion

3. 1 Temperature rise simulation

Figure 2 shows the results of numerical calculations, based on Eqs. (1) and (3), of the

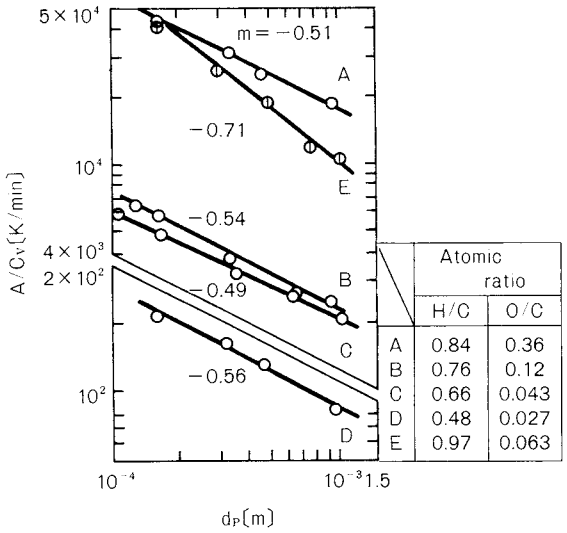

Fig. 1 Variation of frequency factor with particle diameter

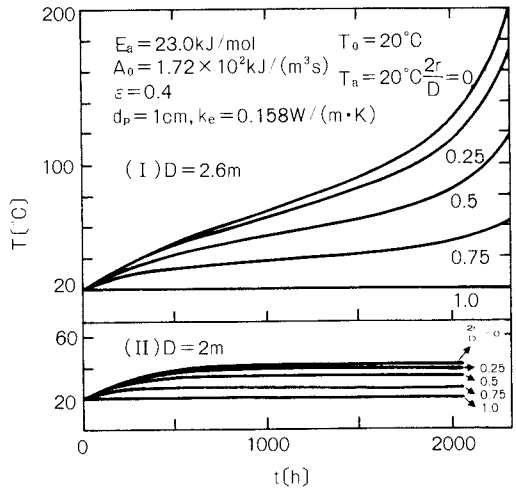

Fig. 2 Temperature histories of spherical coal deposit in simulated natural oxidation under constant oxygen concentration

temperature rise with an equal oxygen concentration in all portions of the well-ventilated coal deposits. The target coal is Joban coal mentioned in the previous report[4]. We set particle diameter d_p as 1 cm; deposit initial temperature T_o and ambient temperature T_a as 20°C; and deposit diameters as (I) D = 2.6 m and (II) D = 2 m. $2r/D$ means a dimensionless version of the distance from the deposit center. When D = 2 m, temperature rises slightly but heat generation speed equals heat radiation speed at a low temperature ($dT/dt = 0$), resulting in no occurrence of spontaneous combustion. When D = 2.6 m, after heat generation speed surpasses heat radiation speed and nears 100°C, heat is rapidly accumulated and temperature rises quickly ($dT/dt > 0$), leading to spontaneous combustion. Both temperature and the temperature rise rate maximize at the sphere center. **Figure 3** gives an example of the case in which the oxygen content in the deposit of the same coal as in **Fig. 2** is consumed and decreases as reaction proceeds. The oxygen concentration curve indicates that oxygen declines gradually over time, because oxygen consumption rate surpasses oxygen resupply speed due to molecular diffusion. **Figure 3**, therefore, shows no such exponential-function-like rise as in **Fig. 2**. However, it does indicate temperatures surpassing coal ignition temperature (about 200 ~ 220°C). This finding shows that the coal storage size used here is inappropriate. **Figure 4** shows the results with the coal particle diameter set at double that used in **Fig. 2** and **3** and the deposit diameter D set at 10 m. An increase in particle diameter and a resulting decline in reaction rate due to a drop in apparent frequency factor [Eq. (9)] and oxygen consumption cause the temperature to rise slowly despite the large deposit diameter (D = 10 m) and its high heat accumulation effect. After 3,000 hours, however, the intralayer maximum temperature reaches 135°C. The position at which the temperature is maximized is, unlike in **Figs. 2** and **3**, near $2r/D$ = 0.75 nearer to the deposit surface. Near the center of the sphere, reaction slows down as oxygen quantity declines so that, we believe, temperature is maximized nearer to the surface from the center. Some existing papers[8,9] already report that temperature may diverge ($dT/dt > 0$) near the surface of spontaneous-ignitable powder when it is exposed to a high-temperature atmosphere. **Figure 4** indicates that a similar phenomenon occurs when such material contacts ordinary ambient temperature. This shows that spontaneous ignition and quality degradation cannot be prevented suf-

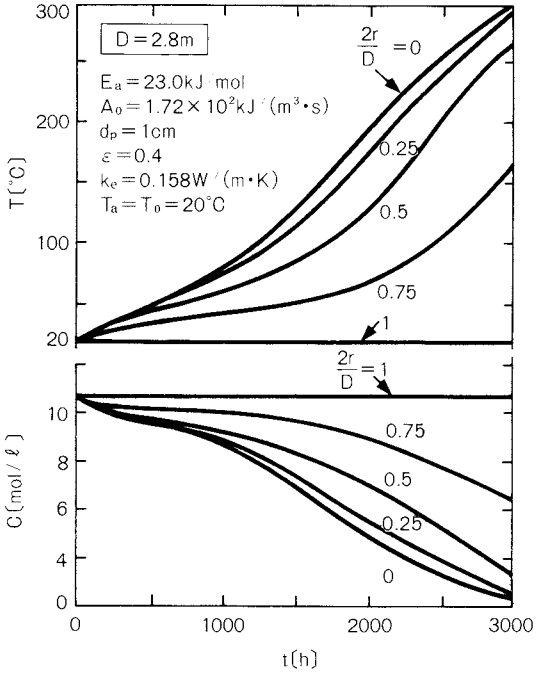

Fig. 3 Temperature and oxygen concentration histories in simulated natural oxidation

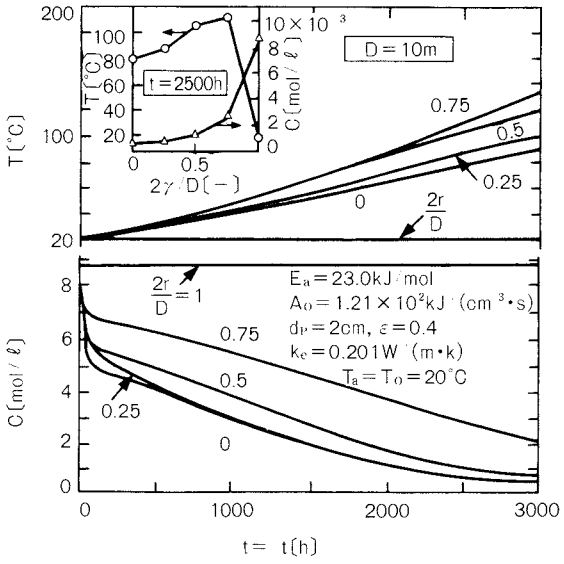

Fig. 4 Temperature and oxygen concentration histories in simulated natural oxidation for a large coal deposit

ficiently by detecting the temperature at the center of deposits alone.

3. 2 Changes in coal pores due to oxidation

Even before the ignition temperature is reached, oxidation brings about changes in basic composition and a loss in coal[10]. To confirm this, we examined the rise due to oxidation in amount of water adsorbed on the coal sample (80 ~ 100-mesh), shown in **Fig. 1** E, which was left in a constant-temperature drier containing enough air. More specifically, we conducted the experiment in the following order:

(1) shutting up an oxidized sample, together with a saturated salt water solution having a constant vapor pressure, in a desiccator in a vacuum state;
(2) leaving the desiccator in a 20°C constant-temperature water bath for a certain period of time, until adsorption reaches its equilibrium; and
(3) determining the amount of water absorbed V [m³/g·coal] on the basis of the rise in sample weight.

Similarly, we measured V using different types of saturated salt water solution with various vapor pressure p. **Figures 5** and **6** indicate the results (adsorption isotherms) plotting the above V value with regard to relative vapor pressure p/p_0 (p_0 is the saturated vapor pressure of 20°C water). **Figure 5** indicates the effect of oxidation temperature on adsorption isotherms on samples oxidized for one day. No considerable rise is seen in the amount of water absorbed at temperatures below 110°C. In the case of samples at 140°C or more, on the other hand, the amount of water absorbed climbs considerably. This shows that, here, oxidation proceeds faster than at temperatures below 110°C, thus considerably promoting the loss of mass and the development of micropores. The above results, as mentioned in clause 2.2, correspond to the report that the oxidation mechanism generally differs above and below about 120°C[12].

Figure 6 shows the effects of oxidation period on adsorption isotherms at 75°C (low-temperature side) and 140°C (high-temperature side) on oxidized coal samples. At 75°C, the amount of water absorbed did not increase to a considerable extent even after about a one-month oxidation period, showing a very slow rate of oxidation. At 140°C, on the other hand, mass loss proceeded considerably with the passage of time. To prevent excessive quality degradation and mass loss, therefore, we should inhibit temperature from becoming so

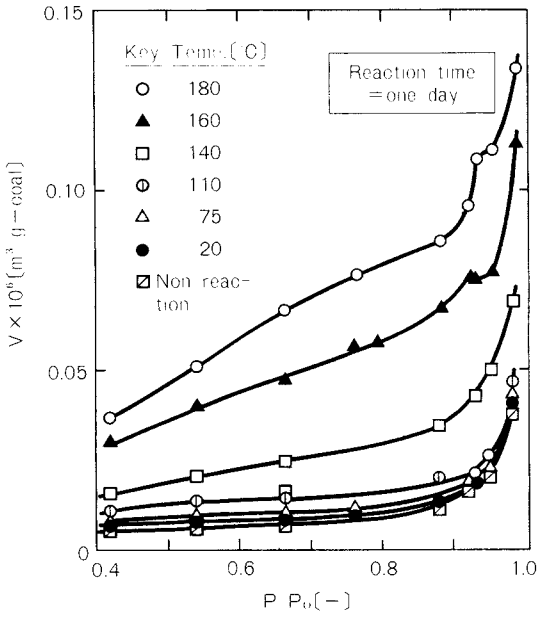

Fig. 5 Effect of oxidation temperature on adsorption isotherms of water vapor at 20°C on coal samples oxidized for one day

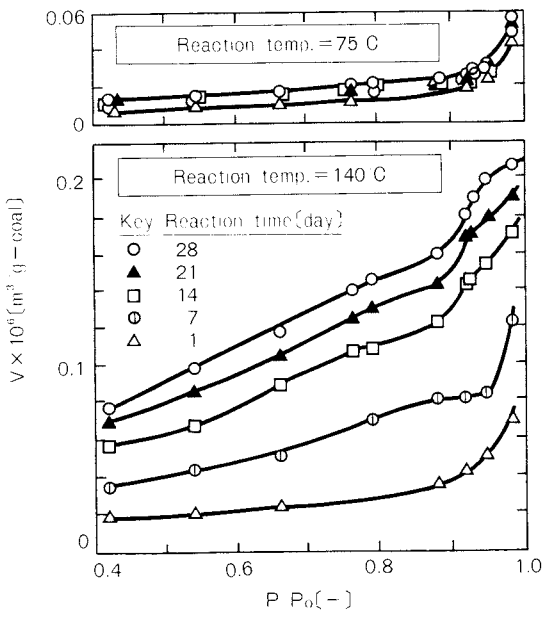

Fig. 6 Effects of oxidation temperature and time on adsorption isotherms of water vapor at 20°C on oxidized coal samples

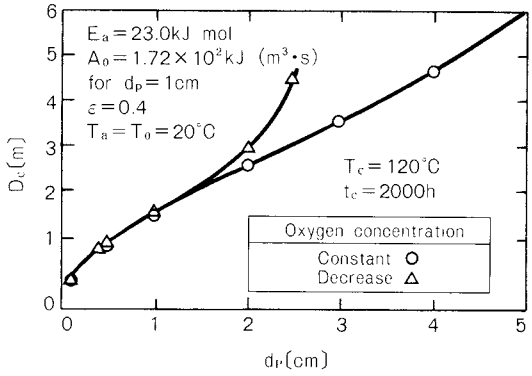

Fig. 7 Effects of particle diameter and oxygen concentration on a maximum critical size in coal storage

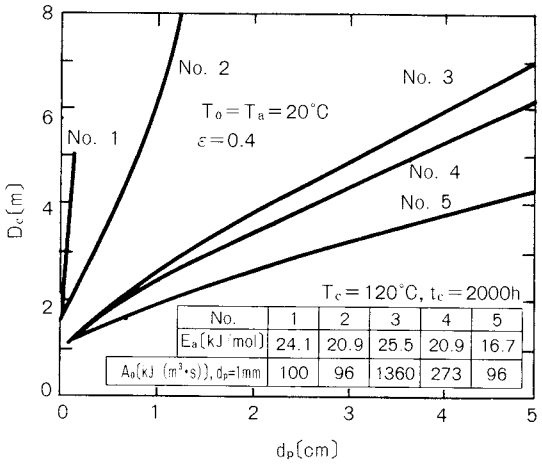

Fig. 8 Effect of coal reactivity on a maximum critical size in coal storage

high level that leads to considerable coal loss during the required storage period. Although, strictly speaking, the upper limit temperature in storage T_c, we believe, varies according to the type of coal, we assumed T_c = 120°C in the subsequent part of our study.

3. 3 Estimation of maximum storage amount

We evaluated the maximum diameter D_c of spherical coal deposit which satisfies the following requirements:

- Temperature should not reach ignition temperature, and quality should not drop;
- Storage period is set at t_c;
- No point in the layer should exceed 120°C.

Figure 7 shows the maximum critical size as a function of coal particle diameter, where T_c = 120°C and t_c = 2,000 hrs. (about 83 days). The coal sample is the same as that used in **Figs.** 2 ~ 4. The upper side region of each curve in the figure provides hazardous sizes for coal storage. The figure shows two cases:

- the case in which oxygen concentration is constantly of the same composition as that of the air; and
- the case in which oxygen is consumed and decreases due to the reaction.

As d_p increases, the maximum critical size rises. As mentioned before, this is presumably due to a rise in effective thermal conductivity (i.e., an increase in heat radiation effect) as d_p increases, while the apparent frequency factor drops (i.e., heat generation slows down). The figure shows that, when oxygen consumption is allowed for, ordinary-sized deposits having d_p of about 3 cm or more rarely lead to spontaneous ignition or mass loss. In the case of outdoor storage, deposits are compacted to prevent the air from flowing in due to convection. This method is effective, as indicated by the above results. If it is guaranteed that no air will enter the deposits, we can estimate the storage size by preparing similar drawings according to the type of coal. However, it is still possible that some cause or other may lead to the formation of an air passage in the coal deposits. To prevent such a risk, designers should predict the maximum critical size on the safety side, i.e, under such a condition that air is resupplied sufficiently. This condition alone applies to the subsequent part of our study.

3. 4 Effect of coal reactivity on maximum critical size

Onizuka *et al.*[12] conducted experiments on large quantities of coal and reported apparent activation energy E_a and apparent frequency factor A converted on the basis of particle diameter 74 μm. Of their various types of coal, we chose five characteristic types of coal and calculated their respective maximum critical sizes D_c. The results are shown in **Fig.** 8. D_c varies greatly according to the difference in type of coal, i.e., the difference in E_a and A. The factor E_a, we believe, generally exercises more influence than A.

3. 5 Determination of maximum critical size using a dimensionless term

We conducted a dimensional analysis of fac-

tors related to the maximum critical size and obtained the following dimensionless term:

$$X = \frac{QT_c}{C_v(T_c - T_o)}$$

$$Y = \left\{\frac{k_e D_c^2 \cdot (T_c - T_o)/D_c}{QD_c^3/4}\right\}^{-0.5}$$

$$= \left\{\frac{4k_e(T_c - T_o)}{QD_c^2}\right\}^{-0.5}$$

$$\eta_1 = \frac{T_c}{T_c - T_o}, \quad \eta_2 = \frac{T_a}{T_c - T_o}, \quad \eta_3 = \frac{T_o}{T_c - T_o}$$

$$\eta = \eta_1 \cdot \eta_2 \cdot \eta_3 \qquad (10)$$

where T_c, upper limit temperature in storage, was set at 120°C. Q refers to the average heat generation speed defined by the following euqation:

$$Q = \frac{1}{T_c - T_o}\int_{T_o}^{T_c}\left(C_v \frac{dT}{dt}\right)dT$$

$$= \frac{1}{T_c - T_o}\int_{T_o}^{T_c} A\exp(-E_a/RT)dT \qquad (11)$$

X and Y^2 are amounts proportionate to (amount of heat generated/amount of heat accumulated) and (heat radiation speed/heat generation speed)$^{-1}$ respectively until time t_c. Assuming various types of coal[12] and particle diameters, we calculated maximum critical size D_c and then determined X and Y. The results are indicated in **Fig. 9**. $\eta = 33.7$ holds on the assumption of $T_a = T_o = 20$°C and $\eta = 70$ holds on the assumption of $T_a = T_o = 40$°C. Interestingly, the X vs Y curve scarcely depends on t_c and is expressed as a single curve when the maximum storage period t_c ranges from 1,000 hrs. (about 42 days) to 3,000 hrs. (125 days = 4 months). Use of **Fig. 9** enables us to estimate the maximum deposit size, which is the subject of our present paper, without performing numerical calculations of differential equations.

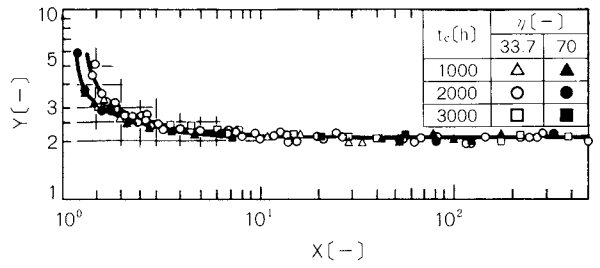

Fig. 9 Dimensionless plot for the estimation of D_c

4. Conclusion

To study ways to store coal stably for a long period, we simulated a maximum critical size with which coal can be stored without the risk of spontaneous ignition or excessive mass loss due to natural oxidation. With a constant sufficient supply of oxygen, coal temperature was maximized at the center of the deposit. With some decline in oxygen due to oxidation, on the other hand, temperature was maximized near the coal surface. Heat accumulation speed depended largely on activation energy and apparent frequency factor which govern coal reactivity. Measurements of amounts of water adsorbed on oxidized coal revealed that coal mass loss increased considerably at temperatures above 120°C. We, therefore, set the upper limit storage temperature at 120°C. Then, for various types of coal, we calculated their respective maximum storage amounts which must be observed to hold the stored coal below 120°C over a specified storage period. We then indicated the results in a dimensionless manner for engineering applications.

Nomenclature

A	:	apparent frequency factor	$[J \cdot m^{-3} \cdot s^{-1}]$
A_0	:	A at $Po_2 = 0.21$ atm (=0.021MPa)	$[J \cdot m^{-3} \cdot s^{-1}]$
C	:	oxygen concentration in gas phase	$[mol \cdot m^{-3}]$
C_v	:	specific heat	$[J \cdot m^{-3} \cdot k^{-1}]$
D	:	diameter of spherical coal deposit	[m]
D_c	:	critical value of D in coal storage	[m]
ϑ	:	mass diffusivity	$[m^2 \cdot s^{-1}]$
d_p	:	particle diameter	[m]
E_a	:	apparent activation energy	$[J \cdot mol^{-1}]$
ΔH	:	heat of reaction	$[J \cdot mol^{-1}]$
k_e	:	effective thermal conductivity	$[J \cdot m^{-1} \cdot s^{-1} \cdot K^{-1}]$
p/p_0	:	relative vapor pressure	[–]
r	:	radial distance in spherical coordinate	[m]
T	:	temperature	[K, °C]
T_a	:	ambient temperature	[°C]
T_c	:	upper limit temperature in storage	[°C]
T_o	:	initial temperature of coal deposit	[°C]
t	:	time	[s]
t_c	:	storage time	[s]
V	:	amount of water adsorbed	$[m^3 \cdot g^{-1}]$
X_1	:	amount of oxygen consumed	$[mol \cdot kg^{-1}]$
ϵ	:	void fraction of coal deposit	[–]

References

1) Baum, M.M.: *Combustion and Flame*, **41**, 187 (1981).
2) Fujita, S.: *Kagaku Kogaku*, **28**, 251 (1964).
3) Iki, S. and K. Higuchi: *J. of the Mining and Metallurgical, Japan*, **89-1025**, 455 (1973).
4) Iki, S. and K. Higuchi: *ibid.*, **90-1033**, 175 (1974).
5) Kuchta, J.M., V.R. Rowe and D.S. Burgess: Int. Bu. of Mines, PGH., PA. 24815, U.S. Government Printing Office, 1980-603-102/100.
6) Kunii, D. and J.M. Smith: *AIChE J.*, **6**, 97 (1960).
7) Lawn, C.J., P.J. Street and M.M. Baum: 18th Int. Symp. on Combustion, p. 731 (1981).
8) Liang, H. and T. Tanaka: *J. Soc. Powder Technol., Japan*, **23**, 326 (1986).
9) Liang, H. and T. Tanaka: *Kagaku Kogaku Ronbunshu*, **13**, 63 (1987).
10) Marinov, V.N.: *Fuel*, **56**, 165 (1977).
11) Nishikawa, S., T. Nakayama and K. Yoshida: Preprints for 16th Antumn Meeting of The Soc. of Chem. Eng., Japan, SD101, Toyota (1982).
12) Onizuka, S. and T. Watanabe: Technical Report by Hitachi-Zosen Co., **43**, 13 (1982).

Review

Recent Works on Powder Mixing and Powder Coating Using an Optical Measuring Method†

Manuel Alonso, Munetake Satoh and Kei Miyanami
Department of Chemical Engineering
*University of Osaka Prefecture**

1. Introduction

During the last few decades a great amount of effort has been addressed to the description, qualitative in most of the cases, of the basic mechanisms operating in the mixing of particulate solids. Given a particular process, the specific mechanism by which mixing proceeds depends fundamentally on the characteristics of the motion of the powder within the mixer, which in turn depend both on the physical properties of the powders and the characteristics of the mixing equipment.

Another aspect of the powder mixing process is that concerning the quality of the resulting mixture and the time required for the particular mixer in consideration to yield the mixture of the desired quality. To evaluate the quality of the mixture it is necessary to know its composition at different points, task that has traditionally been done by stopping the mixer at a prescribed time to withdraw a number of samples from as many places within the mixture and analyzing the composition of each one of the samples. This procedure is, however, impractical if the performance evaluation of different types of mixer in order to select the most suitable for a given duty is to be accomplished.

Both the flow pattern of powder within the mixer and the temporal variation of the mixture quality can be followed up by a recently developed on-line type optical measuring method. The method has already been applied to the evaluation of the mixing characteristics of a number of mixers. The results of these works are reviewed in the first part of this paper. The second part of the review is devoted to the recent works of the authors on powder coating, works for which the continuous optical measuring system has also shown its applicability.

* 4-804 Mozu-Ume machi, Sakai, 591
TEL. 0722-52-1161

Received May 2, 1989

2. The optical measuring system

The composition of a mixture of different colored powders can be known by measuring the intensity of the light reflected by the mixture, onto which a light of certain wave length and constant intensity from a light source is projected. The block diagram of **Fig. 1** shows the photometer and the computer system developed for these purposes. The details of the measuring system are to be found elsewhere [1] and, as an illustration of the capabilities of the method, the calibration curves relating the intensity of the reflected light (expressed in terms of output DC potential) to the concentration of the key (colored) component for a number of binary mixtures are shown in **Fig. 2**.

In mixing experiments, several probes containing two optical fibers each (see **Fig. 1**) are inserted into the mixing vessel and fixed at dif-

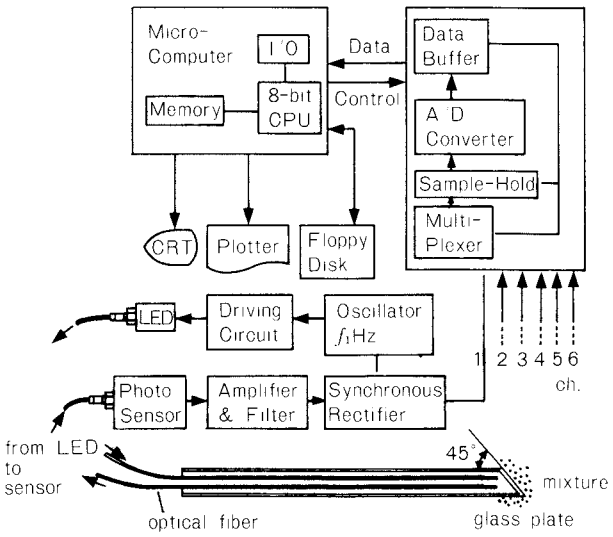

Fig. 1 Photometer and computer system

Table 1 Physical properties of the powders used

Component A (white)				Component B (dark)			
Material	Key	d_p [μm]	[kg/m^3]	Material	Key	d_p [μm]	[kg/m^3]
Alumina	WA#80	129~297	3970	Silicon carbide	SiC# 46	250~590	3240
					SiC# 80	125~297	3240
					SiC#180	50~125	3240
				Iron	Fe	125~297	7860
Glass	Gl	150~350	2500	Glass dyed	Gl	150~350	2500
Kaoline	K	4~160	2860	Iron oxide	Fe_2O_3	~5	5770
PVC	PVC	40~200	1540	Zircon sand	Zr	105~350	4650

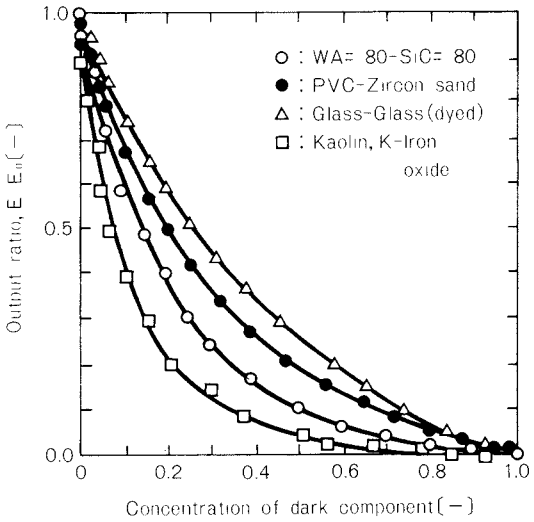

Fig. 2 Calibration curves for several binary powder mixtures

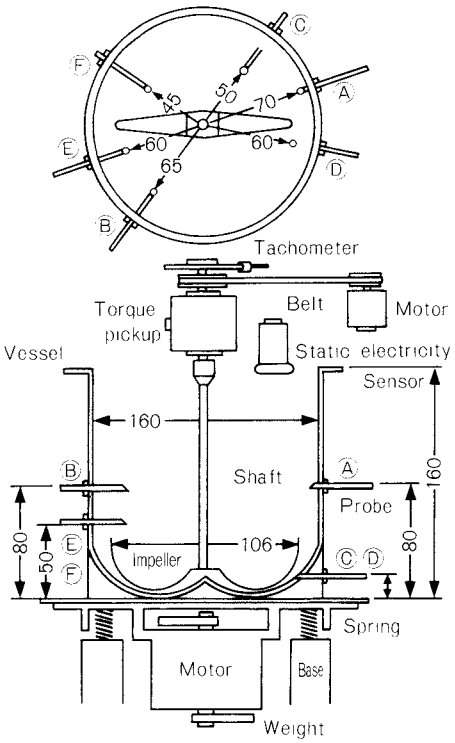

Fig. 3 High speed stirred mixer

ferent positions. In this manner, with the data supplied by the sensors and the calibration curve of the powder system in consideration, the composition of the mixture at different points can be continuously measured.

3. Classification of mixing processes

Mixing processes can be classified into several types according to the physical characteristics of the powders to be mixed. With the purpose of establishing this fundamental classification, a number of experiments were carried out [2] in a vibrated high speed stirred mixer (Kawata Ltd., type SFC-5) using various combinations of powders and different operating conditions. The physical properties of these powders are listed in **Table 1**. As shown in **Fig. 3**, the six probes used for measuring the concentration were inserted horizontally at different depths into the vessel and also at different distances from the wall. In the experiments, first the A component (white) is placed within the vessel, which is then vibrated at the prescribed frequency N_V (Hz), and the impeller is also set in motion at the desired speed N_R (rpm). Once the A component has been agitated for a while under those fixed conditions, the B component (colored) is added at time $t = 0$ onto the bed in the form of a pulse input.

The concentration curves obtained and their corresponding mixing curves are shown in **Fig. 4**. The degree of mixing appearing in the Y-axis of the mixing curves is defined as

$$M = 1 - \sigma_M / \sigma_0 \qquad (1)$$

where σ_M is the standard deviation of the concentrations measured at the six sampling points and σ_0 is the standard deviation of the completely unmixed state, i.e. at time $t = 0$.

In the remaining of this section the typical

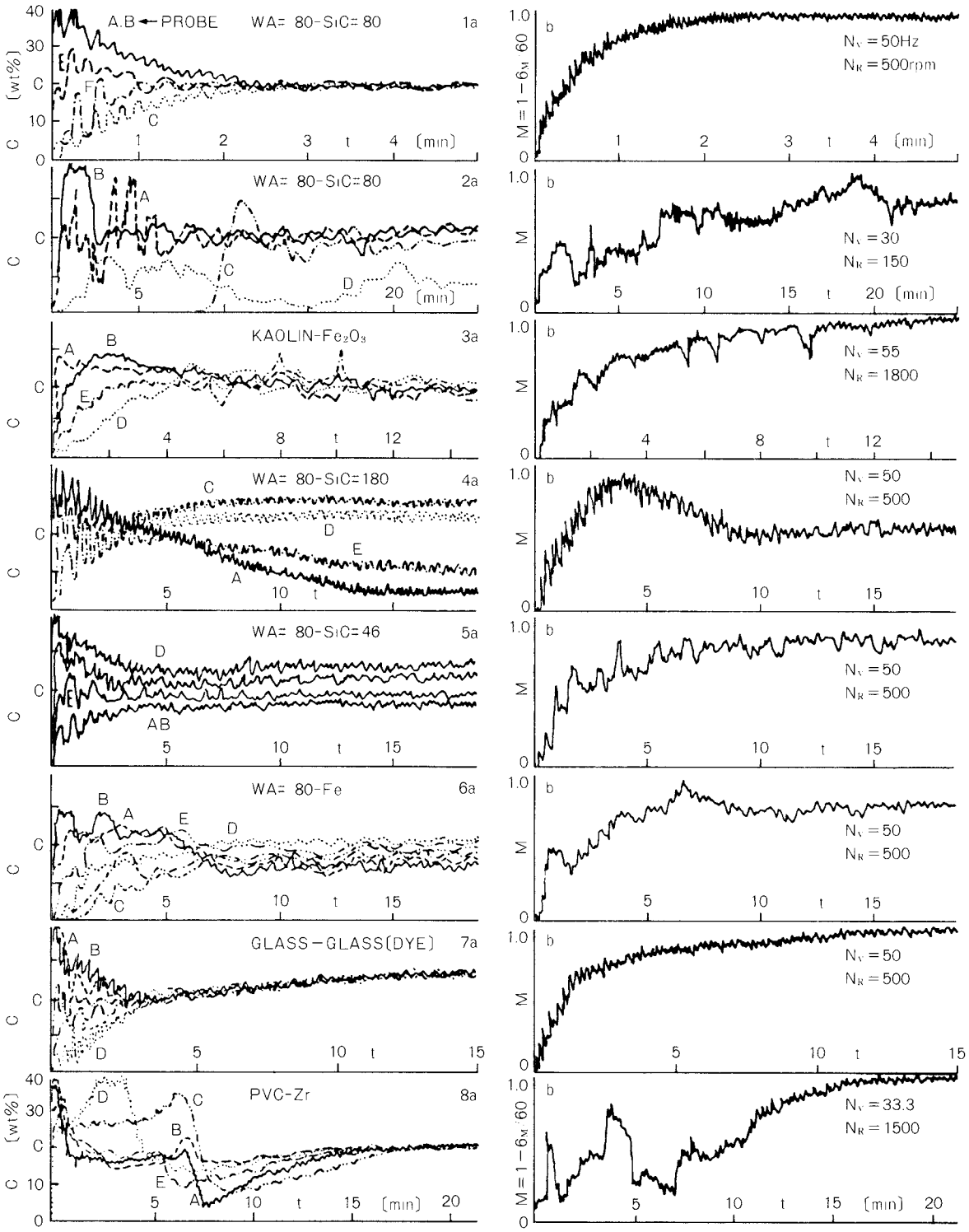

Fig. 4 Concentration curves and mixing curves for the different types of mixing processes

patterns of the mixing curves shown in **Fig. 4** are briefly described. First, it is noticed that the concentration curves in the left of the figure give information concerning the flow pattern of the powder. In particular, in some cases it is clearly seen the periodic circulation of the key component (black) up and down within the mixer and, in other cases, the delay of the key constituent in reaching the lower part of the vessel. This information is useful for the understanding of the basic mixing mechanism operating in this mixer.

3. 1 Coarse powders with similar physical properties

3. 1. 1 Proper operating conditions

When two powders of similar physical properties and good flowability are mixed, the powder flows homogeneously within the vessel, which means that the circulation period is the same everywhere (**Fig. 4-1a**), resulting in a monotonous increase of the degree of mixing (**Fig. 4-1b**). Also, the final degree of mixing attained is very good (almost 1).

3. 1. 2 Bad selection of operating conditions

Fig. 4-2a, 2b shows the results obtained for the same powder system as in 1) but at different operating conditions (lower vibration frequency and lower impeller rotation speed). In this case, the mixing is poor, the circulation of powder within the vessel is very irregular and a complete mixed state cannot be attained even after a long mixing time.

3. 2 Cohesive fine powders

Fine cohesive powders tend to form agglomerates, which have to be broken up in order to achieve a good mixture quality at the microscopic level. Therefore, in this case (**Fig. 4-3a, 3b**), the mixing time is much longer than in the case of large-sized particles.

3. 3 Powders differing in particle size

In this case, the results depend on the way in which the components are charged into the mixer.

3. 3. 1 Addition of fines onto the coarser particles bed

As seen in **Fig. 4-4a**, the fines percolate through the bed of the coarser particles, as a result of which a concentration gradient opposed to that existing at time $t = 0$ is progressively established. During this downwards flow of fines a point is reached at which the fines concentration is approximately the same everywhere. At this point, the degree of mixing attains its maximum value (**Fig. 4-4b**). As the downwards flow of fines continues, the mixture loses progressively this temporary homogeneity and the degree of mixing decays until the steady state is reached. This is thus a typical case of mixing followed by demixing or segregation.

3. 3. 2 Addition of coarser particles onto the fine particles bed

In this case (**Fig. 4-5a, 5b**), the larger particles, which occupy the upper part of the vessel at time $t = 0$, descend very slowly towards the lower part of the mixer. This downwards flow of large particles is not enough, however, to equalize the concentration within the bed and a mixture of poor quality is attained. As opposed to the former case, the degree of mixing increases monotonically.

3. 4 Powders differing in density

This case (**Fig. 4-6a, 6b**) is somewhat similar to that of the mixing of different-sized particles. In fact, there is a downwards flow of the heavier component and at a given time the mixing curve passes through a maximum, after which segregation takes place. However, the segregation effect is not as strong as in the case of different particle size.

3. 5 Coating of coarse particles by fine adhesive particles

Figure 4-7a, 7b shows the case of mixing of a coarse material with the same powder coated by a fine sized material. At the beginning, mixing proceeds in the same way as that occurring in **Fig. 4-1a, 1b**, since the physical properties of both components are (except the color) the same. After the concentration has been leveled off everywhere within the mixer, it is seen a further increase in the 'concentration' of the key component. Actually what is increasing is the blackness of the mixture. This occurs because the fine particles of dye (which are likely to exist initially in the form of agglomerates)

attached to the black component, are being transferred to the white particles of their vicinity. In this manner, the dye is progressively being dispersed over the surface of all of the coarse material. This process will be later treated in more detail.

3. 6 Electrostatic effect in powder mixing

It is observed (**Fig. 4-9a, 9b**) a very irregular pattern at the beginning, with mixing stages followed by segregation periods due to the difference in particle density. However, after a certain time the mixing curve becomes monotonous and a fairly good final degree of mixing is attained. The surface electrostatic potential was also measured continuously during this mixing run and it was found that the potential first increased and later decreased continuously attaining a highly negative steady value after about 15 minutes of mixing. The electrostatic behavior of the powder bed was thought to be the main cause of the irregular pattern observed in the mixing curve.

The cases discussed in this section are the typical mixing processes which can be found in the practical situations. In the remaining of the present review, two of these cases, namely, the mixing of cohesionless powders with similar physical properties and the coating of coarse powders by fine adhesive particles, are discussed more extensively.

4. Mixing of non-segregating cohesionless powders

Using the optical measuring method described above, the mixing performance of two new types of powder mixers was studied. For the experiments, glass powder was mixed with the same powder coated by a black dye. Therefore, this is the case corresponding to **Fig. 4-7a, 7b**, discussed before. However, as long as macromixing is concerned, the coating stage occurring here can be neglected. Furthermore, since the powders used do not segregate, the final degree of mixing is very close to one and the rate of mixing (or equally well the mixing time) is the only parameter to take into account for the evaluation of the optimum operating conditions. The mixing time is taken to be that at which the concentrations measured by the probes become equal, that is, the point at which the concentration curves (**Fig. 4-7a**) converge.

4. 1 Rocking mixer®

This type of mixer (Aichi Electric Co., RM-30) consists in a rotating drum with simultaneous rocking motion in the longitudinal direction (**Fig. 5**). The mixing mechanisms operating in this type of mixer are [3] diffusion and convection. Due to the rocking motion of the vessel, the powder circulates quite freely from the one end to the other of the mixer. Besides, the motion of the powder also has a diffusive component, consequence of the rotating movement of the mixer. **Figure 6** shows the influence of the operating conditions on the mixing time. It is noticed that the rate of mixing, which is very low when only rotation is imparted to the mixer, is greatly enhanced by the rocking component of the vessel's motion. The effect of rocking is perhaps

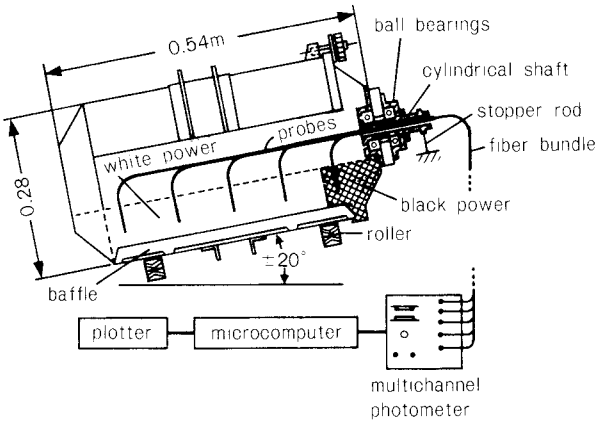

Fig. 5 Rocking Mixer®

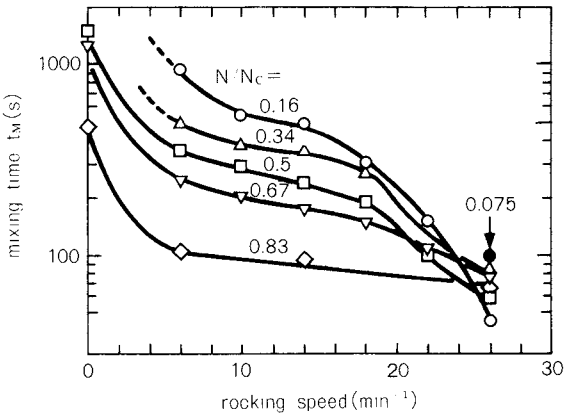

Fig. 6 Influence of rocking speed on mixing time at different rotation speeds

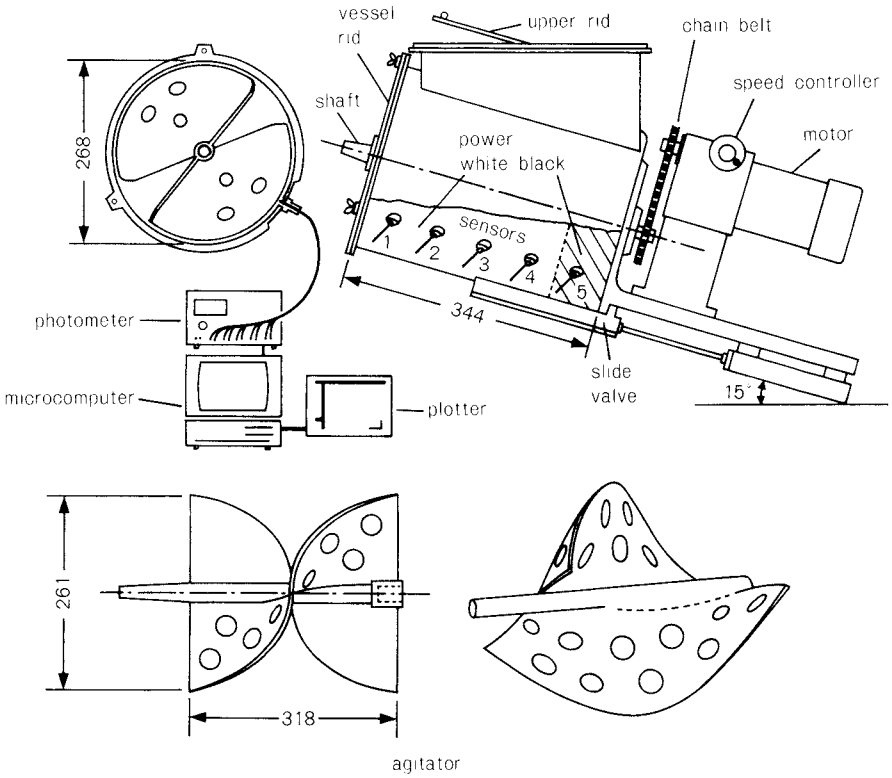

Fig. 7 Twist-Hole Mixer®

more clearly appreciated at high rocking speeds, at which mixing is very fast even at low or very low rotation speeds.

4. 2 Twist-hole mixer®

The mixing chamber of this type of mixer (Matsui MFG Co., Ltd., type TW-20) is cylindrical and the agitator is a twisted perforated plate (**Fig. 7**).

The flow pattern of powder within the mixer consists of [4] an upwards stream due to the rotation of the agitator, a fraction of which passes through the holes of the agitator and returns back to the lower part of the vessel. The relative amounts of upwards and downwards flows depend on the agitation speed, the inclination of the vessel (15° in the experiments) and on the total area of holes in the agitator.

In this study, the optimum values of charge ratio (volume of powder/volume of mixer), agitation speed and total area of holes in the agitation speed and total area of holes in the agitator were obtained. These optimum values resulted to be the following: charge ratio, 31 ~ 38%; agitation speed, 85% of the critical speed; and total area of holes, 25 ~ 30% of the agitator surface area.

5. Powder coating

When a fine cohesive powder is mixed with a coarser granular material, the structure of the resulting mixture consists of a layer of fines adhered on to the surface of the larger particles. In general, the fine powder, because of its inherent cohesiveness, is forming agglomerates. During the coating process the agglomerates of fines have to be broken up if a mixture of good quality at the microscopic level is to be achieved. Accordingly, the amount of mechanical energy inputted by the mixer plays a central role in this type of mixing process. This point has been clearly confirmed throughout our experimental work on powder coating [5, 6] using three types of mixers with different mechanical energy input.

These three mixers are the high speed stirred mixer and the rocking-type mixer described before, and the Angmill Mechanofusion System® [7] (Hosokawa Micron Co., type AM-15F). The use of these three mixing equipments has permitted the elucidation of the basic mechanism involved in the process. A

brief description of the mechanism is presented in the following.

At the beginning, i.e., in the completely unmixed state, the fine component is distributed in lumps within the bulk, thus existing large zones of the bed with no fine particle at all. Accordingly, the first step of the process consists in the reduction of the size of these zones. The agglomerates of fines attach to the surface of the larger particles existing in their vicinity. These few primary coated particles act as carriers of fines, distributing them randomly throughout the mixer. During their travel, the carriers suffer a vast amount of collisions with other large particles, most of which remain, at this early stage of the process, without fines on their surface. In these collisions, the transfer of fines (either as individual entities or in the form of agglomerates) between large particles takes place. The kinetics of fines transfer among carriers was studied experimentally [5] using the optical measuring method described above. It was found that the fines transfer kinetics resembled the kinetics of a second order autocatalytic chemical reaction, with a rate equation of the form

$$dX_c/dt = kX_c^m (1 - X_c)^{2-m} \qquad (2)$$

where X_c is the mass fraction of powder that has been coated at time t, k is the coating rate constant, and m is the partial order of the coating 'reaction'. The reaction analogy was, however, limited by the fact that not only the rate constant k but also the 'partial order to reaction' m depended on the operating conditions. On the contrary, the overall order of reaction (two) is independent of the operating conditions and hence characterizes the coating process.

The fines transfer kinetics has also been simulated by a discrete model based on a population balance relating the distribution of fines within the carriers at a given time to that existing at a later time [8]. The results of the simulation are in agreement with the kinetics expressed by Eq. (2), although X_c is to be reinterpreted as the fraction of carriers which at time t are coated by the average number of fines per carrier existing in the mixture.

Once the fines transfer process has led to a spatially uniform distribution of fines within the carriers, the agglomerates of fines are gradually dispersed onto the surface of the larger particles, which results in an increase in the coated surface area. The dispersion of fines, which is actually occurring since the earliest stages of the process, takes also place by friction and collision between the particles.

In the rocking-type mixer, the mechanical forces acting upon the particles are relatively weak and do not suffice to break up the smaller or more cohesive agglomerates of fines and, as a result, the quality of the mixture attained is, from a microscopic point of view, relatively poor.

The high speed mixer, because of its higher mechanical energy input, yields mixtures of better quality. However, even this type of mixer was not able to disperse completely the agglomerates of fines in experiments with coarse particles of PMMA and fine particles of magnetite [6]. The degree to which the fines (black) are dispersed onto the large particles (white) can be qualitatively examined by measuring the blackness (or, conversely, the lightness) of the mixture. **Figure 8** shows the temporal variation of the lightness of the mixtures prepared by the high speed mixer at different agitation speeds. It is readily noticed the influence of the mechanical force imparted by the mixer on the rate and degree of dispersion of fines.

The mixtures obtained through a five-hour mixing in the high speed mixer were furthered processed in the Angmill Mechanofusion System [7] (**Fig. 9**). The corresponding values of the lightness versus time are shown in **Fig. 10**.

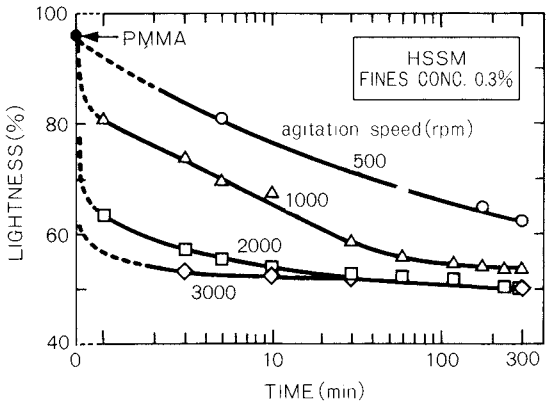

Fig. 8 Influence of the agitation speed on the temporal variation of the lightness of the mixture.(High speed stirred mixer)

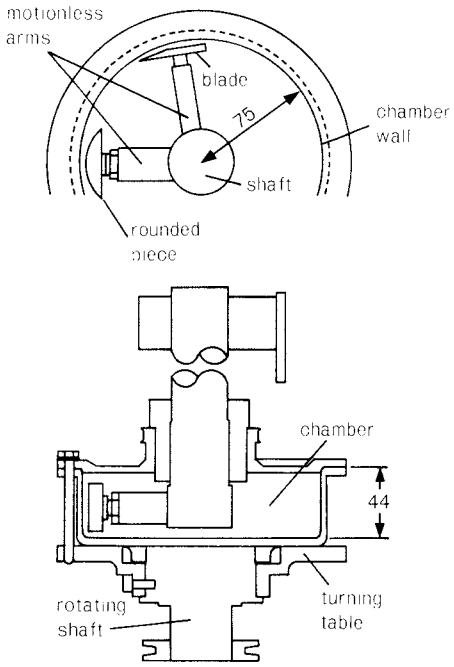

Fig. 9 Angmill Mechanofusion System®

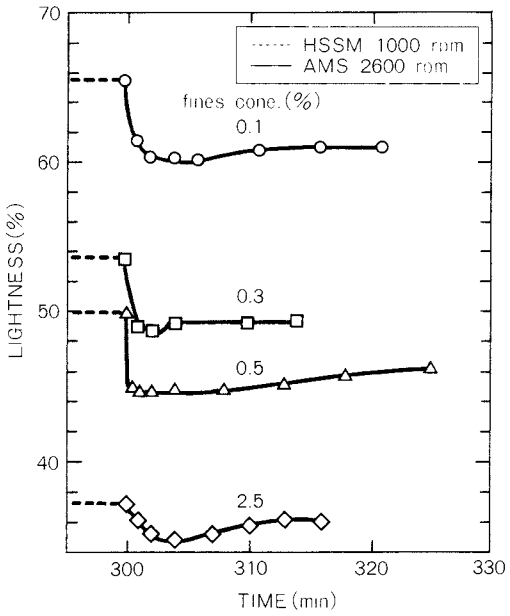

Fig. 10 Temporal variation of the color of the mixture (HSSM : high speed stirred mixer; AMS : Angmill mechanofusion system)

At the beginning, the lightness decreases, which means that the agglomerates of fines remaining after the five-hour mixing in the high speed mixer are further dispersed onto the carriers surface. This demonstrates once again the strong influence of the level of mechanical energy input on the quality of the mixture. **Figure 10** also illustrates a peculiar feature which did not appear in the high speed mixer experiments. After a certain time, the lightness of the mixture passes through a minimum and then increases, reaching the steady state. This phenomenon is a consequence of the gradual penetration of the small spheres of magnetite into the body of the PMMA particles. The mechanofusion process results in a remarkable modification of the particle surface texture.

Up to this point, the basic mechanism of the coating-mechanofusion processing of powders (illustrated in **Fig. 11**) has been reviewed. Further details concerning the modification of the physical properties of the powder (flowability, compressibility) as a result of the coating process are available in the original paper [6].

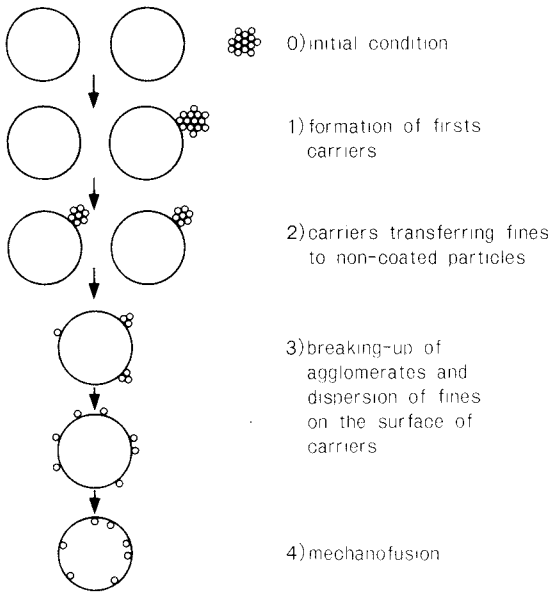

Fig. 11 Mechanism of the coating-mechanofusion process

References

1) Satoh, M. and K. Miyanami: *Bull. Univ. Osaka Pref., Ser. A*, **36** (2), 141 (1987).
2) Satoh, M., Y. Deguchi and K. Miyanami: *J. Soc. of Powder Technol., Japan*, **24** (10), 647 (1987).
3) Alonso, M., M. Satoh and K. Miyanami: *Powder Technol.*, **59**, 65 (1989).
4) Satoh, M., M. Alonso, T. Shigemura, K. Miyanami and T. Suzuki: *submitted to Chem. Eng. Res. & Des.*
5) Alonso, M., M. Satoh and K. Miyanami: *Powder Technol.*, **56**, 135 (1988).

6) Alonso, M., M. Satoh and K. Miyanami: *Powder Technol.*, **59**, 45 (1989).
7) Yokoyama, T., K. Urayama, M. Naito, M. Kato and T. Yokoyama: KONA No.5, 59 (1987).
8) Alonso, M., M. Satoh and K. Miyanami: *submitted to Powder Technol.*

Review

Formation of Particles in Sol-Gel Process

Sumio Sakka
Institute for Chemical Research
*Kyoto University**

Abstract

The formation of particles in starting solutions and its significance for the sol-gel processing of oxide materials are reviewed on the basis of previous works including our work. First, hydrolysis and polycondensation reactions of metal alkoxides in alcohol-water solutions are briefly discussed. Then, it is shown that powders prepared by the sol-gel method using metal alkoxides are suitable as starting powders for high performance glasses and ceramics because the particles produced are fine, monodispersed and uniform in chemical composition. It is also shown that the formation of round-shaped particles larger than, say, 10 nm in sols may lead to porous silica monoliths of plate or rod shape without occurrence of cracks during drying of the wet gel. It should be noted that crack-free gel monoliths can be sintered to monoliths of glass and ceramics. It is shown that essentially one-dimensional long-shaped particles can be produced by adjusting the composition and conditions of processing of the starting solution, which is required for fiber drawing from viscous sols in the course of sol-to-gel conversion.

1. Introduction

In the sol-gel process[1~5], formation of fine oxide particles takes place in sols. In some cases, particles formed in a sol are collected as a powder and formed into a powder compact for further processing, for example, sintering. Although gelation of the whole sol does not occur in this case, one might be permitted to call the process a "sol-gel method", because the individual powder particles may be gel-like. In other sol-gel processes, sols with suspended particles are formed into monoliths, fibers and coating films of gel in the course of the transformation of fluid and viscous sols to solidified gels. Such processes may be called typical sol-gel process.

In all those cases, particles with controlled size, size distribution and shape can be formed in the sol, which is essential for subsequent processing, such as sintering of the power compact and formation of various shapes in the course of sol-to-gel transition.

* Gokasho, Uji-shi, Kyoto-fu, 611
TEL. 0774-32-5428

Received May, 20, 1989

In this paper, previous works on the formation of particles in the sol have been reviewed with special attention given to the effect of particle size and shapes on the formability of the sol and sintering of a gel to ceramics or glass.

The advantages of the sol-gel method are most conspicuously displayed when metal alkoxides are utilized as starting compounds. This paper deals, therefore, mainly with sol-gel methods using metal alkoxides. Also, silica will be the main oxide species discussed here.

2. Reactions of metal alkoxides in sols leading to particle formation

Usually, the sol-gel method starts with a solution containing metal alkoxide, water and alcohol. A small amount of acid or ammonia is added as a catalyst, in order to adjust the reaction of particle formation or to promote the gelling reaction of the solution. A metal alkoxide[6,7], M(OR), where M is a metal atom, R is an alkyl group and n is the valence of M, is first partially hydrolyzed by water or totally as shown by the formula,

$$M(OR)_n + x\,H_2O \longrightarrow M(OH)_x(OR)_{n-x} + x\,ROH \qquad x \leqq n \qquad (1)$$

The value x, which shows the degree of hydrolysis of each metal alkoxide molecule in sol, depends on the type of metal, the content of water in the solution, the kind of catalyst, and the relative rates of hydrolysis and polycondensation. The hydrolysis of alkoxyl groups OR to hydroxyl groups OH is accompanied by a condensation reaction, as shown by the formulae,

$$-M-OH + H-O-M \longrightarrow -M-O-M- + H_2O \quad (2)$$

Condensation by dehydration

$$-M-OH + R-O-M \longrightarrow -M-O-M- + ROH$$

Condensation by dealcoholization (3)

As a result of polycondensation, particles consisting of metal-oxygen bondings may be produced.

The hydrolysis-polycondensation reactions are subject to the influence of many factors. Extensive studies have been made on the reactions of silicon alkoxides, but they are not fully understood yet. One can presume, however, that the growth of particles can be one-dimensional, leading to the formation of long-shaped particles when polycondensation takes place immediately after the hydrolysis of one or two OR groups of a molecule. The growth may be three-dimensional, leading to formation of round particles when polycondensation does not take place until all of the OR groups of a molecule are hydrolyzed to OH groups[8].

The growth of particles and the change in the aggregation state of primary particles take place in sols by the mechanism[9,10] illustrated in **Fig. 1** and listed in **Table 1**. (1) in **Fig. 1** shows that fine particles, that is, siloxane oligomers or polymers, grow as a result of condensation of the hydroxyl groups belonging to them. Ostwald ripening can take place after most of the hydrolyzed molecules are deposited on the particles. In Ostwald ripening, larger particles become larger at the expense of smaller particles, which may be dissolved due to higher activity and deposited on the larger particles, as shown in (2) of **Fig. 1**. Aggregation of particles may occur as a result of collision and bond formation at the contact point of particles. This results in loosely connected secondary particles, as shown in (3) of **Fig. 1**. When the secondary particles are connected infinitely as a network as shown in (4) of **Fig. 1**, it can be said that gelation has taken place. At this stage, if there is no water left and alcohol or other organic solvent is the only liquid, round particles remain without being firmly connected to each other until the gel is sintered by heating at higher temperatures. If water remains at gela-

Table 1 Mechanisms of growth and aggregation of particles[9,10]

Mechanism	Remark
(1) Reaction of a particle with alkoxide molecules	Simple growth of primary particles
(2) Ostwald ripening	Growth of larger particles
(3) Collision of one particle with another	Formation of secondary particles
(4) Association of secondary particles	Network formation
(5) Neck formation by dissociation and decomposition	Strong-bond formation between particles

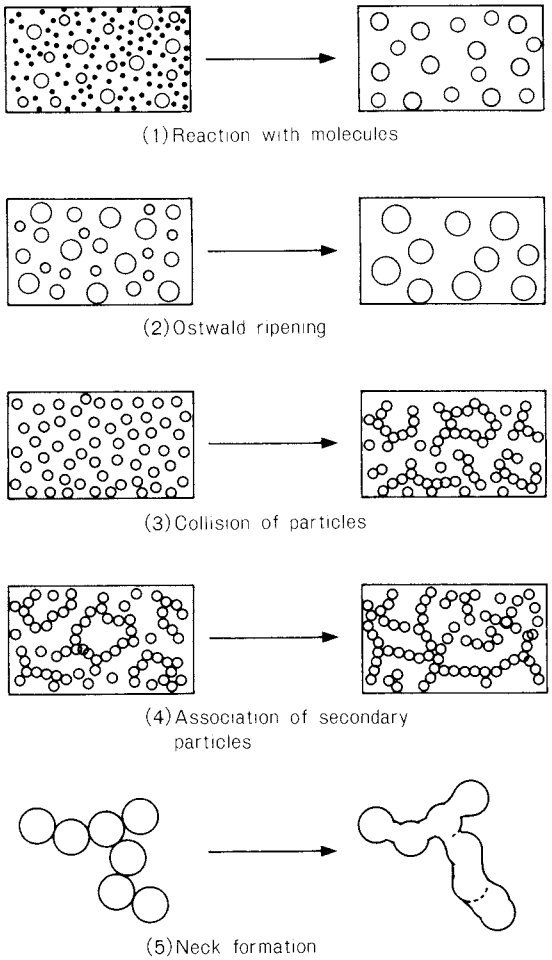

Fig. 1 Growth, aggregation and network formation of particles in sols and gels

tion, aging at temperatures lower than 100~150°C causes round particles to be firmly connected as a result of the dissolution of oxide components, for example the silica component, at the surface of round particles and deposition of the component at the neck points, as shown in (5) of **Fig. 1**.

If compact aggregates are formed instead of loosely bound aggregates (4 in **Fig. 1**) in sols and they are separated from the solvent, precipitation may occur. The resultant precipitates are not usually suitable for further processing, because they are not fine particles, and they no longer show the characteristics of the particles made by the sol-gel method. For the sol-gel method, particles shown in left-hand side of (3) of **Fig. 1** are suitable as starting powders for sintering, and gels shown in right-hand side of (4) of **Fig. 1** are suitable for the formation of monoliths, which form dried porous plates and cylinders, or sintered glass or ceramic plates and cylinders.

When fibers are drawn from a viscous sol without passing through powder processing, the sol must contain polymers or one-dimensinal long particles.

3. Powders prepared by the sol-gel method for sintered ceramics

Generally, high performance polycrystalline ceramics have high mechanical strength and exhibit excellent functional properties when they are characterized by: (1) being well sintered, (2) dense texture without pores, (3) fine grains, (4) high purity, and (5) high uniformity in composition throughout the grains in multicomponent systems. These characteristics can be achieved when the conditions shown in **Table 2** are filled[11]. Powders prepared by the sol-gel method using metal alkoxides can easily satisfy these requirements.

Table 2 Conditions required of starting powders for preparing high performance ceramics*

(a) Fine particles useful for high sinterability
(b) No formation of strong secondary particles
(c) Uniform particles size distribution for uniform pore or void size
(d) Particles of uniform composition corresponding to the bulk composition in multicomponent systems

*These conditions are easily satisfied when the sol-gel method is used.

3. 1 Fine particles without secondary particle formation

Powders consisting of fine particles can be sintered to transparent glasses without pores or to dense, well-sintered ceramics at low temperatures. Low temperature sintering of a powder compact is very important. This is because heating at high temperatures may cause the undesirable decomposition of glasses or ceramics, the volatilization of components and the contamination of ceramics from furnace materials.

Fine particles have a large surface energy which promotes sintering of the powder compact. In order for this effect to be pronounced, particles have to be fine ((a) of **Table 2**) at less than 1 μm. If primary particles are too fine at less than, say, 20 nm, however, larger secondary particles tend to be formed ((b) in **Table 2**) in which primary particles are tightly bonded together, and large pores are often found. Accordingly, it is desirable that the particle size should range between 20 nm-1 μm. It is known that the sol-gel method using metal alkoxide makes it possible to produce particles of such sizes.

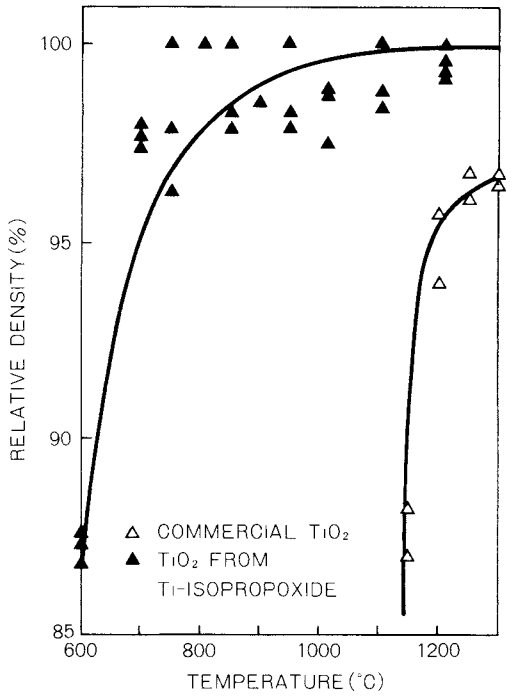

Fig. 2 Relative density vs. sintering temperature for TiO_2 sample prepared by the hydrolysis of titanium isopropoxide. Sintered in O_2 for 2 h. After L. Springer and M.F. Yan (Ref. 12)

Springer and Yan[12] showed that TiO_2 powder compacts made from titanium alkoxides, such as $Ti(OC_2H_5)_4$, $Ti(i\text{-}OC_3H_7)_4$ and $Ti(OC_4H_9)_4$, by the sol-gel method can be sintered at much lower temperatures than the compacts of commercial TiO_2 powders, as shown in **Fig. 2**. An alcoholic solution of titanium alkoxide was sprayed into water through an orifice having a small nozzle for hydrolysis. Titanium hydroxide powder consisting of particles of 20~60 nm in diameter were formed and heated for 2h at temperatures between 600~1200°C. **Figure 2** shows that powder compacts derived from a metal alkoxide are sintered to 99% of the theoretical density at temperatures lower than 900°C, whereas the commercial powder needs temperatures higher than 1230°C for densification to 96% of the theoretical density.

The possibility of obtaining well-sintered ceramics in the sol-gel method at temperatures 300~400°C lower than in conventional methods has been confirmed in the preparation of $BaTiO_3$ ceramics[13] from $Ba(OC_3H_7)_2$ and $Ti(OC_3H_7)_4$, PLZT ceramics[14] from $Pb(OC_5H_{11})_2$, $La(OC_3H_{11})_3$, $Zr(OC_5H_{11})_4$ and $Ti(OC_5H_{11})_4$, Y_2O_3-stabilized ZrO_2 ceramics[15] from zirconium and yttrium alkoxides and SiO_2 glass[16] from tetraalkoxysilanes.

3. 2 Uniform particle size distribution

Monosized powders are useful as materials for ceramics, because it is possible to produce densely packed green bodies with monosized powders. Such bodies can be sintered to fine-

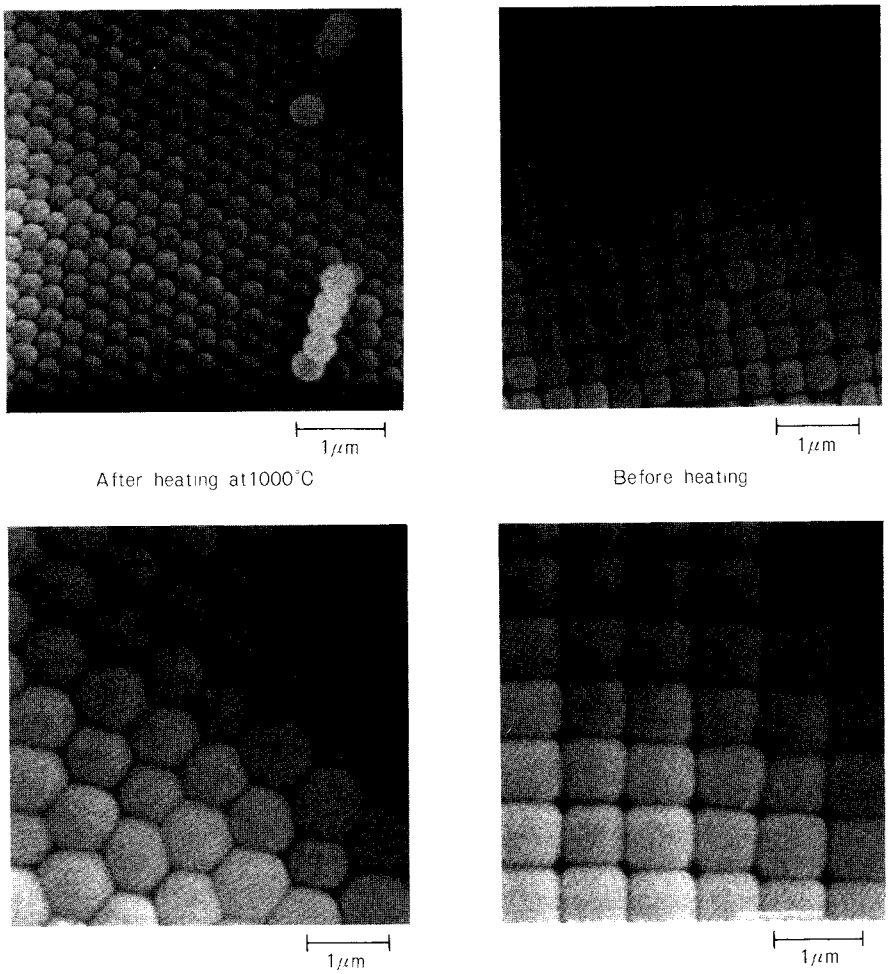

Fig. 3 Arrays of monosized SiO_2 particles prepared from a $Si(OC_2H_5)_4$ solution catalyzed with ammonia. SiO_2 particles form face-centered cubic lattice[22].

grained dense ceramics of uniform grain size. No abnormal growth of grains takes place due to the monosize nature of particles, and dense sintering is possible due to uniform pore size distribution ((C) in **Table 2**).

It is important, however, to avoid agglomeration of primary particles to secondary large particles with large pores fixed in them. One method for avoiding agglomeration is to deposit monodispersed particles from the sol by shortening the distances between them in sol with the distances being kept uniform[11]. Centrifugal deposition of particles on the bottom of the container or volatilization of the solvent can be used.

Monosized SiO_2 particles[17] are prepared by hydrolyzing $Si(OC_2H_5)_4$ in a $Si(OC_2H_5)_4$-C_2H_5OH-H_2O solution catalyzed with NH_3 in a controlled manner. Monosized particles of TiO_2[18,19] and ZrO_2[19,20] have also been prepared from $Ti(OC_2H_5)_4$, and $Zr(nOC_3H_7)_4$ or $Zr(OC_4H_9)_4$, respectively.

When monosized spherical SiO_2 particles are deposited on the test tube wall without agglomeration, particles are arranged in an ordered manner[21], if the condition for making deposition layers is appropriate. Disc-shaped pieces of dried SiO_2, 5~10 mm in length and width and 0.5~1 mm in thickness, show iridescence (rainbow-like color) under visible light due to diffraction of light. The ordered packing of SiO_2 spheres can be seen in **Fig. 3**[22]. Observation[23] of Kossel lines[24] produced by optical diffraction indicates that the particles are arranged in the face-centered cubic packing, forming a crystal of colloidal particles. It is interesting to note that hexagonally (a) and tetragonally (b) packed planes are seen in **Fig. 3**. These layers correspond to different particle surfaces of the face-centered cubic crystal.

3. 3 Uniform composition

In order to have a ceramic which exhibits an aimed function, the composition must be uniform and identical through the multicomponent ceramic, that is, the composition must be the same for all the grains constituting the ceramic and also must be uniform within individual grains of ceramic ((d) of **Fig. 1**). This can be relatively easily achieved by the sol-gel method using metal alkoxides, because the sol-gel method starts from a homogeneous solution, and accordingly the oxide particles may have a uniform composition corresponding to that of the bulk.

Arai[25] synthesized larger-structured aluminate ceramics of $BaO \cdot 6Al_2O_3$ which serves as support of the oxidation catalyst. It was found that the composition of the sintered body was identical in all the grains and was uniform within every grain when the starting powder is prepared by hydrolyzing barium and aluminum alkoxides in the solution containing both alkoxides. The sintering was done at 1600°C.

It was also shown[26] that the so called "new mullite ceramic" consisting of only one phase exactly corresponding to the composition $3Al_2O_3 \cdot 2SiO_2$ can be made by using metal alkoxides. It should be mentioned that this mullite is very well sintered.

4. Formation of shaped gels by the sol-gel method

It this section, particle formation in sols for preparing shaped gels without passing through powder processing will be discussed based mainly on our work on silica.

4. 1 Particles for monolith formation

For direct formation of monoliths, such as sheets, plates and rods, the formation of particles of suitable shape and size in sols is very important.

The major technological problems in the direct preparation of a silica gel monolith are the possible occurrence of cracks and fractures dur-

Table 3 Methods proposed for producing dried silica gel monoliths without crack formation[4]

Method	Investigator
(1) Drying under a supercritical condition	Zarzycki *et al*[9]
(2) Reaction of the solution with pH>7 at a higher temperature	Yamane *et al*[27], Susa *et al*[28]
(3) Use of colloidal silica as the starting material	Rabinovich *et al*[29], Scherer *et al*[30]
(4) Use of mixture of tetraethoxysilane and fine silica particles	Toki *et al*[31]
(5) Use of a special solvent called a Drying Control Chemical Additive	Wallace and Hench[32], Adachi and Sakka[33]
(6) Use of high HCl solution	Kozuka and Sakka[34]

ing the process of a wet gel monolith to a dry gel monolith. The six methods shown in **Table 3** have been proposed[4] to avoid cracks during drying, and they were actually used for producing silica gel monoliths without cracks. The basic principle common to the methods proposed is to lower the capillary force arising from the surface tension of the liquid in the drying gel. One of the potential ways to do this is to make particles large so that the pores might be large. The reciprocal proportionality of the capillary force to the pore diameter can be seen from the formula[35),36)],

$$\Delta P = \frac{4\gamma\cos\theta}{D} \qquad (4)$$

where ΔP is the capillary force, γ is the surface tension of the liquid, θ is the contact angle, and D is the capillary diameter corresponding to the pore diameter.

The authors used methods (5) and (6) to make two types of dried gel monoliths with 30~50 nm particles and 0.1~5 μm particles, respectively. Particle sizes and their significances in making crack-free gel monoliths will be described next.

4. 1. 1 Silica gel monolith with particles of 30~50 nm in diameter

Dried silica gel monoliths based on method (5) in **Table 3** can be made from a solution containing an appropriate amount of ammonia[33)]. **Figure 4** shows the particulate structure of a dried gel (a) and a sintered product obtained by heating the gel to 1050°C (b).

In order to produce a dry gel monolith, a mixed solution of the composition $1Si(OCH_3)_4 \cdot 1(CH_3)2NCHO \cdot 2.2CH_3OH \cdot 10H_2O \cdot 3.7 \times 10^{-4} NH_4OH$ was reacted to gel at 30°C and aged by raising the temperature from 70°C to 160°C in 24 h. The wet gel was then dried by raising the temperature from 70°C to 150°C~160°C.

The porous dry gel is particulate and porous as seen in (a) of **Fig. 4**. The size of particles ranges from 30 to 50 nm, which gives continuous pores of 16 nm in average diameter. The formation of dried gel monoliths without cracks can be ascribed to the low surface tension of dimethylformamide which is retained at the final stage of drying of the wet gel, and to the considerably large pores due to large particles formed in the sol.

It should be noted, however, that the pore size is not uniquely determined by the particle size alone[37,38)]. The surface tension of the liquid filling the pores of the wet gels during drying may affect the pore size found after drying. The larger surface tension causes higher shrinkages of the pores because the pore walls consisting of particles undergo compressive stress arising from the capillary force based on the surface tension of the liquid. It has been found that the use of formamide in place of dimethylformamide in the starting solution gives smaller pores of 6~8 nm in diameter in the dried gel, although the particle size is similar to that in the gel prepared from a solution containing di-

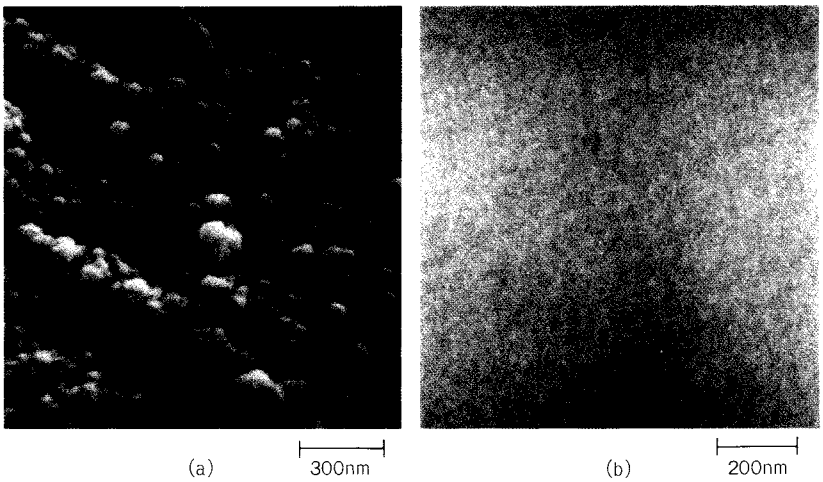

Fig. 4 SEM micrographs of the fractured surfaces of gels (a) dried at 150°C and (b) sintered for 2 h at 1050°C, prepared from the solution 1TMOS : 1DMF : 2.2CH_3OH : 10H_2O : 3.7 x $10^{-4}NH_4OH$[33)].

methylformamide. This makes it difficult to prevent crack formation in the gel during drying.

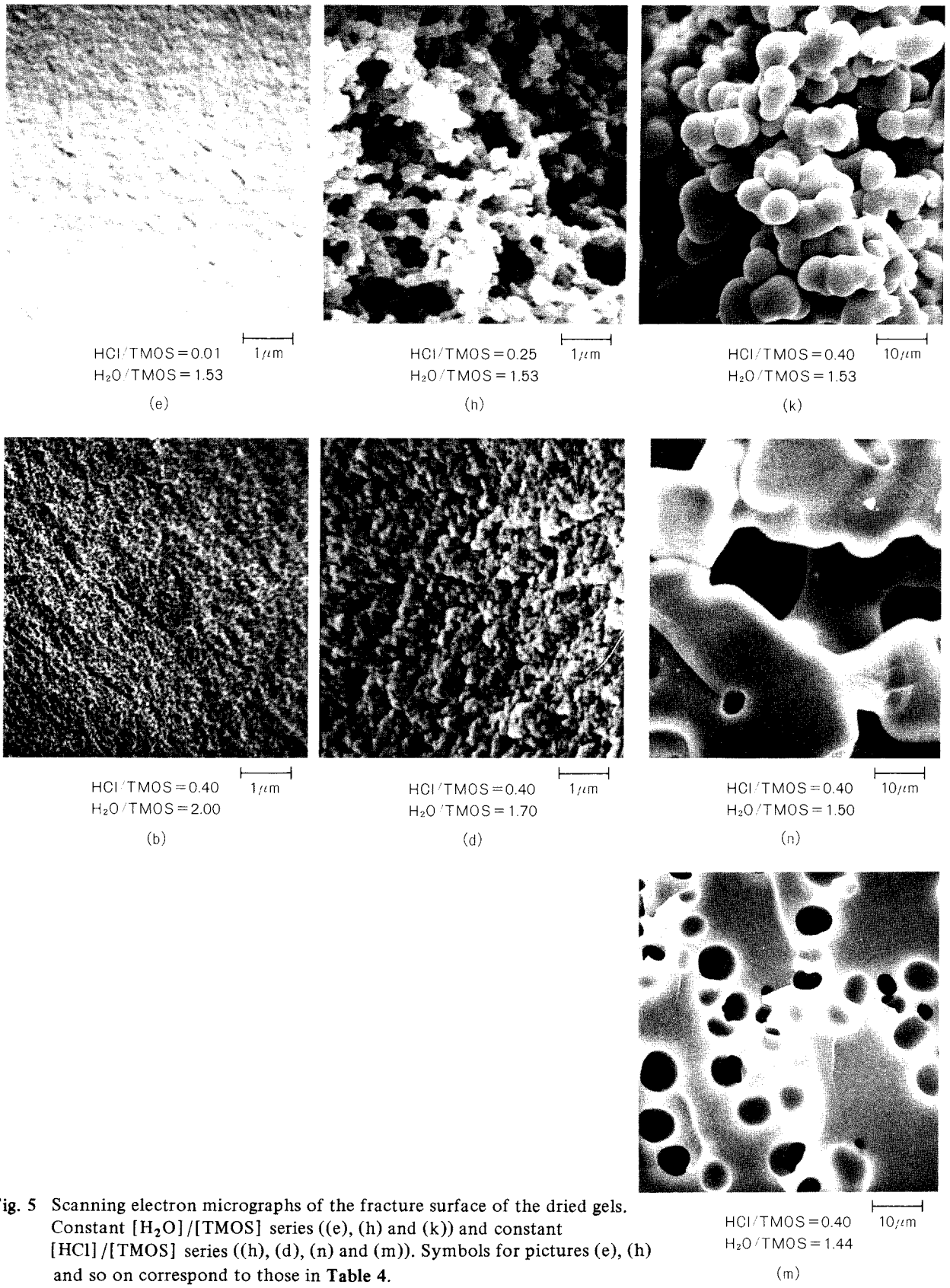

Fig. 5 Scanning electron micrographs of the fracture surface of the dried gels. Constant $[H_2O]/[TMOS]$ series ((e), (h) and (k)) and constant $[HCl]/[TMOS]$ series ((h), (d), (n) and (m)). Symbols for pictures (e), (h) and so on correspond to those in **Table 4**.

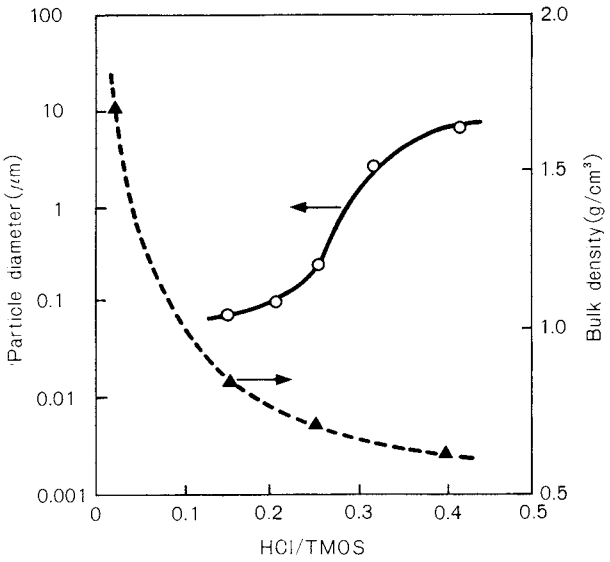

Fig. 6 Dependence of the particle size and the gel bulk density on [HCl]/[TMOS] ratio for the solutions having a [H_2O]/TMOS] ratio of 1.53.

4. 1. 2 Silica gel monoliths with particles of 0.1 μm to 5 μm in diameter

Silica gel monoliths with very large particles of 0.1 μm to 5 μm in diameter can be made by the hydrolysis-polycondensation reaction of tetramethoxy-silanes in solutions of the system $Si(OC_2H_5)_4$-CH_3OH-H_2O-HCl with very low concentrations of water and very high concentrations of HCl. The compositions, appearances of gels and gelling times are shown in **Table 4**[39], and some SEM photographs are shown in **Fig. 5**. **Figure 6** shows the plots of the particle size and bulk density of a dried gel as a function of [HCl]/[$Si(OCH_3)_4$] ratio for the solutions with a constant [H_2O]/[TMOS] ratio of 1.53.

Figure 5 and **6** indicate that in the series of [H_2O]/[TMOS] = 1.53 (e to k in **Table 1**), solutions of high HCl contents at [HCl]/[TMOS] ratios equaling 0.15 through 0.40 give gels with a particulate structure, as seen in photographs h and k in **Fig. 5**, and that the particle size increases with increasing HCl content. In the gel prepared from a solution of [HCl]/[TMOS] = 0.40 (k in **Fig. 5**), round-shaped particles of about 5 μm in diameter are connected to each other, forming SiO_2 skeletons. The inspection of SEM micrographs indicates that the pore size in dried gels increases from 0.1 μm for [HCl]/[TMOS]=0.15 to 10 μm for [HCl]/[TMOS]=0.40 with increasing HCl content.

Since the pore size is large, the wet gels can be dried with no or almost no formation of cracks, as seen in **Fig. 7**. With the composition of [HCL]/[TOMS]=0.40 (k in **Table 4**), crack-free large place (19 cm × 23 cm × 9 mm) as shown in **Fig. 8** can be made. It is interesting to see that crack formation is avoided when the pore size is large, and accordingly, the capillary force is small as seen from formula (4), although the liquid remaining at the final stage of drying may be water with a high surface tension.

The close inspection of the SEM micrographs

Table 4 Composition and properties of $Si(OCH_3)_4 - CH_3OH - H_2O$–HCl solutions[39]

	Compositions			Sedimentation	Appearance at gelation	Appearance of dried gels	Gelling time (h)
	H_2O/TMOS	HCl/TMOS	CH_3OH/TMOS				
(a)	2.00	0.01	2	No	Transparent	Transparent	12.6
(b)	2.00	0.40	2	No	Transparent	Transparent	0.6
(c)	1.70	0.01	2	No	Transparent	Transparent	13.4
(d)	1.70	0.40	2	No	Opalescent	Opalescent	1.0
(e)	1.53	0.01	2	No	Transparent	Transparent	14.5
(f)	1.53	0.15	2	No	Opalescent	Opaque	3.6
(g)	1.53	0.20	2	No	Opalescent	Opaque	2.9
(h)	1.53	0.25	2	No	Opaque	Opaque	2.5
(i)	1.53	0.30	2	No	Opaque	Opaque	1.9
(j)	1.53	0.35	2	Yes	Opaque	Opaque	(1.6)*
(k)	1.53	0.40	2	Yes	Opaque	Opaque	(1.3)*
(l)	1.44	0.01	2	No	Transparent	Transparent	17.2
(m)	1.44	0.40	2	Yes	Opalescent	Opaque	(1.4)*

*No clear determination was made since gelation occurred during sedimentation.

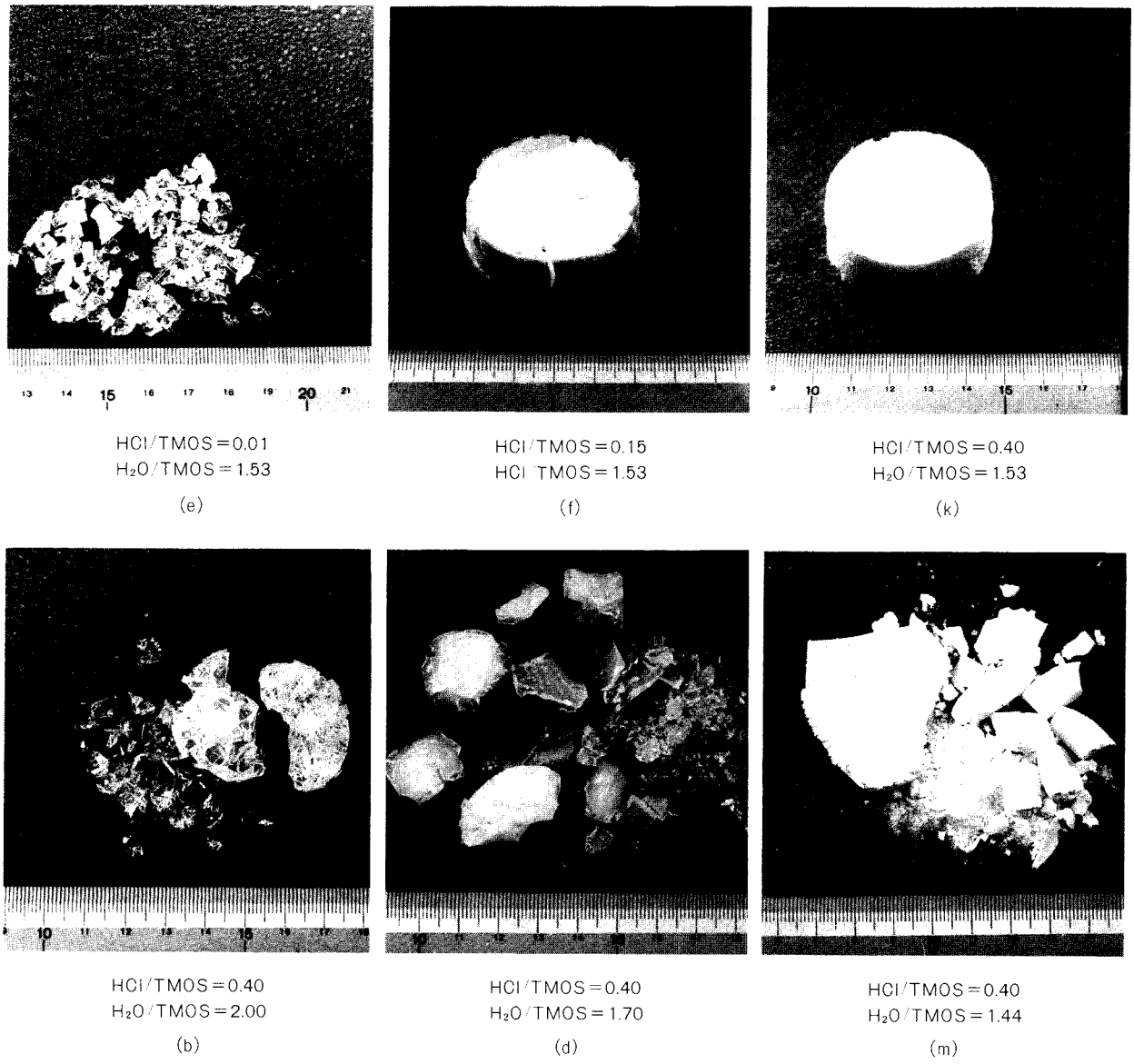

Fig. 7 Appearance of the dried gels. Constant $[H_2O]/[TMOS]$ series ((e), (f) and (k)) and constant $[HCl]/[TMOS]$ series ((k), (b), (d) and (m)). Symbols of pictures (e), (f) and so on correspond to those in **Table 4**.

of gels prepared from a solution with [HCl]/[TOMS]=1.53 and [HCl]/[TMOS]=0.40 (k in **Table 5**) shown in **Fig. 9** indicates that large particles reaching 5 μm in diameter are porous secondary particles consisting of much smaller primary particles[40]. This is also indicated by high specific surface area of more than 150 m^2/g, which cannot be explained, if it is assumed that the observed large round particles are non-porous. The porosity decreases with drying time, as seen from comparison of (a) with (b) in **Fig. 9**. The surface of large particles becomes smoother when the drying time is prolonged to

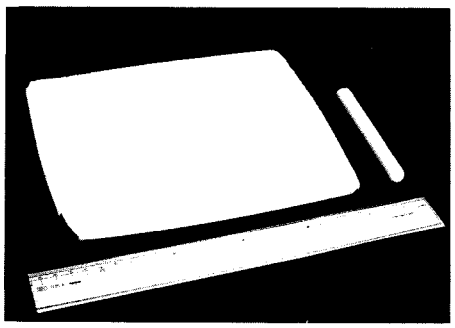

Fig. 8 A crack-free gel plate of 21 cm x 17 cm x 0.9 cm prepared from a TMOS solution of the composition, TMOS : H_2O : HCl : CH_3OH = 1 : 1.53 : 0.25 : 2 in mole (g in **Table 4**)

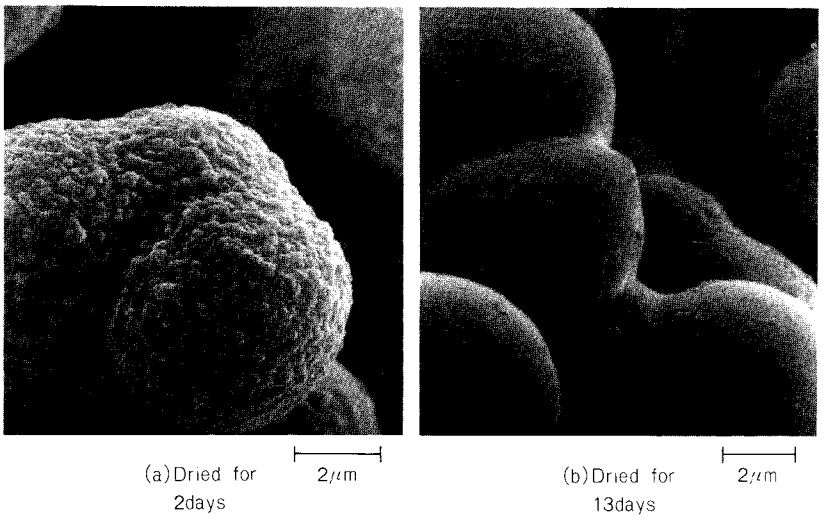

Fig. 9 SEM micrographs of gels prepared from the solution with $[H_2O]/[TMOS] = 1.53$ and $[HCl]/[TMOS] = 0.40$

13 days, although a pretty large surface area of 60 m^2/g is still retained.

In the series of a constant HCl content at $[HCl]/[TMOS] = 0.40$ to which pictures k, b, d, n and m in **Fig. 5** belong, the particulate structure can be seen for $[H_2O]/[TOMS] < 1.50$ (k, b and d), and the particle size increases with decreasing $[HCl]/[TOMS]$ ratio. A still higher H_2O content, however, leads to a higher degree of coagulation of particles, as seen from (n) in **Fig. 5** and to the formation of closed pores in the matrix, as seen from (m) in **Fig. 5**. This structure is harmful to the formation of a crack-free dried gel monolith, because the vaporization of the solution in these closed pores causes the fracture of the gel during drying of the wet gel, as seen from **Fig. 7**.

4. 2 Particles for fiber drawing from viscous gels

For the direct sol-gel preparation of fibers, gel fibers are made by fiber-drawing from the viscous alkoxide solution at near room temperature[41),42)]. **Figure 10** shows the time change of the viscosity[41)] of a drawable $Si(OC_2H_5)_4$-H_2O-C_2H_5OH-HCl solution with a mol ratio $r = [HCl]/[Si(OC_2H_5)_4]$ of 2 which is subjected to a hydrolysis-polycondensation reaction in a beaker having a cover perforated with a few small holes. When the viscosity reaches about 10 poises, the solution becomes spinnable, and fibers can be drawn by pulling a glass rod up from the sol or pulling the sol through an orifice.

It has been found that all starting solutions that become viscous in the gelation process do not necessarily exhibit spinnability. Only solutions with water contents lower than 4 in the $[H_2O]/[Si(OC_2H_5)_4]$ ratio become spinnable when catalyzed with low concentrations of hydrochloric acid[41)]. The occurrence of spinnability has been ascribed to the shape of particles in sols. It has been assumed that only solutions containing long-shaped polymers or particles are spinnable, but solutions containing round-shaped particles or aggregates do not exhibit spinnability. This assumption has been confirmed to be valid by examining the relationship[43)] between the reduced viscosity η_{sp}/C

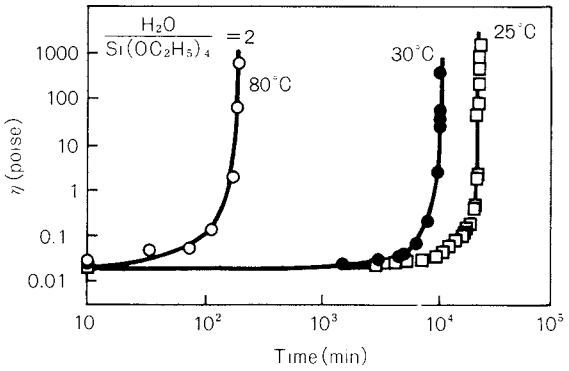

Fig. 10 Variation of the viscosity of a drawable $Si(OC_2H_5)_4$ solution with the molar ratio $H_2O/Si(OC_2H_5)_4 = 2$ at 25, 30 and 80°C as a function of time[4,41)]

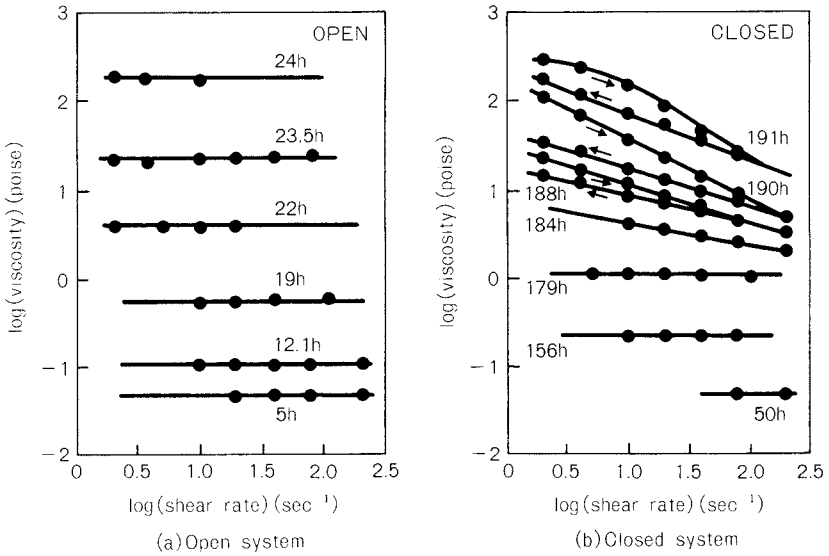

Fig. 11 Viscosity of $Si(OC_2H_5)_4$ solutions at various shear rates in the open and closed systems[42]. Numbers shown in the figure denote reaction time of the solution. Reaction at 60°C. Viscosity measurement at 30°C.

and SiO_2 concentration C, when η_{sp} is the specific viscosity, and the relationship[44] between the intrinsic viscosity $[\eta]$ of the sol and the number-averaged molecular weight, M_n.

Recently, the occurrence of spinnability was correlated with the flow characteristics of the solution, as shown in **Fig. 11**. **Figure 11** shows the viscosities versus shear-rate relationship for a tetraalkoxysilane solution of the composition $Si(OC_2H_5)_4 : H_2O : C_2H_5OH : HCl = 1 : 2 : 1 : 0.01$, which exhibits spinnability when subjected to the hydrolysis-polycondensation reaction in the open system. No spinnability occurs when reacted in the closed system. It is seen in **Fig. 11** that the solution which is reacted in the open system and spinnable at viscosities higher than 10 poises retain Netwonian behavior (**Fig. 11**a) at high viscosities, whereas the non-spinnable solution reacted in the closed system becomes non-Newtonian (**Fig. 11**b) at high viscosities.

Figure 12 shows model structures which illustrate the change of structures of the solution during sol-to-gel transition. **Figure 12**(A) illustrates that linear (one-dimensional) long-shaped particles with less cross-linkages gives Newtonian nature and spinnability to viscous sols. This is because linear particles slip by each other without destruction under large shear rates even at high viscosities, and cross-linkings are formed between linear particles only after gelation. On the other hand, **Fig. 12**(B) indicates that in sols containing round particles, network-like clusters or secondary aggregates with loose bondings are constructed from primary round particles at high viscosities. This may cause shear thinning behavior and non-spinnability.

It is known that, in order to produce long-shaped siloxane particles in the silicon alkoxide solutions, the starting solution should be catalyzed by acid, and the water content should be small. An ammonia catalyst and a high water concentration produce round-shaped particles.

References

1) Sakka, S.: The Science of the Sol-Gel Method, Agne-Shofu-Sha, Tokyo (1988) [in Japanese].
2) Sakka, S.: *Bull. Chem. Soc. Japan*, **87** [3], 243-252 (1987) [in Japanese].
3) Sakka, S.: *Treastise on Materials Science and Technology*, **22**, Glass III, ed. M. Tomozawa and R. Doremus, Academic Press, New York, p. 129-167, (1982).
4) Sakka, S.: Advances in the Fusion of Glass, ed. by D.F. Bickford *et al.*, The American Ceramic Society, 2.1-2.27 (1988).
5) Sakka, S., K. Kamiya and T. Yoko: ACS Symposium Series, 360, Inorganic and Organometallic Polymers, ed. by M. Zeldin *et al.*, American Chemical Society, Washington, D.C., p. 345-353 (1988).
6) Bradley, D.C., R.C. Mehrotra and D.P. Gaur, Metal Alkoxides, Academic Press (1978).
7) Mehrotra, R.C.: *J. Non-Crystal. Solids*, **100**, 1-15, (1988).

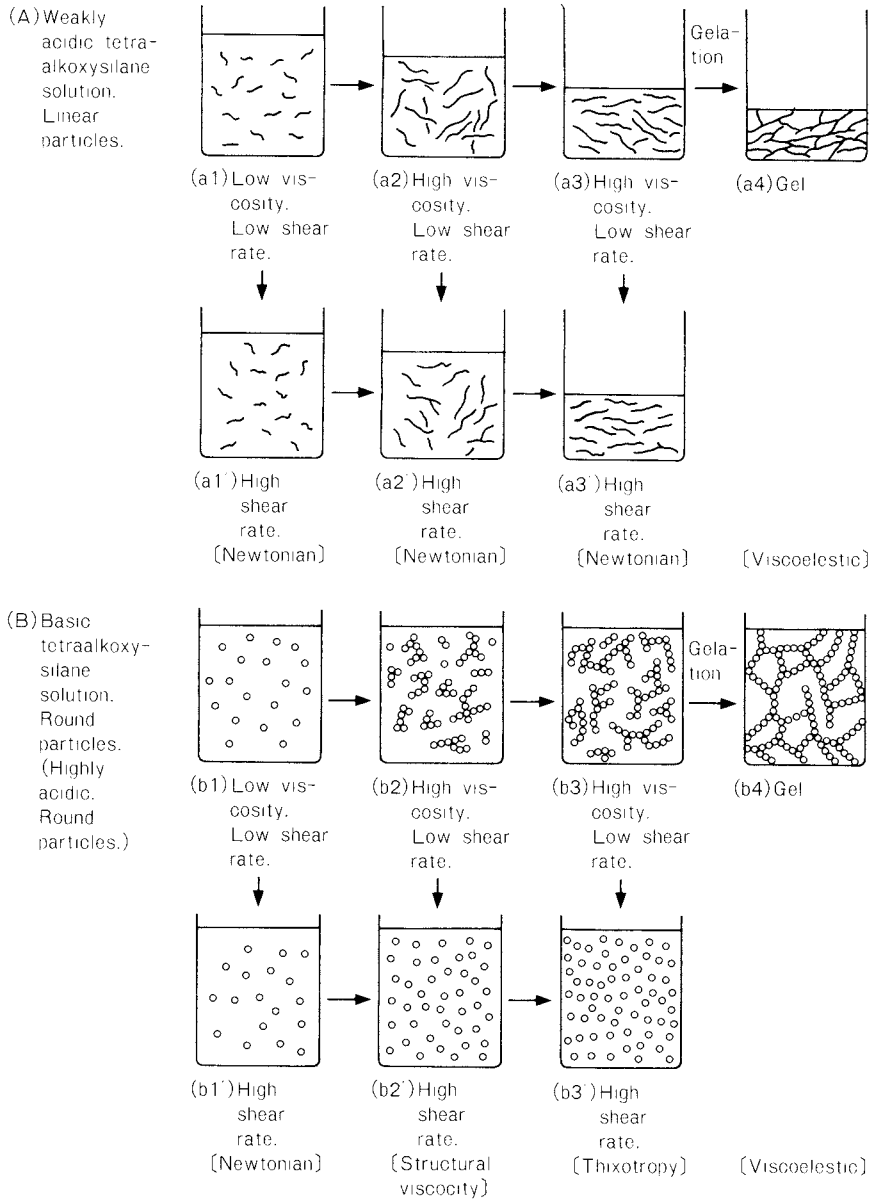

Fig. 12 Development of particles in solutions illustrating the changes in their rheological behavior in the sol-gel transition

8) Kamiya, K., T. Yoko and S. Sakka: *Yogyo-Kyokai-Shi,* **92**, 242-249 (1984).
9) Zarzycki, J., M. Prassas and J. Phalippou: *J. Mat. Sci.,* **17**, 3371-3379 (1982).
10) Iler, R.K.: The Chemistry of Silica, John Wiley, New York (1979).
11) Barringer, E., N. Jubb, B. Fegley, R.L. Pober and H.K. Bowen: The Ultrastructure Processing of Glass, Ceramics and Composites, ed. L.L. Hench and D.R. Ulrich, John Wiley & Sons, New York 315-333 (1984).
12) Springer, L. and M.F. Yan: Ultrastructure Processing of Glasses, Ceramics and Composites, ed. L.L. Hench and D.R. Ulrich, John Wiley & Sons, New York, 464-475 (1984).
13) Mazdiyani, K.S., R.T. Dolloff and J.S. Smith: *J. Amer. Ceram. Soc.,* **52**, 523-526 (1969).
14) Brown, L.M. and K.S. Mazdiyasni: *J. Amer. Ceram. Soc.,* **55**, 541-544 (1972).
15) Phillipi, C.M. and K.S. Mazdiyasni: *J. Amer. Ceram. Soc.,* **54**, 254-258 (1971).
16) Decottignies, M., J. Phalippou and J. Zarzycki: *J. Mater. Sci.,* **13**, 2605-2608 (1978).
17) Shimohira, T. and N. Tomuro: *Powder and Powder Metallurgy,* **23**, 249-254 (1976) [in Japanese].
18) Ikemoto, T., K. Uematsu, N. Mizutani and M. Kato: *Yogyo-Kyokai-Shi,* **93**, 261-266 (1985) [in Japanese].
19) Fegley, B and E.A. Barringer: *Mat. Res. Soc. Symp. Proc.,* Vol.**32**, 187-196, (1984).

20) Ikemoto, T., N. Mizushima, M. Kato and Y. Mitarai: *Yogyo-Kyokai-Shi,* **93**, 585-586 (1985).
21) Onoda, G.Y.: The Science of Ceramic Chemical Processing, ed. by L.L. Hench and D.R. Ulrich, John Wiley & Sons, 504-512 (1986).
22) Adachi, T., M. Okada and S. Sakka: Unpublished data.
23) Observation was made by Prof. T. Yoshiyama and I. Sogami of Kyoto Industrial University.
24) Yoshiyama, T., I. Sogami and N. Ise: *Phys. Rev. Lett.,* **53**, 2153-2156 (1984).
25) Arai, H.: '87 Arita International Symposium on Fine Ceramics, 88-113 (1987).
26) Pask, J.A., X.W. Zhang, A.P. Tomsia and B.E. Yoldas: *J. Amer. Ceram. Soc.,* **70**, 704-707 (1987).
27) Yamane, M., S. Aso, S. Okano and T. Sakaino: *J. Mat. Sci.,* **14**, 607-611 (1979).
28) Susa, K., J. Matsuyama, S. Satoh and T. Suganuma: *Elect. Lett.,* **18**, 449-450 (1982).
29) Rabinovich, E.M., D.W. Johnson, J.B. McChesney and E.M. Vogel: *J. Non-Crystal Solids,* **63**, 155-161 (1984).
30) Scherer, G.W. and J.C. Luong: *J. Non-Crystal Solids,* **63**, 163-172 (1984).
31) Toki, M., S. Miyashita, T. Takeuchi, S. Kanbe and A. Kochi: *J. Non-Crystal. Solids,* **100**, 479-482 (1988).
32) Wallace S. and L.L. Hench: *Mat. Res. Soc. Symp. Proc., Vol.* **32** (1984) 47-52.
33) Adachi T. and S. Sakka: *J. Mat. Sci.,* **22**, 4407-4410 (1987).
34) Kozuka H. and S. Sakka: *Chem. Lett.,* 1791-1794 (1987).
35) G.W. Scherer: *Yogyo-Kyokai-Shi,* **95**, 21 (1987).
36) Zarzycki, J.: "Ultrastructure Processing of Ceramics, Glasses and Composites" ed. by L.L. Hench and D.R. Ulrich, John Wiley, New York, p. 37 (1984).
37. Adachi, T., S. Sakka and M. Okada: *Yogyo-Kyokai-Shi,* **95**, 970-975 (1987).
38) Adachi T. and S. Sakka: *J. Non-Crystal Solids,* **99**, 118-128 (1988).
39) Kozuka, H. and S. Sakka: *Chemistry of Materials,* **1**, 398-404 (1989).
40) Yamaguchi, J., H. Kozuka and S. Sakka: To be published in Proceedings, The 1st Meeting of the Society of New Functional Materials, S. Somiya and M. Doyama, Tokyo (March, 1989).
41) Sakka, S.: *Mat. Res. Soc. Symp. Proc.,* Vol. **32**, 91-99 (1984).
42) Sakka, S.: Rheology of Sols in the Sol-Gel Processing, to be published in Winter School on Glasses and Ceramics from Gels, August 1989, Sao Carlos, Brazil.
43) Sakka, S. and K. Kamiya: *J. Non-Crystal Solids,* **48**, 31-46 (1982).
44) Sakka, S., K. Kamiya, K. Makita and Y. Yamamoto: *J. Non-Crystal Solids,* **63**, 223-235 (1984).

Short Communication

Applications of Mechanofusion System for the Production of Superconductive Oxides†

Makio Naito and Masahiro Yoshikawa
Micromeritics Laboratory
*Hosokawa Micron Corp.**

1. Introduction

"Mechanofusion" is a technique of creating particulate materials with new properties by mechanochemical surface fusion as a result of certain mechanical energy exerted on the surface of different kinds of particles[1,2]. In this paper, some examples of application of this technique for the field of superconductive oxides are introduced.

A new Mechanofusion System (AM-20FS) has been developed on the basis of "Angmill", dry attrition type mill. It enables us to grind different kinds of powder materials down to submicron level, to disperse them uniformly and to create composite particles from them. It was made clear from experiments that Mechanofusion was an effective method to prepare the raw powdery materials of superconductive oxides and multi-component targets for superconductive thin films.

2. A new Mechanofusion System "AM-20FS"

Figure 1 shows a picture of this machine. The basic mechanism is the same as conventional types of Mechanofusion system, but it has the following additional features:

(1) As in most cases fine powders are used as raw materials of oxide superconductors, this apparatus is designed to reduce their adhesion in the Mechanofusion chamber by exerting impact forces to its bottom and vibration forces to the attrition tips fixed on its axis.

(2) As hazardous powders such as Pb or $BaCO_3$ are usually used, the air in the chamber is led to an air filter (HEPA filter) to prevent their leakage during its operation. This filter system is set as an option.

Specifications of AM-20FS are summarized in **Table 1**.

Table 1 Specifications of AM-20FS

Feed charge per batch (powder bulk volume)	: 100 ~ 300 cc
Power required	: 3.7 kW
Dimensions of rotating chamber	: ϕ200 x 70H
Chamber rotation	: max. 2,450 r.p.m.

3. Application to produce superconductive oxides[3]

In case of yttrium-based superconductors, each fine powder of Y_2O_3, $BaCO_3$ and CuO was weighed to satisfy the mixing ratio of Y : Ba : Cu = 1 : 2 : 3. These powders were treated in a batch operation at a high rotation speed for certain time. The processed powder was calcined in an electric furnace for provided time, and treated by AM-20FS. Then the treated powder was compressed to form a compacted pellet, and sintered for several hours followed by annealing at a certain temperature.

Figure 2 shows an example of temperature dependence of resistivity of the produced samples. It is obvious that the critical temperature reaches 90 K class, and the width of transition

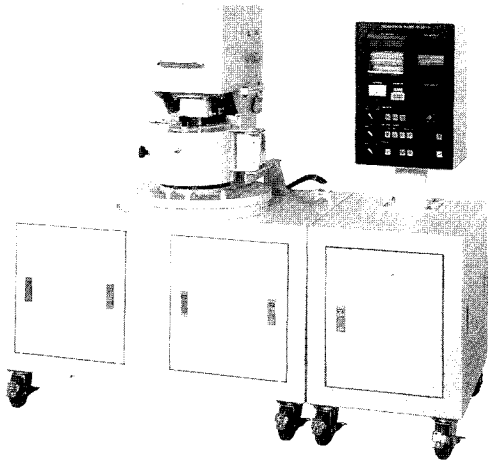

Fig. 1 Picture of AM-20FS

* No. 9, Shoudai Tajika 1-chome, Hirakata, Osaka, 573
TEL. 0720 (55) 2220
† Received Aug. 20, 1989

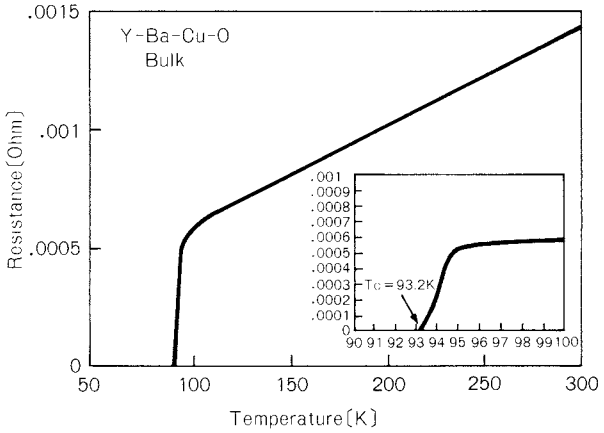

Fig. 2 Temperature dependence of resistivity of Y-Ba-Cu-O sample obtained by our process

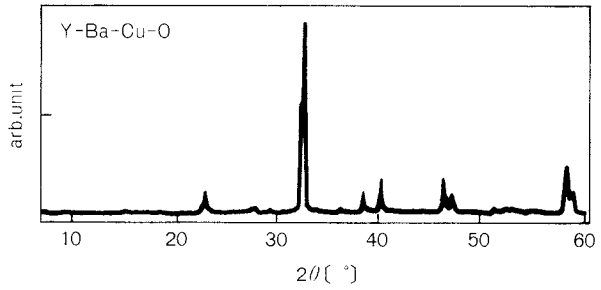

Fig. 3 X-ray diffraction pattern of Y-Ba-Cu-O sample obtained

temperature is narrow. **Figure 3** shows the chart of X-ray diffraction pattern of samples obtained, which shows this sample has the orthorhombic crystal structure of Y-Ba-Cu-O.

Furthermore, the variations in composition of powder treated by the Mechanofusion before calcining were measured to evaluate its uniformity. Each sample of 0.2 g was picked up from the treated powder randomly, and ten samples were analyzed to measure the component ratios of Ba/Y and Cu/Y by an inductively coupled plasma method. As a result, the measured fluctuation coefficient was within 1% in each component ratio. It was found from these experimental results that Mechanofusion was an effective method for preparing Y-Ba-Cu-O superconductors.

As it is well-known, dry mechanical processes such as Mechanofusion method have several advantages compared with wet ones. For example, the former processes do not contain a powder drying operation which is necessary for the latter one. But the dry mechanical processes have much difficulties in treating fine powders properly because of their adhesion phenomena. **Table 2** indicates the dependence of treating methods by using dry vibration ball mill on critical temperature T_c of Y-Ba-Cu-O superconductors[4]. Here the same kinds of powders as the case of our method were used as raw materials. When a dry vibration ball mill is substituted for Mechanofusion apparatus, the T_c shows the lower value of 79.3 K. In such a case, a calcining and grinding process must be usually repeated[5] several times to improve the quality of superconductors as shown in **Table 2**. On the other hand, in case of the process by using Mechanofusion, high quality superconductors were produced through single calcining and grinding process.

Why does Mechanofusion provide such a high quality superconductors effectively? **Figure 4** shows the example of SEM and XMA pictures of a composite particle treated by Mechanofusion before calcining. Here **Fig. 4 (a)** is a SEM photograph, and **Figs. 4 (b), (c)** and **(d)** are a XMA mapping picture of Y, Ba and Cu respectively. It is obvious from these pictures that a composite particle in **(a)** is composed of Y, Ba

Table 2 Effect of mechanical processes of treating powders on critical temperature T_c of Y-Ba-Cu-O superconductors

No.	Machine	Production process before forming			T_c (K)
1	Mechanofusion	Mechano-fusion	Calcining + Mechanofusion		92 ~ 93
2	Vibration ball mill (dry type)	Grinding	Calcining + Grinding		79.3
3	Vibration ball mill (dry type)	Grinding	Calcining + Grinding	Calcining + Grinding	84.7

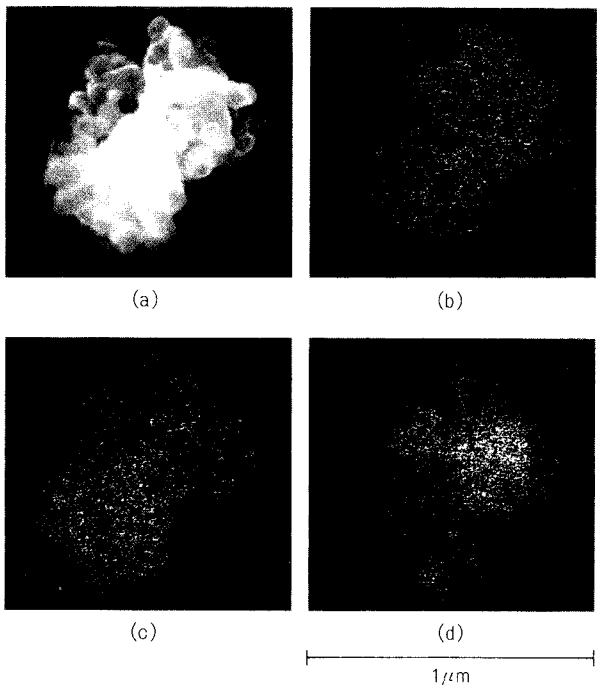

Fig. 4 Pictures of a composite particle treated by Mechanofusion before calcining
(a): SEM, **(b)**, **(c)**, **(d)**: XMA mappings of Y, Ba, Cu component

and Cu particles ground down to submicron level. Furthermore, as it was already explained, the treated powder has a sufficient uniformity of each component. Therefore, it is considerable that a solid phase reaction of the treated powder is conducted efficiently by the grinding and the mixing effects of Mechanofusion.

As another feature of Mechanofusion, the authors[1,2] have already reported that particles of one kind are firmly fixed onto the surface of those of the other kind by exerting certain mechanical forces. It suggests that the contact area of different kinds of particles processed by Mechanofusion is larger than that of the powder mixture under usual compaction. It is thought this effect also might promote the solid phase reaction.

The Mechanofusion is also applied for preparing Bi-based superconductors. **Figure 5** shows the example of temperature dependence of resistivity of Bi-Pb-Sr-Ca-Cu-O composite obtained by our process, where the T_c-value indicates 106 K. We are now trying to produce Bi-based superconductors which has higher amount of high-T_c phase.

4. Applications to produce superconductive thin films[6,7]

Multi-component targets have been widely used to fabricate the thin films of superconducting oxides. As it is well-known, these targets have been produced with a process, which contains the mixing of each component with a ball mill or a co-precipitation method. But when Mechanofusion is applied, it will be a convenient method to produce them.

Figure 6 shows the relationship between the electric resistance and the temperature of a Bi-Pb-Sr-Ca-Cu-O thin film. Here, it was formed by a rf sputtering apparatus with a Bi-Pb-Sr-Ca-Cu-O powder target, and treated in an electric

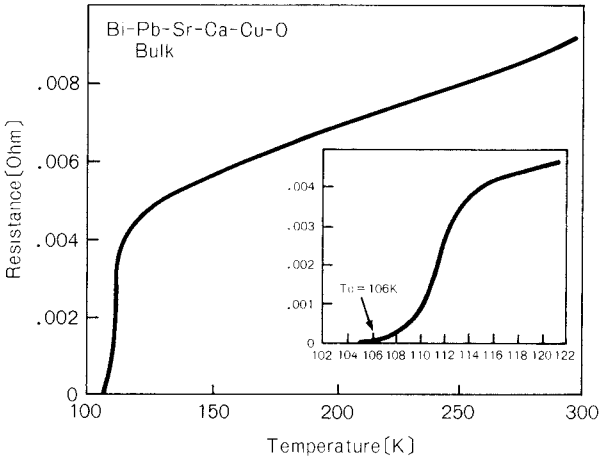

Fig. 5 Temperature dependence of resistivity of Bi-Pb-Sr-Ca-Cu-O sample obtained by our process

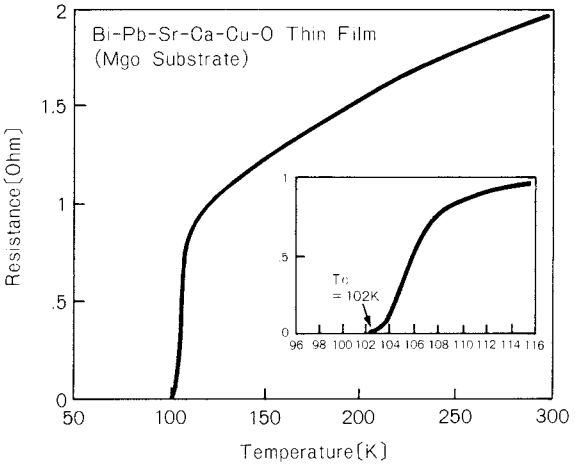

Fig. 6 Relationship between the electric resistance and the temperature of Bi-Pb-Sr-Ca-Cu-O thin film

furnace for about 170 hours. The powder target was produced by treating raw materials with Mechanofusion and calcining them. As the T_c-value shows 102 K, it is proved that this target has also good performance.

As another case, Fig. 7 shows the temperature dependence of resistivity of Y-Ba-Cu-O thin film fabricated by using an ion beam sputtering method. Here the sintered target prepared by Mechanofusion was used as a sputtering resource. As the T_c-value indicates 88 K, it is found that this sintered target has a good performance. These experimental results show that Mechanofusion contributes to the production of multi-component targets of superconductive oxides.

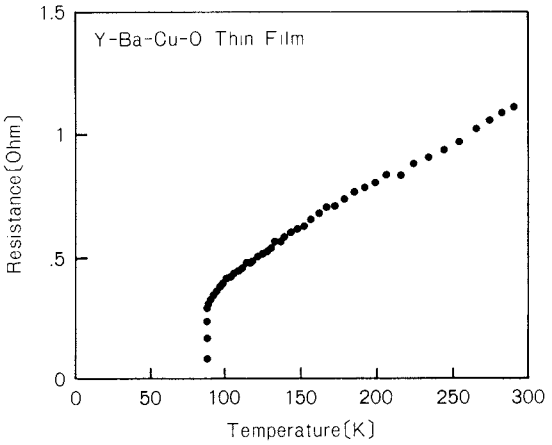

Fig. 7 Relationship between the electric resistance and the temperature of Y-Ba-Cu-O thin film

5. Conclusions

In this paper, it was summarized that Mechanofusion was an effective method for preparing superconductive oxides, and multi-component targets for superconductive thin films.

Acknowledgement

These studies have been supported by the Osaka Cooperative Research Project for High Critical Temperature Superconductors. The authors appreciate all members of this Project.

References

1) Yokoyama, T., K. Urayama, M. Naito, M. Kato and T. Yokoyama: Proceedings of the 2. Japan-Soviet Symposium on Mechanochemistry, p. 281 (March, 1988 Tokyo).
2) Yokoyama, T., K. Urayama, M. Naito, M. Kato and T. Yokoyama: *KONA*, No. 5, p. 59 (1987).
3) Naito, M., M. Yoshikawa and T. Yotsuya: to be published in *Powder and Powder Metallurgy*.
4) Yokoyama, T., A. Kondo, G. Jimbo, M. Naito and M. Yoshikawa: Preprint of the autumn meeting of Soc. Chem. Eng., Japan, G302, p. 338 (1989).
5) M. Hirabayashi: *Bulletin of the Japan Institute of Metals*, **26**, 943 (1987).
6) Yotsuya, T., Y. Suzuki, S. Ogawa, H. Imokawa, M. Yoshikawa, M. Naito, R. Takahata and K. Otani: *Japanese Journal of Applied Physics*, **28**, L972 (1989).
7) Yotsuya, T., H. Imokawa, M. Yoshikawa, M. Naito, K. Otani, Y. Suzuki and S. Ogawa: Proceedings of International Cryogenic Materials Conference (July, 1989, Los Angeles, USA).

The Symposium on Powder Technology

The Party of Powder Technology (Japan) held its 22nd symposium at the Sunshine Prince Hotel in Tokyo on August 26, 1988. The symposium was given on the theme of "The Composite Powder Synthesizing Technology and Property Evaluation." Approximately 230 participants listened to and discussed the 6 lectures on the theoretical elucidation of this leading-edge technology, the evaluation methods of composite powder properties, and the application technology of the composite powder. The titles of the lectures are listed below.

Session 1 Properties and Evaluation Methods of Composite Powder

Chairmanship: Kei Miyanami (University of Osaka Prefecture)

• Synthesizing techniques of composite powder	Masafumi Arakawa (Kyoto Institute of Technology)
• Property evaluation of composite powder	Makio Naito (Hosokawa Micron Corporation)

Session 2 Applications of Composite Powder Synthesizing Technology

Chairmanship: Genji Jimbo (Nagoya University)

• Mechanochemical phenomena in composite powder synthesizing technology	Tamotsu Senna (Keio University)
• Synthesizing method of composite functional sintering materials using inclined composition control	Ryuzo Watanabe (Tohoku University)
• Applications of mechanofusion	Tohei Yokoyama (Hosokawa Micron Corporation)
• Effects of mechanofusion treatment on metallic powder	Kouichi Tanno (Miyagi Technical College)

24th Technical Meeting

promoted by the Society of Powder Technology, Japan
held in Tokyo June 22 and 23, 1989

Theme: Recent works on precision grinding technology for fine particles

In this meeting, the three main lectures shown below and 18 technical lectures were presented relating to the diversified purposes of grinding, utilization methods of grinding equipment, grinding-related technology, and so on.

- Precision classification of fine particles (Satoshi Okuda, Doshisha University)
- A few comments on particle size evaluation – The relationship between measuring methods and obtained representative particle size – (Yasuo Kousaka, University of Osaka Prefecture)
- Diversified fine particle grinding equipment and its trends (Genji Jimbo, Nagoya University)

25th Summer Seminar

promoted by the Society of Powder Technology, Japan
held in Kannami July 11 through 13, 1989

Theme: Particle dispersion – The concepts and methods –.

In this meeting, the two main lectures shown below and 18 technical lectures were presented relating to the above theme.

- Properties of various types of fine particle dispersion systems viewed from the behavior of dielectric constant of dispersing fine particles (Tetsuya Hanai, Kyoto University)
- Dispersion/aggregation of particles and behavior of dense slurry (Masafumi Arakawa)

Powdertec Japan '88

The 7th Powdertec Japan, the biannual exposition of powder processing apparatus and equipment, was held at the International Trade Center in Harumi, Tokyo November 7 through 11. Exhibitors and visitors significantly increased compared to the previous expositions. A total of 201 exhibitors displayed their products and 81,000 people visited the exposition. (The total number of exhibitors and visitors at the previous exposition was 164 and 74,000, respectively.)

As a special program, a booth for displaying powder measuring, testing, or controlling facilities was provided, as well as two "Powder Squares." In this booth, 25 exhibitors displayed their products.

November 8 through 11, the Powder Technology Congress '88 was also held at Hotel Urashima, located near the exhibition center, to discuss the following 7 categories in 7 individual sessions. A total of 36 lectures were given at these sessions.

- Powder technology for pioneering the 21st century
- Design and evaluation of functional powder
- Fine particle relating technology supporting new material/composite material development
- Synthesis of functional powder and design of ceramic structure
- Electrostatic behavior of fine particles and their applications
- Promoting FA (factory automation) and utilization of AI (artificial intelligence) in the powder processing industry
- The latest technology relating to sub-micron particles

Photos: *Powdertec Japan '88*

Academic publication concerning powder technology in Japan (1988)

Journal of the Society of Powder Technology, Japan Vol. 25 (1988)

Title	Author(s)	Page
• Changes in the Crystal Structure of Powder Produced by a Rotating Friction Mill	S. Morohasi, N. Sasakura, N. Ooi and S. Yashima	11–18
• A Method for Measuring Dust Resistivity	N. Kogure, M. Shirahase, H. Yoshiyama and I. Tamori	19–26
• An Experimental Study of the Separation of Wood and Bark by Crushing	H. Fudoh, H. Takahashi, K. Yamaguchi and K. Endoh	77–80
• A Study on the Velocity of Particle Generation in Rapid Coagulation of Polymer Latex	H. Yasui, W. Okada and H. Morikawa	81–87
• Experimental Study on Particle Size Reduction Behavior in Vibration Ball Milling	M. Tsunekawa, Y. Yoshida and T. Takamori	88–93
• Flow and Mixing Characteristics for a Rotary-type Solid Mixer with Rocking Motion	M. Satoh, M. Marukusu, K. Miyanami, A. Naiki and S. Kondo	139–145
• The Maximum Crushing Capacity of a Wood Particle Crusher	H. Endoh, H. Takahashi, K. Yamaguchi and K. Endoh	146–149
• An Analysis of the Cascade-Forming Circulating Flow of Particles in a Horizontal Rotary Cylinder	T. Moriwaki	150–158
• Three Parametric Equations and Their Adaptability (1) —An Adsorption Equation and Mechanism for an Extended Type 1 Isotherm Classified by BDDT—	H. Utsugi, A. Endoh and N. Suzuki	196–203
• The Relationship between the Average Coordination Number and Void Fraction in Randomly Packed System of Uniform-sized Spheres Developed by Four Kinds of Computer Simulation	M. Suzuki and T. Oshima	204–208
• Morphological Characteristics of β-Sic Ultra-fine Particles Synthesized by a Newly Developed Radio-frequency (r.f.) Thermal Plasma System	A. Gotoh, H. Ikasaki, M. Kawamura, K. Sakanaka, T. Kameyama, A. Motoe and K. Fukuda	209–215
• The Adaptability of a Three-Parametric Adsorption Equation to Experimental Isotherms on Adsorbant with Micropore —Three Parametric Adsorption Equation and Its Adaptability (II)—	A. Endo, N. Suzuki, A. Komori and H. Utsugi	280–286
• Fractional Dimensions of Particle Projected Shapes	M. Suzuki, Y. Muguruma, M. Hirota and T. Oshima	287–291
• The Compressive Crushing of Powder Bed	Y. Kanda, S. Takahashi, Y. Hata and T. Honma	292–296
• The Mechanism and Limit of Fineness of a Planetary Mill Grinding	Q. Zhao, S. Yamada and G. Jimbo	297–302
• Controlled Release from Wax Coated Granules by Tumbling Agglomeration Method	T. Maki, N. Umeki and Y. Ozawa	338–343
• The Kneading an Dispersion of Magnetic Recording Materials and its Evaluation	K. Terashita, M. Mitsui, K. Miyanami, K. Sakamoto and T. Horikoshi	344–349
• The Dispersion of Carbon Black in Resin by Kneading with a Continuous Kneader and the Evaluation of the Dispersion	K. Terashita, N. Yabe, K. Izumida and K. Miyanami	354–358

Title	Author(s)	Page
• Dust Collection Performances of PTFE Porous Film Laminated Felt	M. Hirota, S. Kusaka and T. Oshima	667–672
• The Removal of Unburned Carbon from Fly-ash by a Fluidized Bed with Tapping	N. Yamada, H. Hirosue and E. Abe	732–738
• Deposition Characteristics of Fly-ash Dust on a Moving Bed of Granular Materials	N. Arashi, K. Narato and H. Kuroda	739–744
• Continuous Separation of Unburned Carbon from Fly-ash by a Gas Fluidized Bed with Tapping	N. Yamada, H. Hirosue and E. Abe	751–754
• Influences for Anisokinetic Sampling on the Measurement of Particle Concentration in Ducts	M. Samata	791

Funsai (The Micromeritics) No. 33 (1989)

Title	Author(s)	Page
• Pneumatic Classification of Sub-micron Particles under Low Pressure	H. Yamamoto, M. Machida and A. Suganuma	4–8
• Size and Form of Particles – A Study for Particle Characterizations Aided with the Fourier Coefficients –	T. Shibata, S. Nakayama and K. Yamaguchi	9–16
• Effect of Initial Powder Compact on the Homogeneity of Sintered Product	Y. Harada, K. Kuramitsu and K. Makino	17–23
• Pressure Drop due to Abrupt Enlargements in Sintered Product	Y. Tomita, H. Tashiro	24–29
• Preparation of Polymorphs of Some Crystalline Drug Powders	N. Kaneniwa, M. Otuka, T. Yamaguchi, T. Hayashi, K. Hayashi, T. Matsumoto, N. Watari and O. Unezawa	30

Kagaku Kogaku Ronbunshu Vol. 14 (1988)

Title	Author(s)	Page
• Axial Movement of Spherical Packings in a Mobile Bed	K. Tabei, M. Hasatani and M. Kuroda	26–31
• Effects of Position of Discharge of Air and Particles on Size of Products Comminuted by a Screen Mill	Y. Kuga, J. Koga and I. Inoue	38–45
• Effect of Particle Size on the Gravity Flow of Powders from a Hopper with Efflux Tube	M. Yamashiro and H. Kuno	46–53
• Runaway of Particles through Blades in Louver Type Dust Separator	K. Hiyoshi, M. Fujiwara, K. Okada, N. Miyazaki and T. Munakata	167–173
• Power Requirement and Pressure Drop in the Gas-Solid Stirred Fluidized Bed	T. Takahashi, Z. Tanaka and S. Kaseno	189–194
• Study on Process of Particles Growth in Coagulation of Latex	H. Yasui, W. Okada and H. Morikawa	223–229
• Drying and Agglomeration of Skim Milk Powder by a Vibro-Fluidized Bed	J. Koga, S. Kudo, T. Kobayashi and I. Inoue	252–255
• Characteristic of Aerated Granular Materials Discharging from an Orifice	T. Takeshita, M. Harada, H. Yoshimi, R. Yamazaki and G. Jimbo	304–308

Title	Author(s)	Page
• Power Requirement and Pressure Drop in the Gas-Solid Stirred Fluidized Bed at High Rotational Speed	T. Takahashi, Z. Tanaka, and S. Kaseno	546–548
• Heat Transfer and Fluid Flow Analysis of Sinter Coolers with Consideration of Size Segregation and Initial Temperature Distribution	T. Minoura, Y. Sakamoto, K. Hashimoto and S. Toyama	645–654
• Deposition of Aerosol Particles on a Surface Composed of Different Materials	H. Yoshida, M. Minooka and H. Masuda	655–662
• On Measurement of the Pore-Size Distribution of Contractive Plant Material	Y. Nakanishi and M. Kobari	685–688
• Penetration of Flavor Droplet in Thin Sheet Material	Y. Nakanishi, Y. Mizuno and M. Kobari	794–802

Journal of the Society of Materials Science, Japan Vol. 37 (1988)

Title	Author(s)	Page
• Formation of Silicon Nitride Whiskers from Rice Hulls	Y. Kaneko, K. Ameyama and H. Iwasaki	65–69
• Synthesis of Hydroxyapatite Powder from Rice Bran –Preparative Conditions and Shape–	F. Yamada, Y. Kaneko and H. Iwasaki	1306–1312
• Submicron Grinding of Low-soda Alumina by Ball Milling	K. Tanaka, I. Inada, K. Wakino and I. Uei	1319–1325
• Preparation of Semiconducting Powder by Ball-milling and Its Characterization	M. Nakamura, K. Kinuta and M. Arakawa	1326–1330
• Closed-Circuit Granulation by a Single Horizontal Rotating Conical Vessel –Effect of Circulating Load Ratio on the Properties of Products–	M. Sugimoto and H. Nakazawa	1331–1337
• Electric Resistance as a Measure for Estimating Randomness of Binary Solid Particle System –Sampling Technique–	Y. Fujihara, M. Odaka, K. Ohzeki and Y. Yoshimura	1338–1343
• Dispersion of Carbon Black in Resin by a Continuous Kneader and Its Assessment	N. Yobe, K. Terashita, K. Izumida and K. Miyanami	1344–1348

Journal of the Japan Society of Powder and Powder Metallurgy Vol. 35 (1988)

Title	Author(s)	Page
• Processing and Properties of Highly Dense Oxide Superconducting Ceramics Prepared by Coprecipitation Method	Y. Yamamoto, T. Furusawa, H. Seto, K. Park, K. Kuwahara, T. Hasegawa, K. Kishio, K. Kitazawa and K. Fueki	333–338

Proceedings of the Institute of Electrostatics Japan Vol. 12 (1988)

Title	Author(s)	Page
• Efficiency Test of Honeycomb Type Electrostatic Precipitator	R. Takaoka, A. Yokota, T. Matsumoto, K. Motegi and T. Adachi	204–209
• Electrostatic Surface Potential Measurement with High Resolution Probe	A. Shimada	210–215

Proceedings of the Institute of Electrostatics Japan Vol. 12 (1988)

Title	Author(s)	Page
• Removal of NO_x from Combustion Gas by Corona Discharge Induced by Very Sharp Pulse Voltage	S. Masuda and W. Yan	277–283
• Experimental Studies on NO_x and SO_x Removal by Pulse Corona Discharge	T. Urabe, Y. Wu, M. Ono and S. Masuda	354–359
• Electric Field Analysis in and around Various Voids by Fluid Flow Visualizations	K. Kaneko, R. Ohayama, H. Tabei and M. Yamazaki	360–367
• Intermittent Energization for Fly-Ash Precipitation	N. Tachibana	433–440
• Fundamental Characteristics of Cage Type Ion-Flow Anemometer	K. Asano, Y. Higashiyama and H. Okuyama	441–449

New Product News

Hosokawa Micron Corp. presents three types of Mechanofusion System for its new products.

MECHANOFUSION SYSTEM

Mechanofusion® is a novelty technology for creation of new particulate materials. By generating mechano-chemical reaction upon two or more materials, they turn out to be a new material that has new physical and chemical properties. The Mechanofusion process can be applied for a variety of combinations of particulate materials.

□ Mechanofusion System AM-20FS for the Production of Superconductive Oxides

Hosokawa Micron Corp. has developed a new technique to efficiently prepare the raw powdery materials of superconductive oxides with excellent reproducibility, and successfully created a laboratory model AM-20FS.

Specifications of AM-20FS

- Throughput per batch : 100 ~ 300 cc (powder bulk volume)
- Power required : 3.7 kW
- Revolutions per minute : Max. 2,450
- Dimensions of rotating chamber : ϕ 200 x 70 H

□ Mechanofusion System AM-15F (Standard Laboratory Type)

Features

- Producing functional particulate materials
- Powerful disintegration and blending
- Capable of controlling particle size and shape
- Create many new ideal materials

Specifications

- Throughput per batch : 100 ~ 150 cc (powder bulk volume)
- Power required : 1.5 kW
- Revolutions per minute : Max. 2,650

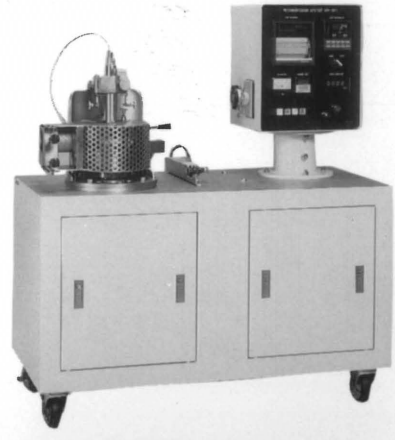

□ Mechanofusion System AM-15F (Glove Box Type)

Features

- Mechanofused treatment in an inert atmosphere
- Same function and capacity as standard type of AM-15F
- Changeable to the standard type of AM-15F

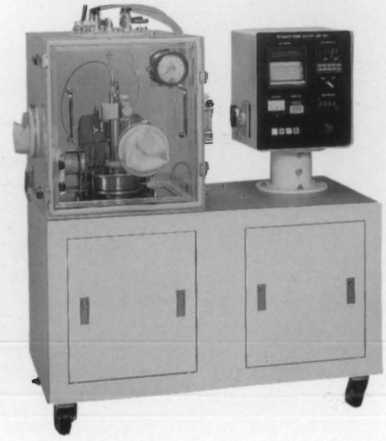

HOSOKAWA MICRON

LEADERS OF POWDER PROCESSING TECHNOLOGY, ENVIRONMENTAL SYSTEMS, FILTER MEDIA AND PLASTIC PROCESSING SYSTEMS.

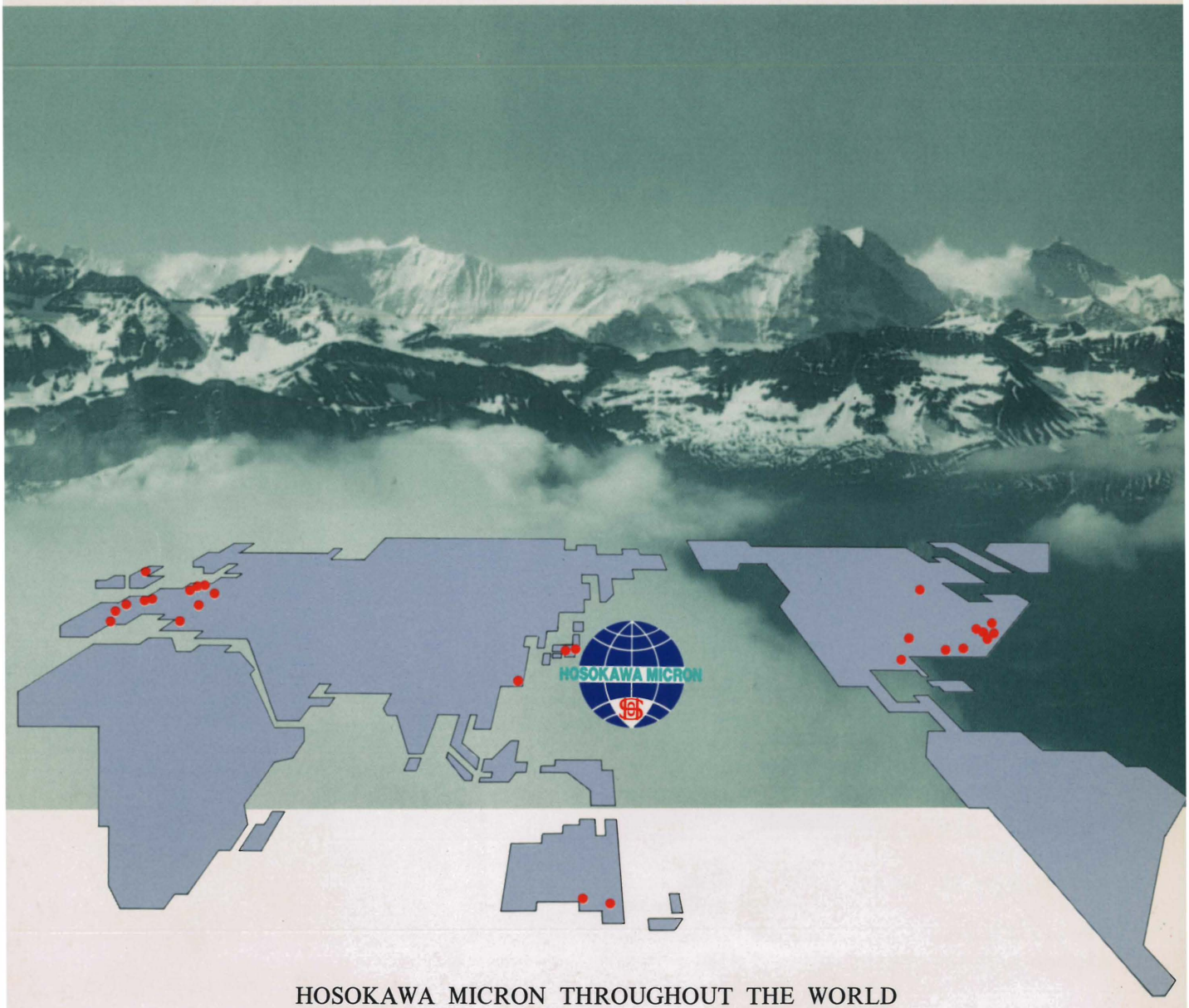

HOSOKAWA MICRON THROUGHOUT THE WORLD

Asia/Australian Block
Hosokawa Micron Corporation
5-7, 3-chome, Hommachi, Chuo-ku, Osaka 541, Japan
Telephone: 06-263-2555 Fax: 06-263-2552

Americas Block
Hosokawa Micron International Inc.
780 Third Avenue, New York, NY10017, U.S.A.
Telephone: 212-826-3830 Fax: 212-826-6612

European Block
Hosokawa Micron International BV.
World Trade Center, Strawinskylaan 249,
1077XX Amsterdam, Holland
Telephone: 020-73-5551 Fax: 020-76-2061